Hot subluminous stars:
On the Search for Chemical Signatures
of their Genesis

vorgelegt von
Heiko Andreas Hirsch
aus Schwabach

Als Dissertation genehmigt von der Naturwissenschaftlichen Fakultät der Universität Erlangen-Nürnberg

second revised version

Contents

List of Figures

List of Tables

Zusammenfassung

Diese Arbeit beschäftigt sich mit *heißen unterleuchtkräftigen Sternen* (englisch: *hot subdwarfs*) vom spektralen Typ O. Man darf sich von ihrem Namen nicht fehl leiten lassen, die Leuchtkräfte dieser Sterne sind immer noch ca. 10–1000 mal so hoch wie die der Sonne, sie emittieren den allergrößten Teil ihrer Strahlungsenergie im Ultravioletten. Erste Sterne dieses Typs wurden bereits in den 1950er Jahren klassifiziert. Da sie, ebenso wie Quasare, blaue Objekte sind, werden sie häufig in Himmelsdurchmusterungen in hohen galaktischen Breiten entdeckt, deren eigentliche Ziele Quasare und andere extragalaktische Objekte sind. Die unterleuchtkräftigen Sterne lassen sich grob in zwei Klassen einteilen, in O- und B-Sterne, oder kurz *sdO* und *sdB*, entsprechend ihrer englischen Bezeichnung *subdwarf type O/type B*.

Ihre Bedeutung in der Astronomie erhalten die sdOs und sdBs durch die Beobachtung von starken UV-Flüssen in sehr alten Sternpopulationen, wie z.B. Kugelsternhaufen und elliptischen Galaxien. UV-helle Himmelsregionen sind meist Sternentstehungsgebiete, die allerdings in Kugelsternhaufen und elliptischen Galaxien nicht vorkommen. Es hat sich herausgestellt, daß sich dieser UV-Exzess durch Populationsmodelle erklären läßt, welche die unterleuchtkräftigen Sterne berücksichtigen. Außerdem sind viele der sdBs veränderliche Sterne, sie zeigen radiale und nicht-radiale Pulsationen. Mit Hilfe von asteroseismologischen Modellen kann bei diesen Sternen der innere Aufbau erforscht werden. So läßt sich z.B. die Masse des Sternes bestimmen, eine Meßgröße, die Astronomen sonst nur in seltenen Spezialfällen (bedeckungsveränderliche Doppelsterne) bestimmen können. Auch für die Kosmologie sind sdBs und sdOs von Belang, da sie Supernova Ia Vorläufer sein können.

Die Natur der heißen sdO Sterne ist weniger gut verstanden als die ihrer kühleren und weit zahlreicheren Geschwister, der sdB Sterne. Mittlerweile ist die Zugehörigkeit der sdBs zum Horizontalast (engl.: *horizontal branch, HB*) fest etabliert, diese Sterne sind also alte, heliumbrennende Sterne nach dem Rote-Riesen-Stadium. Genauer befinden sich die sdBs auf dem heißen Ende des HB, dem Extremen Horizontalast (*extreme horizontal branch, EHB*). Dieser unterscheidet sich vom normalen HB durch die sehr dünnen Wasserstoffhüllen der Sterne, wir sehen also sozusagen direkt den nackten heliumbrennenden Kern. Für den Verlust der Wasserstoffhülle macht man starken Massenverlust im Rote-Riesen-Stadium verantwortlich. Der genaue Mechanismus ist noch nicht geklärt. Denkbar sind sowohl starke Sternwinde, als auch die Wechselwirkung zweier Sterne in engen Doppelsternsystemen. Die Frage nach dem "richtigen" Mechanismus ist Gegenstand vieler aktueller Forschungsarbeiten.

Während die kühleren sdB Sterne mit vergleichsweise einfachen LTE Rechnung zu analysieren sind, müssen die deutlich heißeren sdOs im NLTE gerechnet werden. Auch

deshalb ist die Zahl der publizierten sdB Analysen (etwa 300) deutlich größer als die von sdOs. Für letztere gibt es neben ein paar einzelnen Analysen letztlich nur die Arbeit von Ströer et al. (2007). In dieser werden die Spektren von etwa 50 sdOs analysiert. Es stellte sich heraus, daß die heliumarmen sdOs als Nachfolger von sdB Sternen anzusehen sind. Für die heliumreichen sdOs dagegen konnte keine definitive Antwort bezüglich ihres Entwicklungszustandes gefunden werden.

Um eine möglichst große Datenbasis zu haben, wurde für diese Arbeit auf den *Sloan Digital Sky Survey (SDSS)* zurückgegriffen, eine der größten photometrischen und spektroskopischen Himmelsdurchmusterungen. Dazu wurden etwa 14 000 Sternspektren visuell anhand von schnell erfassbaren spektralen Merkmalen klassifiziert. Mit diesem Teil der Arbeit verfügen wir nun über eine sehr umfassende Datenbank an klassifizierten heißen Sternen aus der im Moment wohl meist beachteten Durchmusterung. Der Großteil der Spektren stellte sich wie erwartet als Weiße Zwerge heraus, darunter befanden sich einige vorher unbekannte magnetische Weiße Zwerge. Insgesamt wurden ca. 1 500 Objekte als heiße unterleuchtkräftige Sterne erkannt, 200 davon als sdOs. Für diese sdOs wurden die Effektivtemperatur, die Schwerebeschleunigung an der Sternoberfläche und das Verhältnis von Helium zu Wasserstoff in der Atmosphäre bestimmt. Damit konnte eine statistisch asussagekräftige Datenbasis gewonnen werden. Zwei Entwicklungsszenarien bleiben im Rennen: Das Verschmelzen zweier Weißer Zwerge und das "verspätete Heliumzünden" eines Roten Riesen (*late hot flasher*).

Im ersten Szenario verlieren zwei massearme Helium Weiße Zwerge (HeWD) durch Abstrahlung von Gravitationswellen Energie und nähern sich immer weiter bis der masseärmere schließlich seine Roche-Oberfläche überschreitet, zerrissen wird und vom Begleiter akkretiert wird. Es existieren aber keine detaillierten Berechnungen für dieses Szenario.

Late hot flasher sind Sterne, bei denen das zentrale Heliumbrennen (*helium flash*) erst beginnt, nachdem sie bereits anfangen sich zum Weißen Zwerg zu entwickeln. Ausführliche theoretische Rechnungen dazu sind vor kurzem veröffentlicht worden (Miller Bertolami et al. 2008). Eine starke Anreicherung der Sternhülle mit Kohlenstoff und teilweise auch mit Stickstoff wird darin vorhergesagt.

Die Unterscheidung zwischen beiden Szenarien ist mit unseren bisherigen Mitteln der quantitativen Spektralanalyse nicht möglich, da wir bisher nur Wasserstoff- und Heliumhäufigkeiten bestimmt haben. Mit dem Einsatz neuer Atmosphärenmodelle, die auch Kohlenstoff und Stickstoff berücksichtigen, wurden in dieser Arbeit die Parameter und Häufigkeiten von knapp drei Dutzend sdOs neu bestimmt. Die gemessenen Effektivtemperaturen haben sich mit den neuen Modellen kaum geändert, aber die gemessene Schwerebeschleunigung an der Sternoberfläche, $\log g$ mit g in cm/s^2, ist um 0.2 dex niedriger ausgefallen als in bisherigen Messungen. Das löst einige Probleme mit Sternen, die sich bisher bei hohen Schwerebeschleunigungen unter der Heliumhauptreihe befanden, während dort eigentlich kein stabiles Heliumkernbrennen möglich ist. Andererseits wird die Verteilung insgesamt zu niedrigerem $\log g$ verschoben, obwohl die Zeitskala der theoretischen Sternentwicklung die sdOs nahe an die Heliumhauptreihe rückt.

Die gemessenen Kohlenstoffhäufigkeiten zeigen eine bimodale Verteilung: Knapp die Hälfte der Sterne zeigt Kohlenstoff, teilweise angereichert bis zum 10fachen des solaren Wertes, ein klares Indiz für das Anreichern der Hülle mit Produkten des 3α-Heliumbrennens. Stickstoff ist bis auf ein paar Ausnahmen leicht über dem solaren Wert. In den Sterne mit wenig bis gar keinem Kohlenstoff kann keine Mischung aus dem Kern in die äußeren

Schichten erfolgt sein, nur die Produkte des CNO-Zyklus sind sichtbar. Es gibt drei kohlenstoffreiche Sterne mit extrem geringen Stickstoffhäufigkeiten, weniger als ein Zehntel des solaren Wertes. Diese sind schwer zu verstehen: es muß Kernmaterial in die Hülle gemixt werden, aber keine CNO-Produkte, oder es darf kein CNO-Brennen stattgefunden haben.

Überraschend auffällig ist die Verteilung der Rotationsgeschwindigkeiten: Fast alle kohlenstoffreichen Sterne zeigen projizierte Rotationsgeschwindigkeiten der Sternoberfläche von $v_{\mathrm{rot}} \sin i = 10 \ldots 30 \, \mathrm{km \, s^{-1}}$. Dieser Befund ist insofern unerwartet, als die sdB Sterne sehr langsame Rotatoren sind ($v_{\mathrm{rot}} \sin i < 10 \, \mathrm{km \, s^{-1}}$), sofern sie nicht in engen Doppelsternsystemen durch Gezeitenkräfte aufgedreht wurden. Dieser Unterschied schließt einen entwicklungsgeschichtlichen Zusammenhang zwischen sdB Sternen und kohlenstoffreichen sdOs aus. Sterne mit sehr geringem Kohlenstoffanteil dagegen zeigen kaum meßbare Rotationsverbreiterungen in den Linienprofilen.

Insgesamt acht der kohlenstoffreichen Sterne sind von ihren Häufigkeiten her als *late-hot-flasher* Kandidaten anzusehen. Besondere Probleme bereiten die stickstoffreichen, kohlenstoffarmen Sterne, die so in den theoretischen *late-hot-flasher* Szenarien nicht vorkommen. Das Szenario der verschmelzenden Weißen Zwerge könnte für diese Objekte zutreffen, in Ermangelung detaillierter Rechnungen ist das jedoch nicht überprüfbar. Auch die drei Sterne mit sehr geringem Stickstoffgehalt bei übersolaren Kohlenstoffhäufigkeiten sind schwer erklärbar. Eine Möglichkeit sind sehr niedrige primoridale Metallizitäten, die Sterne wären dann also Halo-Objekte. Dies kann in Zukunft vielleicht anhand von Häufigkeitsmessungen schwererer Elemente überprüft werden. Oder auch mit Hilfe von kinematischen Betrachtungen kann die Zugehörigkeit dieser Sterne zur Halopopulation geklärt werden.

Abstract

This thesis deals with the *hot subluminous stars* of spectral class O. Although the name suggests otherwise, these stars are still 10 to 1 000 times more luminous than the sun, they emit most of their radiation energy in the ultraviolet range. First stars of this type have been categorised in the 1950ies. Since they are blue objects they often are discovered in surveys at high Galactic latitudes aiming at Quasars and other extragalactic objects. The hot subluminous stars can be divided into two classes, the subluminous O and subluminous B stars, or short *sdO* and *sdB*.

The sdOs and sdBs play an important role in astronomy, as many old stellar populations, e.g. globular clusters and elliptical galaxies, have strong UV fluxes. UV bright regions often are "stellar nurseries", where new stars are born. Globular clusters and elliptical galaxies, however, do not experience star formation. This UV excess can be explained by population models that include the hot subluminous stars. Many sdB stars show short-period, multiperiodic light variations, which are due to radial and nonradial pulsations. Asteroseismology can explore the inner structure of stars and estimate e.g. the stellar mass, a variable that astronomers can only determine in very lucky circumstances (eclipsing binaries). Hot subdwarf stars are also important for cosmology because they qualify as supernova Ia progenitors.

The nature of the sdO stars is less well understood than that of their cooler and more numerous siblings, the sdBs. The connection of the sdBs to the horizontal branch is established for many years now, accordingly they are old helium core burning objects after their red giant phase. More precisely, they are on the *extended horizontal branch (EHB)*, the hot end of the horizontal branch. EHB stars are characterised by a very low envelope mass, i.e. we see more or less directly the hot helium burning core. Strong mass loss in the RGB phase is regarded as responsible for this phenomenon. The exact mechanism, however, is still under debate.

While the cooler sdBs can be analysed with relatively simple LTE model atmospheres, the hot sdOs require much more sophisticated NLTE calculations. The large effort required for sdO analyses resulted in a relatively low number of publications on the subject, when compared with the numerous publications on sdB stars. Besides a few detailed studies of individual objects, the ≈ 50 stars analysed by Ströer et al. (2007) is the only extensive work on sdOs. They explained the helium poor sdOs as progeny of the sdB stars. But for the helium enriched sdOs, no definite statement about their evolutionary status could be found.

In order to get a large sample of sdOs, this work made use of the Sloan Digital Sky Survey (SDSS), one of the most extensive photometric and spectroscopic surveys in astronomy. About 14 000 spectra were classified by visual inspection by means of easily recognisable

spectral features. We now have a large database with classifications of hot stars. The majority of the spectra were classified as white dwarfs, among them a number of previously unknown magnetic white dwarfs. 1 500 objects were identified as hot subluminous stars, about 200 of them are sdOs. We determined effective temperatures, surface gravities and atmospheric helium abundances for these objects. Two evolutionary scenarios remain valid options for the sdOs' origin: The merging of two helium white dwarfs and the delayed helium flash of a red giant star ("late hot flasher").

In the first scenario, two low mass white dwarfs in short period orbits lose orbital energy by radiation of gravitational waves. As their orbit shrinks, the less massive one will fill its Roche lobe and get disrupted and accreted on the companion. Unfortunately no detailed calculations of the explosive nucleosynthesis exist for this scenario.

The late hot flashers are stars that do not experience the helium core flash until they leave their red giant phase and already evolve towards the white dwarfs. Miller Bertolami et al. (2008) published detailed theoretical calculations for this scenario. They predict a strong enrichment with carbon and in some cases with nitrogen by mixing processes.

A differentiation between both scenarios was not possible so far, as we only determined helium abundances. The creation of new NLTE model atmospheres which include carbon and nitrogen enabled us to measure their abundances in three dozen sdOs. Effective temperatures did not change much with the application of the new models, but the surface gravity was found about 0.2 dex lower than in previous analyses. This provides a solution for a handful of stars that until now were situated below the helium main sequence, which would not allow stable helium core burning. On the other hand, the whole distribution is shifted towards lower gravities while the theoretical calculations predict an accumulation of stars at higher surface gravities, near the helium main sequence.

The measured carbon abundances reveal a bimodal distribution: half of the objects have carbon enriched up to 10 times the solar value, a clear indication of 3α processed material mixed from the core into the envelope, the other half shows carbon strongly depleted. With some exceptions, nitrogen is above solar abundances, up to a factor of ten. Stars with very low carbon content cannot have experienced mixing of matter from the core into the envelope, only CNO-processed matter is exposed. Three stars with high carbon abundances are found that have a very low nitrogen content. These stars are not easily understood: matter from the core must have been brought into the envelope, but not the CNO-processed matter.

A surprising correlation is found for the rotational velocities with abundances: nearly all stars with high carbon abundances also have high projected rotational velocities $v_{\mathrm{rot}} \sin i = 10 \ldots 30\,\mathrm{km\,s^{-1}}$. Because the sdB stars are very slow rotating with $v_{\mathrm{rot}} \sin i < 10\,\mathrm{km\,s^{-1}}$ (unless spun up by tidal interaction in close binary systems), this disqualifies any evolutionary connection between sdBs and the carbon rich sdOs. Those stars without carbon on the other hand show no significant rotational broadening in their line profiles.

Altogether eight stars can be considered as compatible with having experienced a delayed helium flash. Those stars with high nitrogen abundances but only very little atmospheric carbon are not predicted by any late hot flasher calculation. They are considered candidates for the white dwarf merging scenario, which we cannot yet verify due to missing calculations. Another remaining problem are the three stars with high carbon, but very low nitrogen abundances. One possible explanation would be a very metal poor (halo) origin for these objects, which could be verified in the future by a quantitative analysis of

the heavier metals. Alternatively the examinations of the kinematic properties of the stars could provide clues concerning their membership to the halo population.

Chapter 1

Introduction

Hot subdwarf stars represent a poorly understood phase in the evolution of old low mass stars. Therefore we start with a short overview of stellar evolution[1] of stars with $0.08\,M_\odot \lesssim M \lesssim 2.5\,M_\odot$. In this context we place the hot subdwarf stars and point out their peculiarities. A detailed description of the rivalling formation channels is then presented in chapter 2.

1.1   Hot subdwarfs in the general context

Many aspects of the stars' lifecycle are known very well. Most of their lifetime they spend on the *main sequence* in the *Hertzsprung Russell Diagram (HRD)*, which displays luminosity versus temperature (Figure 1.1). After hydrogen exhaustion in the core, the burning shifts into the shell and the star becomes a *red giant* on the *red giant branch (RGB)*. Eventually, the degenerated core violently ignites helium burning *(helium flash)*, and the star settles on the *Horizontal Branch (HB)*, a nearly horizontal region in the HRD. The star now has two sources of luminosity: the helium burning core and the hydrogen burning shell, slowly burning its way outwards. History repeats itself and after helium exhaustion in the core, a helium burning shell in the now helium enriched region above the core and below the still burning hydrogen shell is established. Again the star inflates to gigantic dimensions and is called an *AGB* star (*asymptotic giant branch*). On the AGB the stars ejects their envelopes into interstellar space, visible as planetary nebulae for some 10 000 years, while the degenerate C/O core slowly cools down and becomes a *white dwarf*.

In spite of this clear picture of stellar evolution we have reached, there are stars of which we know their future, but don't know how they came into existence in the first place. The stars we shall consider are hot stars showing spectral signatures typical of B- and O-stars. But with their high surface gravity and correspondingly small size of $R \approx 0.1 - 0.3\,R_\odot$ compared to those of O- and B-stars on the main sequence, $R \approx 10 - 20\,R_\odot$, they have lower luminosities than their huge relatives. Hence they are commonly called *subluminous stars* of spectral type O and B, or — as the (perhaps misleading) term *dwarfs* is already used for the main sequence stars – *subdwarf O (sdO)* or *subdwarf B (sdB)* stars. They were first discovered by Humason & Zwicky (1947) and systematically analysed by Newell

---

[1]A more extensive overview of low mass stellar evolution can be found in Catelan (2007a) and references therein.
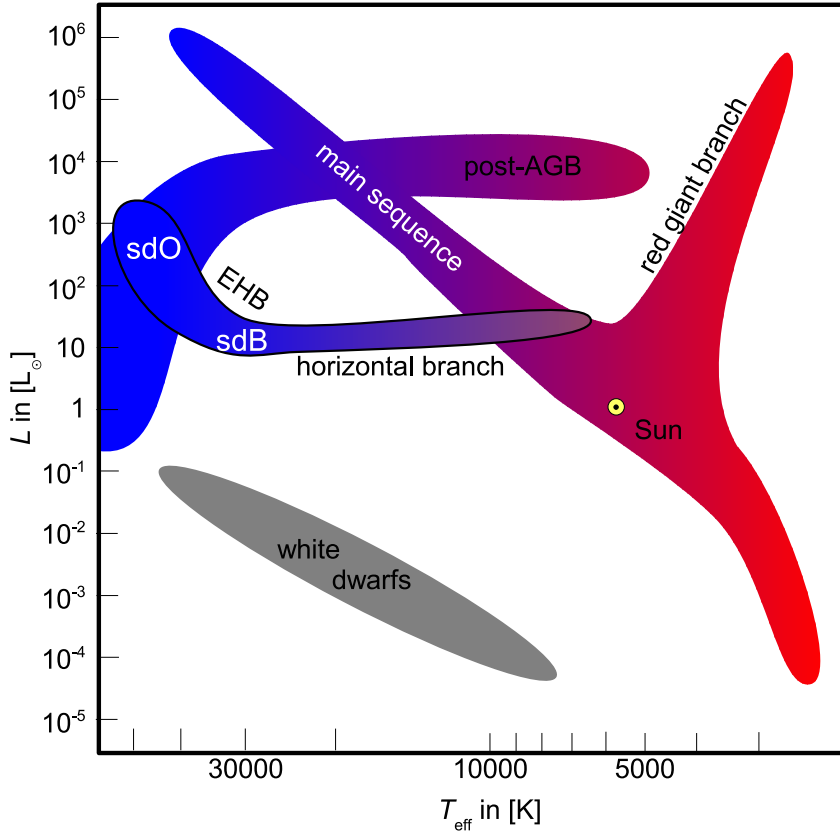
Figure 1.1: The Hertzsprung-Russell diagram: luminosity plotted over effective temperature. Important regions are outlined. The hot subdwarfs are on the very left at hot temperatures and luminosities around $100\,L_\odot$.

(1973) and Greenstein & Sargent (1974). Many surveys in the following decades, like the Palomar Green Survey (PG; Green, Schmidt & Liebert 1986), the Hamburg ESO Survey (HE; Wisotzki, Wamsteker & Reimers 1991) and the Hamburg Quasar Survey (HS; Hagen et al. 1995), originally aimed at quasars, turned out to be dominated by faint blue stars, amongst them many hot subdwarfs (see Fig. 1.2). The *Sloan Digital Sky Survey (SDSS)* provides the latest additions to the list of identified hot subdwarfs. This survey has more than 1 000 hot subdwarfs in its spectroscopic database.

Hot subdwarfs evolve directly into white dwarfs and are the main precursors for the less massive ones. They are responsible for a phenomenon called *UV upturn* or *UV excess (UVX)* in spectra of elliptical galaxies and the bulges of spiral galaxies (Catelan 2007b)[2]. To the surprise of astronomers, these old and red objects show an increase in flux for wavelengths shorter than 2 000 Å. The extent of the UV excess is governed by basic parameters such as the population's age, the helium content, the metallicity and mass loss rates (Han, Podsiadlowski & Lynas-Gray 2007). Hence the importance of the subdwarf stars in understanding the properties of galaxies is apparent and our knowledge of galactic evolution

---

[2]For an extensive review of the UVX phenomenon see O'Connell (1999).
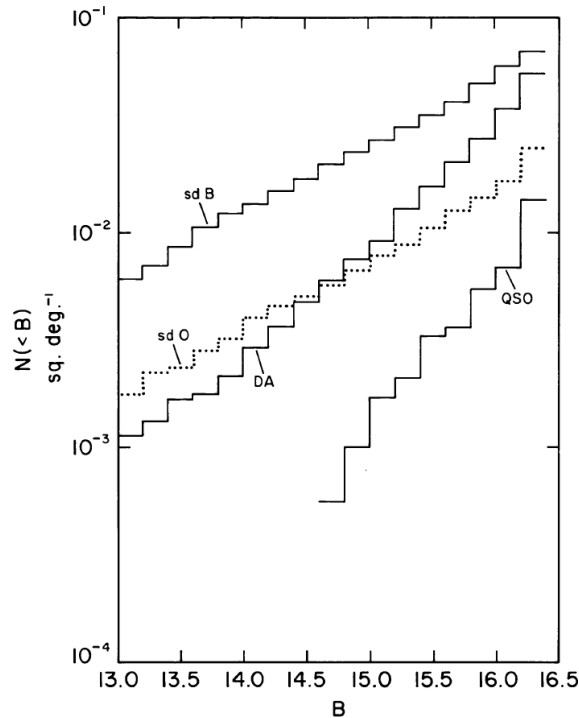
Figure 1.2: Cumulative object counts over magnitude. Taken from Green, Schmidt & Liebert (1986).

cannot be complete without understanding the hot subdwarfs.

Altmann, Edelmann & de Boer (2004) used the kinematics of sdBs for Galactic population studies. Hot subdwarfs are even relevant for cosmology, as some of them might qualify as SN Ia candidates (Geier et al. 2007a; Maxted, Marsh & North 2000). Geier et al. (2008) suggested that a substantial number of sdBs have an invisible compact companion, i.e. a neutron star or a black hole.

1.2 Properties of subdwarfs

Heber et al. (1984), Heber (1986) and Saffer et al. (1994) identified the hot subdwarfs as the field counterparts to the *Extended Horizontal Branch* seen in globular clusters. It is now well established that the sdBs are helium burning cores of about half a solar mass, covered by a very thin hydrogen envelope of $M_{env} < 0.02 \, M_\odot$. In contrast to the normal HB stars, this envelope is too thin to sustain hydrogen shell burning. The EHB is a sequence of stars with about the same core mass and of ever thinner envelope masses, reaching from the normal HB with $M_{env} > 0.025 \, M_\odot$ down to the Helium Main Sequence (HeZAMS, Paczyński 1971) of pure helium stars, i.e. $M_{env} = 0 \, M_\odot$. Essentially, with diminishing envelope mass we see more and more directly onto the star's hot core.

The number ratio of sdO to sdB stars is found to be 1:3 in the PG survey (see Fig. 1.2). Though sdBs and sdOs occupy neighbouring areas in the HRD, they are quite different. First, sdO stars do not lie directly on the EHB and their relation to it is not clear. They

can in part be identified with either post-EHB, post-RGB or post-AGB stars. Second, sdBs are extremely helium poor, with $y = N_{\mathrm{He}}/N_{\mathrm{H}} \approx 10^{-4}$ (in the more common logarithmic notation $\log y \approx -4$)[3]. SdOs, on the other hand, show a variety of helium abundances over several magnitudes, ranging from $\log y = -3$ to $\log y = +3$. Based on this, an evolutionary connection between these two types of stars has always been considered questionable. It is not clear, how diffusion (the game between gravitational settling and radiative levitation), thought to be responsible for the helium deficiency of sdBs, should turn them again into helium rich objects. Radiative forces were shown to be at least one order of magnitude too weak (Michaud et al. 1989). Groth, Kudritzki & Heber (1985) found a He II/He III convection zone in the photosphere of helium rich sdOs. A helium poor photosphere, however, does not develop convection and therefore cannot turn into a helium rich one.

Some subdwarfs are known to show wind signatures (Heber et al. 2003b; Rauch 1993), however only in stars on the lower end of typical surface gravities. Hamann et al. (1981) derived mass loss rates by winds in the range $\dot{M} = 10^{-9} \ldots 10^{-12}\, M_{\odot}/\mathrm{yr}$, albeit for very low surface gravities ($\log g = 4.2 \ldots 4.8$). Diffusion calculations were carried out by Unglaub (2008) and predict that for most sdB stars homogeneous winds are not possible, i.e. the winds are expected to be metallic. This implies that the gravitational settling of helium is not hindered by stellar winds.

Another interesting property of the subdwarfs is their ability to show pulsations. Since the theoretical prediction of pulsations in sdB stars by Charpinet et al. (1996) and their discovery a year later (Kilkenny et al. 1997), asteroseismology models have made a giant leap and are now applied on a regular basis to determine stellar masses, see for example Brassard et al. (2001). Theoretical knowledge is still scarce, but first steps into modelling pulsation instabilities in sdOs were made by Rodríguez-López et al. (2006) and Jeffery & Saio (2007), who found the models unable to excite pulsation. Surprisingly the sdO star SDSS J160043.6+074802.9, a spectroscopic binary, was serendipitously found to be a pulsator with at least 10 short period modes of 60–120 s (Woudt et al. 2006). An extensive search for pulsators by Rodríguez-López, Ulla & Garrido (2007) found 31 out of 56 sdOs to be promising candidates. Recently, with the inclusion of radiative levitation, Fontaine et al. (2008) were able to construct models for SDSS J160043.6+074802.9 which show pulsation instabilities caused by the κ-effect (a local opacity bump due to iron). In the near future asteroseismology could therefore be used to probe the stellar structure of sdOs and reveal clues to their nature and origin.

Finally, the sdBs are generally very slow rotators, at least those not in short period binaries. Upper limits given for measured projected rotational velocities are $v_{\mathrm{rot}} \sin i \lesssim 10\,\mathrm{km\,s}^{-1}$ (Heber & Edelmann 2004; Edelmann, Heber & Napiwotzki 2006; Geier 2009). For short period binaries however, rotational broadening is clearly visible for many stars and is seen as a result of tidal locking (see e.g. Geier et al. 2007b).

Recently Ströer et al. (2007) reported that all helium rich sdOs show lines of carbon and/or nitrogen in their optical spectra, while none of the helium poor objects does. They suggest a new classification scheme introducing the subclasses C-, N-, CN- or 0-type. With the solar helium abundance ($\log y = -1$) found to be a dividing line between the 0- and the other types, they call all sdOs with supersolar helium abundance *helium-enriched* and

---

[3]We will use number ratios for abundances throughout this thesis, unless explicitly stated otherwise. $\log y$ is the helium-to-hydrogen ratio, but given the large variation of this ratio, carbon and nitrogen abundances used in later chapters will be relative to the total particle number.

the stars with $\log y < -1$ *helium-deficient*.

We provide the reader with an impressive justification for the CN-types in Fig.1.3. Four spectra, each one of an 0-, C-, CN- and N-type sdO, have the most important carbon, nitrogen and helium lines flagged. These spectra were taken with the FEROS spectrograph at the ESO 2.2m telescope and folded with a Gaussian of $0.3\,\text{Å}$ FWHM. The selected wavelength range is very small, otherwise the narrow and crowded metal lines would hardly be seen and impossible to be distinguished. In the chosen range, however, the 0-type hydrogen rich sdO at the bottom only appears as a straight line with the exception of He II $4\,686\,\text{Å}$, due to the lack of metal lines. For a complete list of spectral lines see table E.1.

1.3 Spectral classification

The spectral classification of hot subdwarfs and related objects is best defined in the optical part. Although there exist elaborate schemes with numerous subclasses (see Drilling et al. 2003; Jeffery et al. 1997), in practise the following simple method is used most often.

HBB/HBA Horizontal branch stars of spectral type A and B: $T_{\text{eff}} < 20\,000\,\text{K}$. Narrow Balmer lines as deep as 50% or more relative to the continuum.

sdB Subdwarf type B: $T_{\text{eff}} = 20\,000\ldots30\,000\,\text{K}$. Broad Balmer lines of moderate depth. No helium or only He I $4472\,\text{Å}$ is visible.

sdOB Subdwarf type OB: $T_{\text{eff}} = 30\,000\ldots40\,000\,\text{K}$. Broad Balmer lines of moderate depth. Spectrum shows He I lines and He II $4686\,\text{Å}$.

sdO Subdwarf type O: $T_{\text{eff}} > 40\,000\,\text{K}$. The Balmer lines are shallower than in sdBs. He II and He I for the cooler ones are visible.

HesdO Subdwarf type O, helium rich: The He II Pickering series dominates the spectrum, Balmer lines are not or hardly visible. A considerable number of He I can be seen, depending on T_{eff}.

HesdB Subdwarf type B, helium rich: rarely used, this designates sdB stars with exceptionally strong He I lines.

Sometimes quite annoyingly, the division into all these classes is often neglected in literature and "sdB" is used for all (He)sd(O,OB,B) stars. Also frequently used is "sdB" for sdBs and sdOB for all hotter subdwarfs. When referring to subdwarfs in globular clusters, the term "EHB star" is the most frequent one, a photometric classification in the colour-magnitude diagram. This includes both sdBs, sdOBs and sdOs.

When confronted with an optical spectrum, the number of visible Balmer lines n in the spectrum is a helpful criterion for a first classification. With growing surface gravities the pressure inside the atmosphere rises, leading to "pressure ionisation" of the higher atomic levels. Giant stars therefore have the highest number of Balmer lines, $n > 23$, horizontal branch A-stars (HBA) have $n < 19$ and for HBB $n = 15\ldots14$. Subdwarfs show only 10–12 Balmer lines while the high gravity white dwarfs have $n < 10$ (Greenstein & Sargent 1974).

Note that, following Ströer et al. (2007), in this work we do not distinguish between HesdO and sdO, with the helium abundance of $\log y \approx 0$ being the approximate dividing line. In this work we use the terms *helium-enriched sdO* and *helium-deficient sdO* instead, where the solar helium abundance $\log y = -1$ was established as the defining abundance.
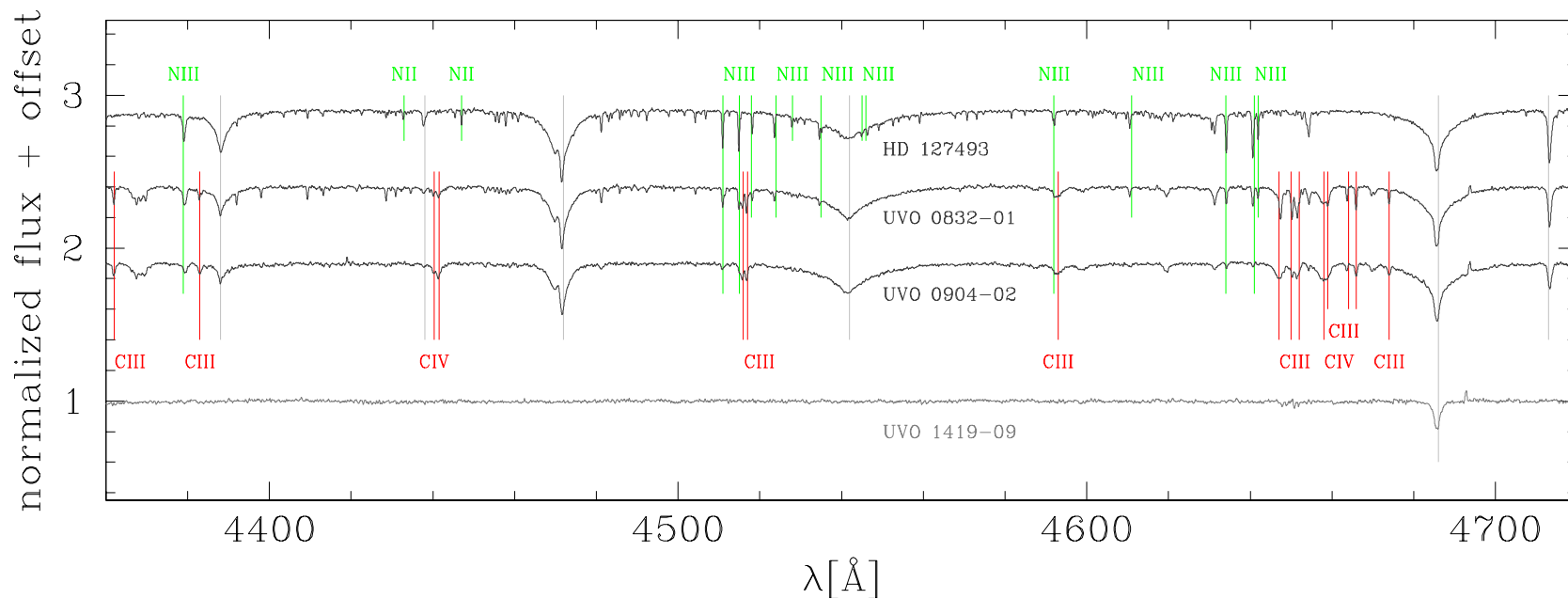
Figure 1.3: Top to bottom: helium-enriched N-type, CN-type, C-type and helium-deficient 0-type. Helium and hydrogen lines are marked by grey lines, the most prominent features of carbon and nitrogen are marked by red and green lines. The emission feature redwards of He II 4686 Å is not real. For better clarity features from titanium, oxygen, silicon, neon, etc have not been labelled, see table E.1.

Chapter 2

Evolutionary scenarios & formation channels

A number of scenarios trying to explain the subdwarfs' evolution have been put forward. The question, however, as to how the stars lose nearly all of their envelope at exactly the right time before the helium core flash, is still unanswered.

2.1 Binary star evolution

Mengel, Norris & Gross (1976) were the first to explore the interaction of two stars in a binary system as a possibility to get rid of the envelope. In a sufficiently close binary system, if one component becomes a red giant and extends its radius beyond the Roche lobe, mass will be transferred through the inner Lagrangian point L_1 onto the companion star. This is the *stable Roche lobe overflow (RLOF)*. If the mass transfer occurs faster than the companion can accrete the material, a hot envelope around the accretor may form, which eventually will also fill the Roche lobe (Iben & Livio 1993; Paczyński 1976). A *common envelope (CE)* engulfing both stars is the result. Through dynamical friction, orbital energy is deposited into the CE, leading to a spiral-in of both stars and the ejection of the surrounding material. Even two such events are possible with both stars successively reaching red giant dimensions and initiating mass transfers, stable or unstable.

Maxted et al. (2001) found two-thirds of all sdBs in binary systems with short periods from hours to days and their companion stars to be mostly white dwarfs. This was supported by the work of Edelmann et al. (2005). While setting on a somewhat lower number fraction, Napiwotzki et al. (2004b) confirmed the high binary fraction, but not for the helium-rich sdOs, where only one out of 23 stars shows signatures of radial velocity variations. Close binary evolution seems to be a very important channel for the sdBs and the helium-deficient sdOs, but not so for the helium-enriched ones.

Another possible channel is the merging of two low mass helium white dwarfs (Webbink 1984; Iben & Tutukov 1986; Iben 1990). Two low mass white dwarfs with sufficient small separation and helium cores instead of the C/O cores of most white dwarfs — formed for example via a RLOF and a CE phase — will lose orbital energy due to radiation of gravitational waves. Filling its Roche lobe, the less massive one will be disrupted and accreted on the primary, which will eventually gain enough mass to start helium burning. Any hydrogen left in their atmospheres will probably be mixed into the deeper and hotter

Stable Roche-Lobe Overflow   **Common Envelope Ejection**

Two MS-Stars, mass ratio q < 1.5   Two MS-Stars, mass ratio q > 1.5

RLOF in RGB Phase of the more
massive star, stabe accretion by the
companion star

RGB donor transfers more mass
than its MS companion can accrete

The degenerate He-core remnant of the
RGB star may still ignite He-burning,
resulting in a wide sdB+MS system

The companion star also fills its Roche
lobe, leading to a CE. Both stars lose
orbital energy within the CE.

Eventually the CE is ejected and if the
degenerate He-core of the former RGB
star ignites helium, a close MS+sdB
binary is the result.

Figure 2.1: Roche Lobe Overflow (RLOF) and Common Envelope (CE) ejection, based on Podsiadlowski (2008).

interior and will be burnt rapidly. This channel leaves behind a core helium-burning object with very little or no hydrogen in the atmosphere.

Saio & Jeffery (2000) and Jeffery & Saio (2002) explored this scenario in more detail. They predicted an enrichment of the remnant's atmosphere with nitrogen as the CNO processed helium ash of the donor star covers the helium-burning interior of the newly formed subdwarf. Jeffery (2002) suggested V652 Her to be the product of such a merging process. Calculations of Gourgouliatos & Jeffery (2006), however, showed that the merging product will rotate faster than its breakup velocity. Angular momentum therefore has to be lost during the merging process or a few million years thereafter, for example by mass loss that transports orbital energy outwards, or by magnetic fields, which are commonly invoked for braking. And indeed, kilo-Gauß fields have been observed in hot subdwarfs, both in sdBs, helium-rich and helium-poor sdOs (O'Toole et al. 2005; Valyavin et al. 2006).

In their extensive binary population study Han et al. (2002, 2003) considered these three channels of binary evolution: i) common envelope ejection, ii) stable Roche lobe overflow and iii) the merging of two HeWDs. A number of unknown parameters were varied, resulting in a dozen simulation sets differing in the critical mass ratio for stable versus unstable RLOF q_{crit}, the common envelope ejection efficiency α_{CE} and the thermal contribution to the envelope's binding energy α_{th}. The last two parameters can be understood

through the condition for common envelope ejection:

$$\alpha_{\mathrm{CE}} |\Delta E_{\mathrm{orbit}}| > |E_{\mathrm{grav}} + \alpha_{\mathrm{th}} E_{\mathrm{th}}| \tag{2.1}$$

where $\Delta E_{\mathrm{orbit}}$ is the change in orbital energy through spiral-in process, E_{grav} is the gravitational binding energy of the envelope and $\alpha_{\mathrm{th}} E_{\mathrm{th}}$ is a fraction of the thermal energy in the envelope. The right hand side of this equation is obtained by full stellar structure calculations. This elaborated parametrisation is a more realistic picture of the physics behind the process, but on the other hand brings along the risk of too many free parameters. Through comparison with published samples of binary sdB stars of known period, they found the best match for the Roche lobe overflow efficiency α_{RLOF} (ratio of mass accreted by the secondary to mass lost by primary) to be $\alpha_{\mathrm{RLOF}} = 0.5$.

Although binary interaction easily provides the required mass loss, this picture cannot be complete: Moni Bidin et al. (2006) searched for radial velocity variable stars in globular clusters and were forced to assume a binary fraction of less than 20% in NGC 6752. A possible solution was presented by Han (2008), who predicted a rise of the contribution of mergers to the EHB population with time. Dynamical interaction in GCs is more common than in the field and could therefore either harden or disrupt binaries, the former leading to a shorter timescales for mergers.

2.2 Canonical evolution

As the helium flash at the tip of the RGB always occurs at about the same helium core mass $M_{\mathrm{core}} \approx 0.46 \ldots 0.5 \, M_{\odot}$, only slightly dependent on metallicity and helium abundance, the horizontal branch is defined by helium core burning stars differing only in their hydrogen burning shell masses. With decreasing M_{env} the star is situated at the bluer (hotter) part of the horizontal branch until, at envelope masses less than $0.02 \, M_{\odot}$, no hydrogen shell burning is possible anymore. This is the *extended horizontal branch (EHB)* and such stars will not climb the AGB but directly evolve to the white dwarfs *(AGB-manqué stars)*.

One possible way to remove the envelope are strong stellar winds. Especially RGB stars are known to show winds. The mechanism for this, however, is far from understood (Espey & Crowley 2008) and we still rely on the empirical Reimers' mass loss formula (Reimers 1975):

$$\dot{M} = -4 \cdot 10^{-13} \, \eta_{\mathrm{R}} \frac{L}{gR} M_{\odot} \, \mathrm{yr}^{-1} \tag{2.2}$$

with luminosity L, surface gravity g and stellar radius R in solar units. Reimer's mass loss parameter $\eta_{\mathrm{R}} \geq 0$ depicts the mass loss efficiency and is usually given as $\eta_{\mathrm{R}} \lesssim 0.6$ for RGB stars (Dorman, Rood & O'Connell 1993).

Most calculations do not follow the entire evolution from the zero-age main sequence to the post (extended) horizontal branch stages as the helium flash itself is difficult to model. So this episode is frequently skipped and calculation continues directly on the horizontal branch. Mass loss is simulated by the remove of the envelope near or at the tip of the RGB. This is a valid simplification as the wind only affects the convective envelope and not the core until the very late stages when the envelope is reduced to a few thousandths $M_{\odot}$ (Castellani & Castellani 1993).

Dorman, Rood & O'Connell (1993) carried out extensive calculations for post-(E)HB evolution. They simulated the horizontal branch by stellar models acquired from helium

cores of RGB stars with a small hydrogen rich envelope ($0.003\,M_\odot \leq M_{\mathrm{env}} \leq 0.5\,M_\odot$) added. To account for the carbon production during the helium flash, the cores were enriched in carbon. These models were then evolved from the zero age EHB (ZAEHB) to the terminal age EHB (TAEHB), defined by helium exhaustion in the core, and further through helium shell burning. A lifetime of $\approx 110\,\mathrm{Myrs}$ for stars on the EHB and $\approx 20\,\mathrm{Myrs}$ on post-EHB evolution was predicted and the authors concluded that the ratio of EHB to post-EHB objects is expected to lie around 1 to 5 or 1 to 6.

The main problem with this scenario is the finetuning required for the mass loss. If mass loss is too strong the star will skip the HB stage and become a low mass helium white dwarf. Too small mass loss on the other hand will place the star on the red end of the horizontal branch. The hottest stars produced by canonical evolution have $T_{\mathrm{eff}} \approx 31\,000\,\mathrm{K}$ (Brown et al. 2001). All hotter subdwarfs, i.e. all sdOBs and sdOs, must be matched by post-EHB evolution.

2.3   Late hot flashers

A red giant with strong, but still plausible mass-loss rates can reach a mass comparable to its core mass. At that point, the star will "peel off" the RGB before the onset of helium core burning and move at constant luminosity across the HRD to high temperatures and finally settle on the WD cooling curve (*RGB-stragglers, flash-manqué stars*). However, depending on the mass loss efficiency η_{R}, the core may still ignite helium even with the star on the WD cooling curve (Castellani & Castellani 1993). These stars are called *late hot flashers*. Calculations by D'Cruz et al. (1996) showed that for a fairly wide range of $\eta_{\mathrm{R}} = 0.65\ldots 1.1$, depending slightly on metallicity, the star will become a hot He-flasher with core masses of $M_{\mathrm{core}} = 0.45\ldots 0.5\,M_\odot$. Also they concluded that in principle there should be no lower limit for the envelope mass. Sweigart (1997) suggested that internal rotation of RGB stars can lead to helium mixing from the hydrogen shell into the envelope, resulting in higher mass loss rates by increasing the luminosity at the tip of the RGB.

This late hot flasher scenario was further developed by Brown et al. (2001) by continuous calculation of stellar models up to the helium flash. Mass loss was calculated by eq. 2.2, for $\eta_{\mathrm{R}} = 0\ldots 0.817$ (no flash mixing), $0.818 \leq \eta_{\mathrm{R}} \leq 0.936$ (flash mixing) and $0.937 \leq \eta_{\mathrm{R}} \leq 1.0$ (flash-manqué). Though the calculations were terminated due to numerical problems when flash mixing started, they predicted most if not all of the envelope hydrogen to be consumed and a surface carbon abundance of 4% by mass, a result supported by full computation of the late hot flasher evolution by Cassisi et al. (2003). The envelope remaining for the flash mixing cases is nearly constant $M_{\mathrm{env}} \approx 6 \times 10^{-4}\,M_\odot$ and independent of the actual mass loss parameter. Moehler et al. (2004, 2007) applied these models to some success for the blue hook stars in NGC 2808 and ω Cen. The need to differentiate the late hot flashers into *deep mixing* and *shallow mixing* was first discovered by simulations of Lanz et al. (2004). In Figure 2.2 (taken from Lanz et al. 2004), four sequences for different mass loss parameters leading to hot EHB stars are plotted: The top left panel shows a standard helium flash at the tip of the RGB leading to the cooler HB stars. The flash may also occur at the top of the WD cooling track ("early hot flasher", see top right panel). Only in bottom panels in Figure 2.2, the late hot flashers, the flash convection reached into the envelope, mixing hydrogen into the helium burning core and helium and carbon from the core into the envelope. Finally carbon and helium
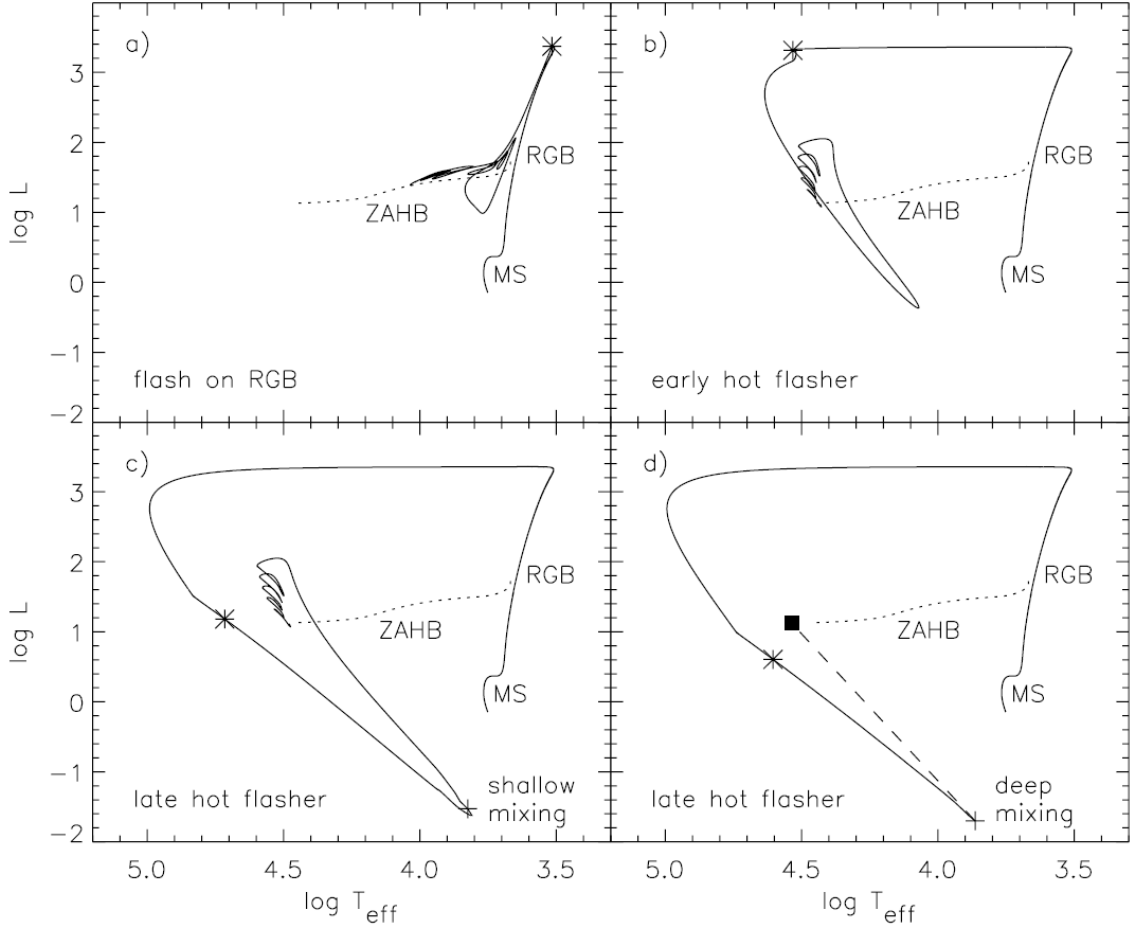
Figure 2.2: Four sequences of evolution from the main sequence to the horizontal branch for different mass losses. The peak of the helium flash is marked by an asterisk. *Top left:* Normal mass loss, the HeFlash occurs at the top of the RGB and a normal HB star is formed. *Top right:* Early hot flasher. *Bottom left:* Late hot flasher with shallow mixing. *Bottom right:* Late hot flasher with deep mixing. Figure taken from: Lanz et al. (2004).

are dredged up to the surface. This is very similar to the "born again" scenario, suggested for the formation of extremely hydrogen deficient R CrB stars. Those are stars already on their post-AGB evolution when experiencing a very late helium shell flash which mixes hydrogen into the star's interior (e.g. Renzini 1990).

Miller Bertolami et al. (2008) did extensive stellar evolution calculations for different mass loss rates and stars of different initial metallicities. Schematic Kippenhahn diagrams from their paper are depicted in Figure 2.3. The ordinate is the star's radius from the core up to the surface, time runs along the x-axis. Convection is present in the hatched areas, yellow indicates inert regions and red is active energy production and nucleosynthesis through fusion processes. Scales both in time and stellar radius are in arbitrary units.

Shallow mixing (SM): If the star ignites helium early while the hydrogen shell burning is still very luminous, an entropy barrier is maintained by the CNO burning and the
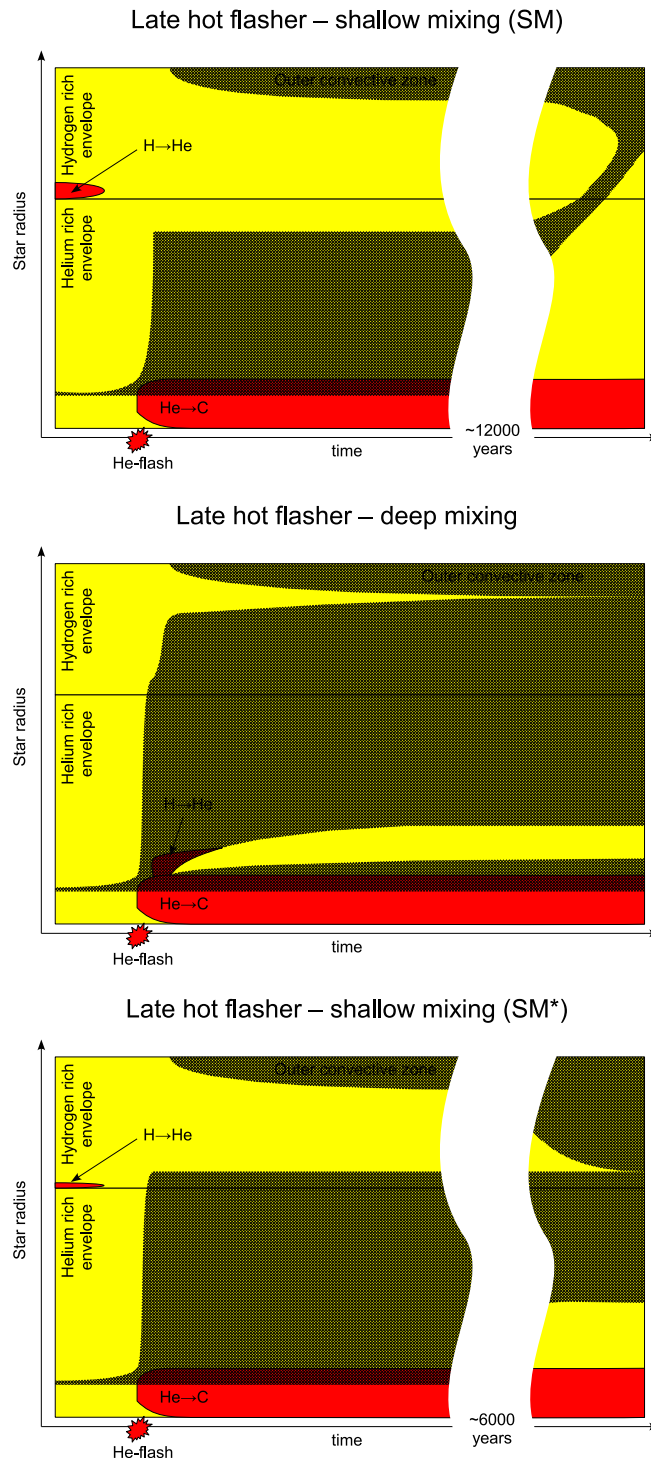
Figure 2.3: Schematic Kippenhahn diagram of the different mixing cases of the late hot flasher scenario. For details see text. Adapted from Miller Bertolami et al. (2008).

interior convection zone powered by the helium flash cannot pass this barrier. In Fig. 2.3, upper panel, this can be seen at the transition from the helium rich to the hydrogen rich envelope where CNO burning before the onset of the helium flash is still active. The interior convection zone powered by the helium burning mixes carbon enriched material into the inner envelope, but initially fails to reach the hydrogen rich outer envelope. Instead the convection zone will shrink and move slowly outwards. Meanwhile the energy produced by the helium burning causes the star's structure to change and it will move towards the EHB. A very shallow outer convective zone, which grows slowly inwards, is established. After $\approx 12\,000$ years both convective zones merge, leading to a dilution of the hydrogen envelope with the nitrogen enriched helium ash of preceding CNO processes and carbon produced in the helium core flash.

Deep mixing (DM): In cases in which the shell hydrogen burning is negligible, as shown in Figure 2.3, centre panel, the inner convective envelope reaches into the outer hydrogen rich layers. This mixes protons into the carbon enriched core where they are burnt rapidly. As a consequence of this additional luminosity, an entropy barrier forms at the hydrogen burning location, splitting the interior convective zone, which — now driven by the hydrogen burning — grows ever further into the upper layers. The result is a runaway process, as the growing convective zone brings down more protons to be burnt which in turn drives the convection further outwards. The hydrogen burning can reach luminosities comparable to those of the He-flash, or even outshine them. This H-flash consumes almost all hydrogen and is the reason for the hydrogen deficiency. In Figure 2.3, centre panel, the rapid growth of the convective zone shortly after its penetration into the hydrogen rich layers is clearly visible. Some ten years later the outer and the inner convection zones meet and the star's surface becomes extremely hydrogen deficient, predicted hydrogen abundances are $X = 10^{-4} \ldots 10^{-6}$.

Shallow mixing with some H-burning (SM*): An "in between" scenario exists, where the shell CNO burning is still active but very weak. See Figure 2.3, bottom panel. Although the inner convective zone reaches the hydrogen rich envelope, the amount of protons mixed downwards is too small to start the runaway process present in the deep mixing scenario. Only a small amount of hydrogen is burnt and after $\approx 6\,000$ years the convection zones merge. The star becomes hydrogen deficient, but with a significant amount of hydrogen left. Numbers given are $X = 10^{-2} \ldots 10^{-3}$.

The shallow mixing gains importance with increasing metallicity: In low metallicity stars, only 4% of the mass range in which mixing occurs is shallow mixing. This rises up to 17% for super solar metallicity.

2.4 Non core burning evolution

As elaborated in the precedent section, the star will fail to ignite the helium core completely if very high mass loss rates are assumed. Their evolution, as calculated by Driebe et al. (1998), leads these flash-manqué post-RGB stars of $M \approx 0.4 \ldots 0.27\,M_\odot$ through the sdO domain on short timescales of $3 \ldots 6 \times 10^5$ years. Heber et al. (2003a) and O'Toole et al. (2006) report on two cooler ($T_{\mathrm{eff}} \lesssim 20\,000\,\mathrm{K}$) post-RGB objects. However, if they are single stars, the progenitors of these objects must be low mass stars ($M < 0.5\,M_\odot$) which have main sequence lifetimes longer than Hubble time. Their evolution must therefore be affected by interactions with a companion star in close binary systems, even closer than

for sdBs because the mass loss must be strong enough to prevent the helium core flash completely. Surface helium abundances are not expected to be changed much and the spectra would still be dominated by hydrogen Balmer lines, exactly as observed.

Canonical post-AGB stars on their way to the white dwarf graveyard also come close to the hotter and most luminous sdOs (Schönberner 1979, 1983). But due to their short lifetimes of only some 10^4 years, their number can be expected to be quite small.

2.5   Summary and discussion

In this chapter we have introduced three different theories for the sdOs' evolutionary status: *(i)* evolved EHB stars (see chapter 2.2), *(ii)* independent production of both sdOs and sdBs through enhanced mass loss (binary interaction, winds, see chapters 2.1 and 2.3), and *(iii)* sdOs on their way through the EHB region "by chance" (post-RGB, post-AGB, see chapter 2.4).

Although not to be dismissed entirely, given the short timescales of *(iii)*, this option must be regarded as highly unlikely, at least for the complete sdO population. Case *(i)* presents not a real solution, but shifts the quest for the hot subdwarfs' origin from the hotter sdOs to the cooler sdBs.

Should the late hot flasher scenario be valid and a major contributor to the subdwarf population, the number of flash-manqué stars, i.e. helium white dwarfs, is also expected to be high (Castellani, Castellani & Prada Moroni 2006). A recent study of WDs in the old and metal rich open cluster NGC 6791 by Kalirai et al. (2009), showed two thirds of them to be undermassive with $M < 0.46\,M_\odot$. Although they are of spectral type DA, their low mass makes them flash manqué stars. This is further supported by the inconsistency of the cluster's ages determined from RGB turn off models and white dwarf cooling sequences, which is subsequently solved with the use of cooling sequences for helium rich WDs. A colour-magnitude diagram of NGC 6791 also shows the existence of EHB stars. Kalirai et al. (2009) concluded that metal rich environments indeed lead to high mass loss rates, most likely through stellar winds on the RGB, as evidence for late hot flashers and flash-manqué stars are present.

However, Lanz et al. (2004) imply an important role of stellar rotation for the late hot flashers. They report two of two observed carbon-rich HesdBs to be fast rotators ($v_{\rm rot} \sin i \approx 100\,{\rm km\,s}^{-1}$). A valid origin for these stars could be RGB stars with fast rotating cores leading to enhanced mass loss and subsequently to late hot flasher events.

Chapter 3

SPAS - Spectrum Plotting and Analysis Suite

For our spectral analysis we used two tools, based on the same principle. We started the analysis with Ralf Napiwotzki's FITSB2, which fits synthetic spectra to the observed spectrum by interpolating within a three dimensional grid of precomputed synthetic spectra (Napiwotzki et al. 2004a). A χ^2 criterion is used for determining the best fit parameters. Statistical errors are computed for T_{eff} and $\log g$ only.

By far the most spectra are not flux calibrated and many are not even normalised and so the continuum between the spectral lines does not provide much information. Using this feature to save memory and computational time, the program does not fit a model to the complete observed spectrum, but rather to a number of user selected ranges of interest, typically containing one or two spectral lines each. The parameter fit is done simultaneously to the ranges.

While FITSB2 is a great and reliable programme, it lacks a certain user-friendliness. Therefore I have chosen to re-implement it, using C/C++ and the Qt toolkit (`http://www.qtsoftware.com/`). This new program, *Spectrum Plotting and Analysing Suite*, or SPAS, provides a graphical user interface for easy and fast access to fit parameters like spectral resolution, fitted ranges, start parameters, and so on. Often needed additional features when working with spectra are:

- display spectra with automatic axis scaling

- zooming in and out

- highlight the laboratory restwavelengths of ions (read in from a text file) for line identification

- smooth the spectrum by folding it with a Gaussian function

- normalise a spectrum by dividing it by the continuum, approximated by a spline based on user selected tags

- add, multiply or divide spectra

- delete data points, like cosmics

Figure 3.1: A screenshot of the plot window, showing a typical HesdO spectrum from the SDSS database in black. Restwavelengths of a selection of spectral lines are marked by the vertical grey lines which highlight and print the species and ionisation stage on screen when under the mouse cursor. The red lines across the complete screen demonstrate the ruler function, where the distance of the current cursor position to a previous position is given in Ångström and flux (see red numbers at the lower right of the screenshot) as well as in velocity and relative flux (red numbers in parenthesis). A fit to the He I 4 472 Å line is also shown (thick red line).

- calculate the signal-to-noise ratio (interpreted as mean / std.dev.)

See figure 3.1 for an example of the plot window, demonstrating the usefulness of this program for a "quick and dirty" evaluation of a spectrum.

For a more elaborate quantitative analysis, models of synthetic spectra have to be fitted. The parameter fit performed both by FITSB2 and SPAS is similar: they use the *downhill simplex* (Nelder & Mead 1965) algorithm from Numerical Recipes (1986). A simplex is an (N+1)-polyhedron in N dimensional space, for example a triangle in 2D or a tetrahedron in 3D space. In the *downhill simplex* algorithm, a test function (here: χ^2) determines the goodness of each vertex and replaces the worst one with a new vertex by mirroring the point through the opposing face, contracting or expanding the simplex in the process. Thus, the simplex will wander through the parameter space, eventually contracting until either the relative difference of the test functions evaluated at each vertex falls below a threshold, or a maximum number of iterations was performed. This algorithm is not the fastest method, but it guarantees to find a minimum, which however is not necessarily the global minimum!

By interpolating first for $\log y$, then $\log g$ and last for T_{eff} within a grid of synthetic spectra using a natural cubic spline, the spectra of the simplex' vertices are computed. If requested, rotational broadening and macro turbulence is applied, then the synthetic spectrum is folded with the instrumental profile. Finally the spectrum is rebinned to the observed data by interpolation between the two nearest neighbouring wavelength points. A
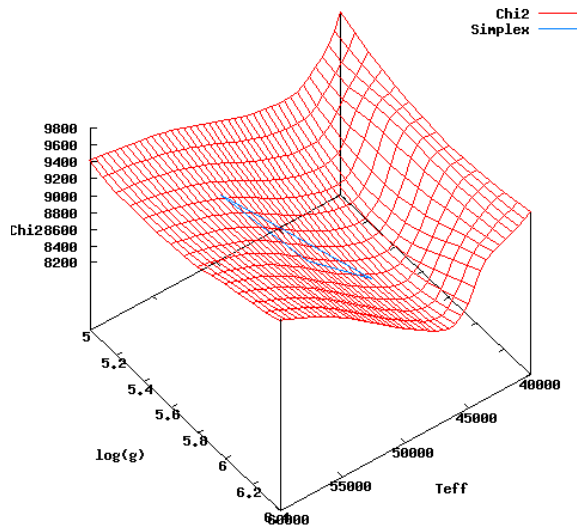
Figure 3.2: Example of a simplex in 2D parameter space.

linear interpolation is used in order to save computation time. As the synthetic models have very narrow spaced wavelength points around the spectral lines, a higher order polynomial fit does not provide any measurable difference.

For the χ^2 computation the model fluxes are scaled to the observed data, which is not necessarily normalised. Dividing the model flux by the observed data and fitting a linear function to these values, a "normalisation function" is derived which now scales the model to the data. Note that by this method, both the observed and the model fluxes are allowed to be in arbitrary units. The only relevant element is the relative strength of the line to the continuum. Artifacts or spectral lines in the observed data not reproduced in the models can interfere with this method of continuum estimation. In these cases, the continuum can be set manually.

Radial velocities are measured by fitting a Gauss+Lorentz function, approximating a Voigt function, plus a linear offset to the line profile. v_{rad} is then computed via $\frac{\lambda - \lambda_0}{\lambda_0} = \frac{v_{\mathrm{rad}}}{c}$, where λ_0 is user selectable and may be adjusted to whatever line is used.

The program has now been used by members of the institute for some time. So far only minor deviations from programs like FITSB2 have been found, which can, for example, be explained by minor changes in routines like the spline generation or the rebinning as well as different floating point precision. The interested reader may get an impression of the user interface by examining figure 3.3, where a screenshot of the fitwindow is displayed.

Error determination is done by *bootstrapping*. Bootstrapping refers to the tale of Munchhausen, pulling himself out of the swamp by his own bootstraps. In a similar way here, the data themselves are used to determine the data's error: The data are *randomly resampled with replacement* a large number of times and a parameter fit is done for each iteration. Then the standard error is the standard deviation of the parameters of the bootstrap distribution. Unfortunately the computational cost of bootstrapping is very high: the data have to be resampled in every iteration, then a sorting algorithm must rearrange the frequency points into order and a complete parameter fit has to be done. However, the errors computed this way are unbelievably low and we omitted their calculation. A
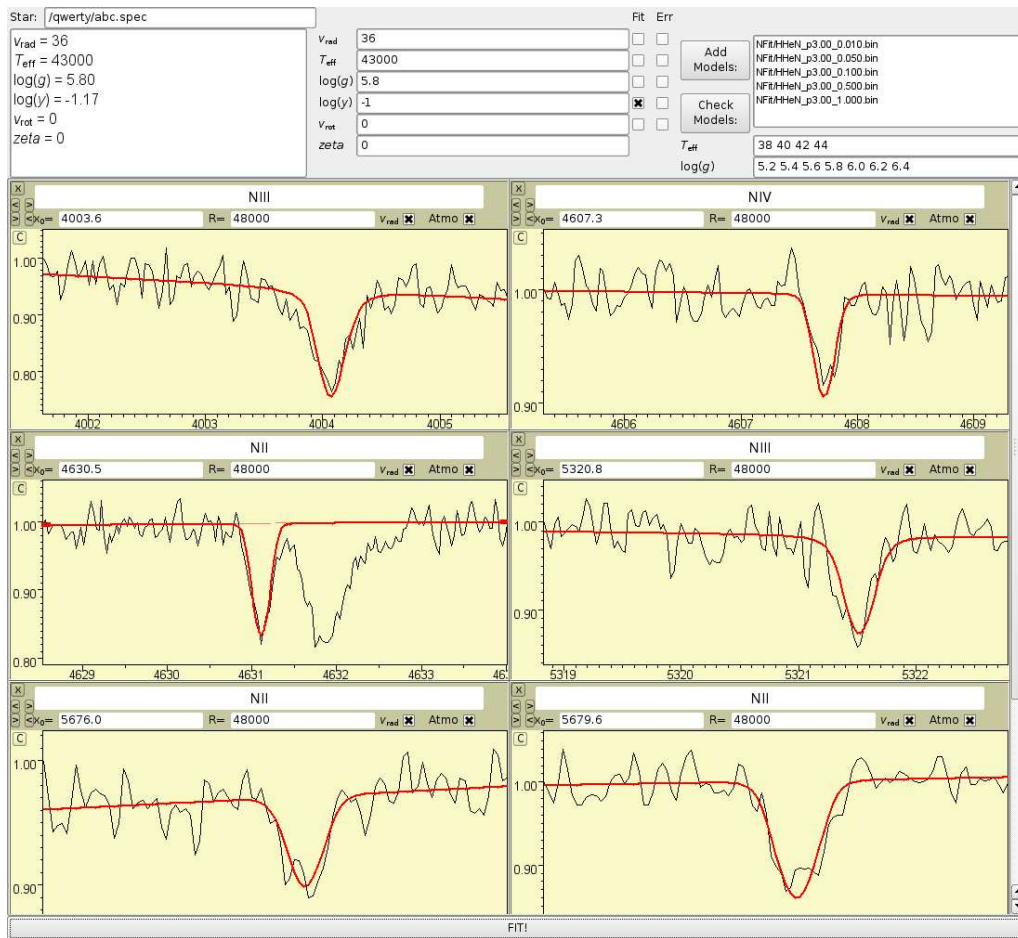
Figure 3.3: A screenshot of the fitwindow. *Upper part*: In the upper right text field the binary model files are entered, for each abundance a separate file. The extension of the modelgrid to be used is defined by the gridpoints entered below. Textfields in the centre allow the selection of start values of the fit, and a selection of parameters to be fitted. Best fit parameters are displayed in the left text field. *Lower part:* Both predefined and arbitrarily chosen fit ranges around important spectral lines are added or deleted by user interaction. In red the best fit model is plotted over the observed data. Note the manual definition of the continuum level for the N II line at $4631\,\text{Å}$, otherwise the Si IV line right next to it would disturb the automatic continuum estimation.

reasonable explanation is the low resolution of SDSS, where too few wavelength points for an effective resampling method are available per spectral line. In the future an established χ^2 method should be implemented. We used statistics of stars with multiple spectra for error estimation in the meantime.

Chapter 4

Stellar atmospheres

In this work we often mention "model atmospheres". What exactly are they, and how are they of use in astronomy?

So far only some supergiants have been resolved spatially (and very poorly indeed) — and the sun, of course. From earth every star has to be regarded as a point source. Literally everything we know about stars is based on their surface-averaged light. A star's atmosphere is the outer region of the star where the light we receive is "created", or physically more correct: The regions where an emitted photon has a chance to escape the star and reach a detector on earth, for example. The properties of the photons we detect, therefore, are determined by the physical conditions of the stellar atmosphere. By modelling the temperature and density stratification and analysing the emergent spectrum, we can draw conclusions about these conditions.

A model atmosphere is the computed temperature and density stratification of a stellar atmosphere for given parameters (always, but not constrained to: temperature and surface gravity). From the model atmosphere a synthetic spectrum can be calculated, simulating the spectrum of the real star. For our spectral analyses we use a model grid, that is a library of synthetic spectra calculated from model atmospheres of different parameters. By finding the synthetic spectrum which reproduces the observed one best, we can derive the parameters of the star.

In this chapter we will briefly discuss the assumptions and approximations used in stellar atmosphere modelling and give an overview of the methods of their calculation.

4.1 Simplifying assumptions

Fusion processes deep in the interior (core, shell burning) are the only noteworthy sources of energy for most stars. This energy is then transported by radiation and convection through the envelope until it is radiated from the stellar surface. The stellar atmosphere is composed of the outermost layers from which radiation still escapes into space[1]. In our cases, we can safely assume an atmosphere in radiative equilibrium, that means energy is transported by radiation only (Groth, Kudritzki & Heber 1985). Its calculation can be quite complex and a number of simplifications are used.

---

[1]Alternatively one can think of it as the layers we can still look through into the star.

An often used simplification is the assumption of LTE, or *local thermodynamical equilibrium*: the discrete volume elements of the atmosphere are treated as being in TE and their level population densities can be calculated with the Saha-Boltzmann laws. Avoiding the assumption of LTE leads to non-LTE (NLTE) calculations. While most cooler sdB stars can be described accurately with LTE, the hotter sdOs need NLTE atmospheres. The dividing effective temperature above which NLTE effects dominate was found at $T_{\mathrm{eff}} \approx 30\,000\,\mathrm{K}$ by Napiwotzki (1997).

We can summarise the assumptions and simplifications for stellar atmosphere calculations as follows:

- **Planeparallel geometry:** This is the assumption that the extension of the atmosphere is negligible compared to the star's radius. It is therefore sufficient to treat the atmosphere as parallel layers through which energy is transported. This holds true for most stars[2] and was confirmed to be a safe assumption for hot subdwarfs by Gruschinske & Kudritzki (1979). With the assumption of planeparallel geometry, the only coordinate needed in describing the atmosphere is the height z from the inner boundary of the atmosphere to the surface.

- **Homogeneity:** It is generally assumed that the matter is homogeneously mixed and no chemical gradient exists.

- **Stationarity:** The star's structure does not change over time. Exceptions are, for example, stellar pulsations or phases of rapid evolution. Still, stationary atmospheres can be valid "snapshots" of the star's current state and pulsations are frequently modelled by integrating over different parcels of the stellar surface with static but different atmospheric conditions.

- **Hydrostatic equilibrium:** The atmosphere's weight is supported by the pressure and follows approximately the barometric height formula. No expansion or shrinking and no mass loss is assumed.

- **Radiative equilibrium:** At every point in the atmosphere the energy absorbed equals the emitted energy.

- **Statistical equilibrium:** Every level's population and depopulation rates are balanced, i.e. the level populations are stationary. This more general condition replaces the restrictive LTE assumption.

- **Particle and charge conservation:** No mass loss is assumed and the plasma has no net charge.

4.2   Radiation transport and its formal solution

The *specific intensity* is the loss (or gain) of energy of a radiation field in time and frequency into (or from) the solid angle $d\omega$ around $\tilde{\mathbf{n}}$ and through the area $d\sigma$ at $\tilde{\mathbf{r}}$ (see Fig. 4.1).

$$I(\nu, \tilde{\mathbf{n}}, \tilde{\mathbf{r}}, t) = \frac{d^4 E}{d\nu\, dt\, d\omega\, d\sigma} \tag{4.1}$$

---

[2]Except e.g. supergiants, Wolf Rayet stars and main sequence O-stars. Due to their low surface gravities and/or stellar winds their atmospheres can have enormous dimensions.

The radiation field can be expressed in terms of moments of I_ν:

- The mean intensity J_ν (0. moment)

- The flux $\mathcal{F}_\nu$ (1. moment), which is related to the astrophysical flux: $\pi F_\nu = \mathcal{F}_\nu$

- The pressure of the photon gas K_ν (2. moment)

The astrophysical flux F_ν is the flux averaged over the star's surface as seen from earth and is the actual observed quantity.

Radiation interacts with matter via processes that can be grouped into true absorption and emission and scattering. True absorption and emission processes destroy or create photons, they couple the matter with the radiation field, i.e. they transfer energy from the radiation field to the plasma (or the other way around). Photoionisation (bound-free transition) and excitation (bound-bound) followed by collisional deexcitation or ionisation are true absorption processes. Their inversions are true emission processes. The bound-bound transitions are responsible for the spectral lines. Scattering does not exchange energy between photons and the gas, but changes the direction of propagation of the photon. Thomson scattering of photons on free electrons or the absorption and immediate re-emission of photons are examples of scattering processes.

Macroscopically, absorption along the path ds is described via $dI_\nu = -\kappa_\nu I_\nu ds$ with the absorption coefficient κ_ν, and emission via $dI_\nu = \epsilon_\nu ds$ with the emission coefficient ϵ_ν. In planeparallel geometry, the path ds with the angle θ to the surface normal can be expressed as $dz = \cos\theta ds = \mu ds$, where z is the depth coordinate. From this immediately follows the formula for radiation transport:

$$\mu \frac{dI_\nu(\mu, z)}{dz} = -\kappa_\nu I_\nu + \epsilon_\nu \tag{4.2}$$

Now, instead of the geometric depth variable z we introduce the *optical depth* $d\tau_\nu = -\kappa_\nu dz$ and with the *source function* $S_\nu = \frac{\epsilon_\nu}{\kappa_\nu}$ we can write equation 4.2 as:

$$\mu \frac{dI_\nu(\mu, \tau_\nu)}{d\tau_\nu} = I_\nu(\mu, \tau_\nu) - S_\nu \tag{4.3}$$
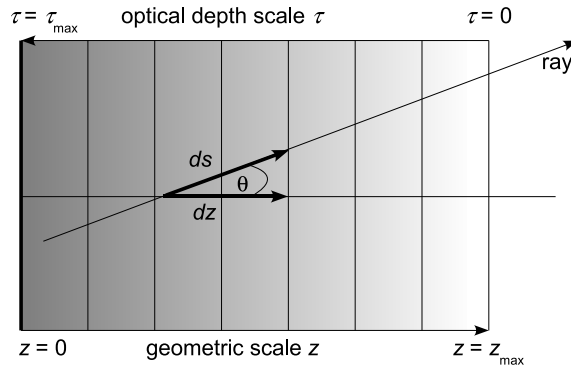
Figure 4.1: Geometric scale and optical depth in planeparallel geometry. The inner boundary of the atmosphere is to the left, the outer boundary is to the right.

The solution of this differential equation gives the *formal solution* of the radiation transport. If the source function were known, the radiation transport could easily be solved. In reality however, S_ν is a function of I_ν itself and is not known. For the mean intensity J_ν the formal solution can be expressed as

$$J_\nu = \frac{1}{2} \int\limits_0^\infty S_\nu(\tau) E_1(|\tau - \tau_\nu|) d\tau \tag{4.4}$$

where $E_1(x)$ is the first exponential integral. With the introduction of the lambda operator

$$\Lambda[f(x)] \equiv \frac{1}{2} \int\limits_0^\infty f(x) E_1(|x - x'|) dx \tag{4.5}$$

one can write

$$J_\nu = \Lambda[S_\nu] \tag{4.6}$$

4.3   Radiative equilibrium

Radiative equilibrium requires that the flux emitted by a volume element equals the flux absorbed by this element:

$$\int\limits_0^\infty \kappa_\nu(S_\nu - J_\nu) d\nu = 0 \tag{4.7}$$

This integral form is equivalent to the differential form demanding constant flux through the atmosphere, or:

$$\int\limits_0^\infty \frac{\partial}{\partial \tau_\nu}(f_\nu J_\nu) d\nu = H \tag{4.8}$$

where f_ν is the variable Eddington factor

$$f_\nu = \int\limits_0^1 \mu^2 u_{\nu\mu} d\mu \quad / \quad \int\limits_0^1 u_{\nu\mu} d\mu \tag{4.9}$$

and $u_{\nu\mu} = \frac{1}{2}(I_\nu(\mu) + I_\nu(-\mu))$ is the Feautrier variable. The integral form is best suited for small optical depths, while deep in the atmosphere both S_ν and J_ν approach the Planck function and equation 4.7 is fulfilled, independent of the temperature. On the other hand a small optical depth with low opacities and no interaction of radiation and matter leads to a temperature-independent flux, rendering the differential form numerically unstable. Thus, typically a linear combination of both methods is used.

4.4   Hydrostatic equilibrium

With surface gravity g and column mass m, we can write the hydrostatic equilibrium as

$$\frac{d}{dm}P = g \tag{4.10}$$

where P is the pressure, that is the sum of gas pressure, radiation pressure and turbulence pressure (if considered):

$$\frac{d}{dm}\left(NkT + \frac{4\pi}{c}\int_0^\infty f_\nu J_\nu \, d\nu + \frac{1}{2}\rho v_{\text{turb}}^2 \right) = g \tag{4.11}$$

4.5 Particle conservation

Let N be the sum of electron density n_{e} and the population densities n_{kli} of level i of ion l of atom k:

$$N = n_{\text{e}} + \sum_{k=1}^{\text{NA}} \sum_{l=1}^{\text{NI}(k)} \sum_{i=1}^{\text{NL}(l)} n_{kli} \tag{4.12}$$

For convenience, the fictitious massive particle density n_{H} is introduced (Werner et al. 2003) as

$$n_{\text{H}} = \sum_{k=1}^{\text{NA}} A_k \sum_{l=1}^{\text{NI}(k)} \sum_{i=1}^{\text{NL}(l)} n_{kli} \tag{4.13}$$

where A_k denotes the atomic weight of element k in atomic mass units. With m_{H} being the mass of a hydrogen atom, the density of matter can then be derived from

$$\rho = n_{\text{H}} m_{\text{H}}. \tag{4.14}$$

4.6 Statistical equilibrium and LTE vs NLTE

If the star were a closed system it would be in thermodynamical equilibrium, described only by its global temperature T. Then the specific intensity I_ν equals the Planck function

$$I_\nu = B_\nu(T) = \frac{2h\nu^3}{c^2} \frac{1}{e^{h\nu/kT} - 1} \tag{4.15}$$

and the the distribution of the velocities of the particles can be described by the Maxwellian distribution:

$$f(v) = \left(\frac{m}{2\pi kT} \right)^{\frac{3}{2}} e^{-\frac{mv^2}{2kT}} 4\pi v^2 \tag{4.16}$$

The occupation numbers of bound states are governed by the Boltzmann formula

$$\frac{n_{\text{up}}}{n_{\text{low}}} = \frac{g_{\text{up}}}{g_{\text{low}}} e^{-\frac{E_{\text{up}} - E_{\text{low}}}{kT}} \tag{4.17}$$

where the $g_{\text{up/low}}$ are the statistical weights of the states, while the number ratios for ionisation stages obey the Saha equation, which is in principle the extension of Boltzmann's law with the upper level being a two particle system (ion + free electron):

$$\frac{n_{\text{up}}}{n_{\text{low}}} = \frac{2}{n_{\text{e}}} \left(\frac{2\pi m_{\text{e}} kT}{h^2} \right)^{\frac{3}{2}} \frac{g_{\text{up}}}{g_{\text{low}}} e^{-\frac{E_{\text{up}} - E_{\text{low}}}{kT}} \tag{4.18}$$

Obviously, a star is not a closed system, it radiates energy which we can detect here on earth. Instead the star is treated as individual volume elements each of which is *locally* in thermodynamical equilibrium (LTE). The local temperature $T(z)$ fixes the energy of the gas via the Maxwell, Boltzmann and Saha equations. Because photons can leave the surface, the radiation field is not a simple Planck distribution but a composition of the individual volumes' $B_\nu(T(z))$.

This view is not entirely accurate, as photons can travel long ways before they are thermalised. They therefore couple the local volumes to each other. With the availability of faster computers the LTE conditions can be loosened (non-LTE, NLTE). Detailed rate equations then take the place of Saha-Boltzmann statistics. This implies the consideration of all processes that populate and depopulate a state. Stationarity then demands the exact balance of all rates, so that the population of levels do not change with time (= statistical equilibrium). Assume that C_{ij} are the collisional rates and R_{ij} are the radiative rates from level i to j, then statistical equilibrium requires:

$$n_i \sum_{i \neq j} (C_{ij} + R_{ij}) = \sum_{i \neq j} n_j (C_{ji} + R_{ji}) \tag{4.19}$$

The crux, however, is that the rates R_{ij} depend on the radiation field which is given by the transfer equation, which in turn depends via κ nd ϵ on the occupation numbers of the states. Therefore NLTE computations are more time-costly by orders of magnitude than LTE, and the latter is the preferred method as long as deviations between both are small. For the sdB stars, Napiwotzki (1997) found that LTE is a valid assumption up to $T_{\text{eff}} < 30\,000\,\text{K}$.

Generally it is hard to predict to what extent the use of NLTE improves the models. As a guideline, high temperatures and low densities demand for NLTE. This can be understood when one recalls that it is radiation that disturbs the assumptions of LTE as the photons couple different layers of the atmosphere and high temperatures go along with high radiation fluxes. On the other hand, a larger number of absorbing particles lowers the photon free mean path, thus higher densities lead to more localised layers. It is well established that sdO stars need NLTE calculations over all their range in effective temperature and surface gravity (Kudritzki 1976; Napiwotzki 1997).

4.7   Methods of computation

Considering $l = 1, \ldots, \text{NL}$ atomic levels and using a precomputed frequency grid with $f = 1, \ldots, \text{NF}$ frequency points, the problem may be stated as the search for the ND solution vectors

$$\Psi_d = \{n_l, n_e, T, n_H, N, J_f\} \tag{4.20}$$

of the atmosphere discretised into $d = 1, \ldots, \text{ND}$ depth points. Here n_e and n_H denote the electron density and massive particle density and the depth indices on the right hand side have been omitted. These vectors are obtained via the solution of a set of coupled non-linear equations:

- Radiation transfer, which determines the mean intensities J_f.

- Hydrostatic equilibrium for the particle density N that depends on $\log g$.

- The radiative equilibrium fixes the temperature T, based on the parameter T_{eff}.

- Statistical equilibrium governs the population densities n_l.

- Electron density n_e follows from particle conservation.

- Fictitious massive particle density n_H for convenience

One method for calculating model atmospheres is the complete linearisation (Auer & Mihalas 1969) of these equations. Their solution via iterations is straight forward but requires the inversion of very large matrices which means very high computational costs. Another way to tackle this problem is the use of lambda iterations: The explicit occurrence of the NF mean intensities J_{f_d} for each depth point d can be circumvented by using equation 4.6, which allows us to iteratively calculate J_{f_d} from population densities and vice versa. Convergence of this scheme, however, is very poor in optical thick cases: every iteration can be regarded as photons travelling their mean free path which is very short for photons in the cores of deep lines. Numerous iterations therefore have to be performed to propagate these trapped photons over a significant distance.

An improvement of the lambda iteration is the accelerated lambda iteration (ALI) by Werner & Husfeld (1985), which is used by most state-of-the-art model atmosphere codes. The idea behind this scheme is to replace the Λ-operator of equation 4.6 by an *approximate* Λ-*operator*, Λ^*. Then the i-th iteration step can be written as

$$J^i = \Lambda^* S^i + (\Lambda - \Lambda^*) S^{i-1} = \Lambda^* S^i + \Delta J^i \tag{4.21}$$

where Λ^* acts on the current, yet to be determined source function S^i while the correction term ΔJ includes only known parameters from the previous iteration. Frequency and depth indices have been omitted. This method is commonly known as "operator splitting". Linearisation and iterative solution algorithms are then used on the remaining set of coupled non-linear equations.

The trick behind ALI is that Λ^* can be chosen completely arbitrarily — in case of convergence ($S^i = S^{i-1}$) equation 4.21 obviously gives the exact solution. Optimal operators are e.g. the diagonal of the full Λ-operator, or a tridiagonal Λ^* (Rybicki & Hummer 1991). The diagonal approximate Λ-operator for example decouples the depth dependence of the solution vectors. With the use of a tridiagonal Λ^* which considers only nearest neighbour interaction in the depth coupling, one can rewrite equation 4.21 to

$$J_d^i = C_{d-1} S_{d-1}^i + B_d S_d^i + A_{d+1} S_{d+1}^i + \Delta J^i \tag{4.22}$$

where the A_{d+1}, B_d and C_{d-1} are the upper, the diagonal and the lower elements of the tridiagonal Λ^*.

Chapter 5

Hot subdwarfs from the SPY project

Before venturing into the depths of the Sloan Digital Sky Survey in chapter 6, we regard it more appropriate to draw the reader's attention to a preceding study of hot subluminous stars from the SPY survey. SPY stands for **S**upernova Ia **P**rogenitor surve**Y**. We will meet SPY again in later chapters, as we will use it for a comparison and extension of our analysis in the afore mentioned chapter 6, and again in chapter 11 where it will undergo a new and — hopefully — improved spectral analysis. So in this chapter, after a short summary of the SPY survey, the papers of Lisker et al. (2005) and Ströer et al. (2007) are introduced and their results summarised.

5.1   The idea of SPY or a short side step into cosmology

Supernovae Ia gained much interest of astronomers, when it was realised that the shape of their lightcurve is related to their luminosity. Since then they have been used as standard candles and are, for example, one fundamental pillar of current ΛCDM cosmologies which require the not yet directly detected dark matter and the even more elusive dark energy in order to describe the observations. SNe Ia are explained by the thermonuclear explosion of a carbon-oxygen white dwarf which exceeds the Chandrasekhar mass ($1.39\,\mathrm{M_\odot}$). Beyond this mass, the carbon ignites and the star is destroyed in the following explosion. A worrying detail, however, is the fact that no one really knows the exact mechanism of the explosion of SNe Ia. Open questions are, for example, what role rotation plays, or what triggers the carbon ignition: Does the gravitational pressure directly ignite carbon, or is it the shockwave travelling inwards after ignition of the accreted helium? In the second case, a sub-Chandrasekhar mass may suffice (see e.g. Livio 2000). One possible scenario is the so called *double degenerate* scenario (DD), the merging of two white dwarfs due to loss of orbital energy by the radiation of gravitational waves. Unlike the sdO progenitor scenario of merging HeWDs (chapter 2.1), the more massive carbon-oxygen type white dwarfs are required. Two recently published studies (Raskin et al. 2009; Rosswog et al. 2009) suggest the head-on collision of white dwarfs as viable candidates for SNe Ia.

SPY aimed at identifying the progenitors in the DD scenario, that are white dwarf binaries with combined masses exceeding the Chandrasekhar limit and orbital periods short enough to allow a merging within a Hubble time (Napiwotzki et al. 2003). The instrument used is the UV-Visual-Echelle-Spectrograph (UVES) (Dekker et al. 2000) at UT2 (Kueyen) at ESO VLT. SPY is run as a bad weather programme in service mode and

uses a slit width of $2''.1$ in order to minimise the loss of light due to bad seeing. After extracting and merging the echelle orders with a modified version of the standard UVES pipeline (Karl 2004), the spectra were "normalised" by the division through a DC white dwarf spectrum. DC white dwarfs have featureless spectra and therefore are often used for normalisation.

As theory predicts a low fraction of such systems at the order of some per cent among white dwarf binaries, SPY uses a large list of over $1\,000$ targets compiled from catalogues of white dwarfs. Essentially, this target list includes all spectroscopically identified white dwarfs with $V < 16.5$ accessible from the ESO Paranal site. By obtaining at least two spectra at random epochs, radial velocity variable stars were found. Together with a spectral analysis, promising candidates were identified and follow-up observations were scheduled. Thus their periods and mass ranges are determined and one can identify the systems which qualify as SN Ia progenitors.

The actual SPY survey has been completed by now, but the work on the data is still ongoing. In the course of the survey, optical spectra of over $1\,000$ white dwarfs were taken and more than 100 double degenerate systems were found, with a handful of systems near the Chandrasekhar limit (Napiwotzki et al. 2005). But the survey also has raised new questions. Helium white dwarfs, for example, were found to have a binary fraction of 42%. But as the single star progenitors of such low mass white dwarfs have very long lifetimes, even greater than a Hubble time, this is in conflict with the expectation of a much larger fraction of radial velocity variable stars, near to 100%, even when taking the detection efficiency into account (Napiwotzki et al. 2007). Furthermore, the mass ratios of DD carbon-oxygen white dwarfs do not match expectations. These examples could indicate fundamental gaps in our understanding of binary star evolution.

Leaving cosmology and supernovae, we bridge the gap between SPY's initial aims and our area of interest by bringing up the fact that the input catalogue used for SPY fortunately contains ≈ 150 subdwarfs which were wrongly classified as white dwarfs before. It is these objects that Lisker et al. (2005) and Ströer et al. (2007) used for their work, and that we will use in this thesis as well.

5.2   Subdwarf B stars from SPY

Lisker et al. (2005) focused their attention on 76 subluminous B stars found in SPY. 52 out of the 76 sdBs were found to be apparently single stars. In 19 stars either spectral lines of cool companions (e.g. the Mg II triplet) were visible, or infrared flux excess was found from 2MASS data (Skrutskie et al. 2006). Spectra of five additional objects have a H_α profile too shallow compared to the best fit model which was interpreted as a flux contribution of an otherwise invisible companion. This can be understood when recalling that the spectra are normalised, thus a *constant* flux offset caused by the secondary translates to a reduced depth of the line *relative* to the continuum. Four more stars showed a peculiar H_α profile, which remained unsolved.

For their quantitative spectral analysis they used a combination of metal line blanketed LTE atmospheres for $T_{\mathrm{eff}} < 32\,000\,\mathrm{K}$ and partially line blanketed NLTE atmospheres (for $T_{\mathrm{eff}} > 32\,000\,\mathrm{K}$). Measured effective temperatures range from $20\,000\,\mathrm{K}$ to $38\,000\,\mathrm{K}$ and the surface gravities are found in between $\log g = 4.8$ and $\log g = 6.0$. Helium abundance is low, as expected, with only two stars showing slightly supersolar abundance. A trend

to higher helium abundance with higher effective temperature can be deduced. Although the statistical 1-σ-errors from line profile fitting were very small, the authors estimated more reliable errors by comparing the two individual spectra available for most objects and settle for $\Delta T_{\mathrm{eff}} = 370$, $\Delta \log g = 0.05 \,\mathrm{dex}$ and $\Delta \log y = 0.04 \,\mathrm{dex}$. Comparison with other published samples revealed no grave discrepancies, especially the magnitude limited nature of SPY was not found to introduce a bias against lower luminosity objects.

Lisker et al. (2005) primarily aimed at validating and refining the binary population simulation by Han et al. (2003), see also chapter 2.1. For this purpose a thorough comparison of e.g. the T_{eff}-$\log g$-distribution and the cumulative luminosity function (CLF) with the predictions of different simulations was done.

Varying the input parameters, Han et al. (2003) created 12 sets of their simulation and found set 2 and 8 as best matches to observations. Both sets were computed for population I metallicity stars and use $\alpha_{\mathrm{CE}} = \alpha_{\mathrm{th}} = 0.75$, while they differed in the critical mass ratio q_{crit} above which no stable RLOF is possible. But statistical likelihood calculations by Lisker et al. (2005) for the distribution of SPY sdB in the T_{eff}-$\log g$-plane clearly revealed simulation set 10 to be the best representation. This set uses the lower thick disk metallicity ($z = 0.004$) and lower efficiencies in the common envelope phase ($\alpha_{\mathrm{CE}} = \alpha_{\mathrm{th}} = 0.5$). No conclusion can be drawn for q_{crit}, as the available simulation sets for lower metallicity all use the same $q_{\mathrm{crit}} = 1.2$. All three sets (2, 8, and 10) assume a correlated initial mass ratio distribution of the binaries (Han et al. (2003) use a constant distribution), in contrast to uncorrelated ratios, where each component is randomly chosen from the initial mass function. However, it should be emphasised that even for the statistically most likely simulation set 10, the agreement in T_{eff}-$\log g$ is not perfect (see triangles (sdBs) in Fig. 5.1), while the CLFs of all sets hardly reproduce the observed data.

5.3 Subdwarf O stars from SPY

No statement about the viability of population synthesis models is complete without considering the hotter siblings of the sdBs, the sdO stars. SPY provides the spectra of 58 subluminous O stars, on which Ströer et al. (2007) base their work. Only one object showed the typical "cool companion spectral lines", a second star had emission features in the cores of $H_\alpha - H_\delta$. These emissions on the Balmer lines may be indicators of a second star in the system whose atmosphere is heated by radiation from the primary. Judging from the B-$(B - J)$ colour-magnitude diagram constructed with 2MASS data for J, another six sdOs were found to have most likely composite spectra. The blue parts of their observed spectra, however, are not expected to suffer from the secondary's influence.

Spectral analysis was performed by the use of an extensive grid of partial line blanketed NLTE model atmospheres, covering helium abundances over several magnitudes ($\log y = -4 \ldots +3$ with step size 0.5 dex). The models were calculated with the PRO2 code (Werner & Dreizler 1999), updated with a new temperature correction scheme by Dreizler (2003), see also chapter 9.1. Model atoms used were hydrogen and helium, the latter being very detailed and adjusted to the sdO temperature regime. T_{eff} covers the ranges from $30\,000\,\mathrm{K}$ to $52\,000\,\mathrm{K}$ in steps of $\Delta T_{\mathrm{eff}} = 2\,000\,\mathrm{K}$ and from $55\,000\,\mathrm{K}$ to $100\,000\,\mathrm{K}$ in steps of $\Delta T_{\mathrm{eff}} = 5\,000\,\mathrm{K}$. Surface gravities range from $\log g = 4.8$ to $\log g = 6.4$ with $\Delta \log g = 0.2 \,\mathrm{dex}$. Some gaps in this grid remain, especially at the low surface gravities and at the high temperatures. Most importantly, the upper limit for the helium abundance is $\log y = +3$
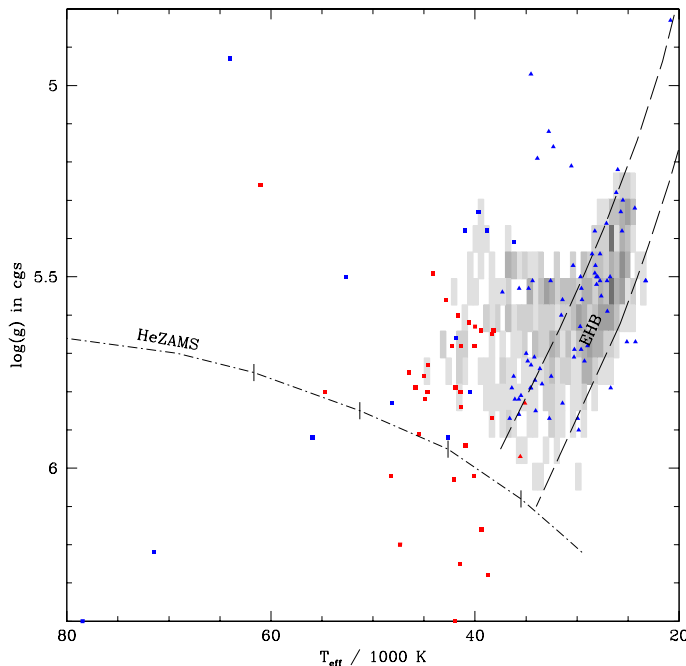
Figure 5.1: Simulation set 10 of Han et al. (2003). The grey rectangles render the predicted density of objects. The darker, the more objects are expected. Overplotted are sdBs (triangles) and sdOs (rectangles) from SPY. Objects with subsolar helium abundances are plotted in blue, while those with supersolar helium abundances are coloured red. For better orientation, the EHB and the helium main sequence (HeZAMS) (Paczyński 1971) are also plotted, the tickmarks on the HeZAMS indicate (from right to left) the positions of 0.5, 0.7, 1.0, and 1.5 $M_\odot$ helium stars.

for $T_{\text{eff}} = 30\,000\,\text{K} \ldots 52\,000\,\text{K}$ and $\log y = +2$ for $T_{\text{eff}} > 52\,000\,\text{K}$. Also using the statistics of the two spectra available for most stars, the errors are reported as $\frac{\Delta T_{\text{eff}}}{T_{\text{eff}}} = 0.026$, $\Delta \log g = 0.097$ and $\Delta \log y = 0.11$.

A connection between helium abundance and the presence of carbon and/or nitrogen lines was found that gave reason for a "CN-scheme" of classification into "C", "CN", "N", and "0" types: All sdOs having sub-solar helium abundances are of 0-type (neither nitrogen nor carbon in their optical spectra), while the C-, N-, and CN-types always have super-solar helium contents. Referring to this result, the terms *helium-enriched* and *helium-deficient* were suggested. They are believed to follow more closely the physical properties of the stars, while the old sdO/HesdO notation is based on the strength of hydrogen and helium lines only. See also Fig. 1.3 in chapter 1.3.

No sdO is situated on the extended horizontal branch, all of them are found at higher temperatures (see rectangles (sdOs) in Fig. 5.1). A puzzling feature are seven helium-enriched sdOs which appear to lie below the theoretical main sequence of pure helium stars (Helium Zero Age Main Sequence, HeZAMS, Paczyński (1971)[1]) and therefore should not

---

[1]More recent calculations of the HeZAMS only differ by $\approx \pm 0.06\,\text{dex}$ in $\log g$, depending on metallicity (Kawaler, priv. comm.). We continue using the old Paczyński HeZAMS, because it covers a wider mass range ($\hat{=} T_{\text{eff}}$ range).
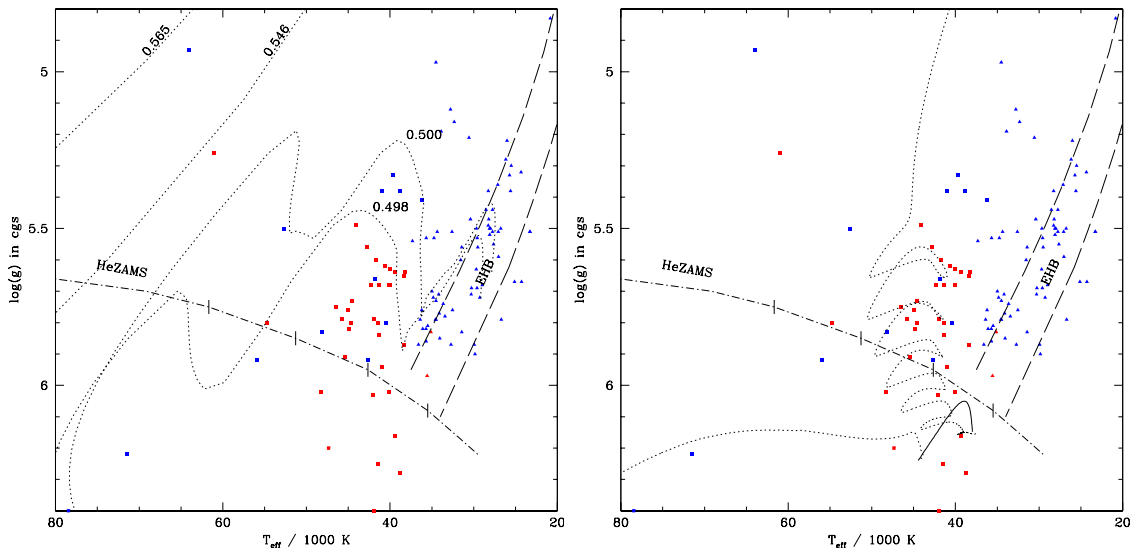
Figure 5.2: Symbols as in Fig. 5.1. *Left:* post-EHB evolution (Dorman, Rood & O'Connell 1993) nicely connects sdBs with helium deficient sdOs. A few stars could be post-AGB evolution (Schönberner 1983) shown in the upper left. The masses in solar units are given for each track. *Right:* Late hot flasher track for $z = 0.001$ (Miller Bertolami et al. 2008). Note that the timescales are 3 Myrs for the first part (dotted line) from the top to $\log g \approx 6.2$, 70 Myrs for the hook near the HeZAMS (solid line) and 50 Myrs for the last horizontal evolution (dotted line). The offset between the stable helium core burning phase of the late hot flasher (solid line, the hook) to the HeZAMS is due to different metallicities. The former assumes $z = 0.001$ and the latter is for solar metallicity.

exist — at least not as helium core burning stars they are thought to be. Systematic errors in the spectral analysis (e.g. due to the neglect of metal line blanketing) are a matter of concern, as pointed out by the authors and they caution against reading too much into it. Three additional helium-deficient sdOs below the HeMS do not pose a problem, as they are found at hotter temperatures and their position is in accordance with post-EHB evolution.

Some statistics of the SPY sample are given in table 5.1. The wide spread and the imbalance of the distribution of the helium-deficient sdOs in T_{eff} is apparent, while the sdBs and helium-enriched sdOs form more homogeneous groups. The helium-deficient sdOs are considered as evolved sdBs, their statistics are in agreement with the large timescales of the stars on the EHB and the increasingly faster evolution on post-EHB tracks (Dorman, Rood & O'Connell 1993). Clearly seen are the large differences for the helium abundances between the helium deficient sdOs/sdBs and the helium-enriched sdOs, also to be interpreted as a connection between the former. Post-EHB evolution of sdBs takes them first to lower gravities before turning onto a curve leading to the white dwarf region, a prediction we find again represented by the larger width and higher mean value of the helium deficient sdOs' $\log g$-distribution compared to the sdBs'. Only the helium enriched sdOs do not fit into this scheme, their significantly higher helium abundance is the strongest argument.

Testing the sdOs distribution in T_{eff}-$\log g$ against evolutionary scenarios (as discussed in chapter 2), the helium-deficient sdOs can easily be explained by post-EHB evolution.

Table 5.1: Statistics from SPY. Mean value, dispersion and the median value for the stars *analysed* are given for the atmospheric parameters. The numbers (1st row) for the complete sample are slightly higher (see text).

	sdO		sdB
	helium deficient	helium enriched	
numbers	13	35	72
$\langle T_{\mathrm{eff}} \rangle$	$50\,000\,\mathrm{K}$	$43\,000\,\mathrm{K}$	$30\,600\,\mathrm{K}$
$\sigma_{T_{\mathrm{eff}}}$	$13\,600\,\mathrm{K}$	$4\,600\,\mathrm{K}$	$4\,000\,\mathrm{K}$
$\langle T_{\mathrm{eff}} \rangle_{\mathrm{median}}$	$42\,700\,\mathrm{K}$	$42\,000\,\mathrm{K}$	$30\,300\,\mathrm{K}$
$\langle \log g \rangle$	5.67	5.82	5.58
$\sigma_{\log g}$	0.40	0.24	0.23
$\langle \log g \rangle_{\mathrm{median}}$	5.66	5.79	5.56
$\langle \log y \rangle$	-2.08	$+1.29$	-2.43
$\sigma_{\log y}$	0.86	1.12	0.85
$\langle \log y \rangle_{\mathrm{median}}$	-1.92	$+1.37$	-2.41

Yet, no conclusive match between theories and observation could be found for the helium-enriched stars. Fig. 5.2 shows the post-EHB (Dorman, Rood & O'Connell 1993), post-AGB (Schönberner 1983) and late hot flasher (Miller Bertolami et al. 2008) tracks together with the hot subdwarfs from SPY. Both late hot flashers and HeWD mergers can explain their general qualities but fail in detailed examinations. The binary population synthesis sets fail completely in covering the hotter ($T_{\mathrm{eff}} > 47\,000\,\mathrm{K}$) subdwarfs and all sdOs with surface gravities higher than $\log g \gtrsim 5.8$, see Fig. 5.1.

As the selection effects of SPY probably will never be understood and there is indication of a selection bias in favour of HesdOs and against sdBs (note the high number ratio of 58 to 76 for sdO to sdB), it is questionable whether the SPY sample is suitable as a tool for a statistical test of binary population synthesis models at all. In the next chapters we will extend the sample size by looking at sdOs from an other less biased survey, the famous Sloan Digital Sky Survey, SDSS.

Chapter 6

Data from the Sloan Digital Sky Survey (SDSS)

"The Sloan Digital Sky Survey (SDSS) is one of the most ambitious and influential surveys in the history of astronomy."
`http://www.sdss.org`

The largest part of data was taken from the public databases of the Sloan Digital Sky Survey. In this chapter we will give a short overview of SDSS, of our strategy of object selection from its gigantic spectral database and we will try to examine the quality and reliability of the parameters derived from these stars.

6.1   SDSS in a nutshell

The Sloan Digital Sky Survey is a magnitude-limited photometric survey in five bands ($ugriz$, centre wavelengths of $3\,600$, $4\,800$, $6\,400$, $7\,600$ and $9\,000$Å) with a sky coverage of roughly one half of the northern Galactic hemisphere ("Pi in the sky") plus some stripes in the southern Galactic hemisphere. It uses a dedicated 2.5m telescope situated at Apache Point Observatory in New Mexico, USA. Additionally to the photometry, a fibre fed spectrograph using 640 fibres of 3 arcsec width is used for follow-up spectroscopy of selected targets from the photometric data. This target selection is aimed at galaxies and quasars, but is unintentionally 'contaminated' by stars due to the ambiguousness of the colour selection, as well as intentionally by stars, for example used for photometric calibration. The spectra are exposed in sequences of 15 minutes each, until a desired signal-to-noise ratio is achieved (S/N > 4 per pixel at $g = 20.2$). Since DR6, the single spectra of the consecutive exposures are also available and provide a possibility to search for short period radial velocity variable stars. For further reading into the SDSS see York et al. (2000) for the technical summary and Abazajian et al. (2007) for the latest data release.

SDSS has proved to be a very useful tool for very different domains of astronomy. Discoveries made with the help of SDSS range from cosmology (e.g. measuring cosmological parameters from the 3D mapping of the galaxy distribution, Tegmark et al. 2003) over

extra galactic (e.g. the discovery of the most distant quasars at $z > 6$, Fan et al. 2003) and Galactic studies (e.g. the discovery of new tidal streams, Newberg, Yanny & Willett 2009) to stellar astronomy (like this work) and even planetary science (e.g. asteroids from SDSS; Ivezić et al. 2001). The publicly available web presence (`http://www.sdss.org`) allows users to select the desired data, for example via an SQL-interface, and download it with common tools like *rsync* or *wget*. Alternatively, objects can be examined online, and also a comfortable interface for generating finding charts is provided. SDSS ended in late 2005 and was succeeded by SDSS-II, consisting of three parts:

LEGACY completing the original SDSS goals

SEGUE (Sloan Extension for Galactic Understanding and Exploration), aimed at stars in our own Galaxy and extending the sky coverage to include the Galactic disk

Sloan Supernova Survey a repeated mapping of areas in the southern stripes

SDSS-II was followed by SDSS-III (`http://www.sdss3.org`), scheduled to work from 2008 to 2014.

Data from SDSS are made public in cumulative 'data releases'. This work is based on DR7 (Abazajian et al. 2007) which includes all earlier data releases and has both LEGACY and SEGUE in one database. Currently, the spectra of 380 214 stars earlier than M type are available.

The spectra from SDSS are flux calibrated, binned in constant logarithmic scale and cover the wavelength from 3 800 Å to 9 200 Å with a resolution of $R \approx 1\,800$. We did not manage to convert the original FITS files to ASCII spectra using ESO-MIDAS, but had to use IRAF for converting into ASCII files containing $\log \lambda$ vs flux. Care has to be taken, as the wavelengths are vacuum and must be converted to air wavelengths!

6.2   Object selection

Due to their hot nature, hot subdwarf stars are found most easily by applying a colour cut. We selected all point source spectra within the colours $(u - g) < 0.2$ and $(g - r) < 0.1$, based on suggestions by R. Østensen. The first condition selects hot stars, while the second one dismisses stars which have an unseen cool companion, which would be indicated by an excess of flux in the red. Each SDSS spectrum has a "target flag" indicating its type. Most sdO stars from SDSS can be found by the flags `HOT_STD`, `STAR_BHB` and `STAR_WHITE_DWARF`. A number of objects, however, does not fall into these categories and our method to select all point sources has proved to be the most complete.

The spectra were classified by visual inspection using the criteria in chapter 1.3. The presence of the Mg II triplet at 5 167, 5 173 and 5 184 Å and/or the G-band between 4 310 Å and 4 330 Å was always interpreted as a sign of a cool companion, indicated by a "+X" in the classification. Also, a clear increase in flux beyond 6 000 Å was interpreted likewise. SDSS's extensive wavelength coverage was very useful in this respect.

Figure 6.1 shows a two-colour diagram with all inspected spectra represented by grey dots. The sdO stars (blue), the sdOB stars (green) and sdO or sdOB stars showing signs of cool companions (red) are overplotted. The concentration of sdO stars in the lower left corner is clearly seen, which corresponds to bluer colours, while stars showing signs of a cool companion settle on the upper boundary of our distribution. A more rigorous
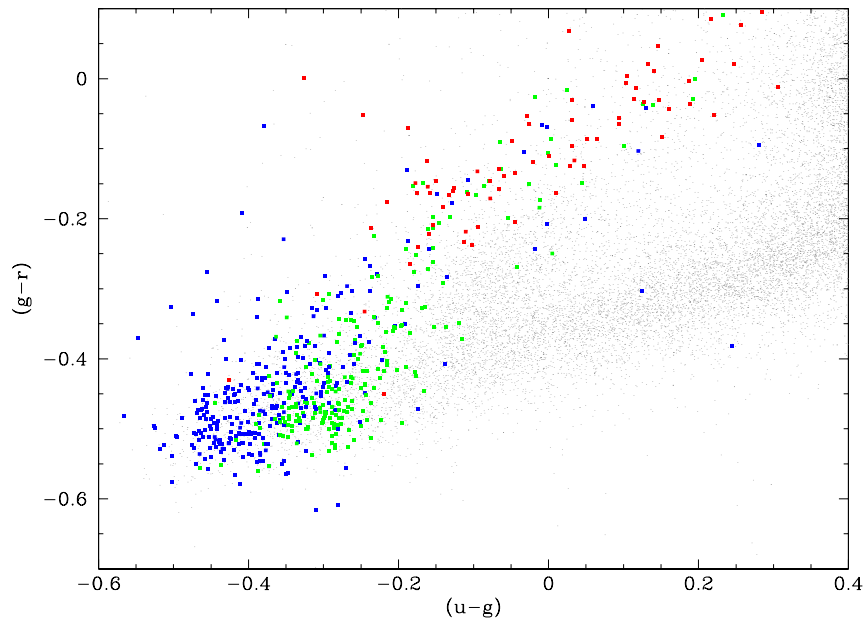
Figure 6.1: Colour-colour diagram of SDSS objects selected by our colour cuts. Blue symbols are objects classified as sdOs, green objects sdOBs and red objects are spectra showing signs of a companion. We see that our object selection is very complete, any selection effect visible in the data is due to SDSS itself.
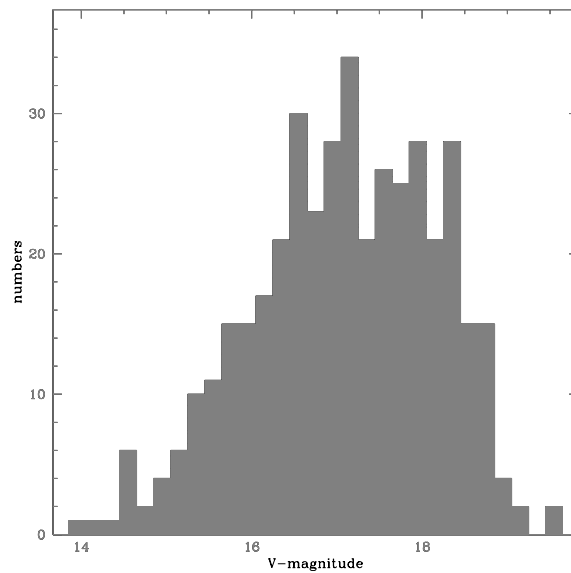
Figure 6.2: Histogram showing the apparent brightness in V of our SDSS program stars. In the range $V \approx 16 \ldots 18.75$ a very even distribution is visible. We find that within this range SDSS does not make a difference between brighter and fainter objects.

colour cut, e.g. $(u - g) < -0.2$, would have helped us in significantly reducing the number of contaminating objects (grey dots in Fig 6.1), but we would have missed some dozen objects. A histogram of the apparent brightness in V for all our program stars of SDSS which we used for the quantitative spectral analysis is plotted in figure 6.2. V is calculated from the SDSS *ugriz*-photometric system with formulae provided by Jester et al. (2005). The vast majority of objects lies between $V \approx 16 \ldots 18.75$. Within this range we look at a very homogeneous distribution, translating to a nearly unbiased selection of spectroscopic targets. From these two images we conclude that our data selection from the SDSS database is very complete, i.e. the number of objects not falling into our colour cuts is very close to zero.
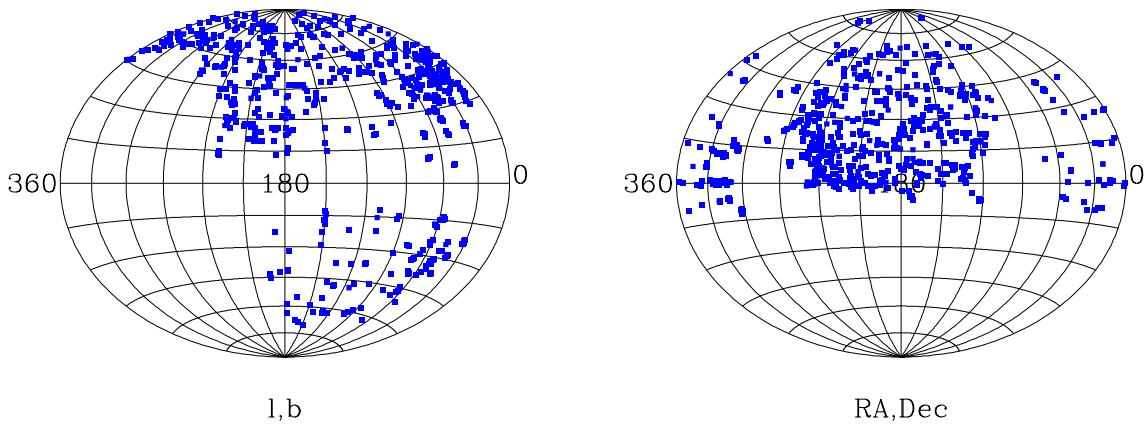
Figure 6.3: Galactic (left) and equatorial (right) coordinates of the programme stars obtained from SDSS. Note the even distribution over the survey area.

In Figure 6.3 the distribution on the sky for the SDSS program stars is plotted. Apart from four or five exceptions, no star lies at Galactic latitudes lower than $l < 15°$. This is understandable considering that SDSS primarily targets extragalactic objects. Even with the SEGUE part of SDSS-II that is aimed at stellar Galactic targets, the number of plates on the Galactic plane is only two dozen. With the strong interstellar reddening in mind we lowered our selection constraints to $(u - g) < 0.8$ and $(g - r) < 0.2$, but no subdwarf was found in the extended colour range.

We find the main component in our sample of $\approx 14,000$ spectra to be DA white dwarfs. Along with the classification and search for hot subdwarfs, a number of white dwarfs were found with clear indications of strong magnetic fields. These objects are easily detectable by their unusual Balmer line profiles due to the Zeeman effect. An example spectrum can be seen in Fig. 6.4. Külebi et al. (2009) analysed the magnetic white dwarfs and determined their magnetic field strength. Most of these objects have field strengths in the order of $1 \ldots 100 \, \mathrm{MG}$. In light of kilo-Gauß magnetic fields in hot subdwarfs, O'Toole et al. (2005) estimated the white dwarf remnants of these objects to display $\approx 500 \, \mathrm{kG}$. Such white dwarfs are rarely found, even though the SDSS nearly tripled the number of known magnetic WDs (see Fig. 7 in Külebi et al. 2009).
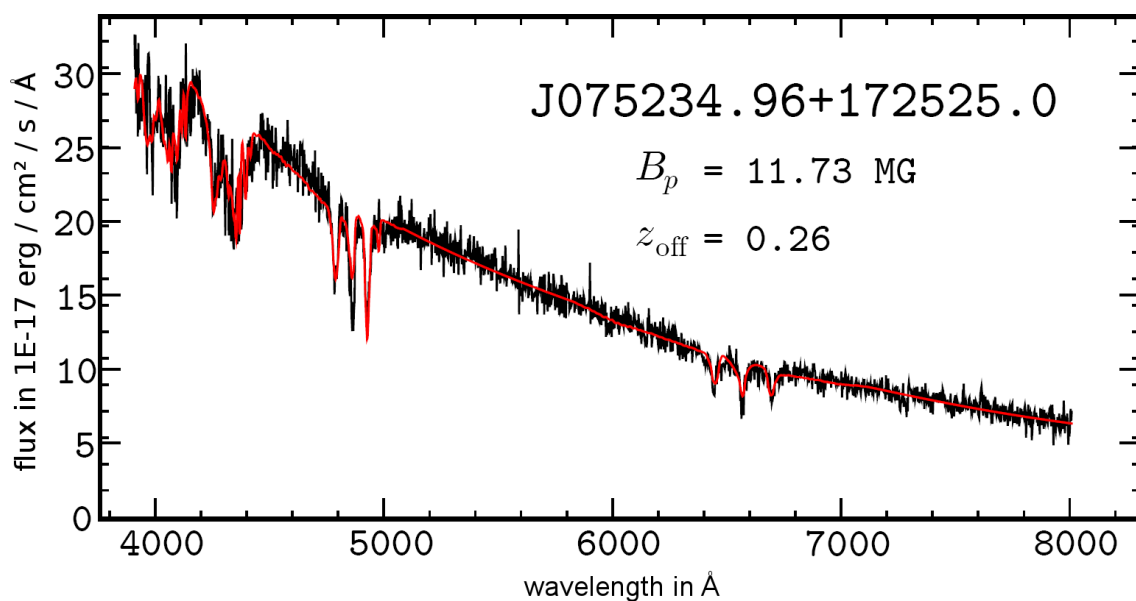
Figure 6.4: An example for a magnetic white dwarf found among objects we classified in our search for sdOs. This object was best fitted with $B_p = 11.73 \, \text{MG}$ and an offset $z_{\text{off}} = 0.26$ of the dipole along the magnetic field axis in stellar radii. Figure taken from Külebi et al. (2009, online version).

The break-down by spectral type is as follows:

- $\approx 10,000$ DA

- $\approx 1,300$ DB

- ≈ 50 DO

- ≈ 20 PG1159

- $\approx 1,000$ sdB

- 304 sdOB

  - 63 with signatures of companions

- 207 sdO

  - 13 with signatures of companions

Due to the low signal-to-noise ratio of many stars in *SDSS*, the classification is sometimes more guessing than knowing. The overwhelming number of DA stars lets us decide to classify many dubious spectra as sdB in order to prevent them from getting lost between DAs. Therefore, the true number of sdBs is most probably lower.

Also, some objects have been observed multiple times. We find in our sample that 34 sdO/sdOB stars have two or more spectra available. In chapter 6.4 we will use them

for an error estimate. The reason might be overlapping spectroscopy areas on the sky, or unsatisfying or erroneous spectra of one of the 640 objects taken. We, however, gladly use these for a more reliable error estimate in the following chapters.

6.3   Spectral analysis

The programmes described in chapter 3 were used for the quantitative spectral analysis. The models were the same as used by Ströer et al. (2007), see chapter 5.3. Usually, H_β, H_γ and H_δ were selected for the fitting procedure, as well as the He II Pickering lines for helium rich objects. However, especially He II 4 200 Å was too weak to be of use most of the times. H_ϵ was often excluded due to its contamination with interstellar calcium (Ca II 3 968 Å) and H_8 was only used in exceptional cases, as it is at the edge of the SDSS spectra and the data quality bluewards of 4 000 Å seriously degrades. Also we chose to exclude H_α in our fits. There are many reports (Ströer et al. 2007, e.g.) about the synthetic models not being able to reproduce this line correctly: The linecore seems to be "filled up", or even shows prominent emission. It is not yet clear, where this discrepancy stems from. The canonical consensus is to blame stellar winds. As the H_α core forms far out in the atmosphere, it is susceptible to many details of the atmosphere modelling, and NLTE effects and line blanketing unaccounted for are also probable. Also, an unseen companion star might fill the line with its continuum.

Unfortunately it is known that atmospheric parameters, especially T_{eff} and to some extend $\log g$, determined via the lower Balmer lines only are not reliable and often overestimate the temperature while underestimating the surface gravity. This problem is dominant for the hydrogen rich objects, not so much for the helium rich ones. Alas, it can't be helped — SDSS spectra do not provide access to the higher lines.

Both He II 4 686 Å and He I 4 472 Å were always included in our fits. The former was always present in the temperature regime of our interest, the latter as the strongest line of its species places helpful constraints on the effective temperature, even in its absence. He I 5 876 Å is situated near a prominent reduction artifact due to Na D doublet at 5 890 and 5 895 Å, visible in nearly all SDSS spectra. Therefore we excluded this region as well most of the times.

The complete list of all sdO(B) stars from SDSS we did a spectral analysis on is found in table D.1 and D.2 in the appendix. Stars from SDSS we classified as sdO(B), but did *not* use for a spectral analysis are summarised in table D.3. The reason for their exclusion of this work is too low signal-to-noise ratio in most cases, while some were found to lie outside of our modelgrid. For a couple of objects with excellent signal-to-noise ratio the line profile fits of the He II and the Balmer lines cannot be brought into agreement They are labelled with "H vs He" in table D.3. This so called "helium problem", is probably due to supersolar metal abundances and appropriate modelgrids accounting for this enhanced metal line blanketing are expected to work on these objects (see Geier et al. 2007a, and references therein).

6.4   Objects with multiple spectra

As we found 34 objects having multiple individual spectra we can readily use them to benchmark the reliability of our results. Unless stated otherwise, the object's final param-
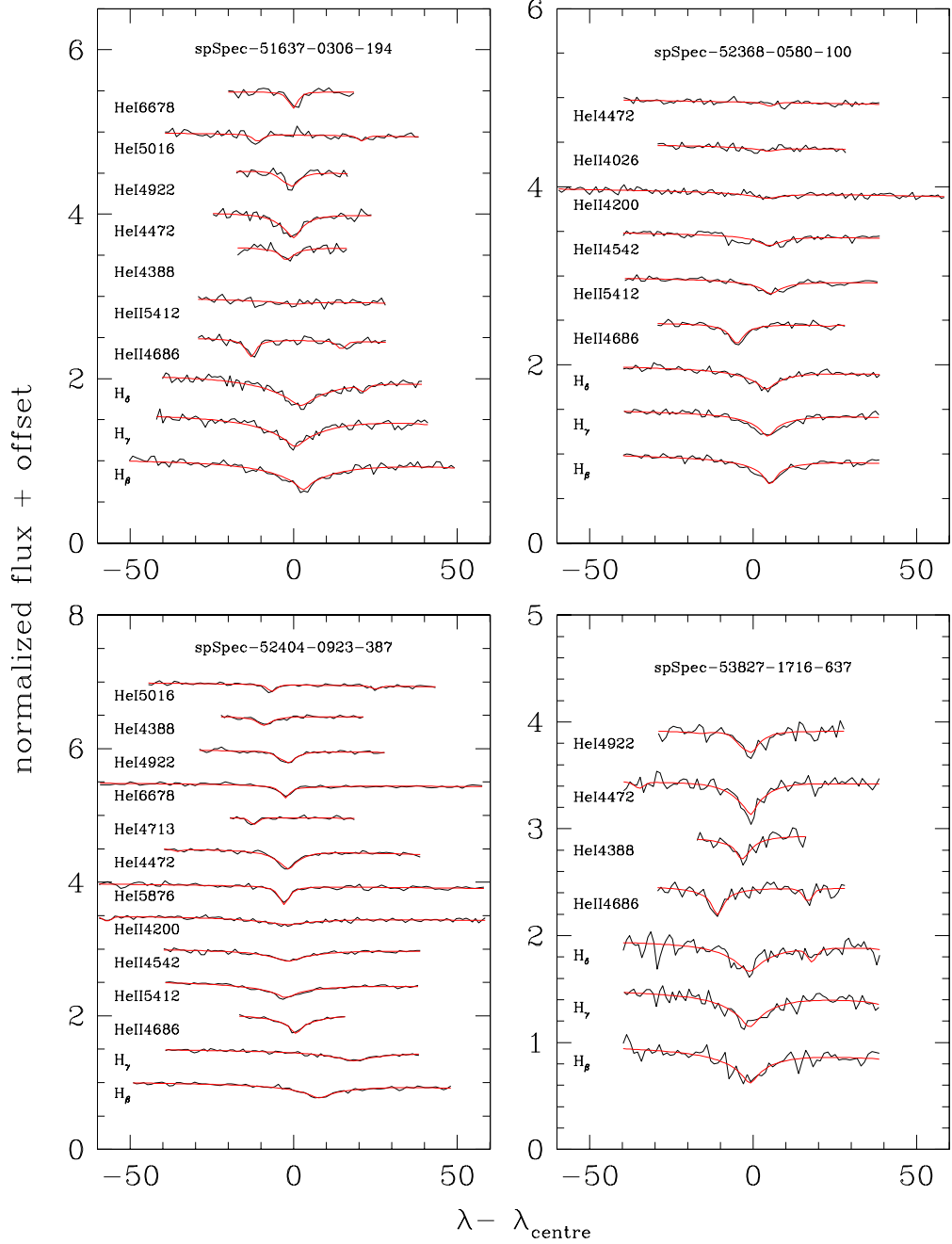
Figure 6.5: Typical example fits. *Top left:* sdOB, $T_{\text{eff}} = 37\,700\,\text{K}$, $\log g = 6.2$, $\log y = -0.7$. *Top right:* Hot sdO, $T_{\text{eff}} = 58\,400\,\text{K}$, $\log g = 5.7$, $\log y = -0.9$. *Bottom left:* sdO with no hydrogen visible in the spectrum, $T_{\text{eff}} = 44\,700\,\text{K}$, $\log g = 6.0$, $\log y = +3$. Note that the lines titled H_β and H_γ are actually the corresponding Pickering series of He II. Also note, that for SDSS this spectrum has an exceptional high signal-to-noise ratio. *Bottom right:* Example for the more common lower S/N. $T_{\text{eff}} = 40\,300\,\text{K}$, $\log g = 5.8$, $\log y = +0.1$.
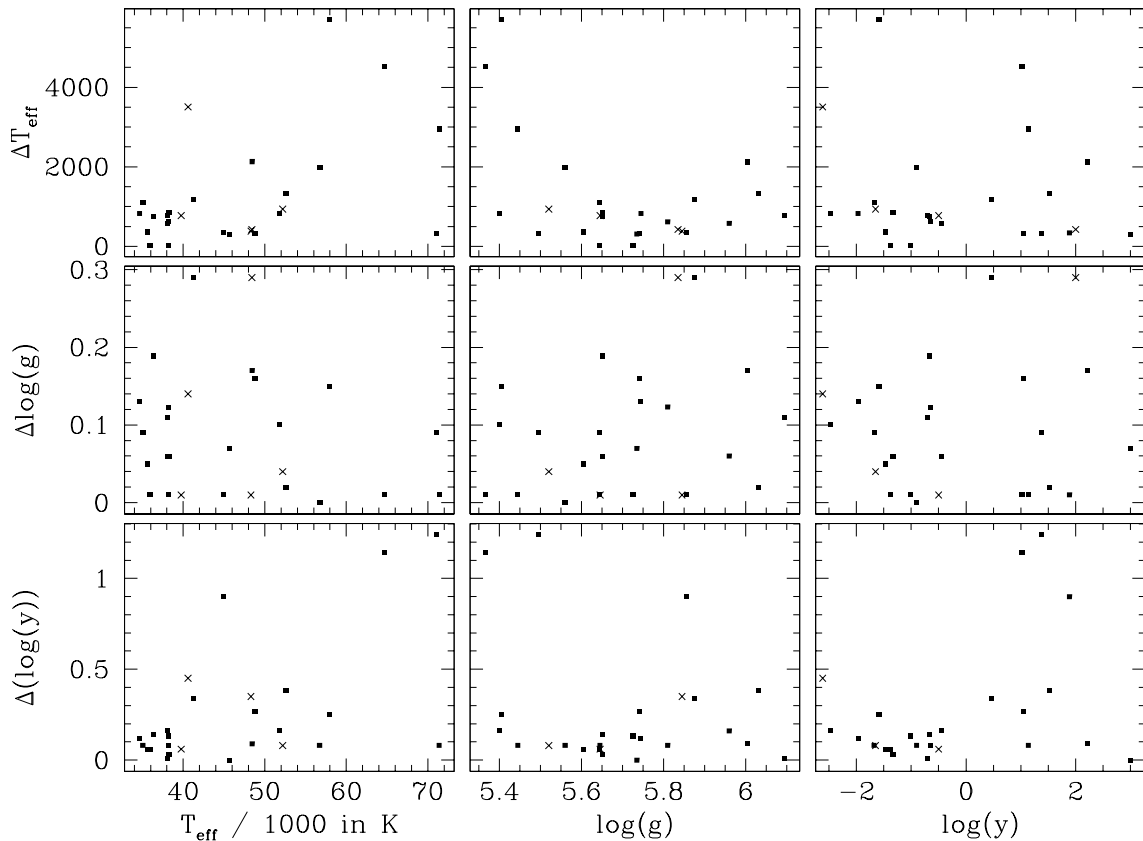
Figure 6.6: The parameters' mean values and their errors of the 22 stars observed twice or more plotted as function of the mean. Black squares are stars with multiple spectra in *SDSS*, the crosses are objects found both in *SPY* and *SDSS*.

eters are the arithmetic mean of all measurements. See chapter A.1 for a comparative list of these objects.

In order to get a handle on the errors, we take a look at the differences in the parameter determination of those stars we have two or more spectra of. Two objects had three and five spectra. In their cases the mean and standard deviation was calculated and the latter multiplied with $\sqrt{2}$, as the standard deviation underestimates the difference by this factor compared to objects with two measurements only. Fig. 6.6 plots these differences over the mean values for T_{eff}, $\log g$ and $\log y$. We see that for $T_{\text{eff}} < 50\,000\,\text{K}$ we have enough data points to confidently estimate the true statistical error to be below $2\,000\,\text{K}$, or 4%. Objects with higher T_{eff} on the other hand — though only a few data points are available — show a tendency to much higher errors, but insufficient data points prevent a solid conclusion. Besides, very hot stars cease to show He I lines in their spectra. We therefore lack the He I/He II balance as a reliable temperature indicator. For most but the hottest stars our model fits predict the strongest He I line to be detectable in spectra of higher signal-to-noise ratio than SDSS spectra provide.

We also see that $\Delta \log g$ is very evenly distributed and independent of the stars' parameters, while the error in helium abundance soars up to very large values for the helium-

enriched stars. This is easily explained by the fact that the resolution and signal-to-noise ratio of SDSS is too low for the Balmer lines to be visible near the dominating He II-lines of the Pickering series. In this case we see a pure helium spectrum, and $\log y = \log \frac{N_{He}}{N_H}$ is impossible to determine, yielding a lower limit for the helium abundance only.

As mentioned above in chapter 6.1, the single 15-minutes-exposures which are added for the final spectrum by the SDSS automatic pipeline are also publicly available since DR6. These could be used for a more significant statistical approach on error estimation, at least for the brighter objects. However, we did not explore this possibility further, as they became available only lately.

Six additional objects are included both in SDSS and SPY. A comparison of the parameters established by Stroer et al. from SPY and our work from SDSS reveals an acceptable agreement of both completely independent samples of different instruments, resolution and wavelength coverage. A list for these objects is found in chapter A.2.

The determination of v_{rad} in our SDSS stars shows a standard deviation of typically about $20\,\mathrm{km\,s^{-1}}$ between individual line measurements, which we take as our error estimate. From these reflexions we conclude that our parameter determination is robust and trustworthy and we settle for the final global errors as follows:

$$
\begin{aligned}
\Delta v_{\mathrm{rad}} &= 20\,\mathrm{km\,s^{-1}} \\
\frac{\Delta T_{\mathrm{eff}}}{T_{\mathrm{eff}}} &< 0.05 \text{ for } T_{\mathrm{eff}} < 50\,000\,\mathrm{K} \\
\frac{\Delta T_{\mathrm{eff}}}{T_{\mathrm{eff}}} &< 0.1 \text{ for } T_{\mathrm{eff}} > 50\,000\,\mathrm{K} \\
\Delta \log g &< 0.2\,\mathrm{dex} \\
\Delta \log y &= 0.4\,\mathrm{dex} \text{ for } \log y < +1 \\
\log y &= \text{lower limit for } \log y > +1
\end{aligned}
$$

6.5   The fast rotator WD 1632+222

In our analysis, we found it exceptionally difficult to obtain a reliable model fit to the spectrum of SDSS J16:34:16.08+22:11:41.0 = PG 1632+222 = WD 1632+222. It turned out, however, that this star has already been analysed by Ströer et al. (2007), who classified this object as a helium-enriched sdO with carbon lines in its spectrum. After a visual inspection of the SDSS spectrum, which is of very good quality, we confirm this classification.

A more careful examination of the object's two spectra (one low resolution, high signal-to-noise ratio SDSS spectrum, and one high resolution low S/N SPY spectrum) revealed clear signatures of rotational broadening. For comparison, we reanalysed the SPY spectrum once without rotational broadening, and a second time with $v_{\rm rot} \sin i$ as a free fit parameter, which gave a best fit for $v_{\rm rot} \sin i = 101\,{\rm km\,s}^{-1}$. On both fits, the helium abundance was fixed at $\log y = +3$. Figure 6.7 shows both model fits, the strong rotational broadening especially of the weaker He I lines is clearly visible. The effective temperature changed moderately from $T_{\rm eff} = 40\,000\,{\rm K}$ to $T_{\rm eff} = 39\,000\,{\rm K}$ and the surface gravity from $\log g = 6.00$ to $\log g = 5.79$. Now using the SDSS spectrum for parameter fitting, we found the best fit for the projected rotational velocity to be $v_{\rm rot} \sin i = 207\,{\rm km\,s}^{-1}$. Both fits (with and without rotational broadened model spectra) settle for very similar $T_{\rm eff}$ and $\log g$, namely $T_{\rm eff} \approx 38\,600\,{\rm K}$ and $\log g = 5.66$.

However, not too much significance should be attached to these values of the parameters as both the SDSS and the SPY spectrum is very difficult to use for a reliable model fit: First, we face a pure helium star, and secondly, the star has a relatively low temperature. Combining these two facts we find the spectrum does not show very pronounced He II lines because neutral He I still dominates over singly ionised He II, while the Balmer lines are not visible simply because the star has no hydrogen in its atmosphere. While a Gauss-Lorentzian fit on 7 He I lines of the SDSS spectrum yielded $v_{\rm rad} = -17 \pm 22\,{\rm km\,s}^{-1}$, a fit on 5 He I lines of the SPY spectrum settled for $v_{\rm rad} = +36 \pm 17\,{\rm km\,s}^{-1}$. This star does not only rotate very fast, but it also could be a radial velocity varible helium-enriched sdO!

This star is interesting and merits further investigation in the future. Its high rotational velocity could be interpreted as a direct link to the HeWD merger scenario. On the other hand, stellar rotation could play an important role for the late hot flasher scenario, as it is supposed to increase the luminosity at the tip of the RGB and could therefore explain enhanced mass loss. Moderate rotation ($v_{\rm rot} \sin i \approx 7\,{\rm km\,s}^{-1}$ on the HB) increases the helium core mass by $\approx 10\%$ on the (E)HB (Brown et al. 2008) which creates hotter helium-enriched sdOs in the late hot flasher scenario. But also the possible binary nature of this star yields some important clues: If this star were the result of a white dwarf merger, a detection of radial velocity variability would imply that the progenitor was a triple system, which renders this scenario less probable.
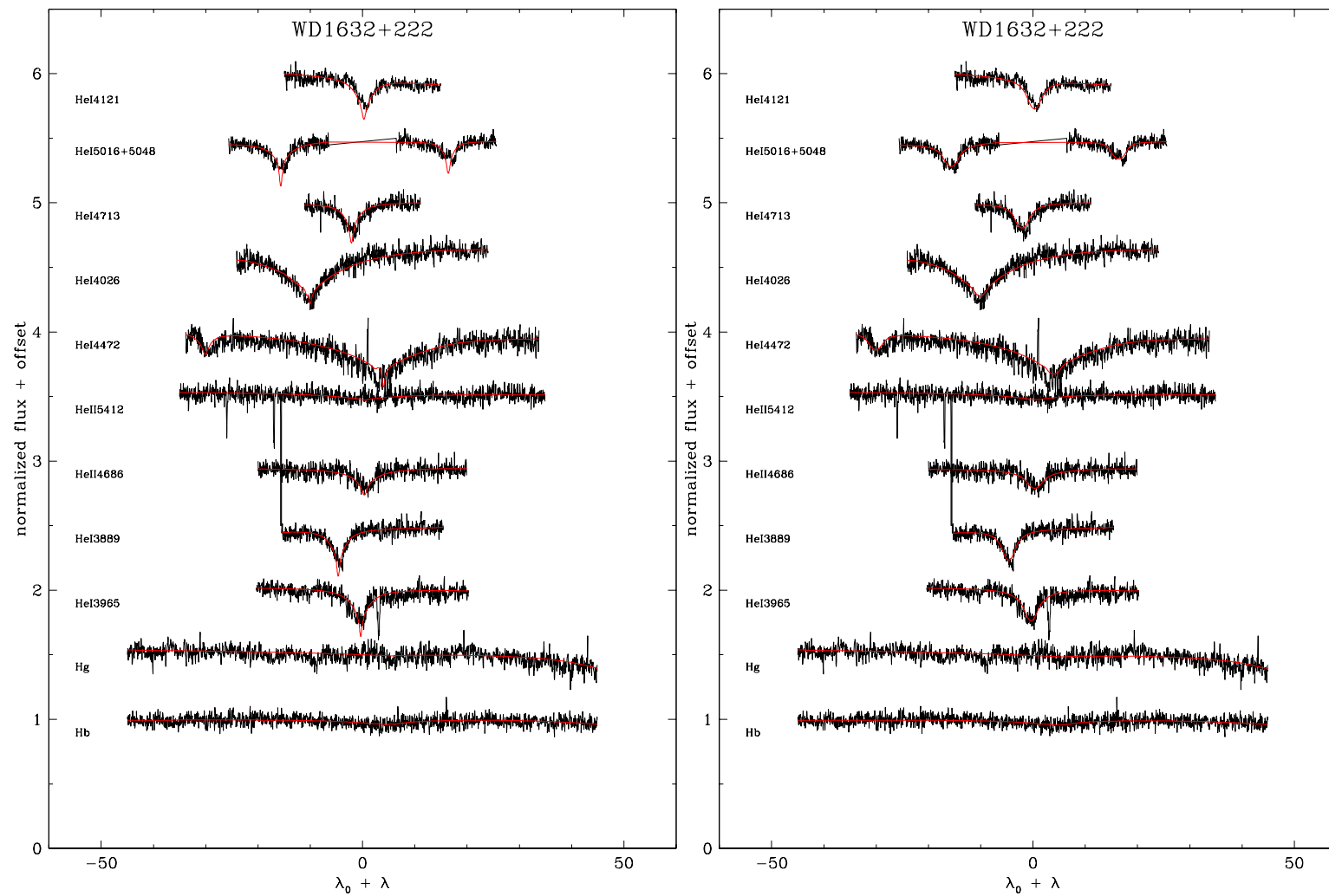
Figure 6.7: Modelfits of the fast rotating star WD 1632+222. *Left:* $v_{\rm rot}\sin i$ fixed to $0\,{\rm km\,s^{-1}}$. *Right:* $v_{\rm rot}\sin i$ fitted as free parameter, $v_{\rm rot}\sin i = 118\,{\rm km\,s^{-1}}$.

Chapter 7

Results of the analysis of SDSS spectra

In this chapter we will summarise and interpret the results obtained from the spectral analysis of the stars from SDSS. We will compare our sample of SDSS stars with the sdO sample from the SPY survey already published by Ströer et al. (2007) and discussed in chapter 5. Having used the same modelgrid as we did, the results are expected to be comparable. Throughout this chapter, the colour coding used is red for helium-enriched sdOs ($\log y > -1$), blue for helium-deficient sdOs. SdOs from SPY are represented by open triangles, those from SDSS as squares. For a more complete picture, we will also use the sdBs and sdOBs analysed by Edelmann et al. (2003) and Lisker et al. (2005), for which we will use grey symbols.

7.1   Helium abundances

The helium abundance seems to play a major role in the discussion of the hot subluminous stars. In figure 7.1 the logarithmic helium abundance is plotted over the effective temperature. Apart from the larger numbers, the distribution of our sdOs (squares) is very similar to that found by Ströer et al. (2007) (open triangles). We, however, find a considerable number of stars with helium abundances at the upper edge of our models ($\log y = +2$ for $T_{\mathrm{eff}} >= 55\,000\,\mathrm{K}$ and $\log y = +3$ otherwise). In chapter 6.4 we have attributed this to the lower quality of the SDSS sample.

A clear increase of the photospheric helium content with the effective temperature for sdB stars is reported by Edelmann et al. (2003) and Lisker et al. (2005). The former find some sdBs with lower abundances than the bulk, but with nearly the same T_{eff}-$\log y$-correlation (Edelmann et al. 2003, Fig. 5). We have plotted these two sequences and their linear extension into the sdO regime by grey dashed lines in figure 7.1. First, we find most sdOs with $\log y < -1$ to be in agreement with the upper sequence. But if we follow our distribution to higher abundances, we can find a kink in this linear sequence, at around the solar helium abundance. The second, lower trend, however, is not continued into our sample. A significant number of the hotter ($T_{\mathrm{eff}} \gtrsim 40\,000\,\mathrm{K}$) stars scatter below the second line and are not on it. Higher helium abundances than $\log y > +1$ do not show any clear trends and scatter widely in T_{eff}. But one should keep in mind that for high helium abundances our spectral analysis was not able to determine $\log y$ very precisely.
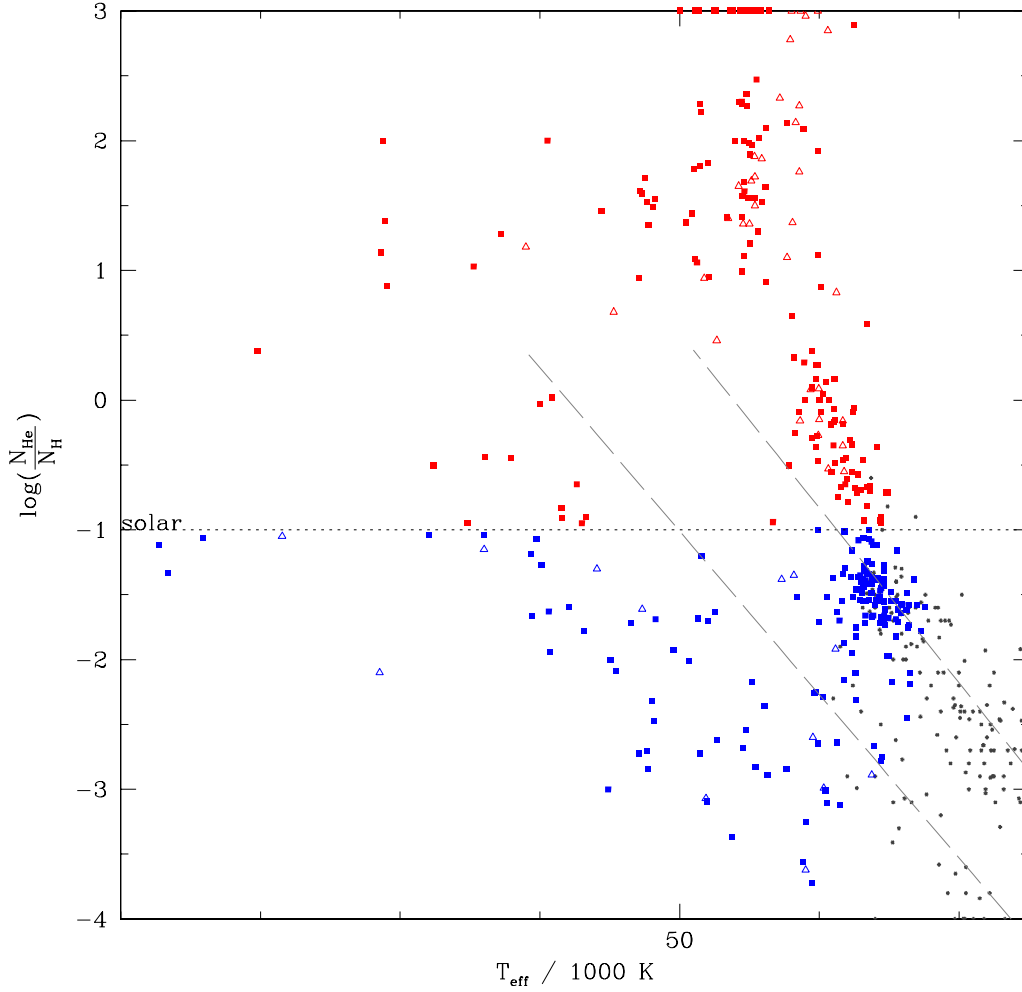
Figure 7.1: T_{eff}-$\log y$-diagram. Blue symbols represent the helium-deficient stars, red symbols are helium-enriched ones. SPY data are plotted with open triangles, filled rectangles are SDSS objects. The solar helium abundance is given by the dashed horizontal line. For a better comparison, sdBs and sdOBs analysed by Edelmann et al. (2003) and Lisker et al. (2005) are plotted as grey symbols. The two grey dashed lines are the two trends in $\log y$ with T_{eff} claimed by Edelmann et al. (2003) and confirmed, at least in part, by Lisker et al. (2005).

7.2 Luminosities

The luminosity of stars is given by

$$L = 4\pi R^2 \sigma T_{\text{eff}}^4 \tag{7.1}$$

with the Stefan Boltzmann constant $\sigma = 0.5670400 \cdot 10^{-4} \frac{\text{erg}}{\text{s cm}^2 \text{K}^4}$ and R the star's radius. Expressed in solar values, the luminosity becomes

$$\frac{L}{L_\odot} = \left(\frac{T_{\text{eff}}}{T_{\text{eff}\,\odot}}\right)^4 \left(\frac{R}{R_\odot}\right)^2 \tag{7.2}$$

with

$$\left(\frac{R}{R_\odot}\right)^2 = \frac{M}{M_\odot} 10^{\log g_\odot - \log g} \tag{7.3}$$

where we adopt a solar effective temperature $T_{\text{eff}\odot} = 5\,780\,\text{K}$ and a solar surface gravity of $\log g_\odot = 4.44$.

Figure 7.2 plots the cumulative luminosity function (normalised number fraction of stars with luminosities lower than a limiting luminosity) of our SDSS sample and compares it with the SPY sample. We used the canonical mass of $0.5\,M_\odot$ for the sdO mass for these calculations. In the left part, both samples are plotted without any differentiation of helium-enriched and helium-poor objects, while on the right side, we distinguish between them. Looking at the complete samples (Fig. 7.2, left), we see a very smooth and nearly linear distribution from $1.4\,L_\odot$ up to $2.6\,L_\odot$, that covers about 90% of our stars. This suggests a very uniform and complete selection of targets in SDSS. At the low luminosity end we explain the tail with the somewhat ambiguous classification into sdBs and sdOBs, where we might have missed some sdOBs. Both SPY and SDSS show a bend in the upper part of the CLF after 90%, which translates to a lower number of hot luminous objects. Overall the CLFs for both samples are quite similar, but the SPY sample has a steeper gradient, which means a narrower distribution over luminosities.

When dividing into helium-enriched and helium-deficient objects (Fig. 7.2, right), the step in the helium-deficient stars' distribution after 60% completeness at $L = 1.9\,L_\odot$ catches the eye immediately. Up to this step, the deviation between SPY and SDSS is
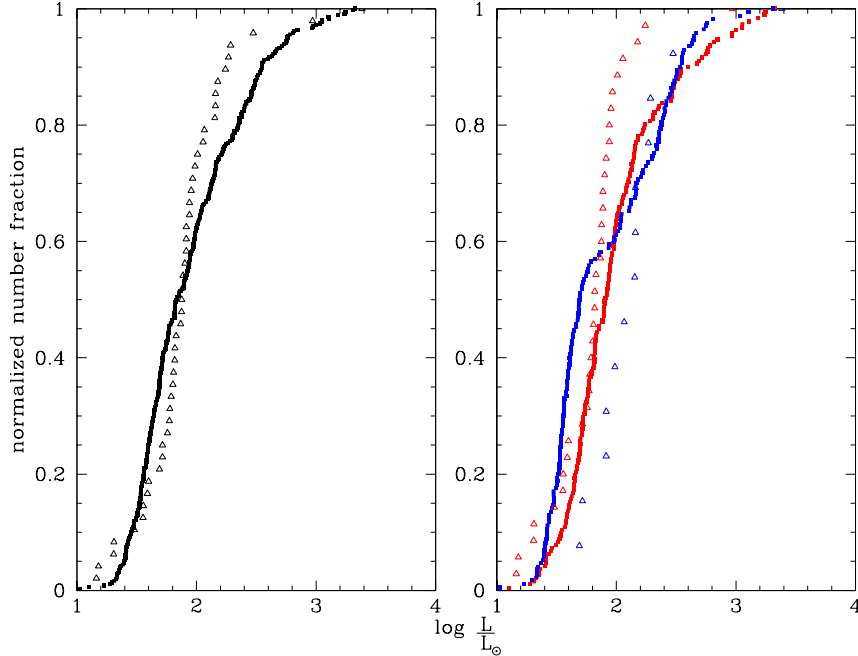
Figure 7.2: Cumulative luminosity function of the SDSS objects and SPY sdOs. *Left:* Squares represent the complete SDSS sample, open triangles represent the complete SPY sample. *Right:* The samples divided into helium-enriched (red) and helium-deficient (blue) stars.

as large as $0.4\,L_\odot$. We attribute this difference to the inclusion of the cooler sdOB stars in our sample. The step and the flatter gradient after the step can be interpreted as follows: While the EHB is still a region of nearly constant luminosity in the HR-diagram, the post-EHB evolution is characterised first by a rise in luminosity up to $\log L/L_\odot \lesssim 2.9$ before gravity takes over and the star fades into oblivion on short timescales (Dorman, Rood & O'Connell 1993). Exactly this behaviour can be seen in the CLF: the high percentage ($\approx 60\%$) of stars with $1.4 \lesssim \log L/L_\odot \lesssim 1.8$, followed by a decreasing slope up to $\log L/L_\odot \approx 3$.

As for the helium enriched sdOs (red symbols in Fig. 7.2), no such sudden change in slopes is apparent. One finds the SDSS sample to provide a larger number of very luminous objects. Where SPY has only 10% of helium enriched object with $\log L/L_\odot > 2$, SDSS has more than 30%, the gap in luminosities widening up to $\log L/L_\odot = 0.5$. We are not sure where this discrepancy stems from. Considering that all subdwarfs in SPY were initially classified as white dwarfs, one would expect more hotter and thus more luminous stars in SPY. This can be understood when recalling that at low effective temperatures the He I lines easily give away the non-WD status of the object. However, it cannot be stressed enough that the real selection effects for SPY are completely unknown, while we regard SDSS as very complete and more or less unbiased. Also, the volume in space covered by SDSS is larger than that covered by SPY when comparing the limiting magnitudes of $V = 18.5$ for our SDSS sample (see Fig. 6.2) and $V = 16.5$ (Napiwotzki et al. 2003). We therefore attribute this difference to better statistics of SDSS.

7.3   Space distribution and kinematics

With the atmospheric parameters known, we have the basic ingredients for the *spectroscopic distance*. The spectroscopic distance uses the physics of the star to measure the distance. However, one parameter not precisely known of most stars is needed: The star's mass.

To our advantage, the mass of sdO stars is known to be around $0.5\,M_\odot$ with very little margins for variations (unless the star were a HeWD merger). Assuming this canonical mass of sdOs and the surface gravity obtained from the spectral analysis, we find the star's radius via eq. 7.3. The apparent magnitude m_V in Johnson-V was calculated from the Sloan-*ugriz* system via equations provided by Jester et al. (2005). Interstellar absorption has been accounted for by correcting the SDSS magnitudes according to the dust maps provided by Schlegel, Finkbeiner & Davis (1998). By interpolating in precomputed tables of $T_{\rm eff}$ and astrophysical fluxes at the stellar surface, we calculated the absolute magnitude M_V. The distance in parsec can then be derived from

$$d = 10^{\frac{m_V - M_V}{5} + 1} \tag{7.4}$$

For ten helium rich objects no model flux was available in our code, in their cases a hydrogen rich atmosphere was assumed, which yielded larger distances. However, the differences to the true distances are less than 10%.

With the calculated distances and the known equatorial coordinates we can plot the position of our SDSS stars in (right-handed) Cartesian Galactic coordinates (sun at $X = -8.5$, positive x-axis in direction of the Galactic centre, y-axis in direction of Galactic rotation), see fig. 7.3. Although the grey coloured Galactic disk shown in the figure suggests
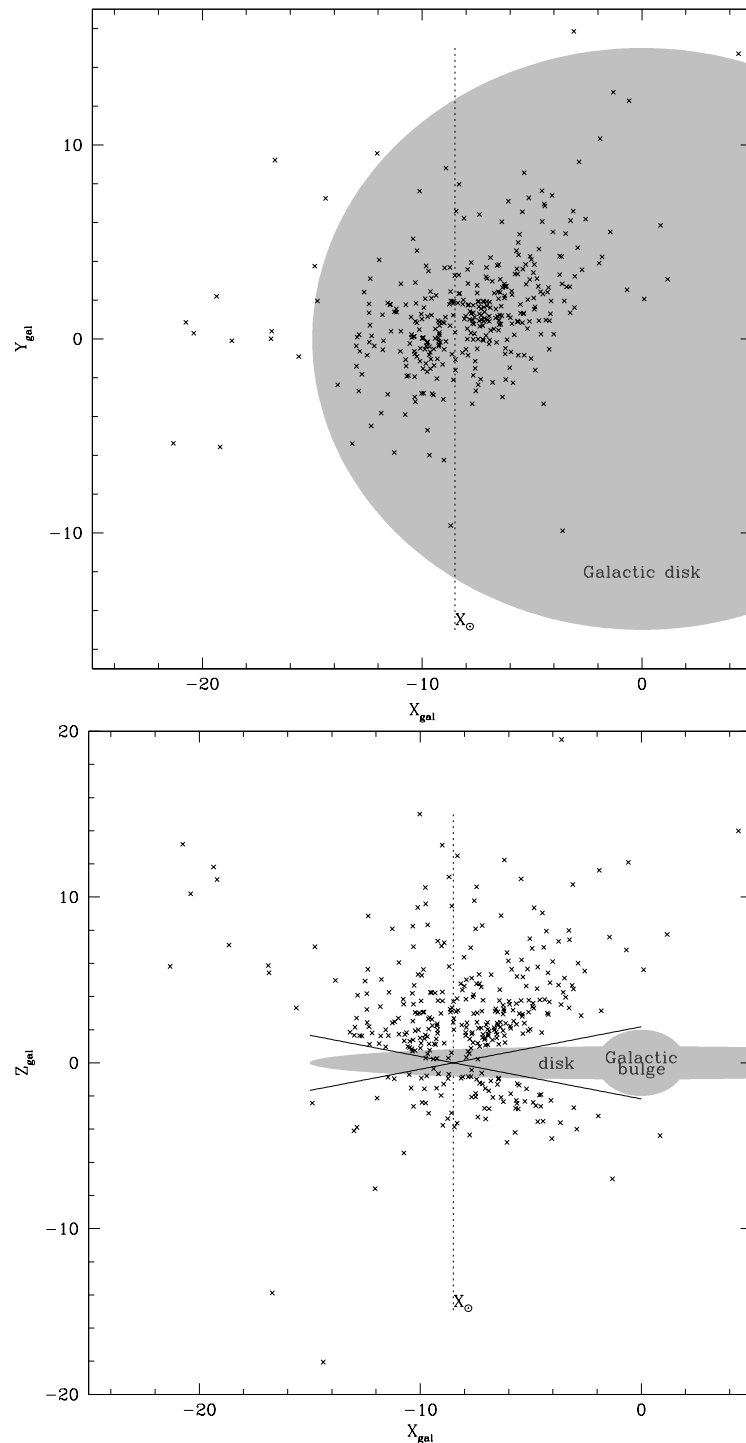
Figure 7.3: Cartesian Galactic coordinates of the SDSS programme stars. *Top*: View from above. *Bottom*: Edge on view. The sun's position is indicated by the stippled line at $X = -8.5$, two lines marking $b = \pm15°$ are plotted. Almost no star lies within this angle. The Galactic thick disk with scale height $1\,\mathrm{kpc}$ and the Galactic bulge are indicated by grey shaded areas. One clearly sees the impressive depth of SDSS, reaching far above or below the disk. From this it is apparent, that most of our program stars belong to the halo population

a sharp cut from thick disk to halo population, the overall star density of the thick disk is ≈ 130 times higher than for the halo (Buser, Rong & Karaali 1999), meaning that the number of stars belonging to the thick disk population dominates over halo stars up to $|Z| \approx 5\,\text{kpc}$. However, a detailed kinematic analysis of sdO stars from SPY done by Richter (2006) found them almost evenly distributed over thin disk, thick disk and halo (34%, 34%, 32%), but with very large error margins. Napiwotzki (2008) used the radial velocity only for a similar analysis and found fractions of 41%, 39% and 20% for thin disk, thick disk and halo, respectively. Therefore, both studies find a significant fraction of SPY sdO stars to belong to the halo population, even though the vast majority of objects is found within $|Z| \leq 1.5$ kpc. Having established the considerably further extend of SDSS into the halo compared to SPY, we conclude that most of our programme stars are likely to belong to the halo population.

Support for this conclusion comes again from Han et al. (2003), who found that lower metallicity corresponds to faster evolution: the distribution of masses along newly created stars, the Initial Mass Function, is far more weighted at its low mass end, producing more long living low mass stars. Therefore in low metallicity environments like the halo more EHB stars are created.

Chapter 8

Testing evolutionary scenarios with the T_{eff}-$\log g$-diagram

Essentially, the T_{eff}-$\log g$-diagram is a Hertzsprung-Russell-diagram (T_{eff}-$\log L$-diagram) turned by 45° counterclockwise. The main advantage over the classical HRD is the use of parameters accessible by quantitative spectral analysis: the effective temperature and the surface gravity. Both have been acquired from the spectral analysis described in the chapters before. Then we can use this diagram to distinguish populations of stars with similar parameters and we can compare the populations' distributions with predictions from stellar evolution calculations.

8.1 Canonical post-EHB evolution

In canonical evolutionary scenarios, the subdwarfs are regarded as a small helium burning core of about $0.43\ldots0.495\,M_\odot$, only slightly dependent on metallicity, with a small hydrogen envelope added. They evolve from the Zero Age Extended Horizontal Branch (ZAEHB, defined by the onset of stable helium core burning) to the Terminal Age Extended Horizontal Branch (TAEHB, defined by helium core exhaustion) in roughly 100 Myrs. The following post-EHB evolution is characterised by increasing T_{eff} and a short rise in luminosity (= lower surface gravities) before settling on the typical WD cooling curve.

In Fig. 8.1 our programme stars are plotted in the T_{eff}-$\log g$-diagram. The EHB is plotted for solar metallicity. With reduced metallicity the EHB is shifted towards higher T_{eff}, about $2\,000\,\text{K}$ for [Fe/H] = -2.26. Two evolutionary tracks for [Fe/H] = -2.26 from Dorman, Rood & O'Connell (1993) are given, each with their masses plotted beside them, the envelope mass reduced from $0.005\,M_\odot$ (upper track) to $0.003\,M_\odot$ (lower track).

First we notice that none of our stars except a handful of sdOBs lie on the EHB band itself. The most obvious step would be to consider all sdO stars to be post-EHB stars. Their post-EHB evolution, however, is about one order of magnitude faster than EHB evolution, and becoming ever faster as long as represented in our figures. Again, the sdBs in our sample are missing and no quantitative comparison between EHB and post-EHB number ratios and distributions can be made.

Still, the helium-deficient sdOs with low surface gravities are represented by the Dorman tracks exceptionally well. The helium-enriched sdOs on the other hand are clustered at
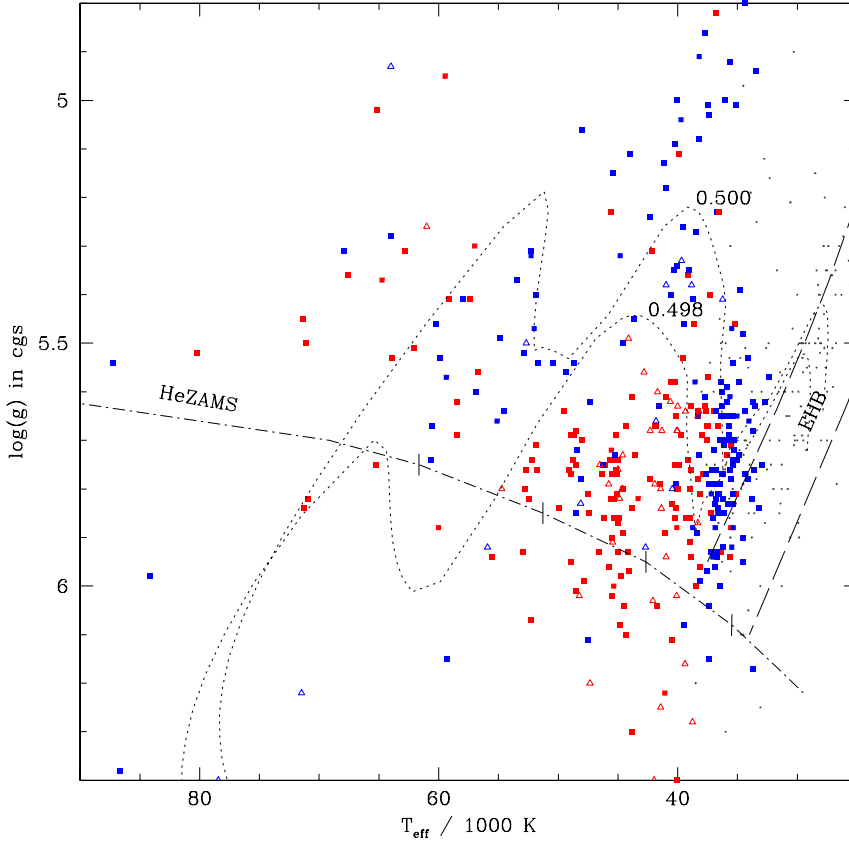
Figure 8.1: T_{eff}-$\log g$-diagram of the SDSS stars. Blue symbols represent the helium-deficient stars, red symbols are helium-enriched. Also, the Zero Age Helium Main Sequence (HeZAMS) is given as well as the EHB by its Zero Age and Terminal Age locations. Post-EHB evolution is represented by the two tracks (Dorman, Rood & O'Connell 1993), each with their respective mass given.

$T_{\text{eff}} \approx 45\,000\,\text{K}$ and the objects with $\log g > 5.7$ cannot be covered by canonical post-EHB evolutionary tracks. This overdensity of helium enriched sdOs is in violation with timescales from post-EHB evolution calculations.

8.2   Binary population synthesis models

Before an extensive comparison between binary population synthesis models and our data can be done, selection effects have to be taken into account. The simulation sets of Han et al. (2003) considered possible selection effects, the *GK selection effect* being the most important one: No subdwarf with a main sequence companion earlier than K was included in their simulation, as these would be visible in the spectrum or even outshine the subdwarf. This is well in agreement with most analysed subdwarf samples, especially with the SPY sample as well as our SDSS sample, where composite-spectrum objects were excluded.

Fig. 8.2 shows our SDSS programme stars plotted over the predicted distribution, where
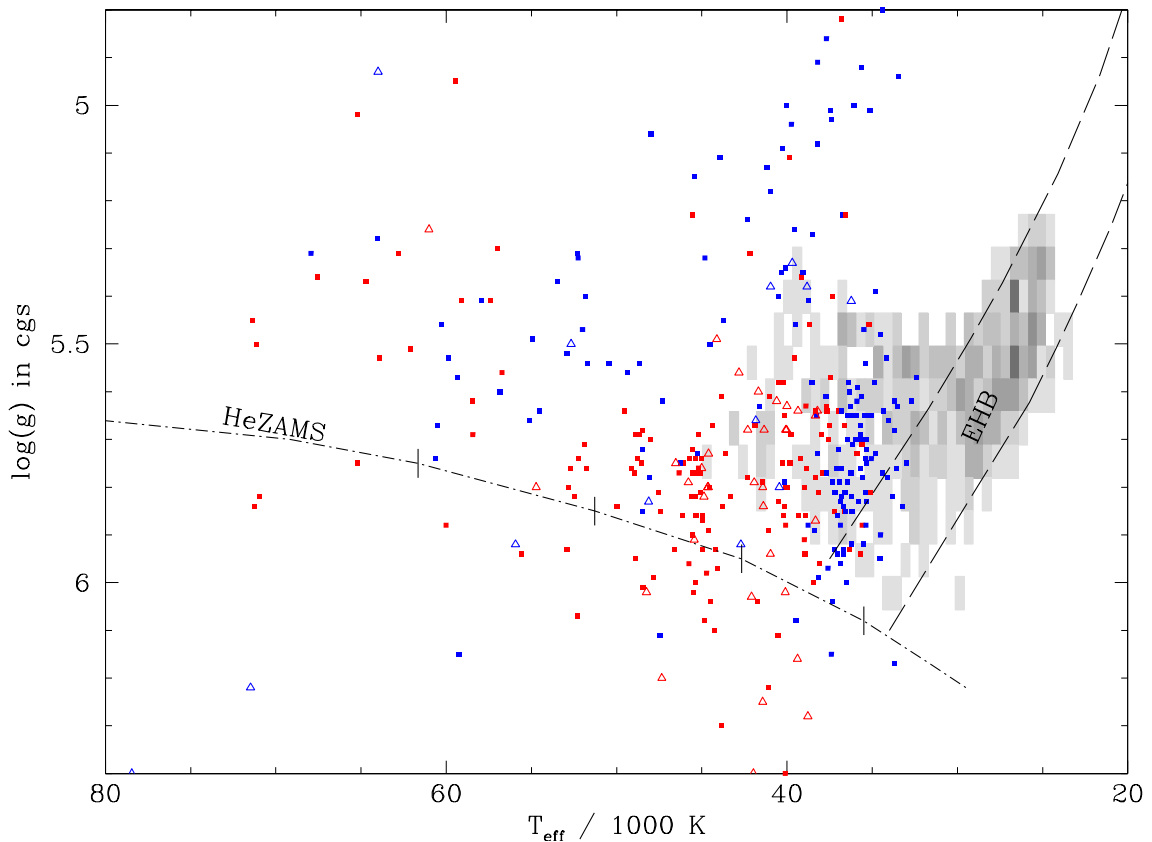
Figure 8.2: SdOs and sdOBs from SDSS compared to simulation set 10 from Han et al. (2003). The grey boxes portrait the predicted number of objects, the darker the box the more objects lie within. Again the EHB and the HeZAMS are plotted. Tickmarks on the HeZAMS indicate the position of 0.5, 0.7, 1.0 and $1.5\,M_\odot$ helium stars (from right to left).

we use simulation set 10 from Han et al. (2003), as found to be the best matching set by Lisker et al. (2005). It becomes apparent that the major part of sdOBs with $T_{\mathrm{eff}} < 40\,000\,\mathrm{K}$ and $\log g = 5.5\dots 6.0$ falls onto the predicted area. But while matched qualitatively at least in part by the simulation, we cannot draw any definite conclusions for the sdOBs because for a quantitative comparison the cooler sdBs are missing in our sample.

However, the simulated distribution completely fails to reproduce the observed sdOBs with low surface gravities, which lie considerably above, and all sdOs but a handful of cooler ones ($T_{\mathrm{eff}} < 43\,000\,\mathrm{K}$ and $\log g \approx 5.5\dots 5.9$). Of the three channels considered, the HeWD merger intrinsically produces subdwarfs with a wider mass distribution and higher temperatures. In order to reproduce the large fraction of helium enriched sdOs at $45\,000\,\mathrm{K}$, the merger channel must play a much larger role than considered by Han et al. (2003). But emphasising the merger channel will also increase the number of merger products with lower mass, which in turn increases the number of helium rich stars in the sdB regime. This contradicts the very small number of helium rich sdBs known.

8.3   non-EHB scenarios

In Fig. 8.3 two alternative explanations are tested: post-AGB (Schönberner 1979, 1983) and post-RGB (Driebe et al. 1998) evolution. The former is represented by two tracks in the upper left part, the latter by the three tracks reaching from top to bottom. Some of the hottest stars are possible post-AGB candidates. With the very short timescales of about 30 000 years between AGB and WD stages in mind, the low number of stars in this region is well explained. Turning towards the post-RGB scenario where a red giant star of sufficiently low mass fails to ignite helium and descends directly down to the white dwarf graveyard as HeWD. The low mass ($\approx 0.5\,M_\odot$) needed for the progenitor of such an object means that it would spend more time than the Hubble time on the main sequence and cannot yet have reached the RGB. Hence, mass transfer in a binary system has to be invoked in order to turn more massive stars ($\approx 1\ldots 2\,M_\odot$) into a remnant of $M \approx 0.4\ldots 0.2\,M_\odot$. A striking similarity between the tracks and the stars' distribution is apparent from Fig. 8.3. At first glance we are tempted to identify all of the sdOs as post-RGB stars. Especially the helium enriched sdOs appear to be a population of stars
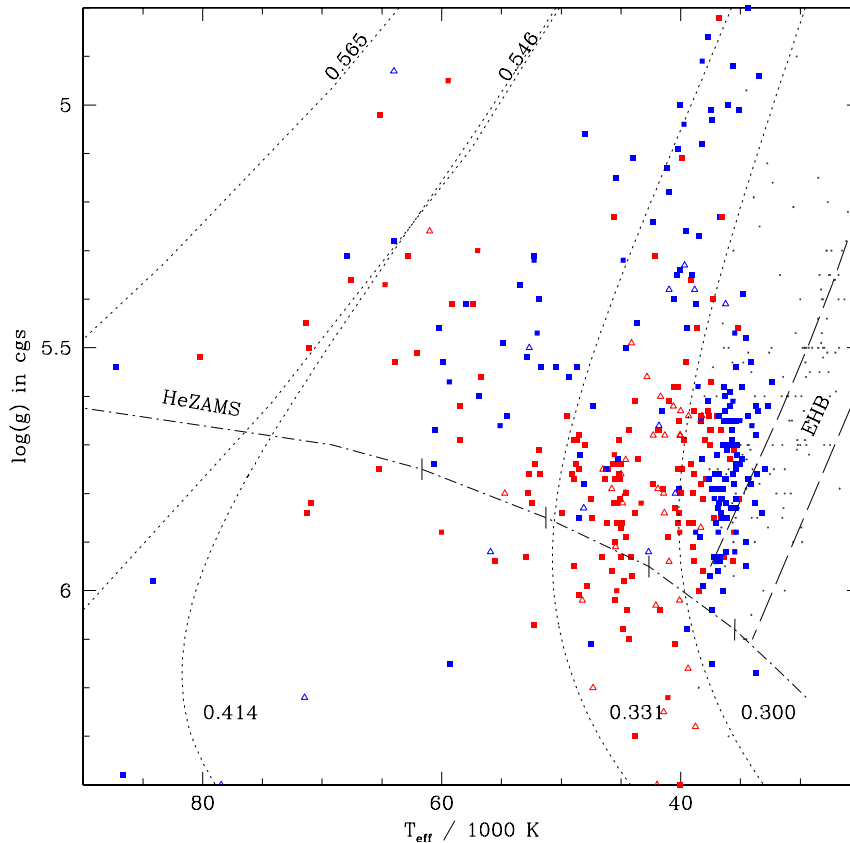
Figure 8.3: Same as fig. 8.1, except the two leftmost tracks plotted are post-AGB from Schönberner (1979, 1983) with the remnants' final masses given at the top of each track. The three rightmost tracks reaching from top to bottom are low mass post-RGB tracks from Driebe et al. (1998).

within a narrow mass range of $M \approx 0.331 \ldots 0.300 \, M_\odot$ leaving the first red giant branch and heading towards the HeWD stage. However, the calculations of Driebe et al. (1998) predict rather thick hydrogen envelopes, in conflict with the helium dominated atmospheres we see in our objects. Thermal instabilities caused by hydrogen shell flashes could dredge up helium and CNO-processed matter, but only occur in stars with masses less than $0.3 \, M_\odot$ (Driebe et al. 1999), just shy of our helium enriched sdOs (see tracks in fig. 8.3). For some of the helium-enriched sdOBs below $40\,000\,\mathrm{K}$ this could therefore be a valid scenario.

Also, as pointed out above, the progenitor has to be within a binary system. Only a very tiny fraction of helium enriched sdOs is known to be radial velocity variable, rendering this scenario highly unlikely to apply to a significant fraction of the stars in question.

8.4 Late hot flasher

Mass loss through strong winds can reduce the envelope mass fast enough so that the star leaves the RGB before the onset of central helium burning. Still, already on its way to the white dwarfs, the star can experience the helium flash and settle on the extended horizontal branch. Depending on the entropy barrier of the hydrogen burning shell, the convection zone powered by the helium flash can reach up to the outer layers of the envelope resulting in a complete burning of the hydrogen ("deep mixing", DM), or the convection zone splits very early and the outer layers are only diluted with CNO processed matter and no burning of hydrogen occurs ("shallow mixing", SM). See chapter 2.3 and references therein.

While the helium-deficient sdOs do not show any signs of metal lines in their optical spectra, the helium-enriched sdOs have strong lines of carbon and/or nitrogen, but also silicon, sulphur, oxygen and neon. Because the late hot flasher scenario predicts a significant (or even complete) mixing of the star's outer layers with the inner regions down to the 3α helium burning core, we regard this scenario as a very interesting candidate to explain the origin of the helium enriched sdOs. With detailed calculations and predictions of the surface composition after a late helium flash at our disposal (Miller Bertolami et al. 2008), this scenario can be tested extensively.

Fig. 8.4 shows our sdO distribution in the T_{eff}-$\log g$-plane. One late hot flasher track (DM flavour) from Miller Bertolami et al. (2008) is plotted. This track consists of three different parts: The descent from low surface gravities towards the HeZAMS (dotted line), the stage of stable helium core burning (solid line) near the HeZAMS and finally the evolution at constant gravity, when the core burning is extinguished (dashed line). The offset between the HeZAMS and the helium core burning phase is due to different metallicities (solar for the HeZAMS, low metallicity $z = 0.001$ for the LHF track). An example for the shallow mixing flavour (SM) is the "hook" (black solid line) at around $35\,\mathrm{kK}$ and $\log g = 5.8$ (Moehler et al. 2004). Pre- and post helium core burning phases have been omitted, but are similar to the DM case. Shallow mixing does not create pure helium atmospheres, but only enhances the helium content moderately ($\log y \approx 0 \ldots 1.4$ for $z = 0.001 \ldots 0.02$).

As can be seen in Fig. 8.4, the position of our helium-enriched sdOs is covered nearly perfectly by the tracks *before* settling on the HeZAMS. Stars with metallicities ranging from solar to halo ones on their way to stable helium core burning would cover the relevant region extensively. It seems we finally found the culprit for the hot helium-enriched subdwarfs with the late hot flashers. A more detailed examination, however, brings some discrepancies to light which we cannot ignore. Most of their lifetime the stars spend in the stable helium
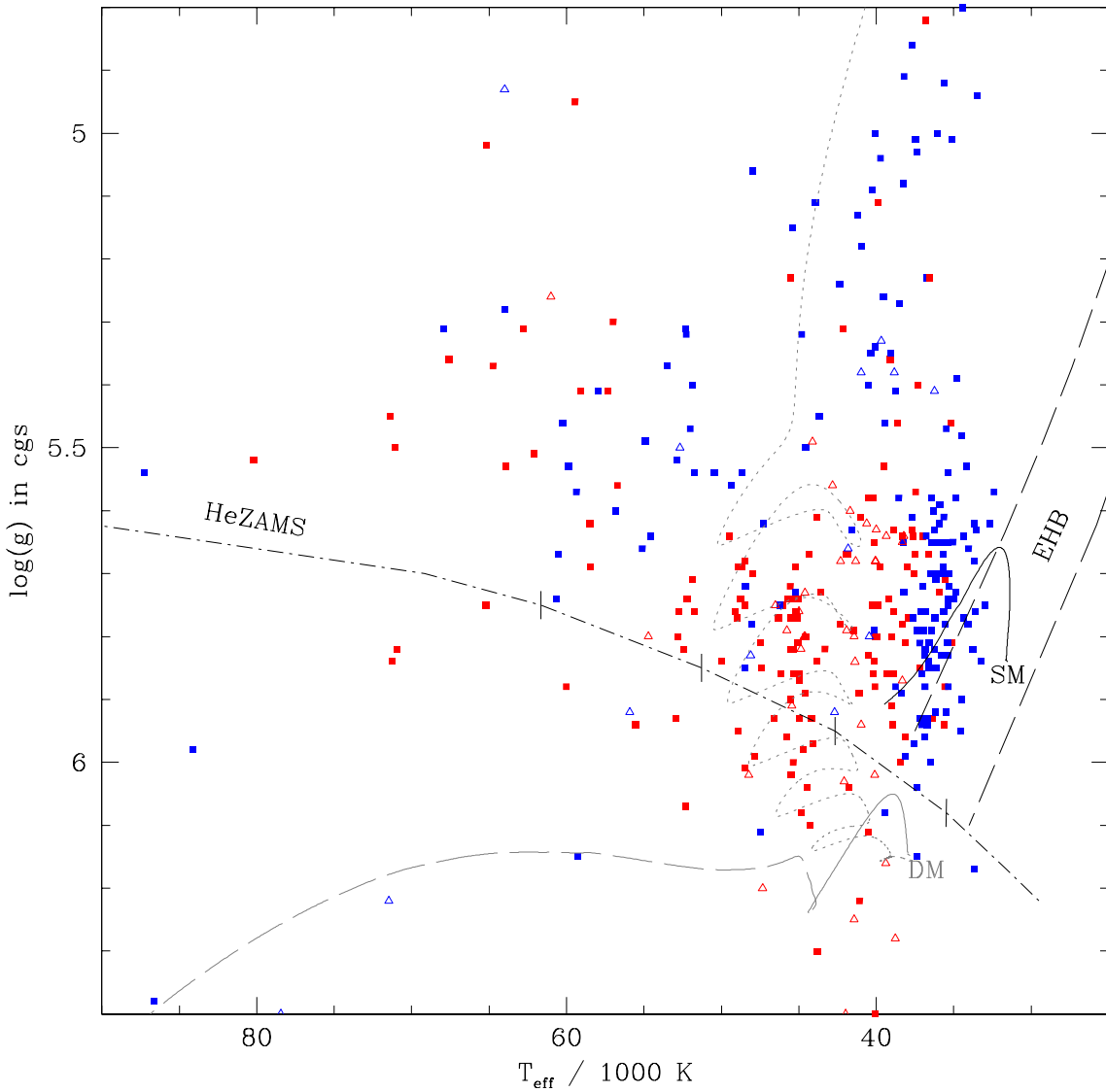
Figure 8.4: Positions of sdO stars in the T_{eff}-$\log g$-plane compared with tracks for late hot flashers, DM (grey, Miller Bertolami et al. 2008) and SM (black, Moehler et al. 2004) cases. LHF tracks can be divided into the fast evolution from low gravities towards the HeZAMS (dotted part), their long stay as helium core burning object (solid parts, the "hooks") and the evolution after helium exhaustion first to higher T_{eff} before entering the WD cooling curve (the nearly horizontal dashed line). Note that for reasons of clarity the dotted and dashed parts of the SM case (upper hook) have been omitted. The offset between the HeZAMS and the stable helium core burning phase of the tracks is explained by the different metallicities, the HeZAMS is calculated for solar metallicities.
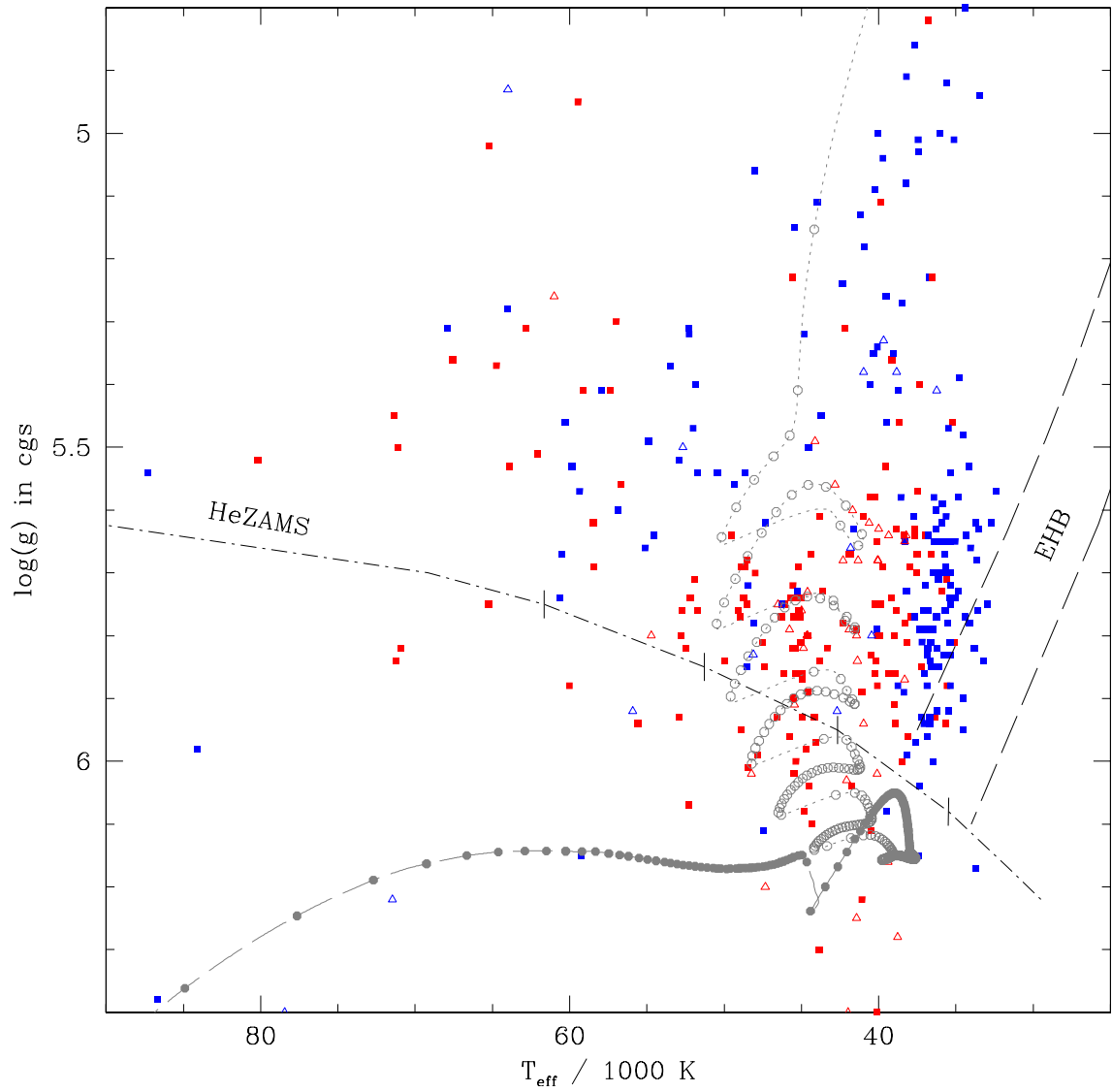
Figure 8.5: See Fig. 8.4. Open circles are placed every 10 000 years, filled circles every 1 000 000 years. Note the extremely fast evolution towards the HeZAMS, compared to the ~100 million of years the star stays in the helium core burning phase, significantly below the bulk of sdOs. The evolution after helium exhaustion again speeds up at timescales of millions of years.

core burning phase represented by the two "hooks" (solid lines). A better impression of the timescales is found in Fig. 8.5, where symbols have been placed on the DM track in intervals of 10 000 years (open circles) and 1 000 000 years (filled circles). We see that only about a dozen of the helium enriched objects fall onto or near the core helium burning part of the tracks, while the following evolution along constant gravity to higher effective temperatures is covered by virtually none of our objects.

One possible explanation for this discrepancy that comes to mind is the direction of evolution in the T_{eff}-$\log g$-diagram: In a *volume complete* survey one expects the number of stars to rise with $\log g$, because the evolution slows down. However, over the range of $\log g = 5.5 \ldots 6.2$, the luminosity of the star drops by more than a factor of three and the sampled volume of a *magnitude limited* survey is reduced to $\approx 20\%$. On the other hand, the horizontal evolution to higher temperatures following helium core exhaustion occurs at nearly constant gravities, the luminosity therefore is expected to rise again. So, if the magnitude limited nature of the survey were the cause of the strange distribution which contradicts the time scales, the population of helium enriched sdOs should again become visible along this track. Obviously, this is not the case.

Another unsolved problem is the fact that all deep mixing scenarios result in atmospheres virtually completely void of any detectable traces of hydrogen. We however find a considerable number of stars with hydrogen content of 1% to 10%, more compatible with shallow mixing scenarios. Very little traces of hydrogen however are enough to turn an sdO with pure helium atmosphere into an object with hydrogen dominated atmosphere within 10^6 years (Miller Bertolami et al. 2008). A trend of decreasing helium abundance with increasing $\log g$ ($\widehat{=}$ age) however is not detectable in Fig. 8.6. Unglaub (2008) has performed detailed diffusion calculations for the hot subdwarfs. He shows that the assumption of homogeneous winds does not hold true for all parameter space: Radiation driven winds mainly act on metals due to their higher opacities. In thin winds, the coupling between metals and hydrogen and helium by Coulomb collisions is not strong enough and while metals are expelled the latter two elements are not affected. He published limits for homogeneous winds for three different metallicities ($z = z_{\odot}$, $z = \frac{1}{3}z_{\odot}$, $z = \frac{1}{10}z_{\odot}$). Unfortunately, the calculations were tailored for the sdB stars and need to be extended beyond 40 000 K to account for most of the sdO stars.

In figure 8.6 these limits are plotted in a T_{eff}-$\log g$-diagram of our program stars. The helium content is given by the size of the symbols and the wind limits are the three solid lines in the upper right part. For a given metallicity the winds are homogeneous above the corresponding line and diffusion is not expected to work. Below the limit, helium and hydrogen decouple from the metals and are at diffusion's mercy. We would therefore expect to find hydrogen dominated photospheres for the stars below the limits, while stars above can show a variety of different abundance patterns, depending on the exact state of equilibrium between gravitational and radiative forces. Such an observation, however, is not made.

Based on Fig. 8.4, it is unlikely that the shallow mixing plays an important role for the hot helium enriched subdwarfs. The track starts far in the EHB, i.e. the sdB regime, where the number of helium enriched objects is very small. That is compatible with the SM evolution taking place below all wind limits, and helium enriched atmospheres are expected to turn hydrogen rich on short timescales. A further examination of the impact of the SM scenario requires to include the sdB stars into our consideration which is not

yet possible.

On the assumption that the helium-enriched sdOs are indeed late hot flashers and experienced deep mixing, some contradictions have to be solved: why are there far more objects in regions of very fast evolution ($\approx 1\,\mathrm{Myr}$) compared to the sparsely populated core helium burning stage ($\approx 100\,\mathrm{Myrs}$)? The problems with diffusion are also unanswered. DM produces pure helium atmospheres, with only traces of hydrogen left. These traces, however, are enough to float to the surface after the star has crossed the wind limits on its descent towards the HeZAMS. This descent occurs on timescales comparable to the diffusion timescales. In any case, once stable helium core burning is established, this stage is maintained more than long enough to have diffusion remove most traces of helium from the atmosphere. In Fig. 8.6 no clear trend in helium abundances versus wind limits is visible. We find different helium abundances scattered throughout the diagram. Especially in the bulk of helium enriched sdOs at $T_{\mathrm{eff}} \approx 45\,000\,\mathrm{K}$ we do not find helium to become less dominant with increasing gravity, as expected with diffusion. Helium rich objects, however, experience convection in their photospheres (Groth, Kudritzki & Heber 1985), preventing diffusion. As a consequence, once enriched in helium the objects stay that way.

8.5   Summary

From the discussion of the binary evolution scenarios we conclude that the helium deficient sdO and sdOBs are EHB or post-EHB stages of stellar evolution. According to the binary population synthesis of Han et al. (2003), the medium gravity sdOBs and helium deficient sdOs at low temperatures can easily be considered to be the result of a lost envelope due to binary interaction. Following the tracks of Dorman, Rood & O'Connell (1993), these objects evolve over the low gravity helium-deficient sdO regime to higher temperatures and continue on the typical WD cooling curves. A more detailed quantitative comparison with the simulation sets requires an analysis of the sdB stars from SDSS and a careful estimate of selection effects in the sample. Helium rich sdOBs are not consistent with the current diffusion scenario and stellar evolution cannot connect them with the hydrogen deficient sdBs.

Some of the hot stars in the upper left part of our plotted areas can very well be in post-AGB stages of stellar evolution. Also post-RGB stars with parameters similar to EHB stars are known to exist (Heber et al. 2003a), but require a companion which should be detectable in RVV surveys. And their helium abundances predicted by theory are much lower than the helium-enriched sdOs show. Though nearly perfectly matched by post-EHB tracks, we dismiss this idea for the helium-enriched sdOs.

Hence we are left with two scenarios: (i) the HeWD mergers and (ii) the late hot flashers. Both scenarios produce hot stars with only a tiny fraction (if at all) of hydrogen in their atmospheres and an enrichment in either CNO- or 3α-processed material. It is now clear, that the T_{eff}-$\log g$-diagram alone with the helium abundance does not provide sufficient information to definitely answer the question of the sdOs' origin. As pointed out in chapter 2.3, Miller Bertolami et al. (2008) did extensive simulations of the late hot flashers and predicted surface abundances for ^{12}C, ^{13}C, N and O. Another topic neglected up to now is the effect of heavily enriched carbon and/or nitrogen content on the atmospheres (line blanketing). In the following chapters we will use H+He+C and H+He+N model atmospheres for a detailed abundance analysis of the helium-enriched stars from SPY.
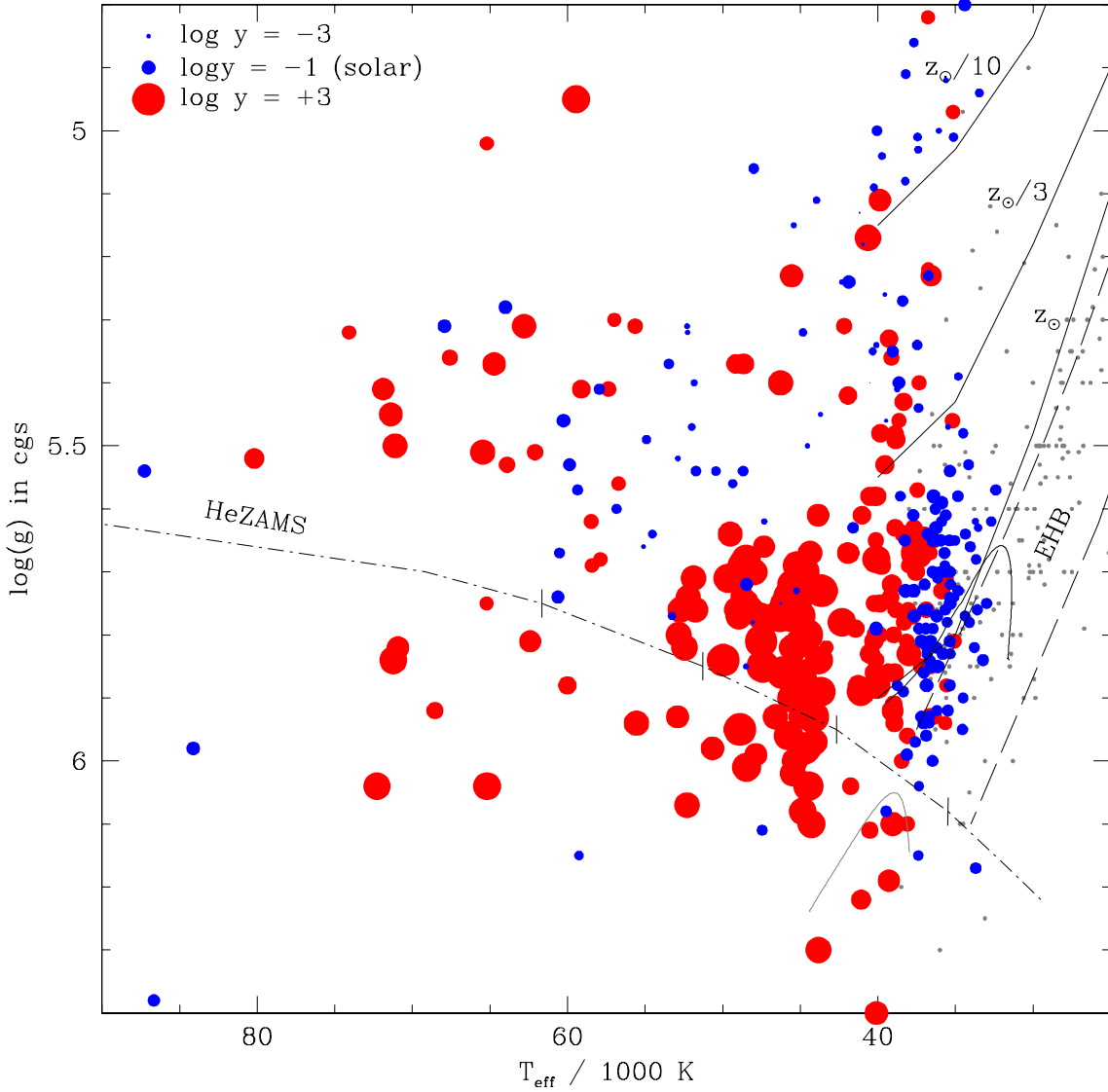
Figure 8.6: T_{eff}-$\log g$-diagram with the helium abundance encoded in the symbols' size. The usual suspects EHB and HeZAMS are plotted again. Windlimits computed by Unglaub (2008) are given by the solid lines in the upper right. They are labelled with their metallicities. No homogeneous winds are possible below those limits, above those limits stellar winds can counteract diffusion.

Chapter 9

Beyond Hydrogen and Helium: Carbon and Nitrogen

Previous quantitative spectral analyses relied on hydrogen and helium models only. As shown in chapter 8, this information is not sufficient to distinguish between different evolutionary scenarios. It was found that the helium-enriched sdOs differ from the helium-deficient ones by the presence of carbon and/or nitrogen lines in their optical spectra. The two most plausible scenarios (HeWD merger and the different flavours of late hot flasher models) do predict measurable differences in the resulting carbon and nitrogen abundances. We therefore constructed two new model grids, one with a detailed carbon model atom and one with a nitrogen model atom added to the existing hydrogen and helium data.

9.1 TMAP

TMAP, the "Tübingen NLTE Model Atmosphere Package" (Werner & Dreizler 1999), is a code for the calculation of stellar atmospheres and their emergent flux on the principles discussed in chapter 4. It uses a preconditioning based on Rybicki & Hummer (1991) to set up linearised rate equations.

A temperature correction scheme based on the established Unsöld-Lucy method for LTE atmospheres was extended to NLTE conditions and implemented in TMAP by Dreizler (2003). With the accelerated lambda iteration the radiative equilibrium is the only remaining constraint that couples all atomic levels after the hydrostatic equilibrium and conservation equations have been separated. Separating the energy balance from the rate equations allows their solution atom by atom, ion by ion. The energy conservation is then ensured by the temperature correction scheme.

The package consists of a number of programmes and auxiliary tools. Initial LTE models are calculated with *LTE2*. NLTE model atmospheres are created with *NGRT*, which requires an initial start model. Both LTE and NLTE start models can be used. Finally, *line1_prof* uses the atmospheric structure from *NGRT* to solve the restricted NLTE problem, i.e. it solves the radiation transport and rate equations with a fixed temperature and pressure stratification. This yields the emergent flux, the synthetic spectrum, which is then fitted to observed data.

TMAP is only the solver of the NLTE equations, atomic data must be provided in input files prepared by the user. In the atomic data file, the user specifies which levels in

which ions and atoms are to be used, and what the energies and statistical weights of the levels are. Levels can be treated either as LTE or NLTE levels. Radiative and collisional transitions with their upper and lower levels have to be specified as well as the formula and optional parameters to be used for their cross section calculation. It is optional to specify explicit frequency grids to be used around a *rbb*-transition. *atoms2* is used for checking the atomic data files for consistency and is able to fill in missing data, e.g. it can construct a complete H I and He I,II atom. For frequency discretisation *setf2* takes the model atom file and constructs an appropriate frequency grid with 5 frequency points around each line transition.
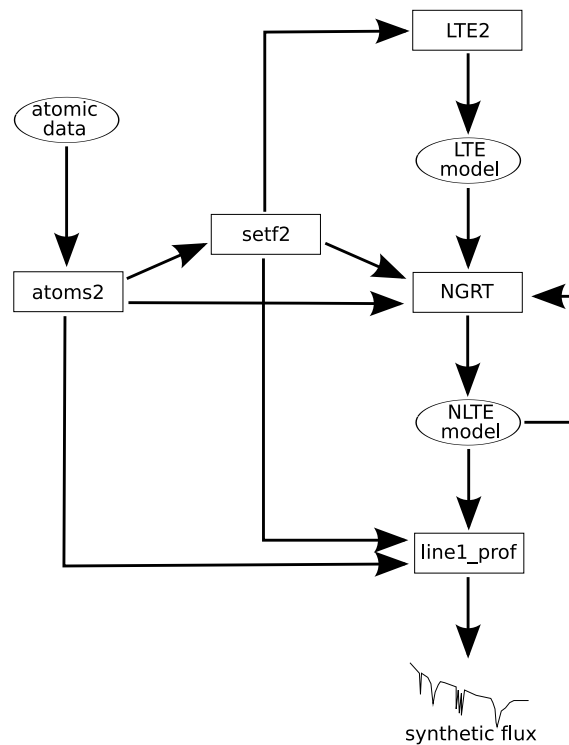
Figure 9.1: Work flow of the TMAP code.

As can be seen in figure 9.1, *NGRT* uses both the initial LTE models as well as already calculated NLTE models as start models. This eliminates the need to construct a new model from scratch for each point in our model grid: Neighbouring, already converged atmospheres can be used as new start models, if the parameters are similar.

9.2   New model atmospheres with TMAP

New atomic models require a recompilation of the TMAP code, as array boundaries like the one for frequency points and energy levels are hard coded parameters and have to be adjusted. Atomic models were acquired from Thomas Rauch's publicly available database (http://astro.uni-tuebingen.de/~rauch/). For nitrogen, the ionisation stages N II, N III, N IV and N V were considered, while the carbon model consists of C II, C III and

C IV only. The hydrogen and helium model atoms from the established models by Ströer et al. (2007) were re-used without alteration. We used the same options for *NGRT* and *line1_prof* as Hügelmeyer (2006) used for his PG 1159 model grid. Convergence for the first models was very slow, but the successive re-use of converged models for new grid points accelerated the process.

The new model grid covers the temperature range from 38 000 K to 50 000 K in 2 000 K steps and 5.0 to 6.4 dex in 0.2 dex steps in $\log g$. Carbon and nitrogen abundances[1] considered are 0.001%, 0.010%, 0.050%, 0.100%, 0.500%, and 1.000%. Helium is represented with $\log y = -1, 0, +1, +2$. The carbon models generally converged without problems. The majority of the nitrogen models, however, did not meet the program's convergence criterion (relative corrections in the ALI iteration $\leq 10^{-4}$). For those that went through the maximum number of iterations, the output was examined to make sure that remaining temperature corrections were small and the desired effective temperature was reached. As we started with a very high number of iterations anyway (1000), re-iterations were hardly necessary. A number of calculations for low temperatures, high abundances of carbon or nitrogen and with a considerable amount of hydrogen failed, the model grid has some gaps in these regions.

The synthetic spectrum was calculated for the wavelength range from 2 840 to 6 125 Å. Longer wavelengths are ignored as the S/N of the observations is significantly worse than in the bluer part of the spectra. Also, H_α line profile suffers from several unaccounted effects and is not used in our analyses. Around the spectral lines the wavelength points are very narrow spaced and more than 28 000 (H+He+C) and 36 000 (H+He+N) frequency points are present in the synthetic spectra.

9.3 Comparison of models

9.3.1 Old H+He and new H+He+C/N models

Of course we performed a direct comparison between the old H+He and the new H+He+C/ N models. Taking the new model grid with fixed metal abundances at the lower limit, $\log(N_C/N) = -5$, we fitted the new H+He+C grid to two synthetic spectra of the old H+He grid, both with $T_{eff} = 42\,000$ K and $\log g = 5.8$ — one with a low helium abundance $\log y = -1$ and one with high a helium abundance $\log y = +1$. The fit to the hydrogen rich spectrum yielded the expected temperature, while the best fit surface gravity was found to be 0.15 dex higher ($\log g = 5.95$). Excluding the higher Balmer lines H_ϵ and H_8 as well as He I/II 4 026 Å from the fit, as was done in Ströer et al. (2007) and in our analysis in chapter 6, leads to an even higher overestimate of $\log g = 6.02$. The same trend was found for the fit to the helium-rich spectrum, where the complete list of spectral lines yielded a slightly more accurate $\log g$ estimate of $\log g = 5.88$, while ignoring the higher Balmer and the He I/II 4 026 Å lines again raised the $\log g$ to $\log g = 5.95$ while T_{eff} remained nearly unchanged. H_ϵ and H_8 proved to be the strongest contribution to these changes. Significant differences between our new and the old models by Ströer et al. (2007) become obvious in a direct comparison (Fig. 9.2): the H+He+C spectra have broader line profiles in every H I and He II line, while He I is more or less compatible.

---

[1] The attentive reader remembers that all abundances in this work are *by numbers*, unless explicitly stated otherwise.
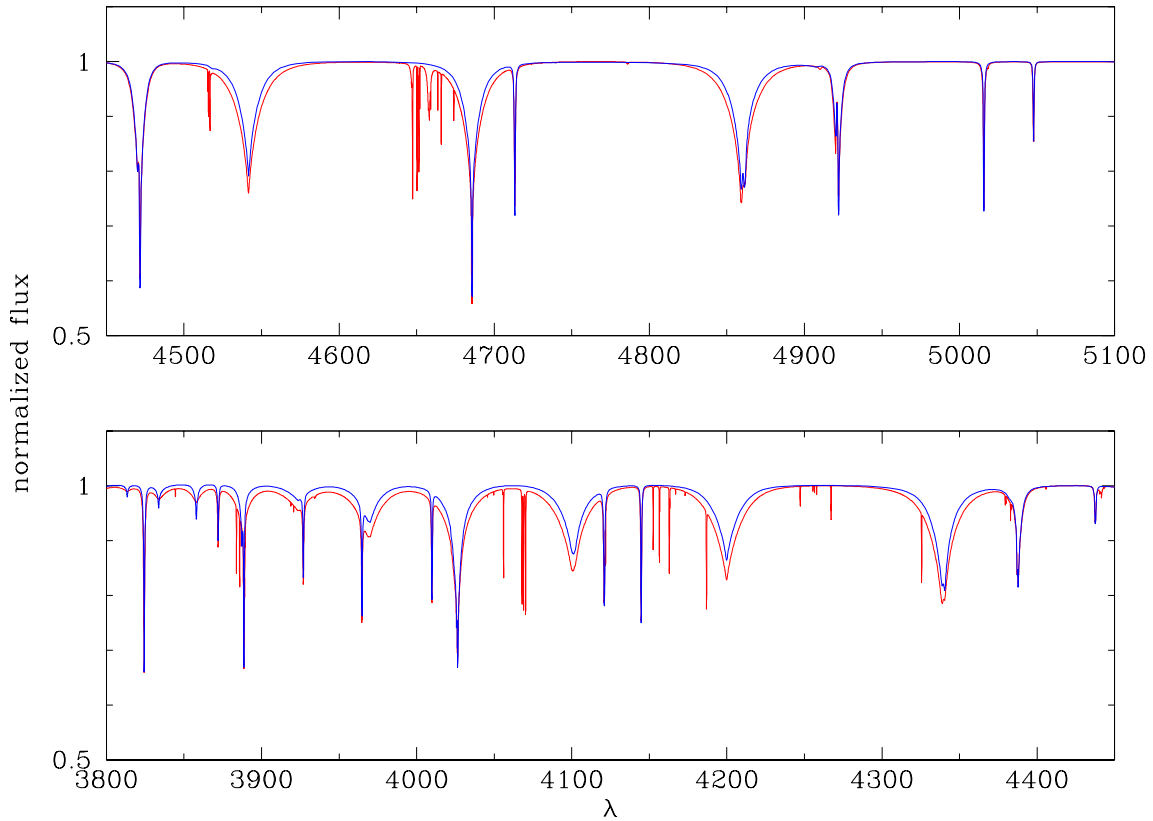
Figure 9.2: Direct comparison of a synthetic spectrum from a model with $T_{\text{eff}} = 44\,000\,\text{K}$, $\log g = 5.6$ and $\log y = 0$. In blue the old H+He model is plotted, red is the new H+He+C one. The difference in the Balmer/Pickering lines is clearly visible, however He I lines like the ones at 4121, 4472, 4713, 4922, 5016 and 5048 Å are nearly identical.

9.3.2   Testing the old H+He versus newly calculated H+He models

We investigated this difference further by calculating new H+He only models with a) the TMAP executable from Ströer et al. (2007), b) our new executable and c) the executable provided by S. Hügelmeyer (priv. comm.). No significant difference was found between b) and c), while the old H+He models still differ from these new test models with hydrogen and helium only.

9.3.3   The role of metal line blanketing

We therefore find some differences in both model grids, but their origin remains elusive. Atomic data for hydrogen and helium used was the same in both cases, as were line broadening tables. The frequency grids are not exactly the same, but do not differ much around the helium and Balmer lines.

Metal line blanketing effects are expected, which however should mainly affect the temperature determination. This can be understood in the following way: far in the UV, metal lines are plenty and very strong. Flux conservation then requires that the blocked

flux from the UV is redistributed along longer wavelengths, like in the optical region we use for our analyses. This increases the flux continuum level which in turn lowers the ratio of line depth to continuum. The old H+He models did not account for line blanketing of carbon and nitrogen, therefore the apparently shallower lines mimic hotter temperatures. With the inclusion of carbon and nitrogen, we expect to improve the line profiles in our models. Estimates of temperatures derived by line profile fitting then should yield better values. As can be seen in table E.1, other metals (like e.g. silicon or titanium) not accounted for in our models are present, which we still ignore.

The flux blocking of the metal lines affects the temperature stratification of the atmosphere, steepening the temperature gradient (backwarming effect). Apparently our naïve expectation considering the flux redistribution only is not sufficient. Instead, the atmospheric structure and the regions of line formation change. This could be an explanation why our measured effective temperature changes not as much as expected, but the surface gravity instead. Still, the differences between the old H+He models and new test models also using H+He only is not solved.

Chapter 10

Bright sdO stars as testbeds

By courtesy of H. Edelmann and L. Morales-Rueda, we had access to high quality high resolution spectra of five of the brightest helium enriched sdO stars known. The data were acquired with the FEROS spectrograph (Kaufer et al. 1999) at the ESO 2.2m telescope. They have a resolution of $R = 48\,000$. Four of these stars have multiple spectra obtained in different epochs, which enables us to make statements on their radial velocity variability.

In this chapter, we will use these spectra as a testcase: we will compare values for T_{eff}, $\log g$ and $\log y$ derived from fitting H+He+C/N models with those derived from the old H+He models.

10.1 Procedure

For every single spectrum the radial velocity was determined by fitting a Gauß+Lorentz profile independently to suitable lines. Due to the overlap of hydrogen Balmer and some He II Pickering lines, no Balmer lines were considered. Prominent He I/II lines like the ones at $4\,026$, $4\,472$ and $5\,875$ Å have more than one multiplet component and a reliable central wavelength could not be found, so they were dismissed, too. The He I-lines at $5\,016$ and $5\,048$, the He II at $4\,686$ as well as the Si IV doublet at 4088.86 and 4116.16 Å were used always. Another dozen of metal lines, mostly nitrogen, carbon and silicon, were carefully selected. The standard deviation of the measurements of all lines is taken as the error in the radial velocity.

Fitting the old models with only hydrogen and helium is straightforward: All three parameters T_{eff}, $\log g$ and $\log y$ are fitted simultaneously. The new models have one additional degree of freedom, the carbon or nitrogen abundance. For these the following iterative scheme was adopted:

1. Keep C or N abundance fixed and determine T_{eff}, $\log g$ and $\log y$ for hydrogen and helium line profiles.

2. Fit $\log(N_{\mathrm{C}}/N)$ or $\log(N_{\mathrm{N}}/N)$ together with $v_{\mathrm{rot}} \sin i$ from C or N line profiles, now with fixed T_{eff}, $\log g$ and $\log y$ determined in step 1.

3. Repeat until the parameters do not change.

All parameter fits converged fast within only three iterations.

10.2   HD 127493

HD 127493 (= CD $-22\,3804$) is a helium-enriched sdO star with moderate helium content for this class: the Balmer lines still dominate over the Pickering lines. Nitrogen lines are abundant, carbon lines are missing. The apparent magnitude in V is $m_V = 10\overset{\text{m}}{.}021$ (Kilkenny et al. 1998), extinction is $E(B-V) = 0.09620$ (Schlegel, Finkbeiner & Davis 1998). A Hipparcos parallax is given as $\pi = 5.21 \pm 1.49\,\text{mas}$, which translates to $d = 192^{+77}_{-43}\,\text{pc}$. For every one of the three FEROS spectra obtained in two consecutive nights we find a radial velocity of $v_{\text{rad}} = -17 \pm 3\,\text{km\,s}^{-1}$. Apart from the usual nitrogen lines, the spectrum is rich in lines of other metals, along with some carbon. See table E.1 in chapter E. An earlier analysis of Simon (1982) found $T_{\text{eff}} = 42\,500 \pm 2\,000\,\text{K}$, $\log g = 5.25 \pm 0.20$ and $\log y = +0.18 \pm 0.18$.

	H+He	H+He+N	H+He+C
T_{eff}	42 286 K	42 484 K	
$\log g$	5.66	5.60	
$\log y$	+0.41	+0.62	
$\log(N_{\text{N}}/N)$		−3.11	
$\log(N_{\text{C}}/N)$			< -5
$v_{\text{rot}} \sin i$		< 10 km s^{-1}	

Both model grids agree perfectly on this object's atmospheric parameters, see Fig. 10.3. But the model fits look different, especially those for H_β and H_γ and for He II 5412 and He II 4542 Å. It seems as if the old H+He models cannot accurately reproduce the broader lines. Also, the line cores — especially of H_β, see fig. 10.1 — are much better reproduced by the new models.

One exception is He II 4 200 Å, where the new models do not fit at all, while the old models have no problems in reproducing this line. In figure 10.2 both are plotted over the
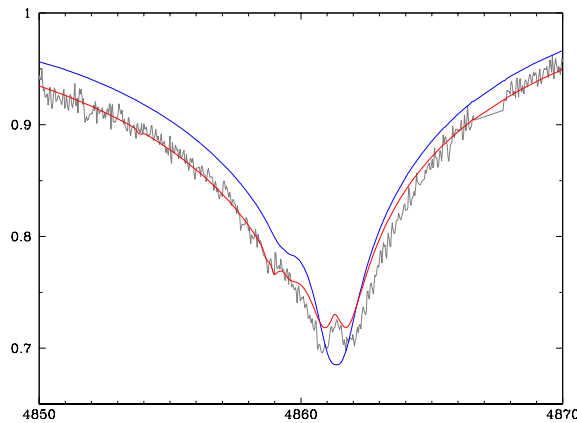
Figure 10.1: Blow-up of the H_β line for a comparison of the observed data (grey) and the best fit models. The old H+He model is plotted in blue, the new H+He+N in red. Keep in mind that both models are normalised to the observed spectrum's continuum (outside the plotted range), the offset visible in the blue line profile is not due to different continua. The H+He+N model fits the observed line profile very well.
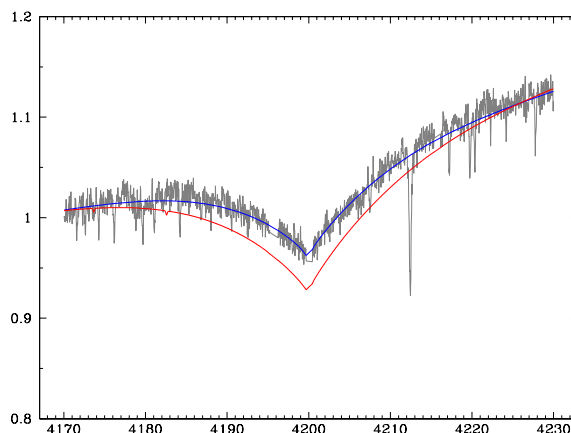
Figure 10.2: The problem with He II 4200 Å. Blue is the old H+He model, red is the H+He+N model.

observed spectrum. Because of this discrepancy, this line was excluded from all parameter fits. Also any nitrogen or carbon line on this line's wings were not used.

The spectroscopic distance derived from fitting the H+He models is 150 parsec, from the H+He+N models it is 161 parsec, where a mass of $0.5\,M_\odot$ was assumed. We find both model fits to be in good agreement with the Hipparcos parallax.

10.3   CD −31 4800

This $m_V = 10\overset{m}{.}56$ star also has a parallax measured by the Hipparcos satellite given as $\pi = 7.62 \pm 1.51$ mas, which translates to a distance of 131^{+32}_{-22} parsec. Radial velocities measured on the single spectra observed on four consecutive nights are 36 ± 3, 36 ± 4, 36 ± 3, and $35 \pm 3\,\mathrm{km\,s^{-1}}$. And on a fifth night 174 days later $36 \pm 4\,\mathrm{km\,s^{-1}}$. Hence the star is not radial velocity variable. By visual inspection we classify the spectrum as N type, though some carbon is still detectable, see table E.1 in the appendix.

	H+He	H+He+N	H+He+C
T_{eff}	44 140 K	43 000 K	43 159 K
$\log g$	6.06	5.84	5.89
$\log y$	+1.84	+2.75	$+2.00^f$
$\log(N_\mathrm{N}/N)$		−3.04	
$\log(N_\mathrm{C}/N)$			−4.97
$v_{\mathrm{rot}}\sin i$		$< 10\ \mathrm{km\,s^{-1}}$	

^{f}Parameter was fixed during model fitting

Large differences between both model grids used are apparent, especially the helium abundance changed by nearly a full magnitude. If we arbitrarily fix the helium abundance to a lower value, comparable with the result derived from the old H+He model grid, the surface gravity increases, though not enough to reach the $\log g = 6$ as derived from the old models. With the fixed lower helium content, the models clearly predict a visible hydrogen

component in the Pickering lines. In the observed data, however, a pure Pickering series without any hydrogen is seen. Earlier works on this star report $T_{\mathrm{eff}} = 44\,000 \pm 2\,000\,\mathrm{K}$, $\log g = 5.4 \pm 0.3$ (Bauer & Husfeld 1995) and $T_{\mathrm{eff}} = 42\,500 \pm 2\,500\,\mathrm{K}$, $\log g = 5.9 \pm 0.25$ (Giddings 1980).

The spectroscopic distance given by the parameters of the H+He model fit is 148 parsec (and well within the Hipparcos parallax error) compared to the 183 parsec from the new models. If we choose to trust the new modelfit, we can vary the star's mass until d_{spec} is in agreement with d_{Π}. We find this estimation of stellar mass to yield $M = 0.26^{+0.13}_{-0.08}\,\mathrm{M_\odot}$, which is — if at all! — at the very low end of theoretical mass distributions. This low mass leaves only the post-RGB stage as a valid evolutionary status for this object, but the star's constant radial velocity and helium dominated atmosphere make this highly unlikely. However, the star lies at a Galactic latitude of $b = -5.5°$ and in a region of high extinction up to $E_{B-V} = 0.6$ (Schlegel, Finkbeiner & Davis 1998) which makes a spectroscopic distance determination questionable at best. It is crucial to derive the interstellar extinction, before any conclusions can be drawn.

With the carbon abundance being detectable and covered by our modelgrid, we also did a parameter fit with the carbon models. As the high helium abundance $\log y > +2$ was outside the grid, this parameter was set to $\log y = +2$ and was not allowed to vary, which explains the slightly different parameters for the best fit model.

10.4   CD −24 9052

This bright ($m_V = 9\overset{\mathrm{m}}{.}6$) sdO star is again of N type and has a low carbon abundance outside of our modelgrid. Five spectra were available, taken over the course of 651 days, radial velocities are 21 ± 3 km s^{-1} in four cases and 20 ± 8 km s^{-1} in one case. We therefore regard this star as not variable.

	H+He	H+He+N	H+He+C
T_{eff}	41 950 K	41 700 K	
$\log g$	5.67	5.49	
$\log y$	−0.12	−0.35	
$\log(N_{\mathrm{N}}/N)$		−3.25	
$\log(N_{\mathrm{C}}/N)$			< −5
$v_{\mathrm{rot}} \sin i$		15 km s^{-1}	

Without question, in figure 10.5 CD −24 9052 is better fitted by our new models than by the old ones. The differences are moderate for the effective temperature and helium abundance. Surface gravities however differ strongly by 0.2 dex.

10.5   UVO 0832 −01

UVO 0832 −01 (= [CW83] 0832 −01) is a $m_V = 11\overset{\mathrm{m}}{.}466$ helium rich sdO star which shows both carbon and nitrogen lines. Only one spectrum was available and radial velocity was measured to $v_{\mathrm{rad}} = 7 \pm 4$ km s^{-1}, compatible with a previous publication of $v_{\mathrm{rad}} = 10 \pm 1$ km s^{-1} (Drilling & Heber 1987).

	H+He	H+He+N	H+He+C	Dreizler (1993)
$T_{\rm eff}$	44 630 K	43 900 K	44 000 K	44 500 ± 1 000 K
$\log g$	5.91	5.67	5.64	5.55 ± 0.15
$\log y$	+1.13	+2.68	+2.00^f	> +1
$\log(N_{\rm N}/N)$		−3.31		−2.9
$\log(N_{\rm C}/N)$			−2.26	−2.3
$v_{\rm rot}\sin i$		21 km s^{-1}	15 km s^{-1}	

^{f}Parameter was fixed during model fitting

With this star, both old and new models have problems with the broader He II lines. For the old models, the best fit shows much too strong Balmer components on the Pickering lines. When forcing the helium abundance to $\log y = +2$ or $\log y = +3$, these hydrogen components vanish, the overall fit however does not improve. Similar parameters as for the new models were found by Dreizler (1993).

10.6 UVO 0904 −02

This helium enriched sdO has both carbon and some traces of nitrogen in its spectrum. We measured $v_{\rm rad} = 20 \pm 4\,\mathrm{km\,s^{-1}}$ and $v_{\rm rad} = 22 \pm 3\,\mathrm{km\,s^{-1}}$ for two spectra, both taken in the same night. Again this is compatible with $v_{\rm rad} = 24 \pm 1\,\mathrm{km\,s^{-1}}$ published by Drilling & Heber (1987). Stellar rotation is easily visible by eye on the strongly broadened carbon lines. The best fit model on the carbon lines has $v_{\rm rot}\sin i = 30\,\mathrm{km\,s^{-1}}$, which in turn even improves the fit of the Balmer and helium lines significantly, although these lines are rather insensitive to rotational broadening. However, three carbon lines had to be ignored during fitting as their shallow and broad profile could not be matched by our models. The low abundance of nitrogen is not expected to have a measurable influence on the stellar parameters, thus only the nitrogen abundance itself and $v_{\rm rot}\sin i$ was measured.

	H+He	H+He+N	H+He+C	Dreizler (1993)
$T_{\rm eff}$	46 650 K		46 170 K	46 500 ± 1 000 K
$\log g$	5.80		5.64	5.55 ± 0.15
$\log y$	+2^f		+1.91	> 1
$\log(N_{\rm N}/N)$		−4.14		−3.26
$\log(N_{\rm C}/N)$			−2.03	−2.14
$v_{\rm rot}\sin i$		33 km s^{-1}	30 km s^{-1}	

^{f}Parameter was fixed during model fitting

Again we find a discrepancy between the old and new models: Using the old models, the helium abundance determined by the best fit is too low; one can easily distinguish the Balmer components in the He II lines, which, however, the observed data clearly do not show. We therefore chose to fix the helium abundance on a rather high value of $\log y = +2$, which is similar to the result of the new models, but more than one magnitude higher than the best fit models predict. This fixed helium abundance eliminates the problem of the visible hydrogen components in the Pickering series, at the cost of a less perfect fit of He I lines. A higher helium abundance also lowers the surface gravity from $\log g > 5.9$ to $\log g = 5.80$, more compatible with our new result.

10.7 Errors

The error estimation by bootstrapping led to very small errors compared to spectrum-to-spectrum variations. For four of the FEROS objects, more than one spectrum was available. Using the statistics of the individual measurements, we derive a more realistic estimate for the errors:

$$
\begin{aligned}
\Delta T_{\mathrm{eff}} &= 250\,\mathrm{K} \\
\Delta \log g &= 0.05\,\mathrm{dex} \\
\Delta \log y &= 0.30\,\mathrm{dex} \\
\Delta \log(N_{\mathrm{N}}/N) &= 0.17\,\mathrm{dex} \\
\Delta \log(N_{\mathrm{C}}/N) &= 0.20\,\mathrm{dex} \\
\Delta v_{\mathrm{rot}} \sin i &= 4\,\mathrm{km\,s^{-1}}
\end{aligned}
$$

In this list, we printed the largest error values. Individual errors can be as small as $\Delta \log(N_{\mathrm{N}}/N) = 0.04$ for HD 127493, for example.

10.8 Evaluation of spectral lines suitable for line profile fitting

In the course of determining the star's parameters, we found the strongest spectral lines of carbon and nitrogen not reproduced by our models: the C IV doublet at 5 801 and and 5 812 Å, C IV 4 438 Å and the N III lines at 4 097, 4 103, 4 867, 4 874 Å. They all are stronger in the observed spectrum than our models predict. Microturbulence generally enhances the already strong lines. Accounting for microturbulences could therefore provide better models. Model calculations with low turbulence velocities of $< 5\,\mathrm{km\,s^{-1}}$ where tried, but all calculations failed. These lines were therefore excluded from the line profile fits.

Fig. 10.3 to 10.7 display the line profile fit of the hydrogen and helium lines for the five bright sdO stars. The fits using the old H+He model atmospheres are on the left hand side, those where the new H+He+C/N models were used are on the right hand side.
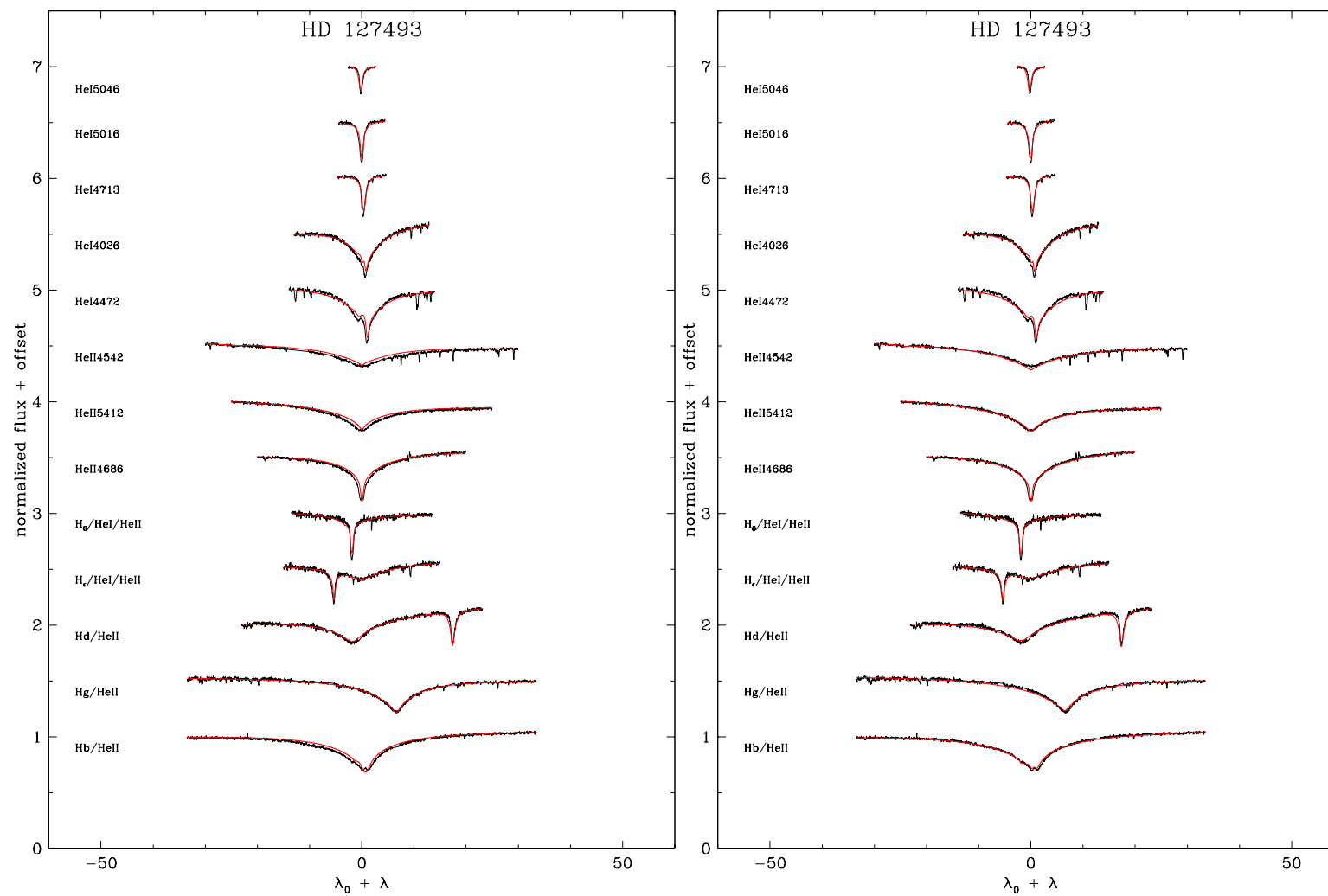
Figure 10.3: The best fit model (red) plotted over the observed data (black). The plot on the left side uses the old H+He models, the right side uses the new H+He+N models.
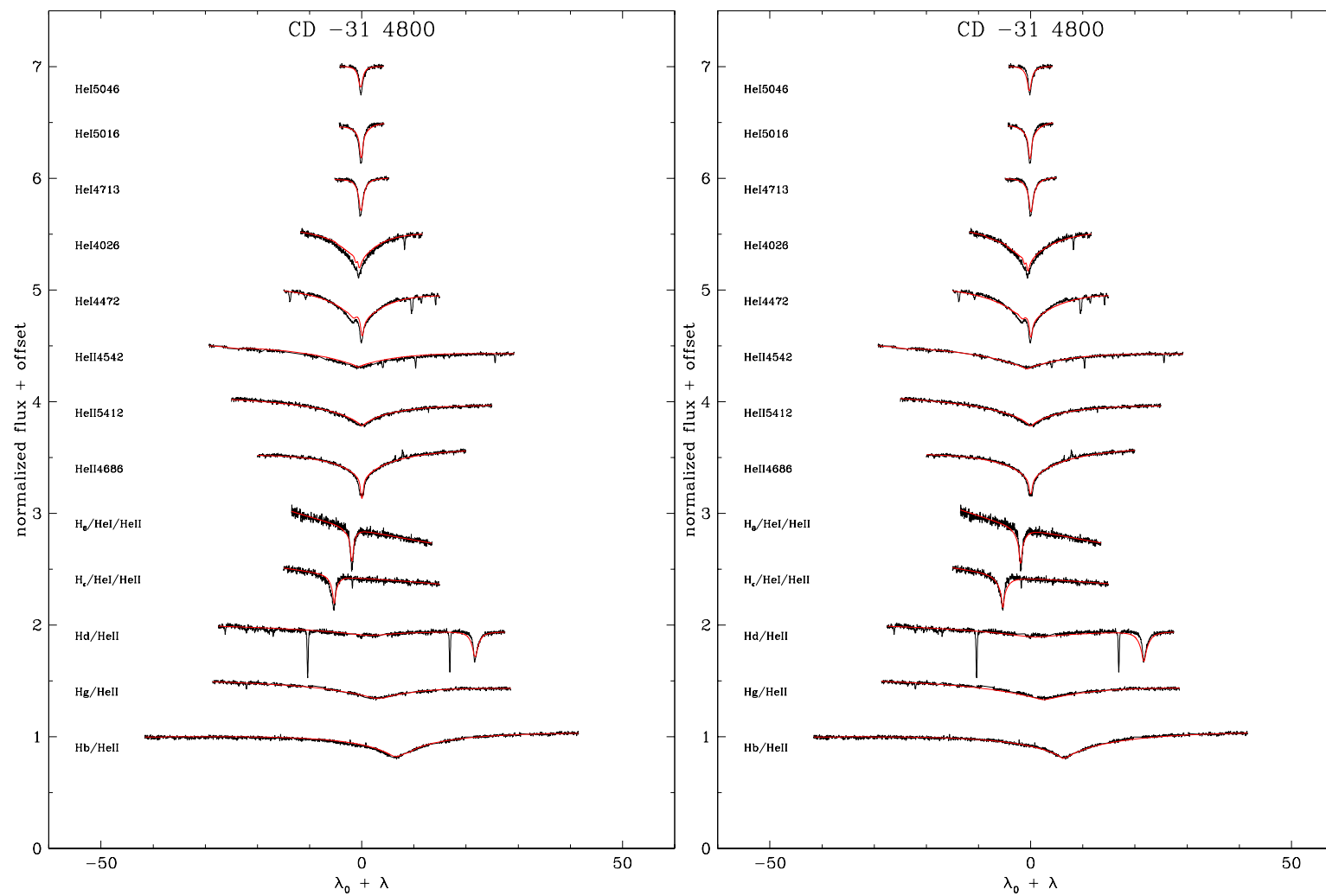
Figure 10.4: See fig. 10.3. *Left:* Old H+He model. *Right:* New H+He+N model.
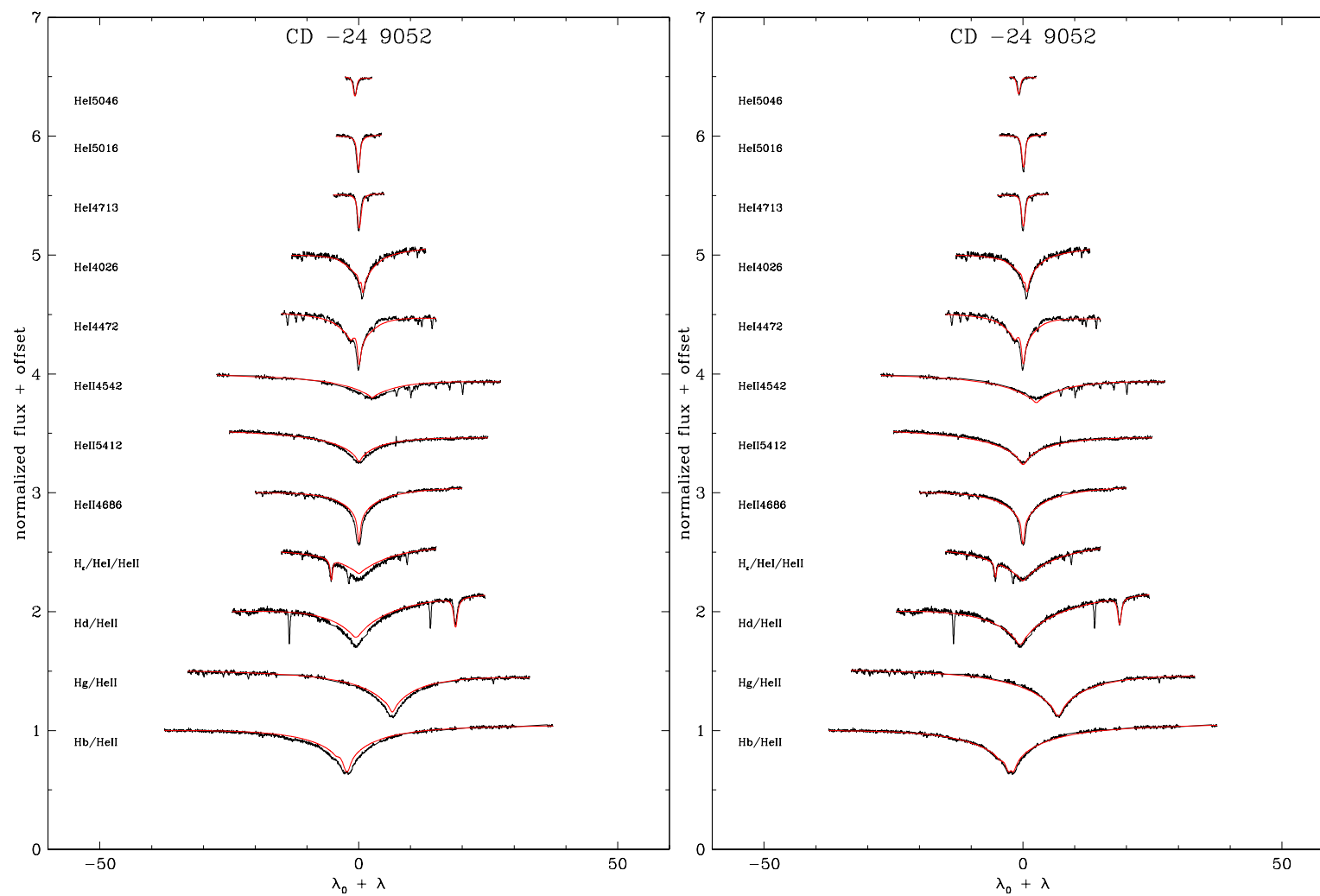
Figure 10.5: See fig. 10.3 *Left:* Old H+He model. *Right:* New H+He+N model.
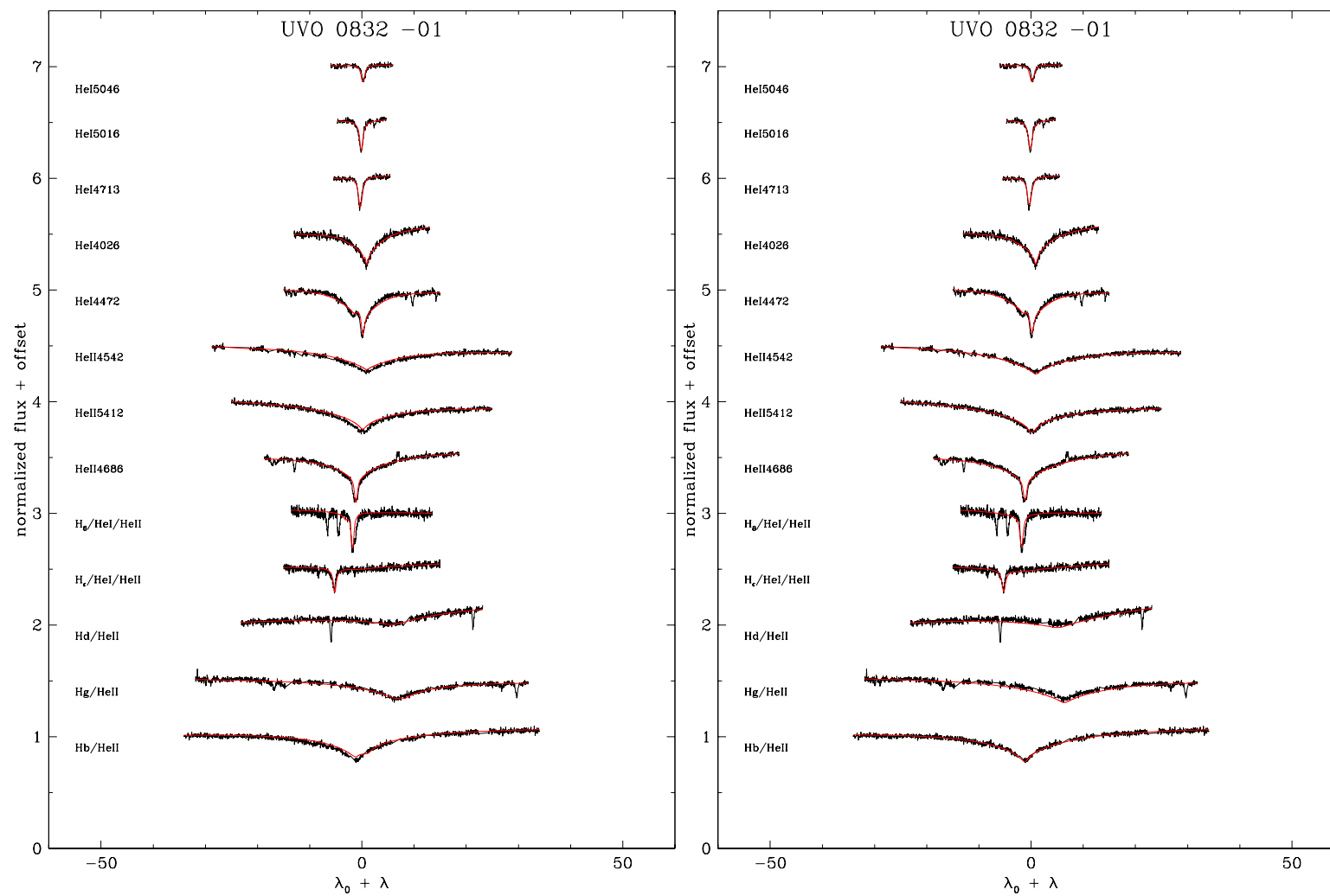
Figure 10.6: See fig. 10.3 *Left:* Old H+He model. *Right:* New H+He+N model.
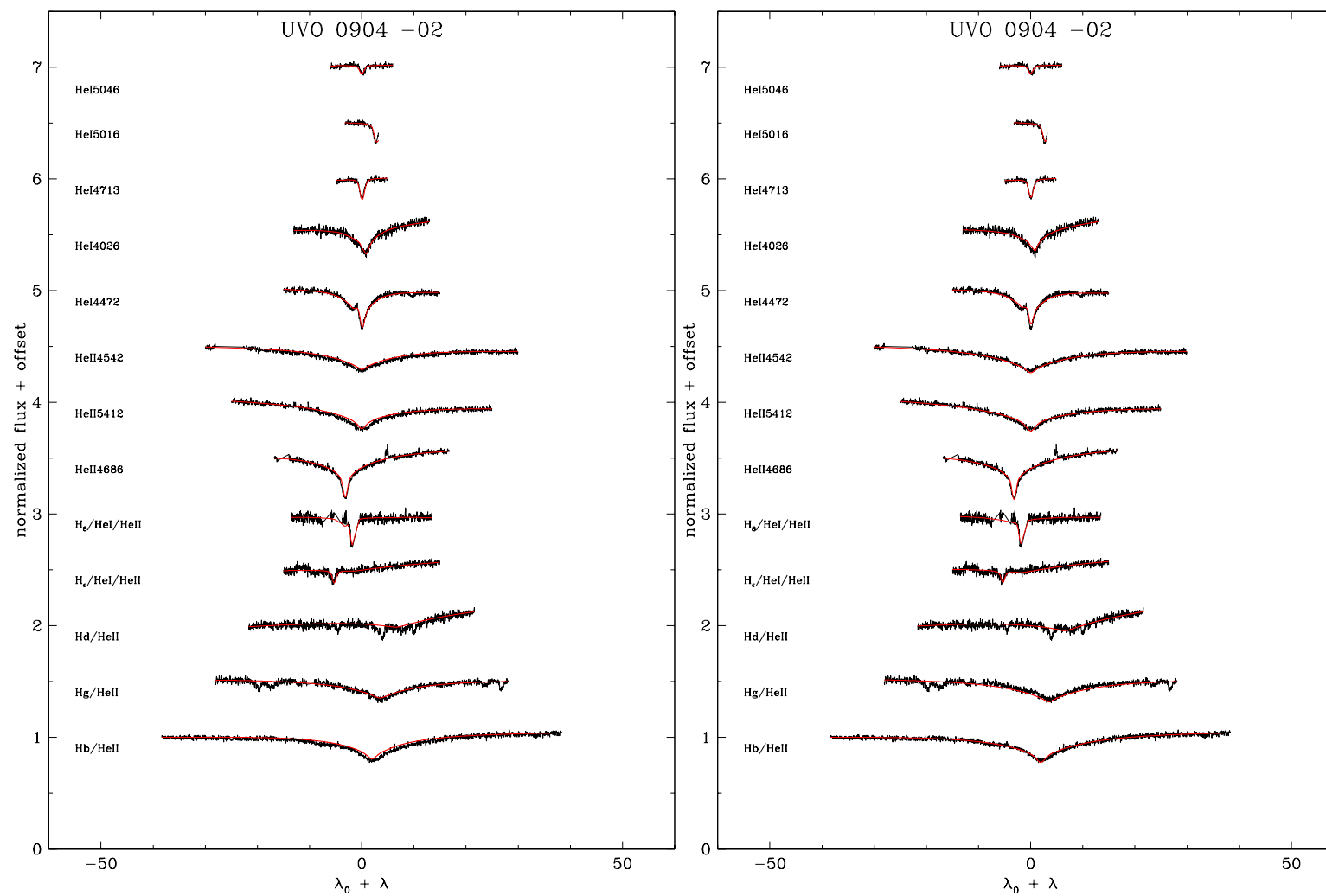
Figure 10.7: See fig. 10.3 *Left:* Old H+He model. *Right:* New H+He+C model.

10.9 Summary

Five spectra of helium enriched sdOs obtained with the FEROS spectrograph were analysed. All radial velocity measurements are in agreement with the helium-rich sdOs to be non radial velocity variable on timescales up to over one year. Any variability must occur on either very long timescales or with very small amplitude, lower than the few km/s of our error estimate.

When using the old H+He models we found it difficult to bring both He I and Balmer lines into agreement while the new H+He+C and H+He+N models fit the observed data much better — with the exception of He II $4\,200$ Å. Only for UVO 0832 -01 the H_γ and H_δ are fitted better by the H+He models. Therefore we regard the addition of carbon and nitrogen to the models a success.

The expected influence of these elements in our model atmospheres is a *lower* effective temperature due to backwarming by the flux blocking of the metal lines. Most of the metal lines are found in the UV and flux conservation requires the blocked UV flux to be redistributed at longer wavelengths, e.g. in the optical part. A higher continuum level lessens the relative line-to-continuum depth. Fitting a not blanketed model, the lines therefore are fitted with shallower profiles, mimicking higher temperatures.

The only spectrum where a significant difference in T_{eff} was observed is that of CD -31 4800; the other four stars are fitted to very similar temperatures by both old and new models. In general, however, the new effective temperatures are slightly lower than the old ones, with a mean difference of $\Delta\langle T_{\text{eff}}\rangle \approx -400$ K. When determining the surface gravities, all the new models predict lower values, $\Delta \log g = -0.24$ is the largest difference. The mean change is $\Delta\langle \log g\rangle \approx -0.15$ dex.

The large differences in the surface gravity and helium abundance are hard to explain solely by the line blanketing effects. Comparisons between TMAP and other NLTE stellar atmosphere codes as described in chapter 9 however strengthen our confidence in our new modelgrid. The Hipparcos parallax measurements of the two stars CD -31 4800 and HD 127493 are consistent with the canonical masses. One possible explanation for the difference when using old H+He and new H+He+N/C models could be that the former is a very large modelgrid. Some errors, e.g. no convergence in a few gridpoints only, could throw the interpolation by cubic splines within the grid quite off the expected values.

We will discuss the evolutionary status of these five bright stars together with the results from the SPY survey presented in chapter 11 and 12.

Chapter 11

The SPY sdOs revisited

In the previous chapter, we analysed high-resolution spectra of five bright sdOs stars of very high signal-to-noise ratio, obtained with the FEROS spectrograph. The number of stars, however, was rather small and not enough to be statistically significant. We will now direct our attention to a sample of stars from the SPY survey. The analyses of SPY sdOs was already introduced in chapter 5, which was based on H+He atmospheres only. The spectra are of lower quality than FEROS, but are still well suited for a quantitative analysis of metal lines. Using our new H+He+C and H+He+N models, we will reanalyse the spectra and determine the carbon and nitrogen abundances.

11.1 Spectral analysis

Because SPY was run as a bad weather programme, the setup used a rather wide slit width of 2.1 arcsec in order to reduce losses due to seeing. Using the DIMM seeing monitor data in the ESO archive, we find every spectrum to be taken with the seeing disk smaller than the slit width. Thus the effective resolution is dependent on the seeing and has to be calculated for each individual spectrum via

$$R = \frac{r}{\text{seeing in arcsec}}$$

with $r = 41\,400$ for the blue channel ($\lambda < 4\,560$) and $r = 38\,700$ for the red channel (Geier, priv. comm.). The SPY spectra cover the wavelengths from $3\,300\,\text{Å}$ to $6\,650\,\text{Å}$ with two gaps between $4\,525\,\text{Å}$ and $4\,600\,\text{Å}$ and between $5\,610\,\text{Å}$ and $5\,675\,\text{Å}$. They were already reduced and normalised by Ströer et al. (2007).

The general procedure was the same as described for the bright sdOs in chapter 10: beginning with carbon fixed to a guessed initial value, we determine T_{eff}, $\log g$ and helium content from fitting models to available hydrogen and helium lines. With these values, the carbon abundance and the rotational velocity is then fitted. This scheme is iterated until convergence is reached. For nitrogen the same procedure is executed, with one exception though: in cases where the rotational velocity differs significantly from the one obtained from the carbon lines, the latter one is used, because we found the carbon lines to be much more reliable for estimating $v_{\text{rot}} \sin i$. This can be understood when one realises that carbon has a number of multiplet lines with wavelengths not too close to blend completely, but close enough to make rotational broadening clearly visible. In particular

the He II 4 121 Å/C III 4 122 Å and the He I 3 889 Å/C III 3 889 Å blends and the multiplet at C III 3 609 Å, but also the C III triplet at 4 069 Å are found to be very useful in this respect.

SPY spectra allowed us to use the Balmer lines (or corresponding He II-Pickering lines) from H_β to H_8. H_α is within the wavelength range, but was not fitted. The main difference to the previous work is the inclusion of C and N and the use of the higher Balmer lines H_ϵ and H_8 for model fitting. Only the lines at 4 686 Å and 5 412 Å were used of He II. For the high helium abundances of our program stars, however, every Balmer line is dominated by a He II component of the Pickering series.. A lot of these objects even have a spectrum compatible with a pure helium atmosphere and the Balmer lines in reality are He II Pickering lines. To avoid problems in estimating the continuum level, the H_δ range was extended far enough to include He I 4 121 Å.

In accordance to the tests for the bright sdO stars, we used the lines presented in appendix B. For example plots of line profile fitting see appendix C.

11.2   Results

Out of 46 sdO stars from SPY analysed previously by Ströer et al. (2007), 33 are helium-enriched. Five of these stars were found to be outside of our grid or to have spectra with too low a signal-to-noise ratio. Our quantitative spectral analysis of the remaining 28 stars revealed 15 objects with detectable carbon lines and 13 objects apparently void of carbon (i.e. $\log(N_C/N) < -5$). Nitrogen on the other hand is present in all but three spectra. For five stars, however, the derived nitrogen abundance is to be considered with caution: In these cases, the χ^2-fitting procedure settled on a $\log(N_N/N)$-value within our grid. An inspection by eye of the line profile fits did not reveal line profiles distinguishable from the noise in the spectrum. The lines used for line profile fitting are at the limit of detectability and abundances derived from them should be regarded as upper limits. Additionally, one has to keep in mind that rotational broadening measured from the carbon lines was applied for the nitrogen measurement, further reducing the detectability of weak nitrogen lines. A more careful search for the strongest N III lines around H_β, H_δ and He II 4 200 Å revealed indeed that the spectra of HE 1203−1048, HE 1142−2311 and HE 1251+0159 are void of any nitrogen. In the remaining two stars, we did find some of the stronger nitrogen lines and therefore tentatively chose to trust the results of the χ^2-fit (see entries marked by an asterisk (*) in table 11.3). Together with the five bright sdO stars we analysed 33 helium enriched sdO stars. 15 stars are pure N-type (nitrogen lines only), another 15 stars are CN-type (carbon and nitrogen) while the remaining three are pure C-type.

11.2.1   Atmospheric parameters

Depending on the number of spectra and whether nitrogen and carbon models were fitted, different numbers of measurements were available. The parameters given in table 11.3 are mean values, and the errors given are standard deviations of these measurements. E.g., in cases of a CN-type star with three spectra available, six measurements of T_{eff}, $\log g$ and $\log y$ were done and three for $\log(N_N/N)$ and $\log(N_C/N)$ each. In this table, abundances are given by *mass fractions*: $\log \beta_i = \log \frac{m_i}{m_H + m_{He} + m_C + m_N}$, with i standing for He, C and N. A statistical view on our new values compared to those from Ströer et al. (2007) is given in table 11.1. For this statistical comparison, the SPY sample of Ströer et al. (2007)

Table 11.1: Comparison of statistics of our newly analysed SPY+FEROS sample to the values derived by Ströer et al. (2007).

	Ströer et al. (2007)	this work
$\langle T_{\mathrm{eff}}\rangle$	$43\,200\,\mathrm{K}$	$42\,600\,\mathrm{K}$
$\sigma_{T_{\mathrm{eff}}}$	$3\,300\,\mathrm{K}$	$2\,800\,\mathrm{K}$
$\langle T_{\mathrm{eff}}\rangle_{\mathrm{median}}$	$42\,200\,\mathrm{K}$	$41\,700\,\mathrm{K}$
$\langle \log g\rangle$	5.78	5.56
$\sigma_{\log g}$	0.18	0.15
$\langle \log g\rangle_{\mathrm{median}}$	5.77	5.59
$\langle \log y\rangle$	$+1.24$	$+1.59$
$\sigma_{\log y}$	1.04	1.13
$\langle \log y\rangle_{\mathrm{median}}$	$+1.40$	$+2.05$

was reduced to the same stars we used in our analysis. Otherwise their stars outside of our modelgrid (the helium deficient sdOs and cooler/hotter helium enriched sdOs) would make this comparison useless.

We first concentrate on the complete sample (3rd column) and compare it with the old values from Ströer et al. (2007) (2nd column). As expected from our comparison between the modelgrids, the mean value for the surface gravity is lower by $\approx 0.2\,\mathrm{dex}$. Apart from this shift, the characteristics of $\log g$ do not change: the width of the distribution is the same and the median is near the mean value, which is interpreted as an indicator for a symmetric distribution with no significant tendencies to lower or higher values. Similar conclusions can be drawn for T_{eff}. For the complete sample, the mean effective temperature is lower by $600\,\mathrm{K}$, which, compared to the typical errors, is not significant. Also the width of the T_{eff}-distribution is lower by $500\,\mathrm{K}$. According to the medians being lower than the mean values, the distribution seems slightly leaned towards lower temperatures. Helium abundances have changed; the new values are significantly higher then the old ones, the pure helium stars ($\log y > +2$) being the major contribution.

We now split the sample into the C-, CN- and N-types, see table 11.2. Note that only 3 pure C-types are available, rendering their statistics a little bit questionable. The C-types apparently are the hottest of the helium-enriched sdOs, with the CN-types cooler by

Table 11.2: Statistical comparison between C-, CN- and N-types.

	C-type	CN-type	N-type
$\langle T_{\mathrm{eff}}\rangle$	$47\,200\,\mathrm{K}$	$43\,800\,\mathrm{K}$	$40\,500\,\mathrm{K}$
$\sigma_{T_{\mathrm{eff}}}$	$3\,500\,\mathrm{K}$	$2\,200\,\mathrm{K}$	$1\,000\,\mathrm{K}$
$\langle T_{\mathrm{eff}}\rangle_{\mathrm{median}}$	$45\,600\,\mathrm{K}$	$44\,100\,\mathrm{K}$	$40\,500\,\mathrm{K}$
$\langle \log g\rangle$	5.54	5.58	5.55
$\sigma_{\log g}$	0.14	0.18	0.12
$\langle \log g\rangle_{\mathrm{median}}$	5.62	5.60	5.58
$\langle \log y\rangle$	$+1.75$	$+2.02$	$+1.14$
$\sigma_{\log y}$	0.56	0.62	1.43
$\langle \log y\rangle_{\mathrm{median}}$	$+1.74$	$+2.23$	$+0.62$

3 400 K and the N-types cooler by 6 700 K. At the same time the width of the distribution in $T_{\rm eff}$ seems to shrink, the N-type concentrating in a very narrow $T_{\rm eff}$-region.

This view, however, is not completely unbiased: our models only cover temperatures as low as 38 000 K. Three stars (CN-type) from SPY had to be omitted because they are below this limit. The N-type distribution is expected to extend into the sdOB regime, not covered in this work. For the C-types, similar objections exist: one carbon rich star from SPY was found to be hotter than 60 000 K, the upper limit of our grid.

The mean surface gravities between the three types do not differ significantly. Also their widths and median values are considered equal. Very large differences can be found for the helium abundances, where the mean value for the N-types is much lower than that for the other two classes. And while C- and CN-types apparently are very homogeneous in their helium abundance, the N-types vary strongly and their distribution leans more to the lower abundances.

11.2.2   Carbon and Nitrogen abundances

In Fig. 11.1 the programme stars' abundances are plotted, sorted by descending carbon abundance. Here we use the logarithmic mass fraction. A bimodal distribution of carbon abundances is clearly seen: either the star has enhanced carbon abundances above the solar value, or the carbon is strongly depleted. Helium is always super solar, which is not surprising as this work is concentrating on the helium enriched sdOs. The variation in the helium abundance is very small, and apart from a handful of objects, the stars can be considered as pure helium stars. In Fig. 11.2 (similar to Fig. 11.1) the abundances are sorted by descending nitrogen abundance. About two thirds of the stars have nitrogen above the solar value (enriched by a factor 3 to 10 w.r.t. the sun), four stars have solar nitrogen abundances values to within error limits. Three stars are mildly depleted in nitrogen (objects 28, 29, and 30), while the three rightmost objects are strongly depleted by more than a factor of 15. For $\log\beta_{\rm N} \lesssim -2.8$ the gradient of the $\log\beta_{\rm N}$-distribution is steepening. But we do not see a clear bimodal distribution for nitrogen, like we did for carbon. One could speculate whether the nitrogen depleted objects 28, 29 and 30 are from a metal poor population. Then the rightmost objects (31, 32, and 33) could be very metal poor (Halo?) stars. In these cases spectral lines from other metals, like silicon, are expected not to be visible. Two of these stars, however, unambiguously have Si IV 4 089 Å and Si IV 4 116 Å in their spectra identified.

11.2.3   Rotational velocities

Fig. 11.3 shows a histogram of the $v_{\rm rot}\sin i$ distribution of our 33 programme stars. The grey shaded histogram is for C- and CN-types, the open histogram is for the complete sample (C-, CN-, and N-types). All except two carbon rich sdOs show a detectable $v_{\rm rot}\sin i$ (between 10 and 30 km s^{-1}), whereas only 5 out of 15 nitrogen rich objects do.

The strong correlation between carbon abundance and projected rotational velocity is apparent immediately. 16 out of 18 stars with carbon also show rotational broadening of the metal lines, while only 5 out of 15 pure N-type stars have $v_{\rm rot}\sin i$ measurable. Fig. 11.3 presents the distribution of projected rotational velocities among the stars. The open histogram is the whole sample (C-, N-, and CN-types), while the shaded histogram takes only the C- and CN-types into account. Note that the gap between $v_{\rm rot}\sin i = 0$ km s^{-1} and
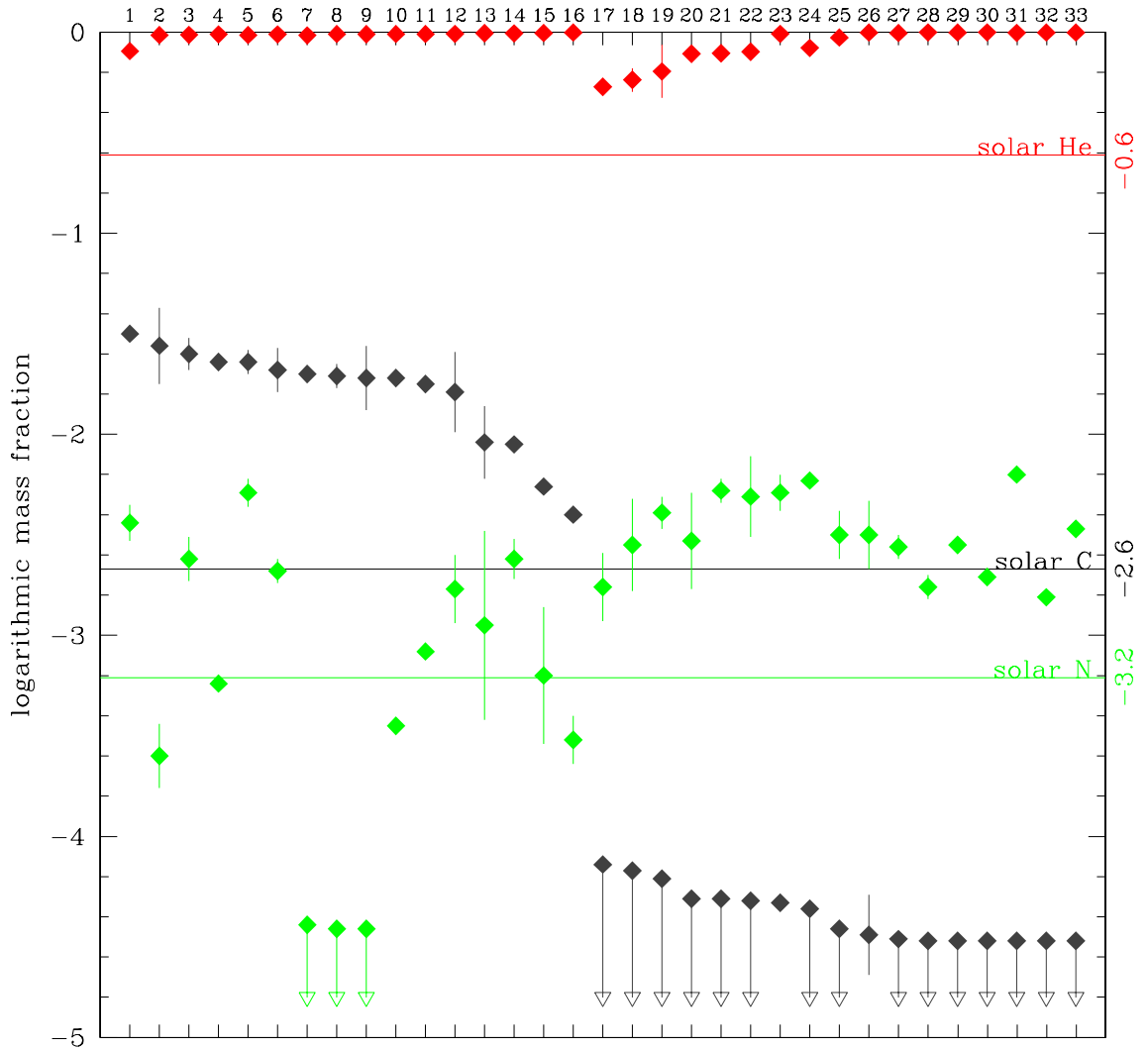
Figure 11.1: Abundances in logarithmic mass fractions of the SPY+FEROS stars, sorted by descending carbon abundance. Red is $\log \beta_{\mathrm{He}}$, grey is $\log \beta_{\mathrm{C}}$, and green is $\log \beta_{\mathrm{N}}$. The solar values are marked by the horizontal lines. Objects where only an upper limit is available are marked by an arrow pointing down.
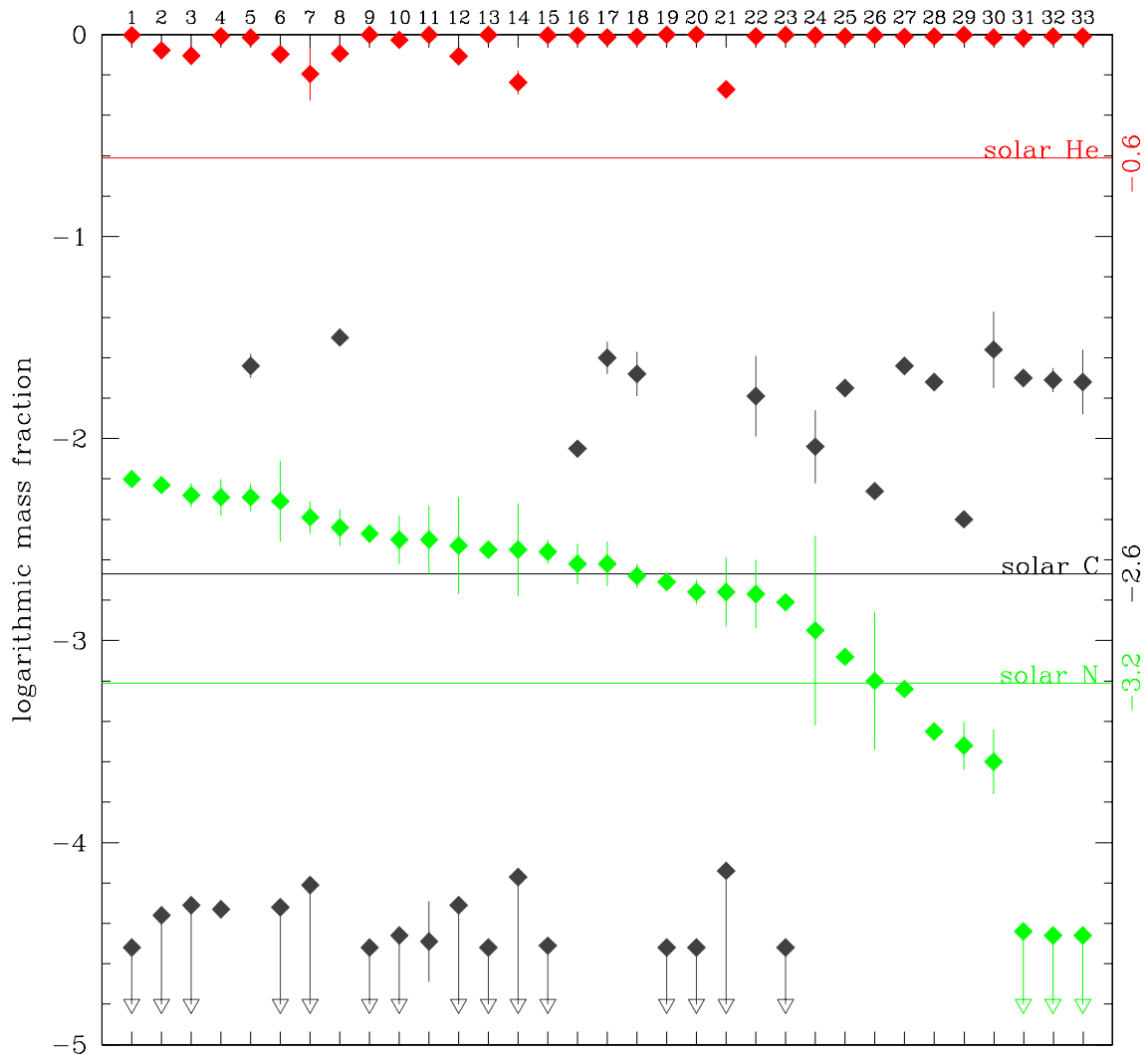
Figure 11.2: Same as Fig. 11.1, but sorted by descending nitrogen abundance.
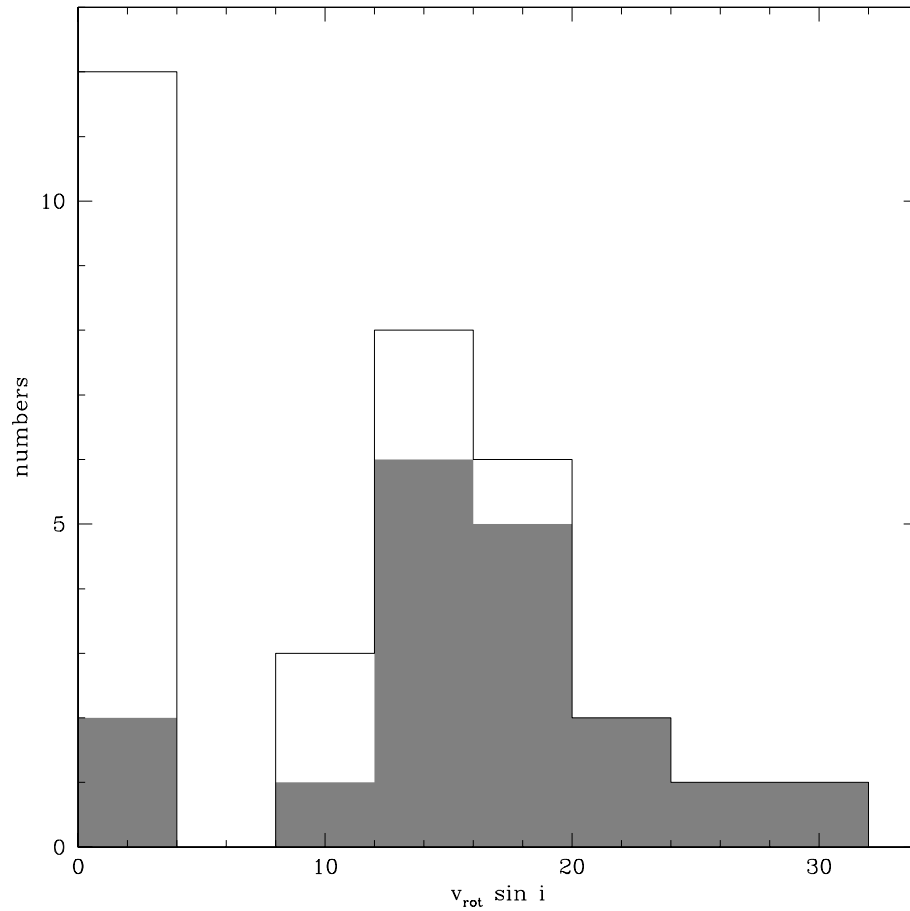
Figure 11.3: The distribution of star counts over the measured rotational velocities. The open histogram is the complete SPY+FEROS sample, the shaded histogram are the carbon enriched sdOs only. Size of the bins has been chosen to represent the typical error value of $\Delta v_{\rm rot} \sin i = 4\,{\rm km\,s^{-1}}$.

$v_{\rm rot} \sin i = 10\,{\rm km\,s^{-1}}$ is not real, the detection limit is $v_{\rm rot} \sin i = 10\,{\rm km\,s^{-1}}$. Consequently, all $v_{\rm rot} \sin i < 10\,{\rm km\,s^{-1}}$ were set to zero.

For comparison, in Fig. 11.4 the $v_{\rm rot} \sin i$ distribution of 49 single sdB stars is provided, taken from Geier (2009). The measured rotational velocities for sdB stars is the shaded histogram. With the open histogram he also provides a simulated distribution calculated under the assumption of a constant $v_{\rm rot} = 8.3\,{\rm km\,s^{-1}}$ and randomly orientated inclination angles i. The dashed histogram is a simulation, too, but with $v_{\rm rot} = 9\,{\rm km\,s^{-1}}$. His detection limit is indicated by the vertical line at $v_{\rm rot} \sin i \approx 4.5\,{\rm km\,s^{-1}}$, all stars below this limit are stacked into the first, dotted bin.

Comparing these two figures, we find a new and very significant difference between the carbon enriched sdOs and the sdBs: where the single sdBs are all found at low rotational velocities below $10\,{\rm km\,s^{-1}}$, the sdOs enriched with carbon have rotational velocities up to $30\,{\rm km\,s^{-1}}$. We note also that the N-type sdOs, in this respect, are similar to the sdBs.
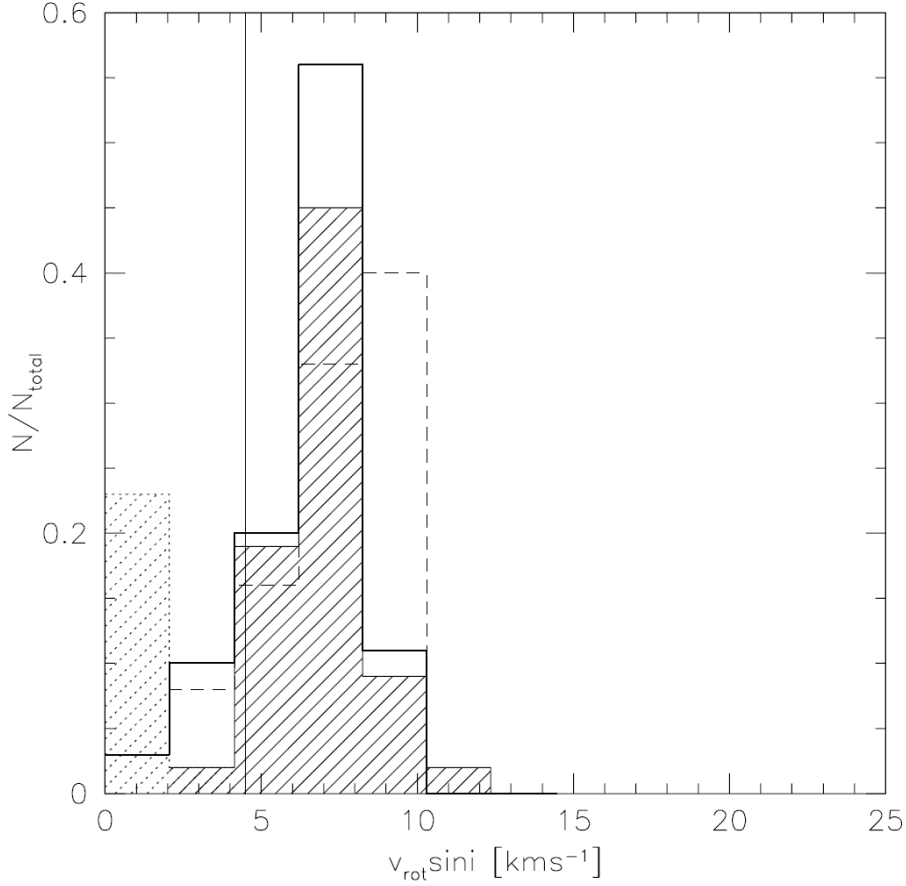
Figure 11.4: $v_{rot} \sin i$ distribution of 49 single sdB stars (shaded histogram), and two simulations (open and dashed histograms). For details see text. Figure taken from Geier (2009, p.99)

11.2.4   Correlations

We now search for correlations of the parameters we discussed in the previous chapters. From Fig. 11.1 and Fig. 11.2 we see no direct correlation of nitrogen and carbon abundances. Some trends, however, are observed: The nitrogen abundance varies between $-3.6 \lesssim \log \beta_N \lesssim -2.2$ for the carbon enriched sdOs. In the carbon poor cases the distribution gets more concentrated between $-2.8 \lesssim \log \beta_N \lesssim -2.2$. Generally the nitrogen is more abundant in the carbon depleted objects than in the carbon enriched ones.

Trends in the helium abundance are hard to observe. All stars are very much helium dominated and variations are hard to see. But with one exception only, all stars with noticeably lesser helium content are also coincident with carbon poor atmospheres.

A presentation of the stars in the T_{eff}-$\log g$-plane is found in Fig. 11.5. Abundances are represented by the symbols' sizes. The splitting of the distribution catches one's eye immediately: with only two exceptions, all carbon *dominated* objects ($\log \beta_C > \log \beta_N$) are found at the hotter end of the distribution, i.e. $T_{eff} > 43\,900\,\mathrm{K}$. Nitrogen is present
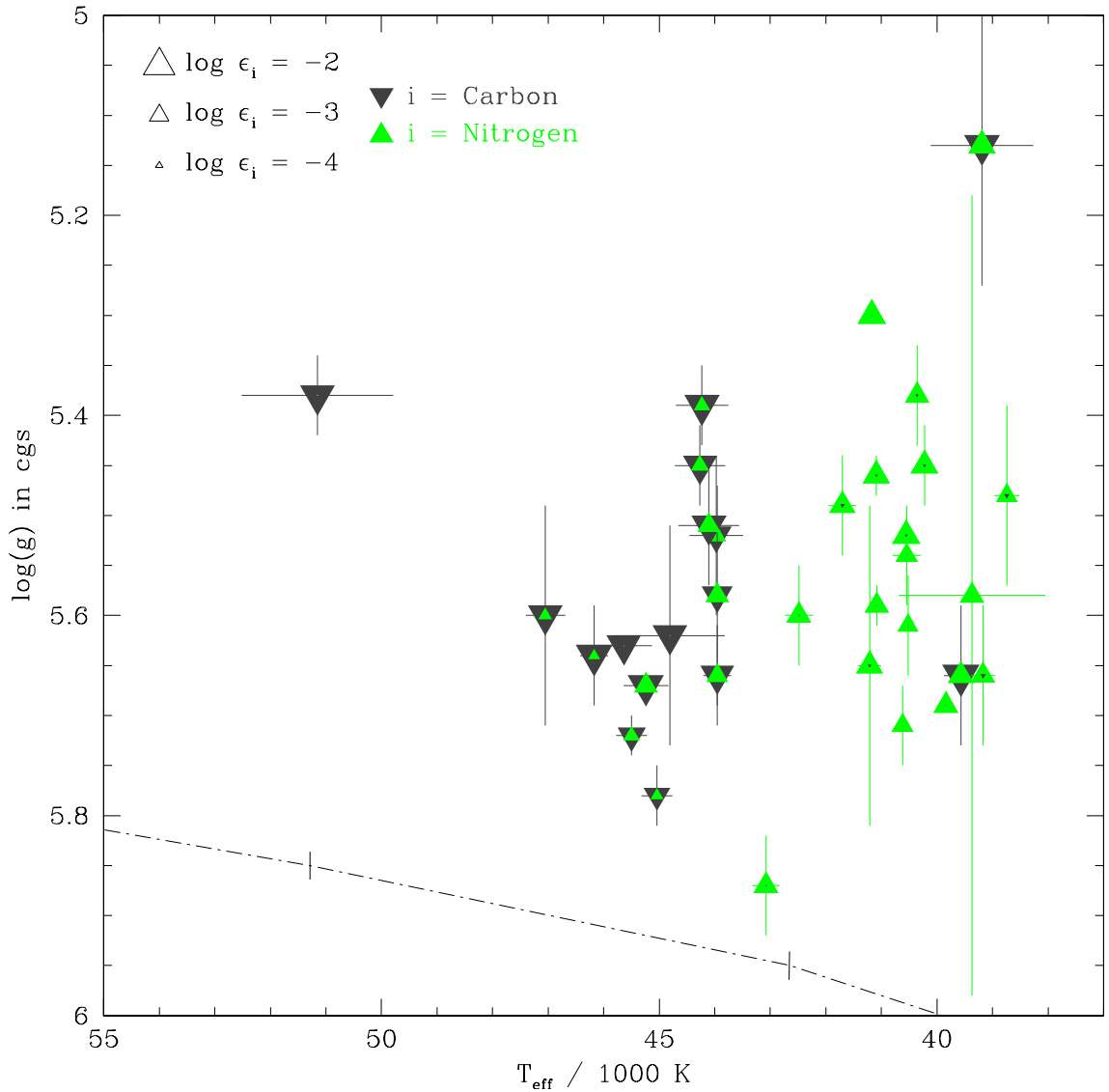
Figure 11.5: T_{eff}-$\log g$-diagram of the SPY+FEROS sample. The logarithmic mass fractions of carbon (dark grey) and nitrogen (green) are coded in the symbols' sizes.

in nearly all objects, and no clear statement concerning a correlation between $\log(N_{\text{N}}/N)$ and T_{eff} can be made. Also no correlation between surface gravity and abundances can be drawn from Fig. 11.5.

We note that no star is found below the HeZAMS anymore, although four of these six objects from Ströer et al. (2007) are included in our sample, the missing two having T_{eff} below our modelgrid. One reason for this surely is the shift of 0.2 dex to a lower mean surface gravity. Alone, however, this shift would not be enough for all four objects. To some degree we also contribute our improved determination of the continuum levels in the line profile fits to this result.

Table 11.3: The atmospheric parameters as derived by fitting new H+He+C and H+He+N models to the observed data. Nitrogen abundances marked by an asterisk (*) were measured on lines nearly indistinguishable from noise. The last five entries are parameters of the FEROS stars analysed in chapter 10. In this table, abundances are given by mass fractions.

Star	T_{eff}	$\log g$	$\log \beta_{\mathrm{He}}$	$\log \beta_{\mathrm{N}}$	$\log \beta_{\mathrm{C}}$	$v_{\mathrm{rot}} \sin i$
HE 0001−2443	39840 ±	5.69 ±	−0.002 ±	−2.47 ±	< −4.52 ±	<10 ±
HE 0016−3212	39186 ± 925	5.13 ± 0.14	−0.014 ±	−2.29 ± 0.07	−1.64 ± 0.06	11 ±
HE 0031−5607	39367 ± 1320	5.58 ± 0.40	$-0.002 \pm 1.12 \times 10^{-04}$	−2.55 ± 0.04	< −4.52 ±	<10 ±
HE 0155−3710	40521 ± 59	5.61 ± 0.05	$-0.002 \pm 4.51 \times 10^{-04}$	−2.81 ± 0.01	< −4.52 ±	<10 ±
HE 0342−1702	41082 ± 117	5.59 ± 0.02	$-0.004 \pm 8.63 \times 10^{-04}$	−2.56 ± 0.06	< −4.51 ±	<10 ±
HE 0414−5429	43970 ± 484	5.52 ± 0.08	−0.005 ±	−2.95 ± 0.47*	−2.04 ± 0.18	16 ± 3
HE 0914−0341	45496 ± 280	5.72 ± 0.02	$-0.004 \pm 3.45 \times 10^{-03}$	−3.20 ± 0.34	−2.26 ± 0.03	15 ± 4
HE 0958−1151	44229 ± 474	5.39 ± 0.04	$-0.011 \pm 7.75 \times 10^{-04}$	−3.24 ± 0.04	−1.64 ± 0.01	23 ± 3
HE 1135−1134	40358 ± 42	5.38 ± 0.05	$-0.107 \pm 3.85 \times 10^{-03}$	−2.53 ± 0.24	< −4.31 ±	14 ± 3
HE 1136−1641	43957 ± 161	5.58 ± 0.11	$-0.006 \pm 1.06 \times 10^{-03}$	−2.62 ± 0.10	−2.05 ± 0.02	16 ± 2
HE 1136−2504	41212 ± 212	5.65 ± 0.16	−0.097 ±	−2.31 ± 0.20	< −4.32 ±	<10 ±
HE 1142−2311	51154 ± 1365	5.38 ± 0.04	$-0.016 \pm 1.84 \times 10^{-03}$	< −4.44 ±	−1.70 ±	15 ±
HE 1238−1745	38743 ± 224	5.48 ± 0.09	$-0.272 \pm 3.88 \times 10^{-02}$	−2.76 ± 0.17	< −4.14 ±	<10 ±
HE 1251+0159	45637 ± 510	5.63 ± 0.01	$-0.010 \pm 5.57 \times 10^{-03}$	< −4.46 ±	−1.72 ± 0.16	13 ± 5
HE 1256−2738	39571 ± 300	5.66 ± 0.07	$-0.094 \pm 1.89 \times 10^{-02}$	−2.44 ± 0.09	−1.50 ±	14 ± 1
HE 1258+0113	39169 ± 219	5.66 ± 0.07	$-0.237 \pm 5.88 \times 10^{-02}$	−2.55 ± 0.23	< −4.17 ±	<10 ±
HE 1310−2733	40225 ± 91	5.45 ± 0.04	$-0.105 \pm 1.85 \times 10^{-03}$	−2.28 ± 0.06	< −4.31 ±	12 ± 1
HE 1316−1834	41170 ±	5.30 ±	−0.003 ±	−2.20 ±	< −4.52 ±	19 ±
HE 1446−1058	45240 ± 405	5.67 ± 0.01	$-0.013 \pm 2.49 \times 10^{-04}$	−2.62 ± 0.11	−1.60 ± 0.08	18 ± 5
HE 1511−1103	41090 ± 86	5.46 ± 0.02	$-0.008 \pm 1.56 \times 10^{-04}$	−2.29 ± 0.09	−4.33 ± 0.03	<10 ±
HE 2203−2210	47049 ± 356	5.60 ± 0.11	$-0.009 \pm 5.69 \times 10^{-04}$	−3.45 ± 0.02	−1.72 ± 0.03	20 ± 1
HE 2347−4130	45040 ± 279	5.78 ± 0.03	$-0.002 \pm 8.74 \times 10^{-04}$	−3.52 ± 0.12*	−2.40 ± 0.01	17 ± 2
WD 0447+176	40545 ± 250	5.54 ± 0.05	−0.001 ±	−2.71 ± 0.01	< −4.52 ±	<10 ±
WD 2020−253	44105 ± 549	5.51 ± 0.06	−0.011 ±	−2.68 ± 0.06	−1.68 ± 0.11	20 ± 2
WD 2204+071	40553 ±	5.52 ±	−0.078 ±	−2.23 ±	< −4.36 ±	<10 ±
WD 2258+155	40619 ± 62	5.71 ± 0.04	−0.001 ±	−2.76 ± 0.06	< −4.52 ±	12 ±
HE 0952+0227	44266 ± 456	5.45 ± 0.04	−0.009 ±	−3.08 ± 0.04	−1.75 ± 0.04	26 ± 1
HE 1203−1048	44806 ± 982	5.62 ± 0.11	$-0.009 \pm 3.58 \times 10^{-04}$	< −4.46 ±	−1.71 ± 0.06	22 ± 5
HD 127493	42484 ± 250	5.60 ± 0.05	$-0.027 \pm 2.35 \times 10^{-02}$	−2.50 ± 0.12	< −4.46 ±	<10 ±
CD −31 4800	43080 ± 250	5.87 ± 0.05	−0.002 ± 0.00	−2.50 ± 0.17	−4.49 ± 0.20	<10 ±
CD −24 9052	41700 ± 250	5.49 ± 0.05	$-0.195 \pm 1.32 \times 10^{-1}$	−2.39 ± 0.08	< −4.21 ±	15 ± 4
UVO 0832 −01	43953 ± 250	5.66 ± 0.05	−0.008 ± 0.00	−2.77 ± 0.17	−1.79 ± 0.20	18 ± 4
UVO 0904 −02	46170 ± 250	5.64 ± 0.05	−0.014 ± 0.00	−3.60 ± 0.16	−1.56 ± 0.19	32 ± 4

Chapter 12

Discussion and conclusion

In this final chapter we will now try to fit the results derived from our quantitative spectral analysis of 5 bright sdO stars and those from the SPY project to different evolutionary scenarios. The two favoured scenarios for the helium enriched sdOs' origin are the late hot flasher and the HeWD merger scenario. Unfortunately there are no quantitative calculations available for the helium white dwarf merger. For the late hot flasher scenario, however, Miller Bertolami et al. (2008) have performed detailed evolutionary calculations. Having derived atmospheric parameter as well as abundances of helium, carbon and nitrogen for three dozen stars, we can now test theoretical predictions.

12.1 Carbon, Nitrogen and Predictions for the Late Hot Flasher Scenario

With the abundance measurements in the previous chapter we found a trend of carbon depletion in nitrogen rich objects. This is a clear sign of CNO processes, where carbon is turned into nitrogen because of a bottleneck in the cycle's reaction rates. Carbon enrichment on the other hand is found in 16 of the 33 stars. The helium flash is the only source for carbon in the atmospheres of stars experiencing a late hot flash: shortly after the flash the inner convection zone splits and the carbon producing 3α-burning core becomes chemically separated from the star's envelope. The more the helium flash is delayed, the shorter is the time window for carbon mixing. The exact result of the competitive processes (carbon production, the amount of carbon mixing and the efficiency of the CNO processes in the hydrogen burning region) depend both on the initial metallicity and the time when the delayed flash finally occurs. Detailed calculations have been performed by Miller Bertolami et al. (2008). We will now compare our measured abundances to their published values.

Fig. 12.1 shows the measured abundances of our programme stars. The panels from top to bottom are for the helium abundance ($\log \beta_{\mathrm{He}}$), the carbon abundance ($\log \beta_{\mathrm{C}}$) and the nitrogen abundance ($\log \beta_{\mathrm{N}}$). Abundances are given in logarithmic mass fractions. Overplotted horizontal lines indicate the theoretical abundances for initial metallicity $z =$ 0.001. The results for two deep mixing scenarios (DM) are given by long and short dashed lines, while the results for shallow mixing with some hydrogen burning (SM*) is given by solid lines. Abundances for shallow mixing without hydrogen burning (SM) is not published
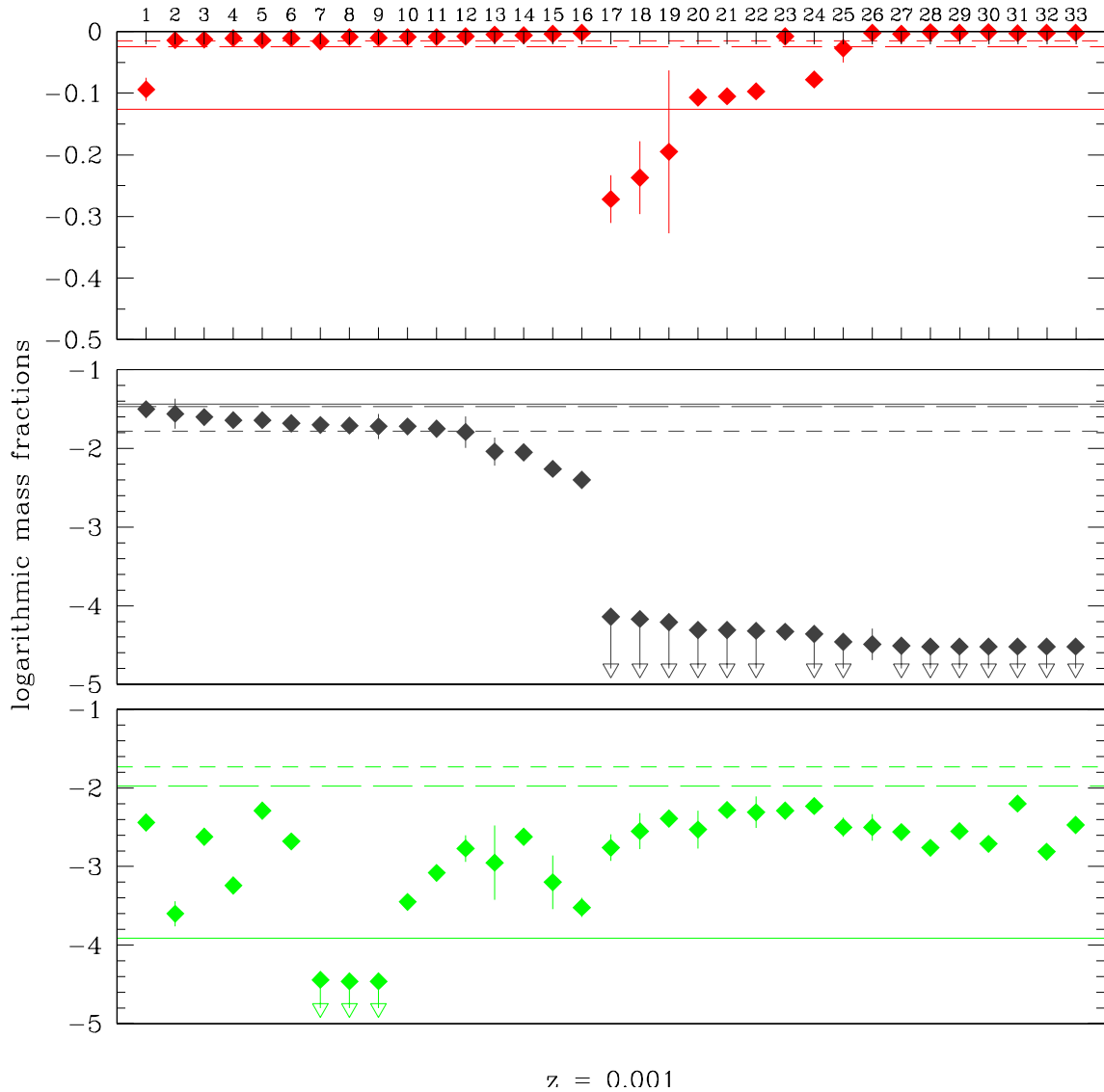
Figure 12.1: Measured abundances in logarithmic mass fractions versus theoretical calculations for late hot flashers. *Top:* helium abundances, *Centre:* carbon abundances, *bottom:* nitrogen abundances. The initial metallicity is $z = 0.001$. Abundances from SM* events are solid lines and abundances from DM events are dashed lines. The long dashes correspond to a higher remnant mass, i.e. the flash occurred earlier than in the short dashed cases.

for this metallicity. Notice the lower helium and nitrogen abundance for the SM* event (top panel, solid line), because the runaway hydrogen burning (a CNO process) does not develop in this case. Figures 12.2 and 12.3 are the same as Fig. 12.1, but use the theoretical abundances for higher initial metallicities ($z = 0.01$ and $z = z_\odot$). For these metallicities, data for the SM flavour is available and plotted as dotted lines. In general, the theoretical carbon abundance does not change much for the different flavours and metallicities whereas the predicted nitrogen abundance depends strongly on metallicity and the late hot flasher flavour (SM, SM*, DM).

12.1.1 The C-rich stars

We first take a look at the carbon abundances (black symbols in the centre panels of Fig. 12.1 to 12.3). Twelve of 16 carbon rich objects (labelled 1 to 12 in the Figures) are more or less in agreement with both the deep mixing (DM) and the intermediate shallow mixing (SM*) flavours. A lower initial metallicity corresponds to better agreement of the measured and the predicted $\log \beta_{\mathrm{C}}$. Even an SM event is possible for $z = 0.01$, but unlikely for solar metallicity. Objects 13 to 16, those with slightly lower carbon abundance, have $\log \beta_{\mathrm{C}}$ too low by $\approx 0.6\,\mathrm{dex}$ (for $z = 0.001$) to $\approx 0.9\,\mathrm{dex}$ (for $z = z_\odot$).

For all 16 carbon rich objects, except object 1, the helium abundances point towards DM events. The first object, HE 1256−2738, with $\log \beta_{\mathrm{He}} = -0.094$ has an even helium-to-hydrogen ratio ($\log y = +0.1$, by numbers), which we can safely detect with our line profile fits. Therefore the uncertainty of this value is very low.

Turning to the nitrogen, we first notice the large changes in the theoretical abundances for SM, SM* and DM flavours and for different metallicities. One finds the atmospheric nitrogen contents from SM events comparable to those from deep mixing. This may seem strange at first glance, as no CNO burning occurs for the former, while the latter burns all hydrogen. However, CNO processed matter from the preceding RGB phase of evolution is brought up by shallow mixing.

In Fig. 12.1, the low metallicity cases $z = 0.001$, $\log \beta_{\mathrm{N}}$ is located between the solid lines (SM*) and the dashed lines (DM), with three exceptions. At first glance these abundances seem to be compatible with late hot flashers somewhere between SM* and DM flavours. This, however, is premature: the mass range for SM* events is *very* small (Miller Bertolami et al. 2008, Fig. 5). Either the hydrogen runaway burning occurs (DM flavour), or it does not (SM). We therefore expect the stars either at SM* abundance levels or at DM abundance levels, i.e. at the solid or the dashed lines, but not in between. Carbon is found very well in agreement with DM cases and possible diffusion effects work both on carbon and nitrogen, the lower nitrogen abundances are hard to explain. This makes it difficult to associate the objects 1 to 16 with any late hot flasher event for metallicity $z = 0.001$.

For the higher metallicities in Fig. 12.2 and 12.2, we find a tendency towards a small offset of $\log \beta_{\mathrm{C}}$ from the predictions. Allowing for a small offset in the nitrogen abundances also, e.g. allowing for diffusion, brings some of the objects into agreement with theoretical calculations for DM events: Objects 3, 5, 6, 12, and 13. And with even larger offsets, the objects 14, 15, and 16 are also compatible with deep mixing.

We therefore find the helium, carbon and nitrogen abundances of the objects in table 12.1 compatible with predictions from Miller Bertolami et al. (2008) for deep mixing events. The metallicities needed for these objects are solar or $z = 0.01$. Small offsets
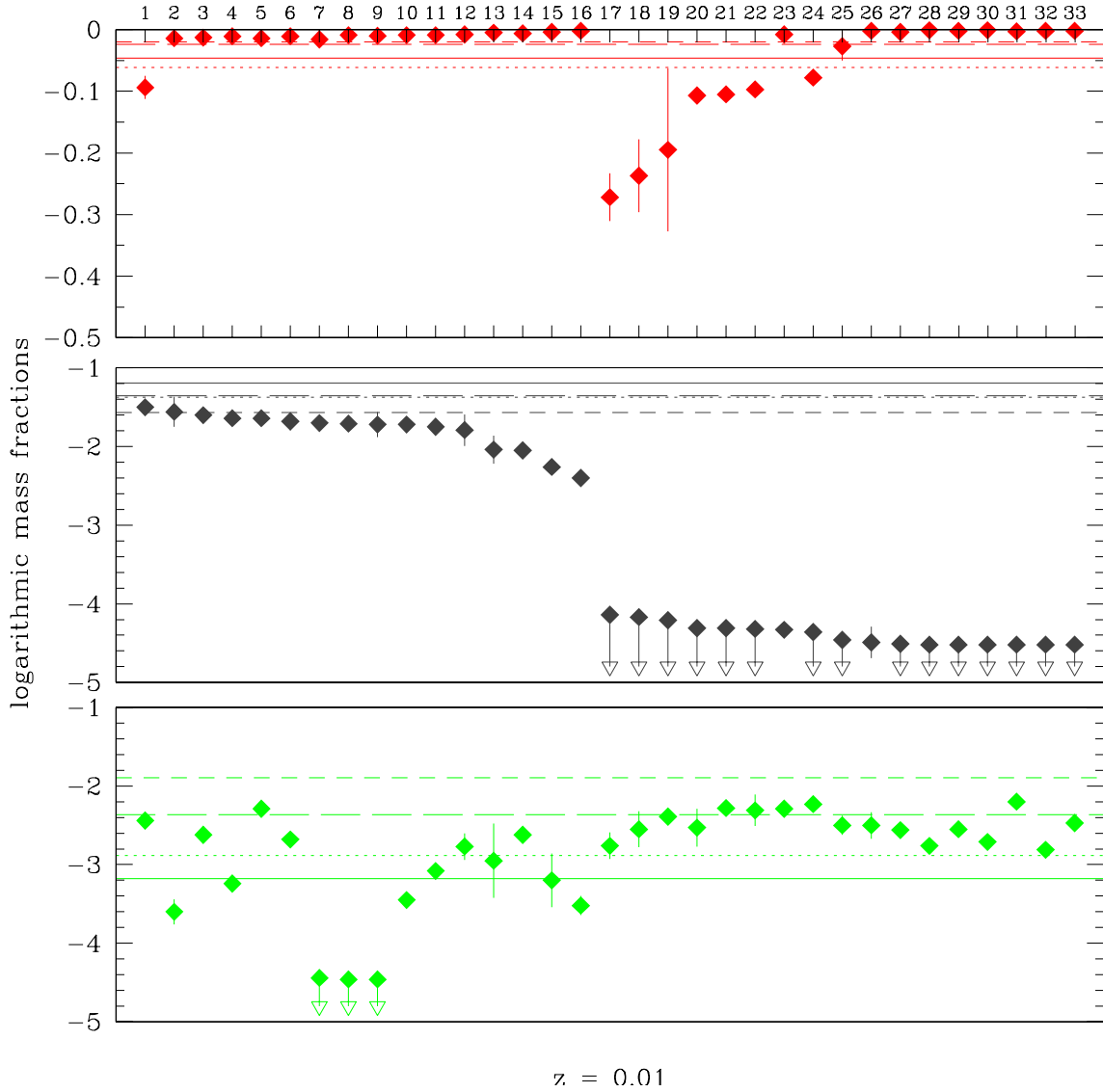
Figure 12.2: Same as Fig. 12.1. The theoretical abundances are for initial metallicity $z = 0.01$. For this metallicity abundance data for the shallow mixing without hydrogen burning (SM) is published by Miller Bertolami et al. (2008). These SM abundances are plotted as dotted horizontal lines. The solid line still is the SM* flavour (shallow mixing with some H-burning) and the two dashed lines are two DM (deep mixing) flavours of late hot flasher events.
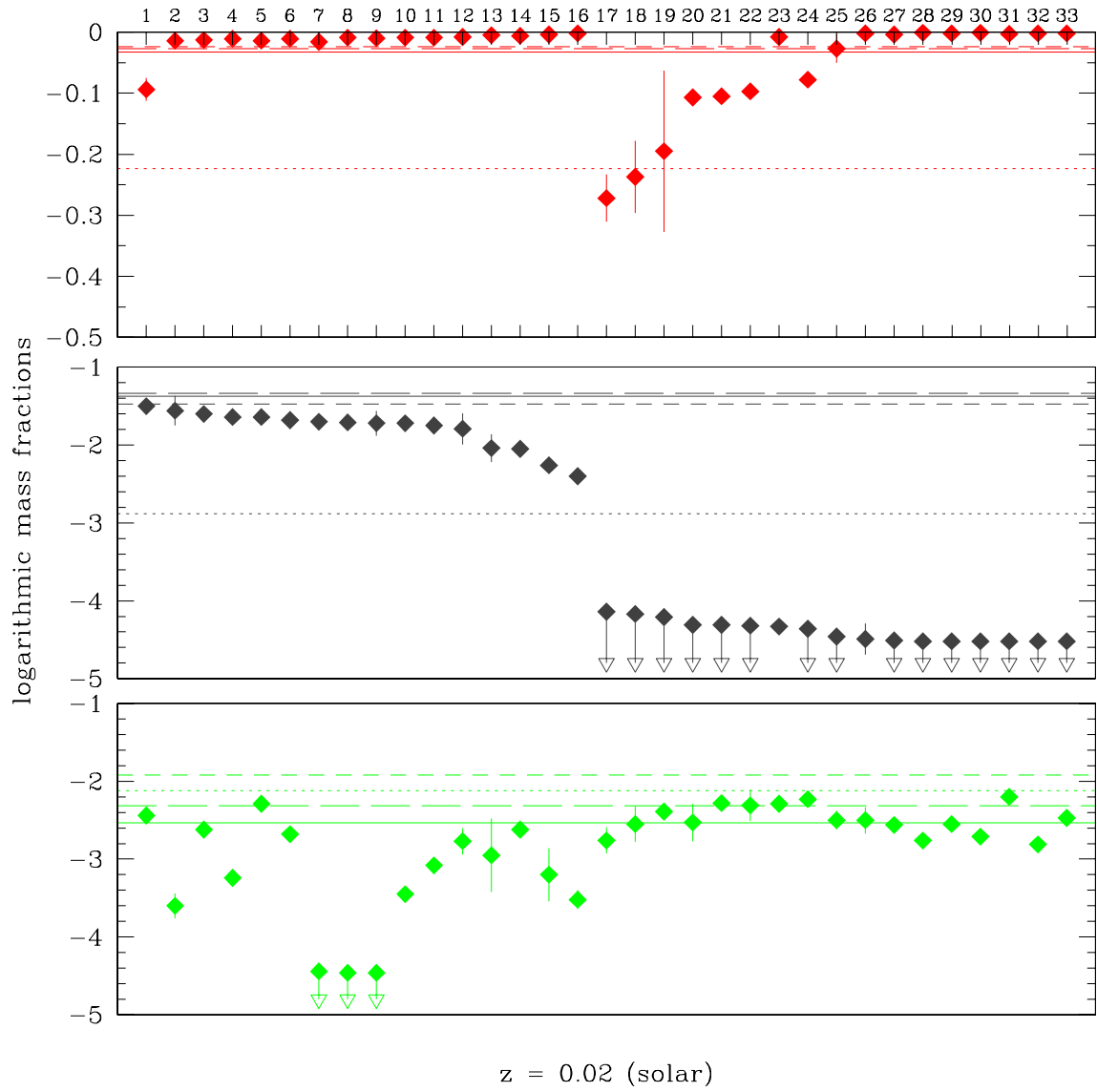
Figure 12.3: Same as Fig. 12.2. The theoretical abundances are for solar initial metallicity $z = 0.02$. Again the dotted line is the SM* flavor, the solid line the "in-between" SM* flavour and the dashed lines are two DM flavours of late hot flasher events.

between predictions and measurements, however, had to be allowed for. The last three objects even require offsets up to 0.9 dex. These offsets could be explained through diffusion. A helium convection zone, however, is probably active in the relevant parameter space, preventing effective diffusion. The three stars 7, 8 and 9 show a strong depletion of nitrogen. Destruction of nitrogen is required in these objects, e.g. via $^{14}\mathrm{N}(\alpha,\gamma)^{18}\mathrm{F}(\beta,\nu)^{18}\mathrm{O}(\alpha,\gamma)^{22}\mathrm{Ne}$. The neon abundances should then be enriched. Or these objects are very metal poor Halo objects.

12.2   C-deficient stars

Turning towards the remaining objects 17 to 33, those depleted in carbon, no late hot flasher scenario for any metallicity is able to explain them. All theoretical calculations predict $\log \beta_{\mathrm{C}} > \log \beta_{\mathrm{N}}$. Even with diffusion, this ratio will not be inverted. There must exist some mechanism that prevents the mixing of helium burning ashes to the surface.

12.3   A comparison in the T_{eff}-$\log g$-plane

The data now is plotted in the T_{eff}-$\log g$-plane, Fig. 12.4, with the nitrogen (green) and carbon (grey) abundances encoded by the symbols' sizes. Dark grey upside down triangles represent the carbon abundances while $\log \beta_{\mathrm{N}}$ is given by the upright triangles in green. All eight objects from table 12.1 that — judged by the abundances — could be late hot flashers are marked by blue circles. A late hot flasher track for solar metallicity is plotted in light grey. First, one finds these LHF candidates more on the hotter side of the track. With the stellar rotation of the carbon rich objects in mind, this imbalance could be explained by calculations of Brown et al. (2008), who studied the impact of rotation on the evolution of low mass stars. Using initial rotational periods of 5 days, they find surface rotational velocities of $\approx 7\,\mathrm{km\,s^{-1}}$ on the ZAHB. The inclusion of stellar rotation proved to increase the mass of the helium core at the onset of the helium flash by $0.048\,M_{\odot}$ — that is 10% of typical values Miller Bertolami et al. (2008) find for their late hot flashers. Thus, fast rotating stars, as observed for our carbon rich objects, will experience the helium flash with larger core masses, shifting the tracks to hotter temperatures. The problem of the timescales still remains unsolved. As can be seen in Fig. 12.4, all stars are found at the

Table 12.1: Objects with abundances in agreement with DM events. The last three objects show strong deviations from the predictions.

Object no	Name
3	HE 1446−1058
5	HE 0016−3212
6	WD 2020−253
12	UVO 0832−01
13	HE 0414−5429
14	HE 1136−1641
15	HE 0914−0341
16	HE 2347−4130
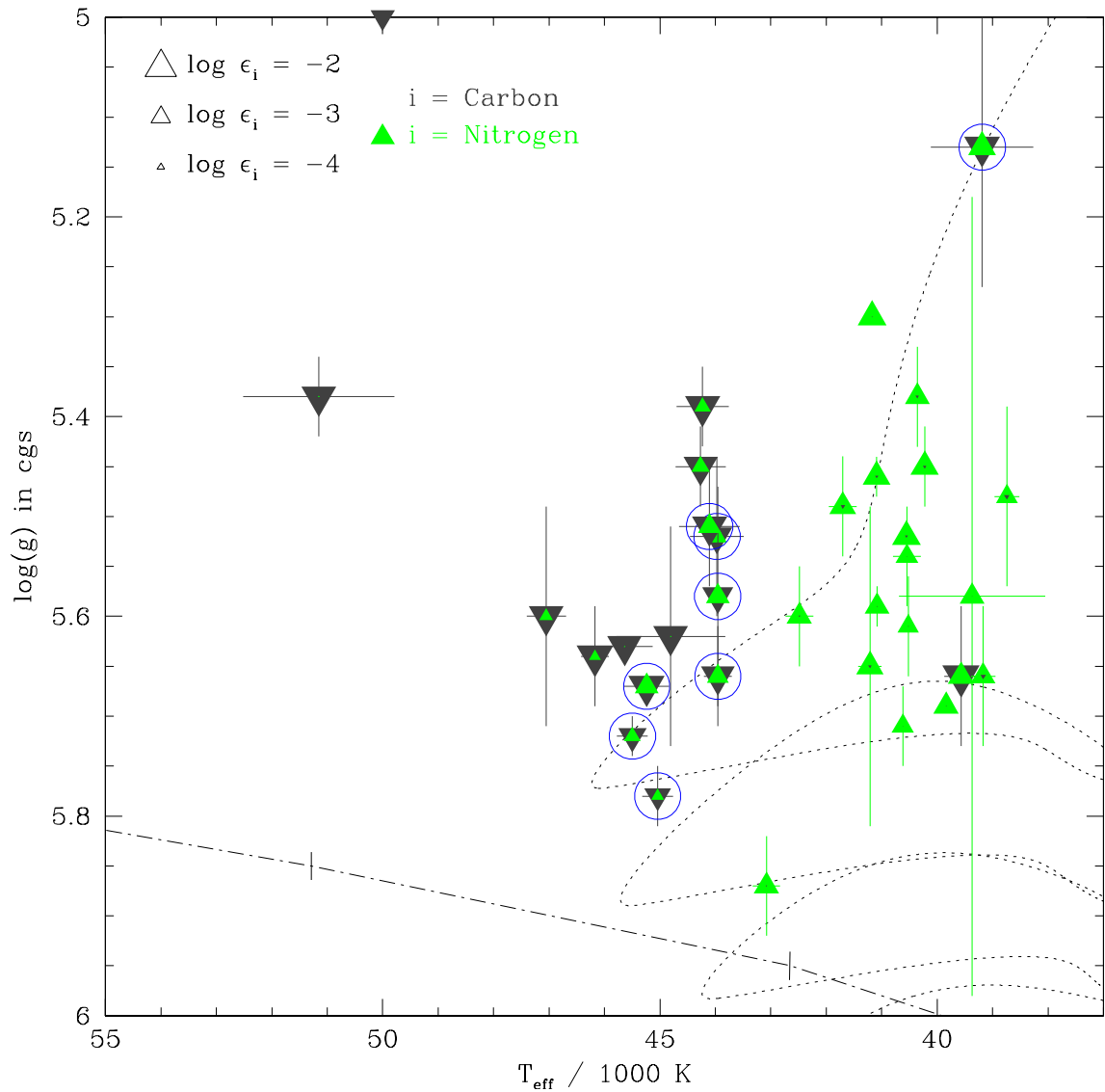
Figure 12.4: Distribution of the helium enriched sdOs from SPY and FEROS in the T_{eff}-$\log g$-plane. The size of the triangles represents the abundance in logarithmic mass fractions. Green is for nitrogen, grey for carbon. A late hot flasher for solar metallicity is plotted over the distribution.

upper part of the LHF tracks, where the stars evolve very fast on timescales of 1 Mio years, compared to the 100 Mio years of stable helium core burning near the HeZAMS (this phase it not shown in this Figure).

12.4 Conclusion

For a more detailed examination of the late hot flasher scenario we reanalysed 28 stars from the SPY survey and additional five bright sdOs. The quantitative spectral analysis was

based on new model atmospheres that include carbon and nitrogen. New values of T_{eff} are similar to those estimated with the old H+He models, but the surface gravities are 0.2 dex lower. Of the six stars found below the HeZAMS (Ströer et al. 2007), four were reanalysed with the new models and none is found below the HeZAMS anymore. Hence, there may very well be no helium enriched sdO below the HeZAMS at all. On the one hand, this is a very satisfying result as these stars are difficult to explain. But on the other hand, the complete distribution is shifted towards lower surface gravities, while the timescales of the theoretical evolutionary calculations expect the majority of objects at higher gravities near the HeZAMS.

A clear-cut dichotomy with respect to the carbon abundance is found. The sdOs are either strongly enriched to supersolar carbon abundances, or strongly depleted. Nitrogen enrichment to supersolar levels is found in 2/3rds of our programme stars. Six stars with nitrogen content comparable to that of the sun may have lower primordial abundances, i.e. they can be thick disk stars.

The C- and N-rich objects are found well separated in the T_{eff}-$\log g$-plane, with the nitrogen rich objects at lower temperatures. Different behaviour in the rotational velocities is found for both groups. The carbon rich objects show significant projected rotational velocities, while the carbon poor objects have too low $v_{\text{rot}} \sin i$ to be detectable ($v_{\text{rot}} \sin i < 10\,\text{km s}^{-1}$). This finding might favour the HeWD merger scenario, where the remnants are expected to have significant angular momentum left. It also rules out an evolutionary link of the C-rich sdOs to the sdBs.

Carbon and nitrogen rich objects can be explained by the late hot flasher scenarios, whereas no available LHF model can explain the carbon deficient ones, for which mixing of helium burning products must be suppressed. The low carbon-to-nitrogen ratio of these objects point at low temperatures ($< 20 \times 10^6\,\text{K}$) (Clayton 1983, Fig. 5-14) for the CN-burning zone, if equilibrium is reached. Also the HeWD merger scenario could be able to explain them, as the CNO-processed helium ashes of the white dwarf are accreted onto its companion.

The most puzzling group of stars are the three carbon rich stars void of any nitrogen, which is indicative of strong nitrogen depletion. The nitrogen might have been burnt to neon by α capture processes, or these stars might have very low abundances as typical for halo stars ($z = z_\odot/1000$). If they were halo stars, their kinematic properties should be tale telling. Accurate proper motions, however, are required to test this hypothesis.

Appendix A

Objects from SDSS with multiple spectra

A.1 Two or more spectra in the SDSS database

SDSS J00:51:07.01+00:42:32.5 (sdO):
$T_{\text{eff}} = 38234 \pm 330$ $\log g = 5.73 \pm 0.06$ $\log y = -1.07$ $v_{\text{rad}} = -52$
$T_{\text{eff}} = 38207 \pm 305$ $\log g = 5.72 \pm 0.05$ $\log y = -0.94$ $v_{\text{rad}} = -80$

SDSS J01:24:30.28+06:48:57.4 (sdO):
$T_{\text{eff}} = 34497 \pm 458$ $\log g = 5.60 \pm 0.12$ $\log y = -1.64$ $v_{\text{rad}} = -73$
$T_{\text{eff}} = 35599 \pm 668$ $\log g = 5.69 \pm 0.12$ $\log y = -1.72$ $v_{\text{rad}} = -55$

SDSS J01:27:39.35+40:43:57.8 (sdO):
$T_{\text{eff}} = 60793 \pm 3477$ $\log g = 5.33 \pm 0.10$ $\log y = -1.46$ $v_{\text{rad}} = -58$
$T_{\text{eff}} = 55101 \pm 2905$ $\log g = 5.48 \pm 0.11$ $\log y = -1.71$ $v_{\text{rad}} = -70$

SDSS J03:33:58.21+00:20:07.4 (sdOB):
$T_{\text{eff}} = 36185 \pm 410$ $\log g = 5.71 \pm 0.10$ $\log y = -0.71$ $v_{\text{rad}} = +161$
$T_{\text{eff}} = 37299 \pm 1806$ $\log g = 5.42 \pm 0.17$ $\log y = -0.78$ $v_{\text{rad}} = +127$
$T_{\text{eff}} = 36401 \pm 855$ $\log g = 5.75 \pm 0.20$ $\log y = -0.57$ $v_{\text{rad}} = +127$
$T_{\text{eff}} = 36083 \pm 809$ $\log g = 5.66 \pm 0.20$ $\log y = -0.69$ $v_{\text{rad}} = +178$
$T_{\text{eff}} = 35984 \pm 712$ $\log g = 5.72 \pm 0.17$ $\log y = -0.54$ $v_{\text{rad}} = +157$

SDSS J07:38:56.98+40:19:42.0 (sdO):
$T_{\text{eff}} = 71272 \pm 2065$ $\log g = 5.45 \pm 0.06$ $\log y = +2.00$ $v_{\text{rad}} = -79$
$T_{\text{eff}} = 70948 \pm 5509$ $\log g = 5.54 \pm 0.12$ $\log y = +0.76$ $v_{\text{rad}} = -75$

SDSS J07:57:32.18+18:43:29.3 (sdO):
$T_{\text{eff}} = 66993 \pm 3971$ $\log g = 5.37 \pm 0.11$ $\log y = +1.60$ $v_{\text{rad}} = -31$
$T_{\text{eff}} = 62475 \pm 3146$ $\log g = 5.36 \pm 0.18$ $\log y = +0.46$ $v_{\text{rad}} = -38$

SDSS J08:19:17.71+42:33:38.7 (sdOB):
$T_{\text{eff}} = 35045 \pm 366$ $\log g = 5.81 \pm 0.09$ $\log y = -2.03$ $v_{\text{rad}} = +12$
$T_{\text{eff}} = 34222 \pm 415$ $\log g = 5.68 \pm 0.10$ $\log y = -1.91$ $v_{\text{rad}} = +20$

SDSS J10:00:19.98−00:34:13.3 (sdO):
$T_{\text{eff}} = 80296 \pm 12273$ $\log g = 5.93 \pm 0.17$ $\log y = -0.78$ $v_{\text{rad}} = +88$
$T_{\text{eff}} = 84116 \pm 5903$ $\log g = 5.98 \pm 0.11$ $\log y = -1.06$ $v_{\text{rad}} = +88$

Despite the quite similar parameters, one parameter fit shows huge errors in T_{eff}, which we explain with the lower signal-to-noise ratio of this spectrum: S/N = 50 compared to S/N = 80 (measured

at $5450\,\text{Å}$). This leads to the He II 5412 line to be lost in the noise of the former while still detectable in the latter and helping to constrain the parameters. We disregard the first spectrum as unreliable and only use the second.

SDSS J11:12:25.70+39:23:32.7 (sdO):

$T_{\text{eff}} = 38060 \pm 484$	$\log g = 5.85 \pm 0.11$	$\log y = -0.67$	$v_{\text{rad}} = +50$
$T_{\text{eff}} = 38626 \pm 511$	$\log g = 5.87 \pm 0.11$	$\log y = -0.70$	$v_{\text{rad}} = +81$
$T_{\text{eff}} = 37771 \pm 586$	$\log g = 5.71 \pm 0.11$	$\log y = -0.59$	$v_{\text{rad}} = +65$

SDSS J11:14:38.57−00:40:24.1 (sdO):

$T_{\text{eff}} = 57714 \pm 3268$	$\log g = 5.56 \pm 0.19$	$\log y = -0.94$	$v_{\text{rad}} = +149$
$T_{\text{eff}} = 55730 \pm 2292$	$\log g = 5.56 \pm 0.15$	$\log y = -0.86$	$v_{\text{rad}} = +116$

SDSS J11:20:56.22+09:36:41.7 (sdO):

$T_{\text{eff}} = 51426 \pm 3345$	$\log g = 5.35 \pm 0.07$	$\log y = -2.55$	$v_{\text{rad}} = +156$
$T_{\text{eff}} = 52250 \pm 287$	$\log g = 5.45 \pm 0.07$	$\log y = -2.39$	$v_{\text{rad}} = +163$

SDSS J14:19:22.55+29:46:50.2 (sdOB):

$T_{\text{eff}} = 35447 \pm 619$	$\log g = 5.58 \pm 0.13$	$\log y = -1.50$	$v_{\text{rad}} = -99$
$T_{\text{eff}} = 35819 \pm 716$	$\log g = 5.63 \pm 0.14$	$\log y = -1.44$	$v_{\text{rad}} = -95$

SDSS J14:31:53.05−00:28:24.3 (sdOB):

$T_{\text{eff}} = 37715 \pm 922$	$\log g = 6.15 \pm 0.17$	$\log y = -0.69$	$v_{\text{rad}} = +0$
$T_{\text{eff}} = 38495 \pm 1499$	$\log g = 6.04 \pm 0.28$	$\log y = -0.70$	$v_{\text{rad}} = +7$

SDSS J14:33:47.59+07:54:16.9 (sdO):

$T_{\text{eff}} = 38391 \pm 381$	$\log g = 5.93 \pm 0.10$	$\log y = -0.37$	$v_{\text{rad}} = -23$
$T_{\text{eff}} = 37809 \pm 555$	$\log g = 5.99 \pm 0.10$	$\log y = -0.53$	$v_{\text{rad}} = -39$

SDSS J16:08:35.68+04:53:45.2 (sdO):

$T_{\text{eff}} = 41859 \pm 610$	$\log g = 6.02 \pm 0.18$	$\log y = +0.63$	$v_{\text{rad}} = -138$
$T_{\text{eff}} = 40670 \pm 616$	$\log g = 5.73 \pm 0.21$	$\log y = +0.29$	$v_{\text{rad}} = -127$

SDSS J16:10:14.87+04:50:46.6 (sdO):

$T_{\text{eff}} = 52000 \pm 1727$	$\log g = 6.04 \pm 0.08$	$\log y = +1.33$	$v_{\text{rad}} = +40$
$T_{\text{eff}} = 53332 \pm 581$	$\log g = 6.02 \pm 0.06$	$\log y = +1.71$	$v_{\text{rad}} = +24$
$T_{\text{eff}} = 51569 \pm 1034$	$\log g = 6.14 \pm 0.04$	$\log y = +1.56$	$v_{\text{rad}} = +28$

SDSS J16:10:59.80+05:36:25.2 (sdO):

$T_{\text{eff}} = 44783 \pm 315$	$\log g = 5.86 \pm 0.09$	$\log y = +2.34$	$v_{\text{rad}} = -222$
$T_{\text{eff}} = 45120 \pm 904$	$\log g = 5.85 \pm 0.10$	$\log y = +1.44$	$v_{\text{rad}} = -216$

SDSS J16:37:02.78−01:13:51.7 (sdO):

$T_{\text{eff}} = 45547 \pm 338$	$\log g = 5.77 \pm 0.08$	$\log y = +3.00$	$v_{\text{rad}} = +18$
$T_{\text{eff}} = 45860 \pm 353$	$\log g = 5.70 \pm 0.08$	$\log y = +3.00$	$v_{\text{rad}} = +15$

SDSS J17:00:45.67+60:43:08.4 (sdO):

$T_{\text{eff}} = 47404 \pm 1870$	$\log g = 5.92 \pm 0.16$	$\log y = +2.26$	$v_{\text{rad}} = -257$
$T_{\text{eff}} = 49537 \pm 2911$	$\log g = 6.09 \pm 0.17$	$\log y = +2.17$	$v_{\text{rad}} = -253$

SDSS J20:47:26.93−06:03:25.7 (sdOB):

$T_{\text{eff}} = 35917 \pm 404$	$\log g = 5.65 \pm 0.10$	$\log y = -1.41$	$v_{\text{rad}} = -11$
$T_{\text{eff}} = 35952 \pm 441$	$\log g = 5.64 \pm 0.12$	$\log y = -1.35$	$v_{\text{rad}} = -14$

SDSS J21:20:53.72−07:15:44.1 (sdOB):

$T_{\text{eff}} = 38692 \pm 1061$	$\log g = 5.68 \pm 0.15$	$\log y = -1.32$	$v_{\text{rad}} = -182$
$T_{\text{eff}} = 37840 \pm 637$	$\log g = 5.62 \pm 0.12$	$\log y = -1.35$	$v_{\text{rad}} = -171$

This object does have a third spectrum which we did not use due to its low signal-to-noise ratio.

SDSS J23:35:41.47+00:02:19.4 (sdO):
$T_{\mathrm{eff}} = 69906 \pm 2234$ $\quad \log g = 5.45 \pm 0.08$ $\quad \log y = +1.10$ $\quad v_{\mathrm{rad}} = -12$
$T_{\mathrm{eff}} = 72870 \pm 1341$ $\quad \log g = 5.44 \pm 0.11$ $\quad \log y = +1.18$ $\quad v_{\mathrm{rad}} = -13$
SDSS J23:39:13.99+13:42:14.2 (sdO):
$T_{\mathrm{eff}} = 48592 \pm 1540$ $\quad \log g = 5.82 \pm 0.15$ $\quad \log y = +0.92$ $\quad v_{\mathrm{rad}} = -389$
$T_{\mathrm{eff}} = 48914 \pm 3233$ $\quad \log g = 5.66 \pm 0.18$ $\quad \log y = +1.19$ $\quad v_{\mathrm{rad}} = -390$
SDSS J16:04:50.44+05:19:09.3 and **SDSS J21:30:54.60−00:41:17.3** had two spectra each, but only one was suitable for spectral analysis.

The following objects had 2 (or more) spectra, but none of them are suitable for a reliable parameter fit:
SDSS J02:24:22.21+00:03:13.5 (5 spectra), SDSS J08:54:22.39+01:36:50.9,
SDSS J09:01:00.01+56:57:13.6,SDSS J11:13:22.90+00:05:30.9,
SDSS J13:36:11.01−01:11:55.9, SDSS J13:57:07.34+01:04:54.4,
SDSS J14:02:47.52+49:33:21.4, SDSS J14:46:57.13+58:09:20.1,
SDSS J15:20:00.81+07:13:48.8.

A.2 SDSS objects which are also in SPY

Note that Stroer et al give global errors as $\frac{\Delta T_{\mathrm{eff}}}{T_{\mathrm{eff}}} = 0.026$, $\frac{\Delta g}{g} = 0.25$ and $\frac{\Delta y}{y} = 0.30$.

SDSS J11:32:41.58−06:36:52.8 (sdO):
SDSS: $\quad T_{\mathrm{eff}} = 48503 \pm 2081$ $\quad \log g = 5.85 \pm 0.10$ $\quad \log y = -2.72$ $\quad v_{\mathrm{rad}} = -22$
SPY: $\quad T_{\mathrm{eff}} = 48122$ $\quad \log g = 5.84$ $\quad \log y = -3.07$ $\quad v_{\mathrm{rad}} =$

SDSS J00:28:52.25+13:54:46.5 (sdO):
SDSS: $\quad T_{\mathrm{eff}} = 42335 \pm 1058$ $\quad \log g = 5.24 \pm 0.10$ $\quad \log y = -2.84$ $\quad v_{\mathrm{rad}} = +28$
SPY: $\quad T_{\mathrm{eff}} = 38830$ $\quad \log g = 5.38$ $\quad \log y = -2.39$ $\quad v_{\mathrm{rad}} =$

SDSS J14:25:51.29−01:33:17.2 (sdO):
SDSS: $\quad T_{\mathrm{eff}} = 51728 \pm 1183$ $\quad \log g = 5.54 \pm 0.07$ $\quad \log y = -1.69$ $\quad v_{\mathrm{rad}} = +36$
SPY: $\quad T_{\mathrm{eff}} = 52662$ $\quad \log g = 5.50$ $\quad \log y = -1.61$ $\quad v_{\mathrm{rad}} =$

SDSS J13:00:59.20+00:57:11.7 (sdO):
SDSS: $\quad T_{\mathrm{eff}} = 40131 \pm 279$ $\quad \log g = 5.65 \pm 0.07$ $\quad \log y = -0.47$ $\quad v_{\mathrm{rad}} = -78$
SPY: $\quad T_{\mathrm{eff}} = 39359$ $\quad \log g = 5.64$ $\quad \log y = -0.53$ $\quad v_{\mathrm{rad}} =$

SDSS J12:54:08.32+01:43:24.1 (sdO):
SDSS: $\quad T_{\mathrm{eff}} = 48633 \pm 466$ $\quad \log g = 5.69 \pm 0.06$ $\quad \log y = +3$ $\quad v_{\mathrm{rad}} = +19$
SPY: $\quad T_{\mathrm{eff}} = 48208$ $\quad \log g = 5.98$ $\quad \log y = +1.03$ $\quad v_{\mathrm{rad}} =$

Appendix B

Spectral lines used for a quantitative analysis of carbon and nitrogen

The following lines were used for the quantitative spectral analysis of carbon and nitrogen:

Carbon

$$C_{III} \, 3\,609\,\text{Å}$$
$$H_8 \text{ and } C_{III} \text{ blend at } 3\,888\,\text{Å}$$
$$C_{III} \, 4056.1\,\text{Å}$$
$$C_{III} \, 4\,069\,\text{Å}$$
$$He_I \text{ and } C_{III} \text{ blend at } 4\,121\,\text{Å}$$
$$C_{III} \, 4\,152.5\,\text{Å}$$
$$C_{III} \, 4\,156.5\,\text{Å}$$
$$C_{III} \, 4\,162.9\,\text{Å}$$
$$C_{III} \, 4\,247.3\,\text{Å}$$
$$C_{III} \, 4\,663.5\,\text{Å}$$
$$C_{III} \, 4\,665.9\,\text{Å}$$
$$C_{III} \, 4\,674\,\text{Å}$$
$$C_{III} \, 5\,249.1\,\text{Å}$$
$$C_{III} \, 5\,253.6\,\text{Å}$$
$$C_{III} \, 5\,272.6\,\text{Å}$$
$$C_{III} \, 5\,771.7\,\text{Å}$$
$$C_{III} \, 5\,826.4\,\text{Å}$$

Nitrogen

$$N_{III} \, 3\,938.5\,\text{Å}$$
$$N_{III} \, 3\,998.6\,\text{Å}$$
$$N_{III} \, 4\,003.6\,\text{Å}$$
$$N_{IV} \, 4\,057.8\,\text{Å}$$
$$N_{III} \, 4\,379\,\text{Å}$$
$$N_{III} \, 4\,510.9\,\text{Å}$$
$$N_{III} \, 4\,601.5\,\text{Å}$$
$$N_{IV} \, 4\,607.3\,\text{Å}$$
$$N_{III} \, 4\,610.6\,\text{Å}$$

N II/III 4 615 Å
N II 4 622 Å
N II 4 630.5 Å
N III 4 634.1 Å
N III/II 4 642 Å
N III 4 884.1 Å
N II 5 010.6 Å
N II 5 045.1 Å
N III 5 314.4 Å
N III 5 320.8 Å
N III 5 327.2 Å
N II 5 666.6 Å
N II 5 676.0 Å
N II 5 679.6 Å
N II 5 686.2 Å

Appendix C

Line profile fits for SPY data
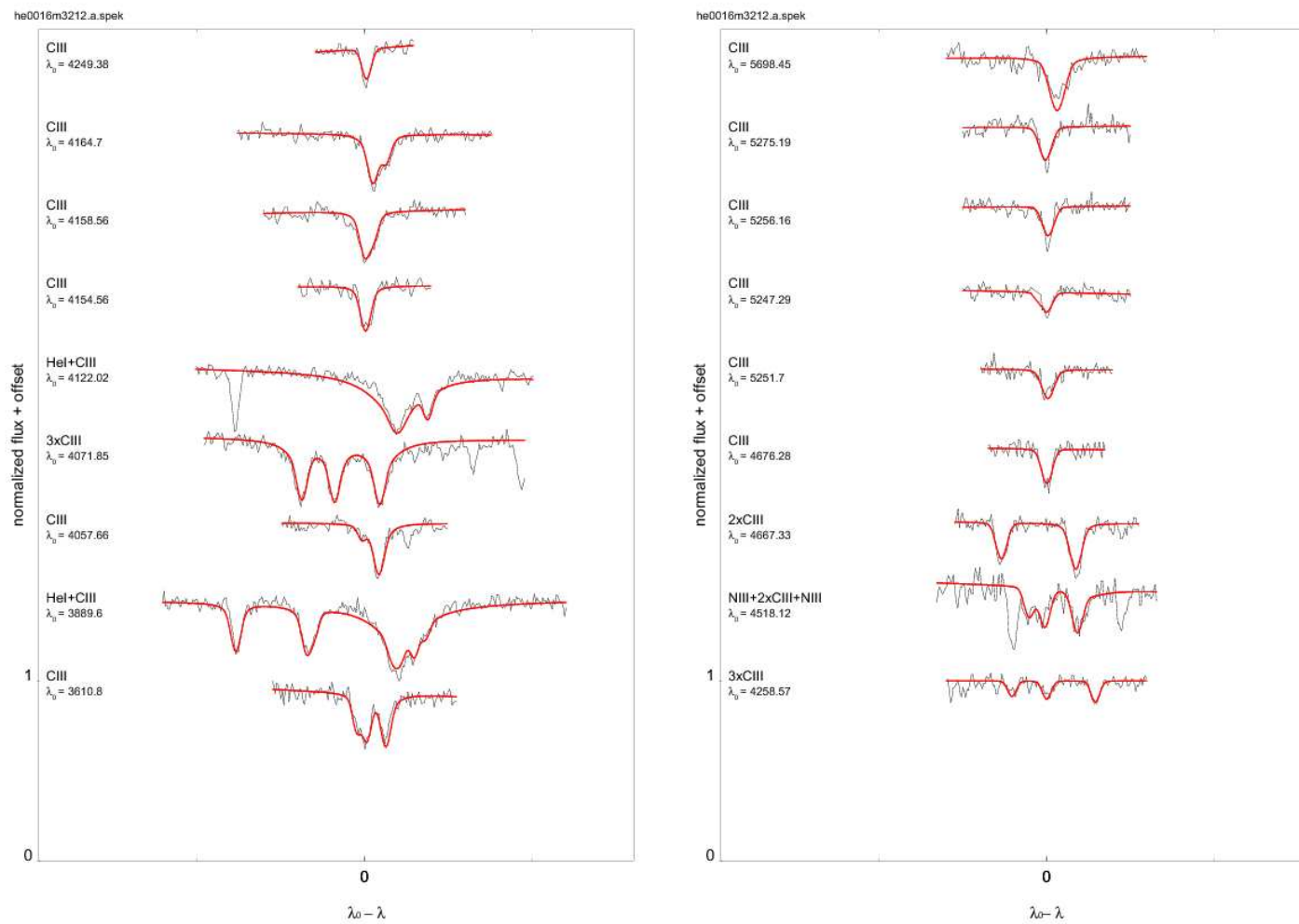
Figure C.1: Line profile fit to carbon lines of HE 0016−3213 (CN-type).
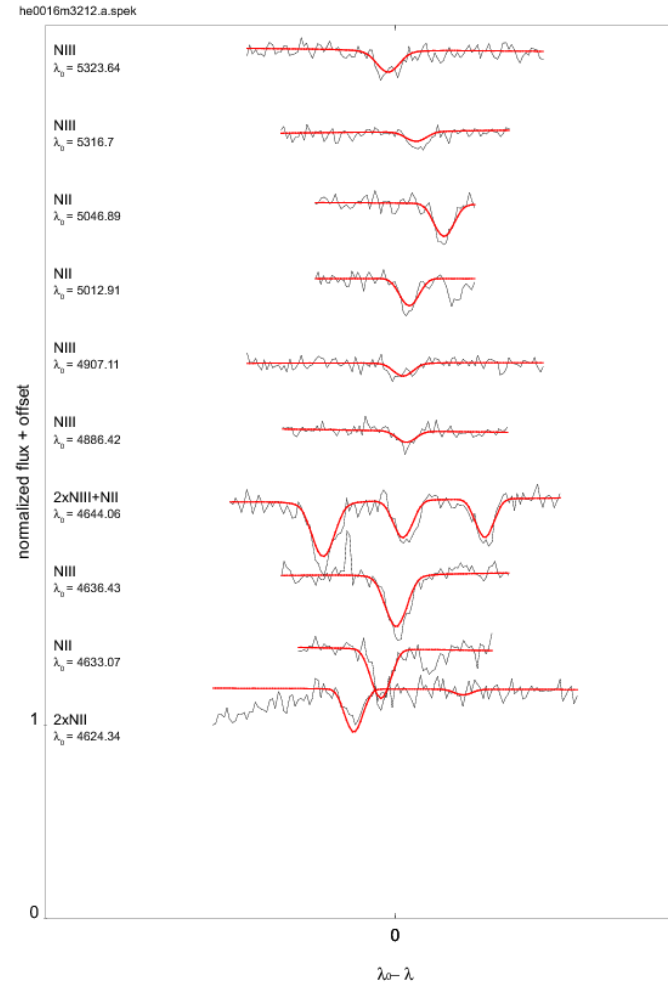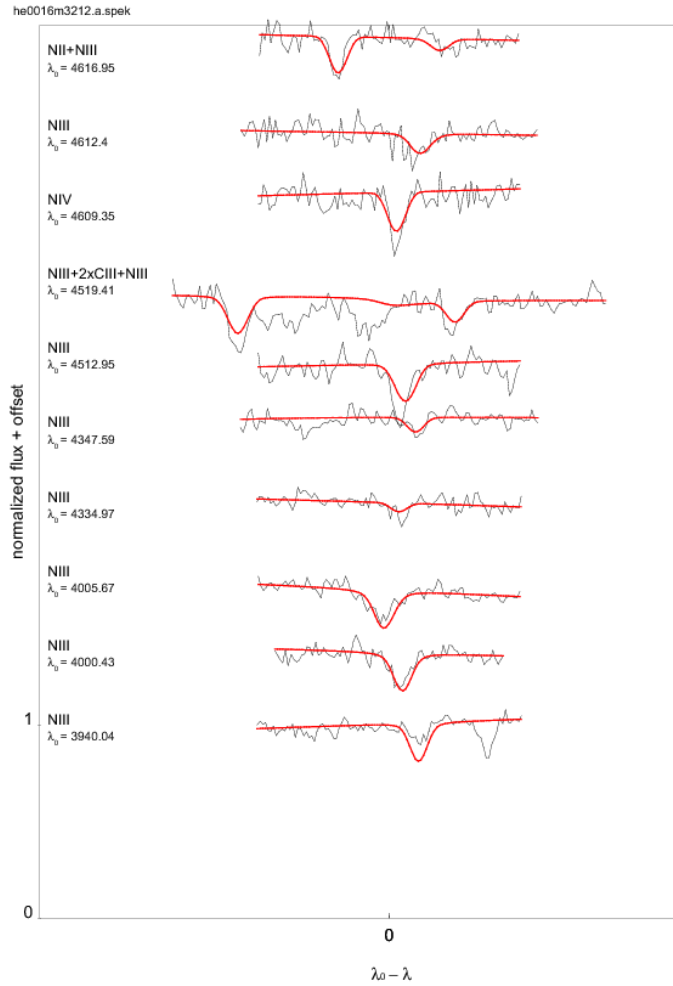
Figure C.2: Line profile fit to nitrogen lines of HE 0016−3213 (CN-type).
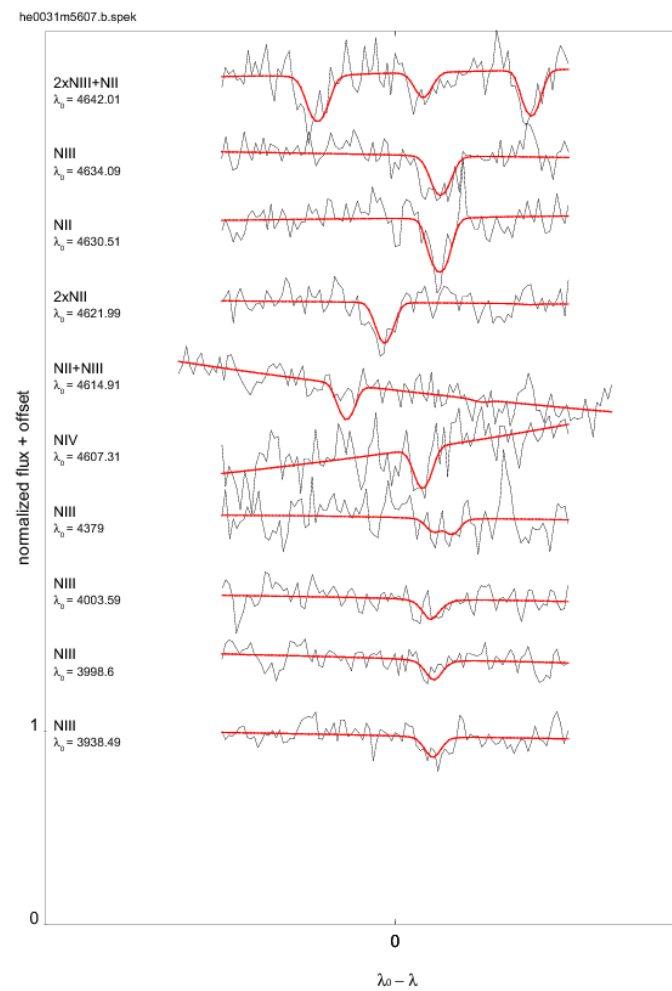
Figure C.3: Line profile fit to nitrogen lines of HE 0031−5607 (N-type).
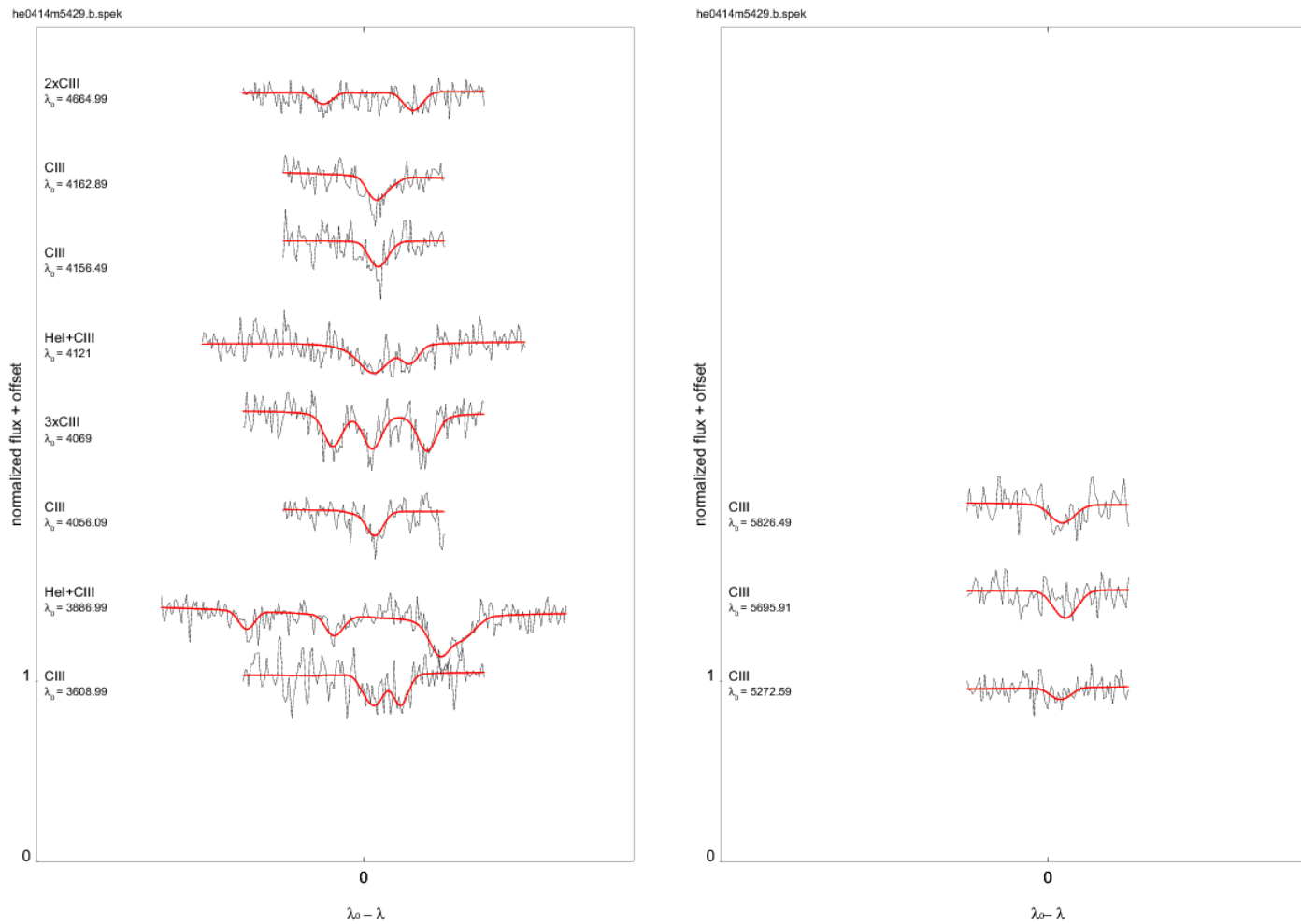
Figure C.4: Line profile fit to carbon lines of HE 0414−5429 (CN-type). Rotational broadening is clearly visible.
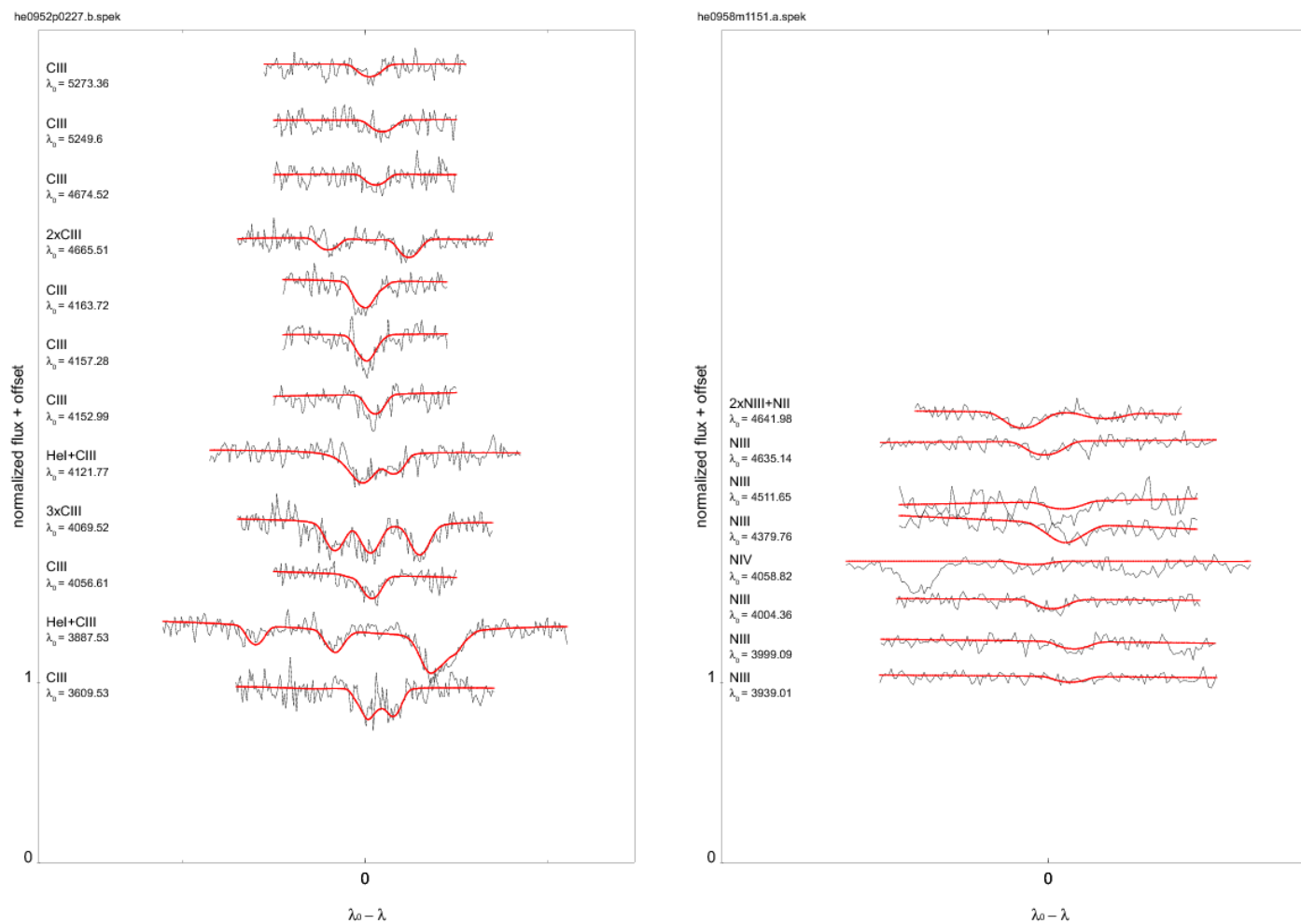
Figure C.5: Line profile fit to carbon (*left*) and nitrogen (*right*) lines of HE 0952−0227 (CN-type). Rotational broadening is clearly visible.
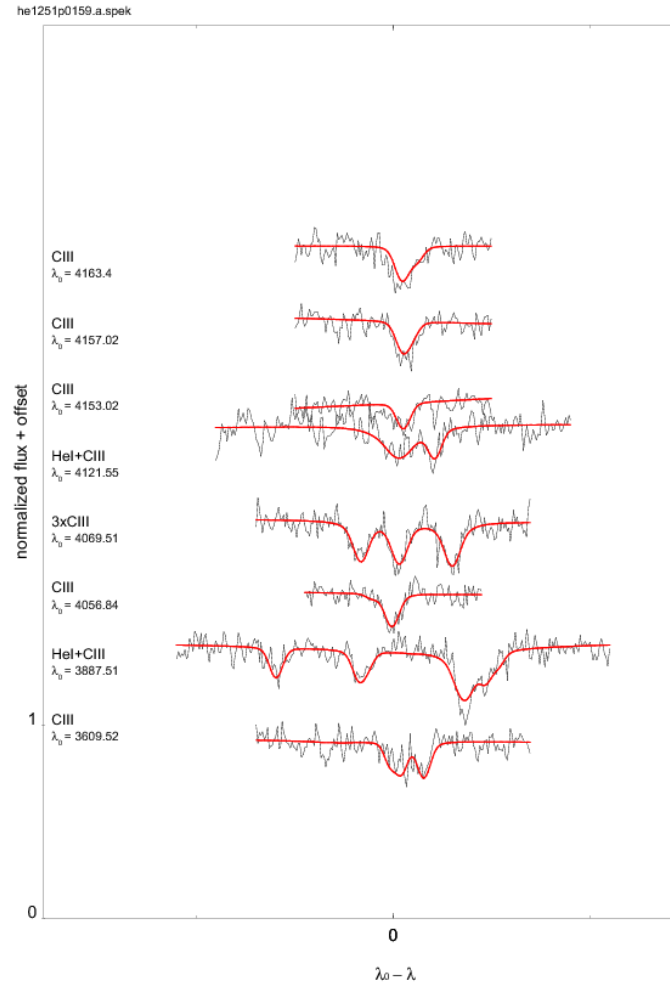
Figure C.6: Line profile fit to carbon lines of HE 1251−2311 (C-type).

Appendix D

Results of the SDSS spectral analysis

Table D.1: Stars classified as *sdO* from SDSS. Luminosity L is calculated under the assumption of $M = 0.5\,M_\odot$.

SDSS J (2000)	T_{eff} [K]	$\log g$ (cgs)	$\log y$	v_{rad} [km/s]	L $[L_\odot]$	SDSS Photometry u	g	r
00:06:07.88−01:03:20.8	44 845	6.08	+1.97	−257	41.3	17.03	17.48	17.96
00:18:37.13+15:21:50.0	43 827	6.30	+1.64	−49	22.7	16.08	16.45	16.90
00:28:52.25+13:54:46.5	42 335	5.24	−2.84	+28	226.9	15.44	15.79	16.17
00:47:55.27+25:20:27.1	40 330	5.35	−2.26	−29	145.1	15.77	16.13	16.59
00:51:07.01+00:42:32.5	38 220	5.73	−1.01	−80	48.8	15.22	15.58	16.08
01:02:51.88+00:04:35.8	36 772	4.82	−0.93	−197	339.7	18.40	18.35	18.56
01:15:17.40+14:28:18.4	40 948	5.18	−3.25	−130	228.0	14.79	15.04	15.53
01:26:02.52−00:48:34.5	65 190	6.04	+2.00	−8	202.2	17.53	18.00	18.48
01:27:39.35+40:43:57.8	57 947	5.41	−1.59	−58	538.4	16.15	16.51	17.01
03:01:55.43+37:54:34.9	60 006	5.88	−0.03	+6	209.8	18.51	18.63	18.81
03:02:11.57+37:11:09.5	39 468	6.08	−1.52	−117	24.8	15.01	15.31	15.73
03:06:07.95+38:23:35.7	41 599	5.63	−1.52	−15	86.2	16.49	16.66	16.96
03:21:07.05+04:51:50.7	39 190	5.74	−0.19	−155	52.7	17.97	18.22	18.51
03:48:22.29+11:33:03.4	43 804	5.84	+2.10	−7	65.3	16.19	16.38	16.51
05:59:50.31+63:58:07.7	43 700	5.45	−2.89	+70	158.8	16.78	17.02	17.36
06:59:07.47+66:49:30.0	44 368	5.67	+1.30	−47	101.7	16.12	16.54	16.95
07:27:26.41+44:48:37.0	47 570	5.77	+1.82	+21	106.7	15.37	15.66	16.08
07:28:24.72+41:49:53.7	39 755	5.69	+0.05	−21	62.6	15.24	15.55	15.89
07:38:56.98+40:19:42.0	71 110	5.50	+1.38	−77	992.5	15.75	16.19	16.64
07:46:13.16+33:33:07.6	45 537	5.77	+3.00	+21	89.6	15.20	15.61	16.10
07:52:49.95+30:59:35.1	41 077	6.22	+0.29	+151	21.1	17.77	18.09	18.49
07:56:03.77+22:26:30.9	54 532	5.64	−2.09	+53	248.7	13.56	13.99	14.44
07:57:32.18+18:43:29.3	64 734	5.37	+1.03	−31	919.5	17.84	18.29	18.77
08:02:59.80+41:14:38.0	45 319	5.77	+3	+9	87.9	14.68	15.04	15.49
08:06:44.05−07:42:32.4	42 168	5.31	−0.50	+83	190.1	16.52	16.72	17.07
08:13:04.04−07:13:06.5	46 038	5.75	+2	+91	98.1	18.01	18.28	18.83

Table D.1 continued (1).

SDSS J	T_{eff}	$\log g$	$\log y$	v_{rad}	L	SDSS Photometry		
(2000)	[K]	(cgs)		[km/s]	$[L_\odot]$	u	g	r
08:13:29.81+38:33:26.9	44 574	5.80	+3	−12	76.8	16.79	17.18	17.69
08:27:51.06+41:09:25.8	51 758	5.76	+1.55	−7	153.1	18.19	18.63	19.13
08:28:02.03+40:40:08.9	43 955	5.11	−2.36	−186	355.7	17.19	17.66	18.20
08:29:44.75+13:23:02.5	38 756	5.41	−2.64	+64	107.7	16.66	16.99	17.43
08:39:35.90+03:08:40.8	52 891	5.52	−2.72	+22	290.1	15.93	16.31	16.82
08:41:25.44+61:03:20.7	43 629	5.73	+3	−124	82.8	17.31	17.60	17.97
08:47:18.93+23:00:30.3	56 847	5.60	−1.78	−91	322.0	14.55	15.03	15.54
08:53:51.78+07:04:17.4	46 604	5.93	+1.41	+77	68.0	16.69	17.02	17.40
08:57:27.65+42:42:15.4	39 865	5.11	+0.87	+209	240.6	17.94	18.26	18.73
09:02:52.99+07:35:33.9	41 105	5.89	+2.09	−139	45.1	16.74	17.09	17.52
09:09:57.82+62:29:27.0	48 682	5.54	−1.68	−48	198.8	15.78	16.12	16.63
09:10:44.90+23:40:44.7	51 879	5.71	+1.49	−80	173.4	17.45	17.89	18.38
09:22:45.80+21:42:39.0	40 647	5.17	+1.69	−51	226.5	18.30	18.65	19.14
09:28:30.55+56:18:11.7	67 931	5.31	−1.04	−143	1280.2	15.14	15.60	16.11
09:33:20.86+44:17:05.5	45 561	5.23	+0.99	+708	311.5	18.24	18.66	19.16
09:37:14.66+49:16:42.8	49 147	5.37	+0.20	−167	305.5	18.21	18.63	19.15
09:48:56.95+33:41:51.0	48 500	5.68	+2.28	+12	141.9	16.99	17.38	17.93
09:49:43.69+30:15:10.4	45 754	5.96	+2.30	+13	59.0	15.76	16.26	16.72
09:59:56.00+35:39:59.1	47 988	5.70	+1.83	+20	129.9	14.64	15.04	15.58
10:00:19.99−00:34:13.3	84 116	5.98	−1.06	+88	643.5	17.07	17.50	18.03
10:12:13.21+06:40:30.7	58 474	5.62	−0.83	−160	344.2	14.94	15.31	15.85
10:13:42.12+26:06:20.0	60 521	5.67	−1.66	−12	352.1	15.98	16.40	16.91
10:21:20.44+44:46:36.9	47 862	5.99	+0.95	−115	65.9	17.30	17.73	18.24
10:23:20.36+46:20:26.8	52 458	5.82	+1.71	+77	140.7	17.41	17.79	18.34
10:35:49.68+09:25:51.9	47 519	5.81	+3.00	+227	96.9	15.58	16.01	16.52
10:42:48.94+03:33:55.3	40 256	5.09	−2.25	+394	262.0	17.33	17.47	17.71
10:43:12.02+18:00:38.7	43 852	5.61	+0.91	−49	111.4	15.75	16.23	16.65
10:57:59.38+47:03:07.4	40 083	5.88	+1.92	−1	41.8	16.66	17.04	17.47
11:00:53.55+03:46:22.8	58 435	5.69	−0.91	+311	292.2	16.54	16.96	17.40
11:02:15.45+02:40:34.1	52 831	5.80	+1.61	+61	151.6	16.81	17.23	17.72
11:02:55.97+52:18:58.1	50 656	5.98	+1.06	−157	84.6	16.37	16.82	17.36
11:09:20.38+26:47:25.3	40 528	5.40	−3.72	−75	131.8	14.85	15.23	15.74
11:12:25.70+39:23:32.7	38 152	5.81	−0.65	+50	40.3	17.01	17.40	17.82
11:14:38.57−00:40:24.1	56 722	5.56	−0.90	+149	350.0	17.76	18.16	18.63
11:18:29.80+27:17:01.9	48 463	5.72	−1.20	+58	129.0	14.96	15.43	15.94
11:20:56.22+09:36:41.7	51 838	5.40	−2.47	+156	352.9	15.88	16.18	16.66
11:22:01.84+24:20:56.8	40 517	6.11	−0.29	−167	25.7	18.10	18.48	18.99
11:22:17.87+37:26:52.8	39 549	5.26	−3.01	−78	165.0	15.30	15.65	16.17
11:24:14.45+40:26:37.1	49 103	5.76	+1.44	+72	124.0	17.21	17.66	18.16
11:24:57.67+15:34:26.6	68 543	5.92	−0.32	+39	325.7	18.00	18.46	18.97
11:25:00.19−07:41:12.7	59 868	5.53	−1.27	−47	465.4	18.16	18.73	19.21
11:28:29.29+29:15:04.3	54 914	5.49	−2.00	+19	361.2	14.39	14.79	15.33
11:32:41.58−06:36:52.8	48 503	5.85	−2.72	−22	96.0	15.54	15.96	16.45
11:37:30.87+46:00:06.2	48 889	5.69	+1.09	−45	143.2	14.48	14.87	15.41
11:41:14.84+42:12:22.4	43 313	5.82	−0.94	−94	65.4	15.30	15.65	16.05

Table D.1 continued (2).

SDSS J	T_{eff}	$\log g$	$\log y$	v_{rad}	L	SDSS Photometry		
(2000)	[K]	(cgs)		[km/s]	$[L_\odot]$	u	g	r
11:46:04.93+08:29:34.9	45 305	5.73	+2.40	+248	96.3	17.68	17.98	18.60
11:50:09.48+06:10:42.1	56 989	5.30	−0.95	+56	648.9	17.67	18.11	18.62
11:51:01.03+54:10:03.4	38 206	4.91	−1.87	−183	321.8	16.60	16.83	17.29
12:03:52.24+23:53:43.3	40 237	5.75	−0.36	+177	57.2	16.35	16.76	17.26
12:05:21.48+22:47:02.2	57 364	5.41	−0.65	+138	517.1	17.24	17.74	18.32
12:06:05.99+08:09:43.4	48 524	5.75	+1.80	−48	121.0	15.42	15.85	16.36
12:06:26.54+66:33:52.5	44 487	6.04	+2.47	−41	43.8	15.42	15.79	16.31
12:11:48.83+16:33:45.1	48 064	5.78	−3.09	+88	108.7	16.15	16.50	16.80
12:14:24.81+55:02:26.2	59 354	5.57	−1.63	−95	410.0	16.10	16.54	17.09
12:16:43.72+02:08:35.9	41 435	5.79	−0.09	+26	58.7	17.99	18.36	18.85
12:21:32.17+16:32:56.4	37 403	5.03	−2.31	+77	224.2	16.71	17.09	17.54
12:36:13.89+11:18:34.1	63 897	5.53	−0.44	+95	603.8	17.47	17.88	18.34
12:38:08.65+05:33:18.2	48 957	5.77	+1.78	+26	119.8	16.92	17.32	17.83
12:38:21.49−02:12:11.4	59 450	4.95	+2.00	+102	1720.3	17.66	18.12	18.65
12:48:19.08+03:50:03.2	65 214	5.75	−0.95	−3	394.8	16.13	16.56	17.10
12:50:29.51+50:53:17.3	86 658	6.38	−1.33	−25	288.6	17.94	18.46	18.99
12:53:01.62+39:46:22.1	46 140	5.86	+3.00	−186	76.8	16.66	17.14	17.60
12:54:08.32+01:43:24.1	48 633	5.69	+3.00	+19	140.2	14.85	15.29	15.79
12:55:51.61+04:32:38.8	62 407	5.81	+0.75	+230	288.4	17.97	18.45	18.93
13:00:59.20+00:57:11.7	40 131	5.65	−0.47	−78	71.3	15.96	16.27	16.66
13:06:25.05+13:16:02.2	41 878	5.24	−1.11	+173	217.2	18.15	18.20	18.42
13:08:39.24+20:11:32.9	38 337	5.64	−0.18	−43	60.7	17.84	18.23	18.69
13:25:42.41−01:46:55.4	39 548	5.53	+0.14	+149	88.6	18.12	18.47	18.93
13:25:56.93−03:23:29.6	53 272	5.77	−2.23	+48	167.9	17.33	17.74	18.25
13:35:43.00+33:05:58.4	44 354	5.91	+1.24	−95	58.4	17.68	18.17	18.65
13:41:33.71+07:18:49.7	38 549	5.58	−1.70	−104	71.3	18.17	18.51	19.03
13:46:21.23+22:48:36.7	39 847	5.75	−0.09	+40	55.0	16.47	16.87	17.39
13:57:28.14+06:50:38.5	44 538	5.50	−2.83	+69	152.7	17.31	17.69	18.24
14:04:53.68+12:44:28.5	40 083	5.80	+0.27	−42	50.2	16.43	16.83	17.29
14:07:15.41+03:31:47.5	55 558	5.94	+1.46	+23	134.3	17.36	17.80	18.32
14:15:05.46+02:02:37.2	43 681	5.89	+2.46	−90	57.6	17.81	18.20	18.60
14:15:49.05+11:12:13.9	45 483	6.02	+1.57	+12	50.2	15.34	15.78	16.28
14:18:12.51−02:44:26.9	70 931	5.82	+0.88	−44	470.3	16.12	16.58	17.08
14:25:51.29−01:33:17.2	51 728	5.54	−1.69	−36	253.5	15.93	16.33	16.82
14:28:03.07+05:58:55.4	40 145	5.84	−0.28	−85	46.1	16.56	16.94	17.40
14:30:06.23+51:03:14.0	45 079	5.77	+3.00	−95	86.1	16.16	16.61	17.12
14:33:47.59+07:54:16.9	38 100	5.96	−0.45	−23	28.4	16.05	16.39	16.88
14:47:09.19+51:16:39.8	48 657	5.37	+0.52	−184	293.5	18.05	18.50	18.99
14:47:38.18+61:50:33.4	59 116	5.41	+0.02	−170	583.2	17.50	17.91	18.41
14:52:03.94+45:33:29.6	49 358	5.56	−2.01	−219	200.6	16.54	16.94	17.45
14:56:00.56+05:59:04.0	50 436	5.54	−1.93	+161	229.1	17.12	17.47	18.04
14:56:14.47+16:57:40.6	40 090	5.68	+2.03	+17	66.2	16.71	17.06	17.51
15:07:04.10+21:22:57.5	47 337	5.66	+0.80	+85	134.8	17.83	18.26	18.80
15:10:30.69−01:43:45.9	44 718	5.98	+3.00	−124	51.4	15.91	16.25	16.71
15:14:15.66−01:29:25.2	48 216	5.76	+1.75	−49	115.3	16.52	16.76	17.11

Table D.1 continued (3).

SDSS J	$T_{\rm eff}$	$\log g$	$\log y$	$v_{\rm rad}$	L	SDSS Photometry		
(2000)	[K]	(cgs)		[km/s]	$[L_\odot]$	u	g	r
15:16:13.21+27:38:54.9	47 463	6.11	−1.63	−22	48.3	15.99	16.34	16.73
15:19:39.27+39:46:26.4	39 833	5.48	+0.03	−318	102.3	18.62	18.80	19.27
15:21:36.25+16:21:50.3	52 221	5.74	+1.35	−165	166.1	16.38	16.81	17.33
15:24:58.81+18:19:40.5	52 000	5.47	−2.32	−47	304.1	17.79	18.06	18.48
15:26:07.88+00:16:40.7	62 093	5.51	−0.45	+50	563.9	16.18	16.59	17.06
15:30:56.33+02:42:22.5	45 548	5.72	+2.30	−45	100.7	14.77	15.20	15.66
15:32:37.94+27:56:36.9	40 070	5.58	+0.14	−159	83.2	17.97	18.28	18.73
15:40:43.09+43:59:50.1	45 574	5.82	+1.41	−48	80.2	15.81	16.24	16.75
15:42:27.88+31:06:01.9	46 269	5.40	+1.42	−184	224.0	16.86	17.30	17.76
15:53:32.95+03:44:34.4	38 851	5.76	−0.48	−28	48.6	16.58	16.69	16.83
15:56:42.95+50:15:37.4	71 231	5.84	+2	−28	490.4	15.40	15.84	16.38
15:56:57.54+26:55:18.2	80 189	5.52	+0.38	−19	1532.7	17.24	17.70	18.13
16:03:04.07+16:59:53.8	44 979	5.93	+1.21	−121	59.0	16.20	16.58	17.07
16:05:34.96+06:27:33.5	36 614	5.67	−0.82	−63	47.2	18.73	19.03	19.47
16:08:35.68+04:53:45.2	41 265	5.88	+0.46	−138	46.9	18.39	18.69	19.10
16:09:32.41+22:37:49.8	45 362	5.86	+1.68	+15	71.7	15.78	16.12	16.54
16:10:14.87+04:50:46.6	52 300	6.07	+1.53	+40	78.2	16.66	17.06	17.55
16:10:59.80+05:36:25.2	44 951	5.86	+1.89	−222	69.2	16.55	16.95	17.43
16:12:45.12+04:12:41.6	45 059	5.81	+1.56	+3	78.4	15.43	15.79	16.25
16:14:42.26+08:21:45.2	53 470	5.37	−1.72	−107	428.0	16.48	16.86	17.28
16:15:07.08+10:55:13.5	46 326	5.77	+3	−103	96.0	17.01	17.40	17.83
16:16:27.11−00:29:33.0	45 189	5.76	+2.36	+28	88.9	17.36	17.70	18.11
16:22:23.33−00:18:36.8	41 185	5.13	−3.56	+19	261.8	17.88	17.88	17.95
16:24:11.53+31:22:52.6	52 726	5.76	+1.59	−178	164.9	16.59	17.00	17.52
16:24:35.66+15:03:55.5	44 586	5.89	+1.56	−53	62.5	17.43	17.84	18.28
16:26:16.70+38:07:10.5	47 414	5.85	+3.00	−10	87.6	14.97	15.43	15.91
16:26:54.20+08:25:35.0	44 285	6.10	+2.02	−4	37.5	14.28	14.69	15.14
16:27:11.80−00:09:50.8	38 935	5.86	+0.16	+28	38.9	18.18	18.45	18.83
16:28:25.87+35:32:05.1	67 580	5.36	−0.50	−325	1117.6	17.93	18.38	18.94
16:29:11.84+20:46:18.1	65 465	5.51	+1.43	−155	696.7	17.73	18.18	18.64
16:30:27.19+18:02:33.2	44 787	5.70	+2.78	−53	98.5	17.77	18.07	18.51
16:35:57.64+62:06:36.1	38 343	5.43	−0.08	−370	98.6	18.15	18.46	18.86
16:37:02.78−01:13:51.7	45 703	5.74	+3.00	+18	97.4	16.82	17.12	17.46
16:40:50.80+36:36:50.9	40 061	5.00	−1.71	−252	316.1	16.74	17.10	17.60
16:55:54.13+11:24:00.8	36 739	5.23	−1.72	+20	131.7	14.25	14.47	14.87
16:59:24.75+27:32:44.4	55 643	5.31	−0.69	−428	576.3	19.14	19.55	19.95
16:59:57.67+28:50:54.0	39 473	5.46	−3.11	−94	103.3	13.84	14.16	14.62
17:00:45.10+39:18:30.3	38 976	5.91	−0.17	−88	34.8	17.56	17.93	18.41
17:00:45.67+60:43:08.4	48 470	6.01	+2.22	−257	66.2	16.79	17.24	17.80
17:02:14.00+19:42:55.1	44 975	5.87	+3.00	−58	67.8	15.16	15.51	15.93
17:05:40.02+29:20:41.2	37 553	5.70	−0.09	−235	48.7	17.79	18.06	18.49
17:09:57.39+22:27:45.0	52 914	5.93	+0.94	−374	113.1	16.84	17.18	17.67
17:13:14.08+40:41:08.9	41 926	5.42	−0.04	−182	144.2	17.52	17.97	18.45
17:24:36.21+27:52:42.0	38 861	5.48	−0.47	−90	92.7	16.78	16.92	17.20
17:27:27.55+09:12:15.5	44 825	5.32	−2.17	−33	237.2	17.09	17.33	17.63

Table D.1 continued (4).

SDSS J (2000)	$T_{\rm eff}$ [K]	$\log g$ (cgs)	$\log y$	$v_{\rm rad}$ [km/s]	L $[L_\odot]$	u	g	r
17:29:19.04+07:22:04.5	55 109	5.66	−3	−88	247.7	16.72	17.05	17.45
17:30:27.19+26:56:39.4	72 281	6.04	+1.85	−43	305.6	16.72	17.08	17.55
17:30:33.53+45:15:37.3	74 085	5.32	−0.92	−275	1769.8	18.14	18.60	19.08
17:30:34.09+27:21:39.8	40 217	5.58	+0.16	−463	84.5	18.31	18.61	19.09
17:44:08.22+25:16:57.5	39 346	5.86	−0.00	−14	40.6	15.97	16.26	16.72
17:45:16.32+24:43:48.3	44 058	5.97	+1.53	−118	49.6	17.07	17.41	17.88
18:07:57.08+23:01:33.0	42 311	5.78	+2.14	+19	65.3	16.62	16.87	17.27
18:32:29.22+40:24:18.4	45 423	5.15	−2.68	−117	369.9	15.19	15.48	15.94
18:33:39.00+42:13:07.8	39 097	5.72	+0.31	−6	54.7	17.94	18.21	18.50
19:20:49.90+37:41:38.8	48 000	5.06	−1.70	−85	567.5	17.07	17.45	17.52
19:27:15.05+38:27:18.7	41 944	5.67	+0.65	−18	81.2	15.08	15.47	15.78
20:05:50.04+76:25:36.4	45 355	6.00	+1.61	−55	51.9	14.25	14.51	14.75
20:08:05.60−10:24:31.7	71 884	5.41	+0.81	−44	1275.1	18.09	18.32	18.60
20:08:15.48−11:01:04.0	49 516	5.64	+1.37	−65	169.0	16.65	16.89	17.15
20:08:36.41−11:46:29.2	45 532	5.90	+2.28	−15	66.4	16.27	16.62	16.85
20:09:59.27−11:55:19.9	41 019	5.61	−0.00	−38	85.3	18.21	18.49	18.80
20:11:24.57−12:12:50.4	39 736	5.04	−2.29	−110	279.1	16.47	16.68	17.03
20:12:40.58−11:00:42.0	64 008	5.28	−1.04	−105	1081.3	15.61	15.91	16.32
20:24:40.92+13:37:29.2	87 261	5.54	−1.12	−80	2052.5	16.12	16.49	16.73
20:27:58.63+77:39:24.5	47 321	5.62	−2.62	−129	147.6	17.52	17.71	17.94
20:34:26.66+14:36:52.8	41 830	5.67	+0.33	−55	80.3	14.65	15.00	15.49
20:43:00.90+00:21:45.0	45 245	5.73	−2.54	−81	95.8	17.28	17.64	18.12
20:46:23.12−06:59:26.8	60 260	5.46	−1.07	−201	561.2	17.12	17.48	17.88
20:49:40.85+16:50:03.6	44 186	5.93	+3	+13	55.0	17.32	17.66	18.12
20:50:30.39−06:19:57.9	49 669	5.71	+2.24	−524	145.7	17.63	18.00	18.41
20:50:48.84+16:45:45.1	65 197	5.02	−0.95	−22	2118.0	16.05	16.43	16.92
21:06:04.96+10:42:15.9	57 885	5.68	−0.87	−263	287.9	17.82	18.19	18.68
21:13:18.36+00:17:38.3	45 381	5.82	+2.00	+19	78.8	15.80	16.14	16.53
21:19:21.36+00:57:49.7	45 198	5.69	+2.27	−27	104.6	15.19	15.58	16.00
21:56:31.55+12:12:37.6	48 889	5.95	+3.00	−46	78.7	16.68	17.03	17.46
22:00:48.67+12:36:12.4	60 619	5.74	−1.19	−344	301.6	17.91	18.30	18.76
22:04:29.52+21:16:10.8	49 967	5.84	+3	−251	110.6	15.20	15.60	16.04
22:05:55.60+05:57:35.8	59 260	6.15	−1.94	−291	107.2	17.55	17.93	18.27
22:07:14.41+07:22:32.1	40 527	5.58	+0.10	+13	87.1	14.23	14.52	14.91
22:07:45.48+22:16:40.6	38 495	5.27	−3.12	−62	144.8	16.93	17.25	17.69
22:08:19.50+06:02:55.5	45 359	5.74	+1.11	−95	94.6	16.21	16.53	16.91
22:19:20.67+39:46:03.5	46 254	5.75	−3.37	−72	99.9	16.76	17.02	17.43
22:22:38.69+00:51:24.9	52 261	5.32	−2.84	−125	438.2	15.72	16.11	16.51
22:45:56.32+24:12:56.9	52 297	5.31	−2.70	−234	449.7	16.85	17.14	17.47
23:27:57.46+48:37:55.2	62 799	5.31	+1.28	−110	935.0	15.26	15.63	15.99
23:35:41.47+00:02:19.4	71 388	5.45	+1.14	−12	1131.1	15.26	15.69	16.18
23:39:13.99+13:42:14.2	48 753	5.74	+1.06	−389	126.2	16.87	17.30	17.75
23:41:17.15+45:41:45.1	40 118	5.79	−1.00	−47	51.6	17.78	18.07	18.52
23:45:28.85+39:35:05.2	45 011	5.74	+1.98	−15	91.7	16.83	17.10	17.52
23:51:08.65+00:26:23.0	41 749	6.04	−0.25	−206	34.0	16.96	17.32	17.75

Table D.2: Stars classified as *sdOB* from SDSS. Luminosity L is calculated under the assumption of $M = 0.5\,M_{\odot}$.

SDSS J (2000)	T_{eff} [K]	$\log g$ (cgs)	$\log y$	v_{rad} [km/s]	L $[L_{\odot}]$	SDSS Photometry u	g	r
00:06:07.88−01:03:20.8	44 845	6.08	+1.97	−257	41.3	17.03	17.48	17.96
00:06:45.56+25:07:38.5	36 883	5.76	−0.46	−309	39.47	19.35	19.58	20.07
01:15:06.17+14:05:13.5	37 680	4.86	−1.95	−185	341.55	17.78	18.08	18.59
01:24:30.28+06:48:57.4	35 048	5.65	−1.68	−73	41.46	15.86	16.18	16.62
02:16:17.10−09:55:13.0	37 058	5.94	−1.35	−50	26.58	15.27	15.60	16.08
03:08:59.88+38:01:04.2	32 402	5.57	−1.59	−1	36.42	16.22	16.26	16.53
03:12:34.62+41:20:38.6	34 503	5.48	−1.82	−11	57.60	16.31	16.51	16.90
03:33:58.21+00:20:07.4	36 390	5.65	−0.66	+150	48.19	17.77	17.97	18.31
03:46:38.36−05:43:59.6	34 551	5.95	−1.55	−23	19.63	14.41	14.66	15.07
05:25:44.93+63:07:26.0	35 922	5.70	−1.54	−54	40.78	17.54	17.61	17.79
05:45:16.42+82:20:02.0	34 404	4.80	−1.16	−58	272.55	14.79	14.98	15.30
05:58:08.88+82:22:18.6	35 819	5.83	−1.37	−83	29.89	15.45	15.66	16.07
06:42:29.22+37:04:13.2	36 477	6.00	−1.42	+12	21.73	14.73	14.91	15.28
06:50:44.30+38:31:33.7	33 714	5.62	−2.45	+46	38.04	16.84	17.06	17.44
06:52:51.84+29:00:23.3	32 692	5.62	−1.78	+8	33.63	14.31	14.56	15.00
07:23:51.47+30:19:16.5	33 692	6.17	−1.49	−5	10.69	14.59	14.81	15.24
07:36:46.36+22:01:15.9	35 579	5.88	−0.94	+41	25.93	17.53	17.84	18.34
07:40:23.56+20:49:37.0	34 843	5.58	−1.48	+57	47.59	14.95	15.25	15.74
07:44:58.09+32:42:59.9	37 406	5.64	−0.70	+56	55.05	17.94	18.22	18.71
07:45:51.13+17:06:00.3	35 489	5.47	−2.75	+39	65.98	16.47	16.75	17.25
07:48:06.15+34:29:27.7	35 323	5.72	−1.61	−76	36.41	16.81	17.09	17.56
07:57:11.83+13:45:08.4	36 912	5.79	−1.49	+22	36.96	15.39	15.68	16.16
08:15:40.66+43:05:24.5	38 887	5.63	−0.15	+151	65.80	18.54	18.81	19.26
08:19:17.71+42:33:38.7	35 045	5.74	−1.97	+12	33.69	15.72	15.98	16.45
08:26:57.29+12:28:18.1	34 509	5.90	−1.69	+95	21.91	16.48	16.78	17.27
08:33:59.65−04:35:21.9	37 348	5.79	−1.46	+174	38.73	17.75	18.06	18.55
08:53:35.09+62:16:42.9	35 657	5.94	−0.93	−164	22.78	17.45	17.67	18.08
08:59:00.32+02:33:13.1	35 539	5.78	−1.67	+36	32.50	15.73	16.02	16.53
09:11:37.60+35:30:35.2	36 469	5.70	−1.34	+110	43.32	17.56	17.77	18.14
09:22:06.80+08:19:29.4	34 045	5.66	−1.58	+2	36.08	15.04	15.32	15.79
09:26:17.51+67:18:53.7	36 249	5.77	−1.49	−32	35.99	16.07	16.24	16.56
09:30:06.79+31:42:58.4	35 370	5.81	−1.38	+44	29.75	16.72	16.97	17.48
09:35:12.16+31:10:00.5	35 371	5.70	−1.41	−10	38.34	15.06	15.34	15.87
09:35:49.71+54:41:01.0	37 725	5.61	−1.36	−122	61.03	17.17	17.52	17.84
09:43:46.62+53:14:29.0	39 128	5.36	−0.55	−159	125.59	17.90	17.98	18.14
09:46:23.02+04:04:56.0	37 043	5.86	−1.40	+53	31.90	15.15	15.43	15.92
09:47:58.91+09:10:12.3	35 085	5.81	−0.71	+4	28.81	16.63	16.97	17.47
09:50:58.04+18:26:18.5	35 342	5.83	−1.66	+158	28.33	15.58	15.87	16.32
10:12:18.95+00:44:13.4	37 661	5.77	−1.16	−19	41.93	17.35	17.65	17.97
10:24:07.23+39:22:53.5	37 780	5.77	−0.31	+92	42.47	17.47	17.84	18.30
10:52:44.44+24:59:25.3	33 677	5.68	−1.75	−6	32.99	16.30	16.49	16.92
10:54:12.67+29:17:11.8	37 215	5.85	−0.57	−125	33.26	16.51	16.81	17.32
11:04:45.01+09:25:30.9	37 446	5.01	−2.10	+176	235.85	15.70	16.00	16.53
11:20:00.37+30:56:59.9	33 534	5.63	−2.19	+18	36.39	13.93	14.24	14.79
11:25:26.95+11:29:02.6	36 356	5.93	−0.70	+45	25.19	16.81	17.10	17.55

Table D.2 continued (1).

SDSS J (2000)	T_{eff} [K]	$\log g$ (cgs)	$\log y$	v_{rad} [km/s]	L $[L_\odot]$	SDSS Photometry u	g	r
11:32:18.41+07:51:03.0	33 581	4.79	−1.73	+59	253.15	17.16	17.10	17.25
11:37:54.10+58:15:24.6	37 374	5.44	−1.91	−4	86.95	15.55	15.91	16.39
12:06:13.40+20:55:23.1	35 130	5.01	−1.97	−25	182.69	17.83	18.13	18.54
12:08:55.52+40:37:16.1	35 341	5.75	−1.27	+127	34.05	17.91	18.27	18.78
12:42:01.73+43:40:23.3	37 519	5.67	−0.06	+11	52.00	16.33	16.67	17.17
12:42:48.89+13:36:32.6	36 071	5.00	−2.67	−188	207.80	17.03	17.28	17.77
12:43:10.59+34:33:58.4	35 199	5.46	−0.71	+146	65.33	17.19	17.58	18.07
12:45:20.88+03:09:51.4	38 472	6.00	−0.67	+13	26.89	18.01	18.34	18.86
12:45:52.82+17:51:12.2	40 221	5.86	+0.27	+113	44.34	17.33	17.68	18.19
12:57:38.33+18:17:24.2	40 507	5.83	+0.38	+39	48.88	17.23	17.60	18.02
12:59:41.87−00:39:28.8	38 408	5.27	−1.56	+42	143.45	16.83	16.80	16.93
13:04:39.57+31:29:04.8	38 314	5.78	−0.46	−25	43.90	16.36	16.77	17.28
13:32:00.95+67:33:25.7	36 655	5.84	−1.55	−103	32.03	16.59	16.94	17.41
13:34:49.26+04:10:14.8	36 565	5.23	+0.59	+80	129.20	16.79	16.98	17.19
13:35:12.81+19:51:55.8	34 108	5.78	−1.57	−58	27.57	17.25	17.57	18.03
13:38:10.31+43:17:43.1	36 756	5.22	−0.97	−30	135.00	16.86	16.75	16.85
13:55:34.70+16:00:17.2	36 889	5.96	−1.38	−55	24.92	15.36	15.67	16.14
13:59:20.78+32:08:46.5	38 049	5.76	−0.59	−6	44.71	18.27	18.57	19.07
14:08:03.07+24:25:49.4	39 971	5.80	−0.00	−23	49.66	17.17	17.41	17.84
14:19:22.55+29:46:50.2	35 633	5.61	−1.47	−99	48.58	16.94	17.20	17.59
14:24:59.58+03:19:43.3	35 608	5.70	−1.45	+17	39.37	15.89	16.21	16.68
14:27:18.20+22:38:51.8	38 650	5.46	−0.75	−173	94.97	17.75	17.82	17.91
14:31:53.05−00:28:24.3	38 105	6.10	−0.70	+0	20.56	17.50	17.81	18.32
14:33:14.74+53:09:35.6	36 833	5.83	−1.55	−124	33.42	16.47	16.87	17.39
14:35:06.34+28:47:50.9	36 195	5.92	−1.67	−77	25.33	15.59	15.88	16.31
14:43:46.62+49:17:33.6	36 827	5.82	−1.44	−89	34.17	16.76	17.00	17.37
14:45:14.93+00:02:48.9	39 040	5.35	−1.37	−23	127.36	17.31	17.34	17.49
14:54:32.11+29:56:50.6	34 836	5.73	−1.55	−78	33.66	16.74	17.08	17.57
15:02:30.30+09:13:57.3	35 366	5.54	−1.31	+21	55.38	16.94	17.28	17.77
15:03:07.11+12:18:32.6	40 264	5.81	+0.10	−68	49.97	18.08	18.41	18.91
15:09:36.18+21:14:33.2	37 592	5.97	−1.52	+21	26.27	16.46	16.64	16.89
15:10:42.05+04:09:55.5	35 893	5.62	−1.55	−55	48.87	16.55	16.85	17.25
15:11:58.23+25:54:11.6	35 661	5.76	−1.52	−40	34.50	17.47	17.72	18.13
15:12:54.55+15:04:47.0	37 354	6.04	−1.82	−36	21.80	17.20	17.54	18.02
15:17:43.47+51:44:45.4	35 996	5.70	−1.58	−55	41.12	16.80	16.94	17.21
15:23:32.81+35:32:37.0	37 656	5.64	−0.55	+20	56.54	16.06	16.43	16.89
15:25:34.15+09:58:51.0	36 149	5.71	−1.66	−50	40.87	17.08	17.38	17.83
15:27:05.03+11:08:43.9	37 676	5.63	−0.34	−50	57.98	16.80	17.08	17.43
15:28:52.27+09:31:44.2	33 594	5.76	−1.58	−25	27.17	15.88	16.18	16.67
15:34:11.10+54:33:45.2	34 816	5.39	−2.17	−88	73.47	16.55	16.74	17.03
15:35:26.07+21:14:41.0	38 000	5.83	+1.32	−32	37.86	16.55	16.73	16.88
15:49:58.29+04:38:20.2	36 140	5.85	−1.12	−138	29.58	17.86	18.13	18.63
15:53:43.39+13:13:30.4	37 918	5.77	−0.78	+31	43.09	18.13	18.31	18.59
15:54:22.35+13:59:14.2	36 988	5.72	−1.40	−96	43.78	16.31	16.54	16.88
16:02:29.77+11:13:31.1	38 000	5.69	−0.61	+18	52.26	17.63	17.69	17.82

Table D.2 continued (2).

SDSS J (2000)	T_{eff} [K]	$\log g$ (cgs)	$\log y$	v_{rad} [km/s]	L $[L_\odot]$	SDSS Photometry		
						u	g	r
16:03:32.84+51:48:27.9	35 892	5.73	−0.36	−67	37.93	17.19	17.49	17.98
16:04:26.18+21:57:14.3	37 202	5.93	−1.36	−93	27.62	16.46	16.74	17.20
16:04:50.44+05:19:09.3	39 048	5.92	+0.73	−205	34.31	18.08	18.35	18.70
16:04:53.45+11:52:18.3	36 863	5.88	−1.06	−35	29.88	17.28	17.56	18.05
16:07:59.27+38:37:46.4	35 580	5.71	−0.90	−54	38.36	16.09	16.43	16.94
16:08:10.63+10:32:11.7	36 999	5.64	−0.69	−39	52.69	16.88	17.09	17.44
16:11:29.89+09:50:04.8	38 133	5.99	−1.29	+17	26.56	17.52	17.82	18.31
16:11:40.50+20:18:57.0	36 579	5.81	−1.33	−58	34.04	18.00	18.24	18.72
16:11:49.34+19:23:50.7	35 684	5.69	−1.72	−51	40.64	15.37	15.65	16.14
16:12:55.05+05:11:52.1	39 281	5.33	−0.06	+38	136.69	18.54	18.67	18.87
16:14:00.07+15:09:47.3	36 222	5.85	−1.36	−14	29.85	16.49	16.82	17.31
16:19:38.64+25:21:22.4	38 992	5.80	−0.35	−165	44.97	16.97	17.29	17.74
16:23:36.30+15:32:36.5	38 931	5.94	−0.07	−46	32.37	16.51	16.84	17.18
16:28:02.26+29:33:41.3	38 648	5.40	−1.26	+3	109.02	18.12	18.35	18.64
16:34:16.08+22:11:41.0	37 492	5.67	+2.89	−49	51.85	14.92	15.18	15.64
16:34:16.63+21:44:58.7	37 095	5.76	−1.54	−24	40.39	16.30	16.57	16.94
16:38:11.76+27:50:20.8	35 352	5.65	−1.56	−30	42.92	16.55	16.80	17.24
16:38:26.29+11:12:19.4	36 195	5.77	−1.26	−8	35.78	18.06	18.35	18.77
16:40:42.90+31:17:34.6	40 093	6.40	+1.12	−275	12.63	16.77	17.09	17.48
16:47:06.94+34:56:55.9	35 150	4.97	−0.88	−199	200.78	18.11	18.43	18.90
16:51:28.40+11:56:37.8	35 397	5.74	−1.70	−178	35.07	17.86	18.15	18.64
16:57:44.15+12:43:56.6	36 647	5.81	−1.32	−40	34.29	17.86	18.12	18.47
16:59:39.69+21:47:04.9	36 782	5.64	−1.32	−47	51.47	17.23	17.53	17.96
17:01:55.40+26:04:03.2	35 887	5.59	−1.12	−79	52.33	18.31	18.52	18.84
17:04:06.88+28:54:16.1	33 782	5.82	−1.62	+16	24.20	16.63	16.86	17.21
17:08:10.97+24:43:41.6	37 339	5.40	−0.71	−101	94.99	17.92	18.20	18.67
17:16:29.92+57:51:21.2	37 451	5.57	−0.68	−317	64.99	17.58	17.92	18.41
17:32:38.13+09:11:43.6	36 420	5.58	−1.00	+29	56.80	18.55	18.67	19.04
17:35:03.18+32:36:22.3	32 992	5.75	−1.58	−28	25.86	14.78	14.95	15.39
17:37:21.87+33:43:29.6	38 844	5.49	+0.13	−279	90.43	18.53	18.82	19.18
17:44:01.68+25:44:44.3	35 314	5.70	−1.73	+16	38.09	17.54	17.76	18.21
17:44:42.35+26:38:29.9	39 054	6.10	+1.17	+23	22.68	17.47	17.70	17.97
18:03:13.45+23:40:00.1	33 465	4.94	−2.10	−80	176.76	16.08	16.23	16.58
18:09:35.27+22:35:40.2	35 472	5.70	−1.71	−5	38.78	16.92	17.12	17.48
18:31:27.13+64:34:42.0	36 701	5.94	−1.66	−103	25.57	14.84	15.14	15.62
18:54:14.11+17:52:00.2	35 361	5.88	−1.43	+17	25.30	16.83	16.84	17.02
19:17:26.13+79:17:41.3	35 491	5.92	−1.40	−39	23.41	16.54	16.75	17.11
20:04:38.68−11:15:26.7	36 814	5.76	−1.28	−47	39.18	17.08	17.29	17.60
20:25:50.42+13:30:40.7	34 393	5.77	−1.71	−188	29.17	16.95	17.18	17.66
20:29:42.46+13:26:28.4	35 437	5.65	−1.55	−1	43.33	18.03	18.32	18.84
20:30:17.81+13:18:49.2	36 702	5.93	−1.39	−14	26.17	16.34	16.56	17.00
20:35:12.89+15:20:29.3	36 570	5.85	−1.24	−26	31.01	18.97	19.28	19.68
20:43:58.55−06:50:25.8	36 619	5.93	−0.13	−324	25.93	17.85	18.18	18.60
20:46:58.83−05:51:00.0	34 155	5.53	−1.64	−73	49.30	16.30	16.55	17.01
20:47:26.93−06:03:25.7	35 935	5.65	−1.38	−11	45.82	17.03	17.29	17.70

Table D.2 continued (3).

SDSS J	T_{eff}	$\log g$	$\log y$	v_{rad}	L	SDSS Photometry		
(2000)	[K]	(cgs)		[km/s]	$[L_{\odot}]$	u	g	r
20:48:04.16+14:35:30.7	37 391	6.15	−1.75	−147	16.99	17.89	18.10	18.36
20:57:58.45+01:08:17.6	37 470	5.34	−1.73	−259	110.60	16.97	16.84	16.86
21:04:54.89+11:06:45.5	40 097	5.34	−2.65	−27	145.03	17.00	17.18	17.41
21:10:45.16+00:01:42.0	38 235	5.08	−2.16	+30	218.20	16.57	16.82	17.22
21:11:51.85+11:19:37.6	36 222	5.82	−1.41	+16	31.98	16.12	16.36	16.72
21:12:20.42+11:29:55.4	36 268	5.63	−1.09	+46	49.79	18.09	18.23	18.43
21:13:38.30−00:09:40.7	38 756	5.88	−1.63	−37	36.51	17.45	17.60	17.74
21:14:21.39+10:04:11.4	35 606	4.92	−2.78	−275	237.19	17.85	18.11	18.55
21:14:25.02+00:55:17.6	37 188	5.81	−1.08	+18	36.36	17.96	18.15	18.47
21:19:24.56−00:49:55.5	37 685	5.73	−1.06	−153	46.10	18.33	18.59	19.08
21:20:53.72−07:15:44.1	38 266	5.65	−1.34	−182	58.92	18.03	17.82	17.72
21:20:55.95−06:39:18.3	33 226	5.84	−1.38	−14	21.62	15.83	15.83	16.08
21:22:44.84−06:51:00.0	36 445	5.79	−1.54	−106	35.12	17.25	17.26	17.44
21:23:30.46+00:42:38.8	36 617	5.85	−0.67	−52	31.17	16.24	16.60	17.06
21:30:54.60−00:41:17.4	39 289	6.19	+0.83	−49	18.88	17.52	17.87	18.32
21:31:12.23+11:29:36.2	38 361	5.89	−1.55	−25	34.24	15.45	15.72	16.15
21:50:49.19+01:03:38.3	36 430	5.65	−1.07	+25	48.40	17.77	18.04	18.50
21:52:27.25+11:57:26.7	36 297	5.60	−1.49	+16	53.52	17.19	17.44	17.83
22:28:50.00+39:19:17.4	34 359	5.64	−1.61	−78	39.19	15.97	16.14	16.56
22:29:32.80−00:48:22.5	35 702	5.67	−1.38	−21	42.64	15.95	16.22	16.60
22:59:13.44+05:50:04.2	36 260	5.65	−1.42	−43	47.50	17.42	17.73	18.14

Table D.3: Stars classified as *sdO* or *sdOB* from SDSS. These objects were *not* used in this work's analysis due to low signal-to-noise ratio, or other reasons stated in the last column.

SDSS J (2000)	spectral class	SDSS Photometry			
		u	g	r	
00:01:11.65+00:03:42.6	sdOB	19.28	19.27	19.36	
00:02:18.48+25:24:15.0	sdOB	19.15	19.54	20.10	
01:03:35.07+01:15:53.4	sdO				
01:25:17.48−09:01:13.2	sdO	18.53	18.94	19.43	
01:37:11.39+14:41:54.3	sdO	20.12	20.06	20.10	
01:38:08.71+24:30:13.3	sdOB	14.99	15.07	15.21	$\log g < 4.8$
01:40:24.08−09:08:14.7	sdO	18.93	19.30	19.78	
01:45:31.86+01:06:29.7	sdO	19.75	20.15	20.66	
01:50:26.10−09:42:26.9	sdOB+X	15.83	15.95	16.12	
02:24:22.21+00:03:13.5	sdOB	18.36	18.73	19.21	
02:32:14.20−07:16:37.4	sdOB	18.84	19.12	19.49	
02:43:23.23+27:50:45.4	sdO	19.19	19.50	19.83	
02:56:22.18+33:09:44.7	sdO	19.28	19.73	20.04	
03:18:23.06+41:55:21.7	sdOB	14.50	14.64	14.93	H vs He
03:21:40.70+05:06:32.0	sdO	20.58	20.58	20.79	
03:37:39.75−06:23:57.3	sdO	19.97	19.85	20.15	
04:41:49.13+10:08:21.7	sdO	18.71	18.86	19.02	
05:39:08.64+82:48:39.7	sdOB	19.45	19.68	19.91	
06:49:16.11+38:34:19.7	sdOB	15.13	15.32	15.73	H vs He
07:24:01.73+41:03:20.9	sdO	18.78	19.11	19.53	
07:24:21.40+38:56:30.6	sdOB+X	16.29	16.26	16.29	
08:02:22.38+18:57:07.9	sdOB	18.93	19.40	19.95	
08:04:38.03+45:32:38.9	sdOB	18.67	18.86	19.22	
08:09:28.25−08:10:18.7	sdOB	14.01	14.32	14.78	H vs He
08:10:17.91+19:17:49.1	sdOB	16.71	16.99	17.48	H vs He
08:13:55.81+55:22:51.8	sdOB+X	18.51	18.59	18.73	
08:17:39.99+16:31:17.1	sdO	18.77	19.19	19.71	
08:21:10.89+18:39:24.2	sdOB	17.56	17.84	18.33	
08:24:34.05+30:28:54.6	sdO+X	15.35	15.25	15.32	
08:25:50.89+15:33:08.0	sdO	18.30	18.77	19.28	
08:27:51.07+41:09:25.9	sdO	18.19	18.63	19.13	
08:29:02.62+22:46:36.7	sdOB+X	15.83	15.86	15.91	
08:41:13.93+20:30:18.7	sdOB	18.80	18.68	18.71	
08:44:23.12+07:53:06.1	sdO	15.64	16.17	16.67	peculiar He II profile
08:51:26.18+00:07:39.9	sdO	19.47	19.87	20.31	peculiar binary
08:54:22.39+01:36:50.9	sdO+X	16.00	15.99	16.16	
08:57:08.54+05:14:53.0	sdO	19.68	19.99	20.46	
08:59:00.33+02:33:13.1	sdOB	15.73	16.02	16.53	H vs He
09:01:00.01+56:57:13.6	sdO	19.54	19.93	20.44	
09:01:00.01+56:57:13.6	sdO	19.54	19.93	20.44	
09:03:28.82+43:46:23.3	sdO	19.09	19.42	19.85	
09:07:22.89+01:46:27.8	sdOB	18.85	19.21	19.65	
09:15:12.06+19:11:14.6	sdOB	18.45	18.79	19.28	
09:21:49.95+06:23:45.8	sdOB	19.34	19.68	20.12	
09:29:20.43+06:03:46.1	sdOB+X	15.45	15.30	15.25	

Table D.3 continued (1).

SDSS J	spectral	SDSS Photometry			
(2000)	class	u	g	r	
09:29:25.36+23:10:51.1	sdO	18.40	18.72	19.20	
09:30:28.56+27:49:11.5	sdO	18.52	18.96	19.48	
09:32:45.91+08:16:18.6	sdOB	15.93	16.21	16.67	$T_{\text{eff}} < 34\,000\,\text{K}$
09:35:21.39+48:24:32.4	sdO	17.66	18.19	18.68	
09:36:12.62+62:27:00.7	sdO+X	15.74	15.78	15.87	
09:56:01.68+09:11:37.8	sdO	18.04	18.46	18.91	
09:58:54.93+24:53:11.8	sdO	18.30	18.70	19.19	
09:59:11.47+22:00:03.9	sdOB	17.60	17.71	17.87	
10:03:14.35+21:51:24.1	sdOB+X	16.17	16.01	16.06	
10:03:34.96+04:09:20.8	sdO	18.85	19.23	19.76	
10:10:21.17+27:41:13.8	sdO	18.08	18.36	18.67	
10:15:21.37+26:35:50.7	sdOB	17.66	17.93	18.46	
10:17:57.37+35:55:17.5	sdOB+X	16.16	16.04	16.07	
10:22:32.37+34:24:56.3	sdOB+X	16.24	16.12	16.13	
10:28:44.63+25:30:18.3	sdO+X	16.11	16.21	16.34	
10:32:42.42+35:09:37.2	sdO	18.79	18.66	18.70	
10:42:42.85+18:10:25.1	sdO	17.81	18.27	18.73	
10:42:59.93+63:09:37.0	sdO	19.14	19.49	19.91	
10:48:38.82+31:54:05.8	sdOB+X	16.24	15.99	15.97	
10:55:25.88+09:30:56.3	sdO	17.65	17.37	17.46	H vs He
11:02:25.71+27:06:00.6	sdO	17.31	17.70	18.24	$\log g < 4.8$, hot, He-enr.
11:04:18.24+04:32:16.4	sdO	17.80	18.08	18.58	
11:05:46.37+10:15:38.9	sdOB	18.01	18.31	18.68	
11:06:50.47+29:35:32.6	sdOB	15.21	15.52	16.00	H vs He
11:08:21.54+29:36:49.0	sdOB	14.90	15.25	15.72	$\log g < 4.8$, cool, He-def.
11:13:22.90+00:05:30.9	sdO	19.37	19.65	20.26	
11:16:33.30+05:25:07.9	sdOB	17.72	17.81	17.96	
11:25:04.73+67:16:58.3	sdOB+X	17.14	17.30	17.46	
11:28:55.24−06:10:04.1	sdO	19.05	19.54	20.05	
11:34:12.77+21:15:14.6	sdO	17.62	18.13	18.65	
11:37:10.76−03:28:42.9	sdO	19.21	19.47	19.85	
11:42:51.76+11:15:07.9	sdO	18.10	18.55	19.00	
11:49:00.55+22:31:04.5	sdOB+X	14.95	14.91	15.03	
11:50:35.62+25:32:05.1	sdOB	18.45	18.80	19.30	
11:54:59.67+28:08:05.2	sdOB	18.36	18.67	19.14	
11:56:54.08−03:25:10.1	sdOB	16.10	16.25	16.61	$\log g < 4.8$
12:00:09.01+06:43:29.1	sdO	18.96	19.26	19.59	
12:01:47.09+15:55:32.6	sdO	18.82	19.20	19.71	
12:03:41.21+25:31:11.4	sdOB+X	14.74	14.96	15.41	
12:12:38.58+42:40:01.8	sdOB+X	15.09	14.97	15.00	
12:17:35.01+19:00:45.2	sdOB+X	16.17	15.95	16.00	
12:19:00.71+00:00:08.1	sdO	19.79	19.54	19.92	
12:20:47.69+20:19:42.3	sdOB	18.88	19.27	19.76	
12:29:38.53+62:35:40.6	sdO	20.00	20.28	20.71	
12:35:13.03+10:29:59.4	sdOB+X	16.59	16.44	16.52	

Table D.3 continued (2).

SDSS J (2000)	spectral class	SDSS Photometry			
		u	g	r	
12:43:46.38+00:25:34.9	sdOB+X	18.82	18.61	18.58	
12:47:47.51+45:08:43.6	sdOB	18.76	19.20	19.75	
12:50:04.24+45:37:51.6	sdO	17.95	18.32	18.76	
12:51:01.48+37:10:49.7	sdO+X	15.55	15.52	15.61	
13:00:25.53+00:45:30.1	sdOB+X	15.51	15.68	15.83	
13:03:18.39+10:31:01.8	sdO	18.07	18.51	19.03	
13:05:21.60+38:59:00.1	sdO	16.12	16.53	17.11	
13:06:38.83+64:59:37.0	sdO	17.91	18.37	18.91	
13:12:48.79+17:41:01.6	sdOB+X	14.93	15.18	15.51	
13:15:13.75−01:26:52.8	sdOB	19.33	19.46	19.82	
13:15:41.12+28:08:56.0	sdO	18.91	18.79	18.90	
13:16:38.48+03:48:18.4	sdOB+X	15.69	15.79	16.03	
13:16:58.35+64:15:22.5	sdOB+X	14.88	14.94	15.07	
13:25:15.23+38:53:01.0	sdOB+X	16.32	16.25	16.34	
13:26:19.95+03:57:54.3	sdOB+X	15.08	15.19	15.41	
13:27:42.57+03:10:09.6	sdO	18.60	19.05	19.56	
13:27:56.78+43:28:17.0	sdOB	18.39	18.20	18.20	
13:28:50.85+28:29:17.5	sdO?	18.23	18.61	19.06	
13:29:28.51+13:49:54.8	sdOB	18.76	19.14	19.69	
13:32:02.60+52:37:34.9	sdO	17.86	18.28	18.81	
13:35:51.62+62:41:09.5	sdOB+X	15.29	15.26	15.19	
13:36:11.01−01:11:55.9	sdOB	18.03	18.33	18.81	
13:42:26.53+29:03:43.4	sdO	18.80	19.18	19.70	
13:45:45.23−00:06:41.6	sdOB	17.39	17.54	17.78	large errors
13:46:13.77+15:03:52.9	sdOB	19.68	20.02	20.47	
13:50:37.58+29:07:18.1	sdO	19.02	19.41	19.94	
13:51:44.13+12:42:55.8	sdO	18.76	19.16	19.66	
13:53:51.68+16:51:25.9	sdO	18.36	18.79	19.32	
13:57:07.34+01:04:54.4	sdOB	17.24	17.24	17.34	
13:58:31.62+63:14:55.4	sdO	17.94	18.35	18.87	
14:01:18.73−01:20:24.8	sdOB	16.67	16.95	17.42	large errors
14:02:02.53+02:54:07.1	sdO	19.67	20.13	20.64	
14:02:47.52+49:33:21.4	sdO	18.01	18.50	19.02	
14:03:17.26+22:10:19.0	sdOB+X	16.05	15.91	15.89	
14:04:43.03+05:21:30.6	sdOB	19.19	19.52	20.01	
14:07:47.84+23:54:24.3	sdOB+X	15.95	16.09	16.27	
14:09:16.11+38:28:32.1	sdO+X	15.91	16.03	16.19	
14:15:36.40+01:17:18.2	sdO+X	16.45	16.88	17.31	
14:15:56.67−00:58:14.8	sdOB	18.02	18.39	18.76	
14:20:17.21+51:39:04.1	sdO	18.23	18.63	19.16	
14:21:04.81+17:36:28.8	sdOB+X	16.18	16.26	16.43	
14:21:38.17+07:53:19.5	sdOB+X	14.69	14.88	15.14	
14:22:41.90+51:35:37.9	sdO+X	15.37	15.70	15.70	
14:29:30.86+02:29:28.3	sdOB	18.91	19.21	19.70	

Table D.3 continued (3).

SDSS J	spectral	SDSS Photometry			
(2000)	class	u	g	r	
14:29:39.35+15:26:23.6	sdO	18.41	18.79	19.22	
14:41:07.00+14:42:33.4	sdO	18.10	18.56	19.07	
14:46:57.13+58:09:20.1	sdOB+X	15.85	15.66	15.66	
14:56:57.72+49:53:10.8	sdOB+X	15.15	15.22	15.38	
14:57:36.81+59:29:27.6	sdO	18.94	19.41	19.96	
14:58:11.90+01:21:40.2	sdO	18.23	18.63	19.07	
15:00:53.98+02:51:43.2	sdO	19.07	19.46	19.90	
15:02:12.12−02:45:57.7	sdOB+X	14.98	14.87	14.87	
15:06:33.07+20:59:07.5	sdOB	18.29	18.55	19.03	
15:12:31.29+00:53:17.7	sdOB	17.70	18.00	18.47	
15:12:46.56+07:15:17.3	sdO	18.96	19.41	19.93	
15:16:40.23+22:57:12.6	sdOB+X	14.96	15.00	15.21	
15:18:08.47+04:10:43.7	sdOB+X	15.15	15.28	15.45	
15:18:42.54+56:49:21.8	sdO	17.61	18.07	18.61	
15:19:39.26+39:46:26.3	sdOB	18.58	18.78	19.27	
15:20:00.81+07:13:48.8	sdOB+X	16.02	16.13	16.36	
15:21:38.60+40:35:02.6	sdO	19.79	20.23	20.60	
15:23:06.95+08:05:41.1	sdOB	18.44	18.79	19.29	
15:25:38.15+13:42:01.0	sdOB	18.00	18.34	18.73	
15:25:53.47+43:41:27.7	sdOB+X	15.07	15.10	15.16	
15:27:07.20+10:16:12.5	sdOB+X	16.18	16.13	16.22	
15:27:08.31+00:33:08.3	sdO	18.27	18.59	19.05	
15:32:17.24+45:46:21.0	sdOB+X	16.27	16.42	16.63	
15:38:42.85+09:34:42.3	sdO+X	15.52	15.68	15.84	
15:39:35.00+13:38:01.0	sdO	17.50	17.92	18.36	
15:39:59.51+16:51:08.1	sdO	17.93	17.94	18.01	
15:42:10.89+01:55:57.2	sdOB+X	16.01	15.91	15.91	
15:42:45.29+12:38:45.2	sdOB	18.92	19.18	19.61	
15:43:53.55+36:11:42.1	sdOB+X	16.34	16.30	16.42	
15:46:41.88+06:25:39.2	sdOB+X	17.46	17.69	17.91	
15:47:58.65+37:17:47.0	sdO	18.37	18.80	19.24	
15:51:19.56+06:49:04.3	sdOB+X	16.04	15.95	16.00	
15:55:51.24+13:32:28.8	sdO	18.59	18.91	19.29	
15:58:19.40+12:30:14.2	sdOB	18.96	19.24	19.72	
16:00:43.60+07:48:02.8	sdO+X	17.22	17.43	17.61	the one pulsating sdO
16:01:09.88+19:32:15.4	sdO+X	16.32	16.01	16.03	
16:04:01.09+00:08:26.0	sdOB	18.37	18.49	18.83	
16:04:50.44+05:19:09.2	sdOB	18.08	18.34	18.69	
16:07:15.22+09:46:29.5	sdO	18.57	18.99	19.46	
16:11:09.13+10:57:05.7	sdO	18.18	18.61	19.05	
16:11:24.41+03:17:17.6	sdOB+X	17.17	17.28	17.44	
16:12:09.12+53:26:41.9	sdO	20.03	20.32	20.61	
16:12:30.86+00:42:37.0	sdO	18.08	18.38	18.79	
16:12:31.90+17:14:41.1	sdO	18.99	19.39	19.89	
16:12:55.04+05:11:52.1	sdOB	18.50	18.66	18.85	

Table D.3 continued (4).

SDSS J	spectral	SDSS Photometry			
(2000)	class	u	g	r	
16:13:40.08+16:03:45.2	sdO	19.24	19.59	20.03	
16:14:31.33+00:40:04.5	sdO	18.35	18.72	19.16	
16:14:37.93+23:17:05.8	sdOB	17.04	17.06	17.09	Balmer too weak for fit
16:15:52.74+14:51:55.2	sdOB	18.20	18.65	19.11	
16:15:56.98+17:31:10.6	sdOB+X	16.61	16.36	16.28	
16:16:03.28+10:12:10.6	sdO	17.19	17.62	18.08	
16:16:31.28−00:38:53.2	sdOB+X	16.56	16.72	16.94	
16:19:15.35−00:56:15.9	sdOB	18.91	19.13	19.46	
16:20:51.03+37:50:59.3	sdOB	18.61	18.76	18.96	
16:20:51.18+63:42:28.9	sdOB	18.92	19.26	19.75	
16:27:29.35+36:29:02.5	sdO	19.15	19.59	20.04	
16:34:16.76+16:01:11.1	sdO	18.94	19.25	19.72	
16:34:53.04+39:47:58.9	sdO	18.08	18.58	19.72	
16:35:22.38+63:36:46.7	sdOB	19.84	20.13	20.56	
16:35:32.55+00:29:54.4	sdOB	19.18	19.41	19.83	
16:36:05.36+13:04:04.1	sdO	18.26	18.59	19.04	
16:37:08.03+13:19:35.1	sdOB+X	18.09	17.81	17.71	
16:37:23.59+31:13:04.4	sdO	18.51	18.83	19.21	
16:42:14.21+42:52:33.9	sdOB+X	15.83	15.68	15.71	
16:46:23.93+34:46:08.0	sdOB+X	16.78	16.59	16.63	
16:50:22.05+31:27:49.7	sdOB+X	15.75	15.91	16.03	
16:54:25.59+22:24:49.4	sdO	18.86	19.21	19.62	
16:57:32.52+21:56:60.0	sdOB	18.57	18.82	19.27	
16:58:41.83+41:31:15.5	sdOB+X	15.83	15.93	16.14	
16:59:00.75+28:47:14.4	sdOB	19.46	19.80	20.25	
17:00:45.09+39:18:30.3	sdOB	17.57	17.95	18.43	
17:01:17.61+18:46:31.7	sdOB+X	17.44	17.50	17.63	
17:03:38.69+22:36:37.2	sdOB+X	15.24	15.10	15.09	
17:05:56.15+36:32:21.9	sdO	16.85	17.20	17.76	
17:06:10.45+30:21:30.3	sdO	18.81	19.16	19.71	
17:15:46.23+61:59:29.7	sdO	17.81	18.17	18.72	
17:17:22.09+58:05:58.8	sdOB+X	16.50	16.67	16.91	
17:23:38.53+60:14:44.1	sdOB+X	15.50	15.50	15.61	
17:33:18.81+55:26:38.9	sdO	17.66	18.08	18.57	
17:40:48.41+25:23:06.0	sdO?	18.63	19.07	19.59	
18:41:09.99+40:50:53.0	sdOB+X	16.16	16.31	16.46	
18:57:14.73+18:25:57.6	sdO	19.04	19.08	19.18	
19:23:24.64+38:02:51.8	sdOB+X	17.24	17.49	17.54	
19:25:58.40+38:32:52.4	sdOB	18.05	18.34	18.65	H vs He
20:26:00.96+12:50:44.8	sdOB	18.72	18.92	19.33	
20:37:29.93+00:19:54.0	sdOB+X	15.94	15.98	16.12	
20:52:54.68−00:50:31.8	sdOB	18.05	18.03	18.05	
21:13:39.69+10:06:40.4	sdOB+X	16.42	16.39	16.51	
21:20:53.72−07:15:44.1	sdOB+X	18.04	17.82	17.74	
21:29:06.03+00:45:09.2	sdOB+X	15.43	15.62	15.69	

Table D.3 continued (5).

SDSS J	spectral	SDSS Photometry		
(2000)	class	u	g	r
21:30:54.60−00:41:17.3	sdOB	17.51	17.85	18.32
21:38:08.11+10:57:41.7	sdOB+X	17.21	17.23	17.35
21:39:40.90−00:10:28.9	sdOB+X	17.32	17.29	17.35
22:25:15.34−01:11:57.0	sdOB	18.09	18.43	18.80
22:28:17.66−07:59:47.9	sdOB	17.66	17.46	17.49
22:39:55.58−00:52:40.1	sdO+X	14.63	14.94	15.25
22:48:00.88+13:01:46.0	sdO	18.62	19.08	19.52
23:19:56.09−09:39:37.6	sdOB+X	16.80	16.97	17.13

Appendix E

Metal lines in the FEROS spectra

Metal lines found in the FEROS spectra between $\approx 3\,750$ and $\approx 5\,876\,\text{Å}$.

Table E.1: Spectral lines identified in the five bright sdO stars.

Wavelength [Å]	HD 127493		CD −31 4800		CD −24 9052		UVO 0832 −01		UVO 0904 −02	
3745.95	N	III								
3753.83							Ne	II		
3754.67	N	III					N	III		
3757.23							O	III		
3759.88							O	III		
3761.17							O	III		
3762.44	Si	IV					Si	IV		
3766.26	Ne	II					Ne	II		
3771.05	N	III					N	III		
3773.15	Si	IV					Si	IV		
3774.03							O	III		
3777.14	Ne	II					Ne	II		
3792.97	N	III								
3793.55	Ne	II								
3794.65	S	III								
3796.11	Si	III								
3800.02							Ne	II		
3806.70	Si	III								
3813.73									O	II
3818.44							Ne	II		
3823.93									N	IV
3829.75	Ne	II					Ne	II	Ne	II
3838.37	N	II								
3844.51	C	III					C	III		
3848.21	Mg	II								
3856.07			N	II					N	II
3860.53							O	II		
3861.50							O	III		
3863.06									C	II

127

Table E.2: Table E.1 continued (1).

Wavelength [Å]	HD 127493		CD −31 4800		CD −24 9052		UVO 0832 −01		UVO 0904 −02	
3876.19							C	II		
3876.41							C	II	C	II
3878.22							C	II		
3879.60									C	II
3883.80							C	III	C	III
3885.99							C	III	C	III
3889.18							C	III		
3892.29	S	II								
3909.66	Ne	II								
3918.97					C	II				
3919.00	N	II								
3919.01			N	II	N	II				
3920.68							C	II		
3922.08	C	II								
3924.47	Si	III	Si	III						
3928.61			S	III	S	III				
3934.50	N	III	N	III	N	III	N	III		
3938.52	N	III	N	III	N	III	N	III	N	III
3942.87	O	II								
3942.88	N	III	N	III	N	III	N	III	N	III
3948.15							C	II		
3949.34					O	II				
3951.51					P	III				
3954.36	O	II			O	II			O	II
3955.85	N	II	N	II						
3957.64			P	III						
3961.57							O	III		
3966.32							O	II		
3976.88					Fe	III				
3979.42	Fe	III	Fe	III	Fe	III				
3981.18	Si	III			Si	III				
3990.91	S	II								
3995.00	N	II	N	II	N	II				
3996.50	N	III			N	III				
3998.63	N	III	N	III	N	III	N	III	N	III
4003.58	N	III	N	III	N	III	N	III		
4007.46	O	II			O	II				
4010.24									Si	III
4012.63					Ti	III				
4017.27	C	II			C	II				
4032.48	O	II			O	II				
4035.08	N	II	N	II	N	II	N	II		
4038.25					Mg	III	Mg	III		
4041.31	N	II	N	II	N	II	N	II		
4043.50									C	II
4043.53	N	II	N	II	N	II				
4044.75	N	II	N	II						
4044.94	O	II			O	II				
4053.11	Fe	III								
4054.52	O	II			O	II			O	II

Table E.3: Table E.1 continued (2).

Wavelength [Å]	HD 127493		CD −31 4800		CD −24 9052		UVO 0832 −01		UVO 0904 −02	
4056.06	C	III	C	III	C	III	C	III	C	III
4057.00			N	II	N	II	N	II	N	II
4057.76	N	IV	N	IV	N	IV	N	IV	N	IV
4059.27			P	III			P	III	P	III
4067.94			C	III			C	III	C	III
4068.91	C	III	C	III			C	III	C	III
4070.30	C	III	C	III			C	III	C	III
4072.15					O	II				
4073.05	N	II	N	II	N	II				
4074.89			C	II	C	II				
4075.86	O	II					O	II		
4076.00					C	II	C	II		
4078.84	O	II	O	II	O	II				
4081.02	O	III			O	III				
4082.28	N	II	N	II						
4085.11	O	II			O	II	O	II		
4087.35	N	II							N	II
4088.86	Si	IV	Si	IV	Si	IV	Si	IV	Si	IV
4097.33	N	III	N	III	N	III	N	III	N	III
4098.88							Ti	III		
4102.90			N	II						
4103.43	N	III	N	III	N	III	N	III	N	III
4106.02									O	II
4116.10	Si	IV	Si	IV	Si	IV	Si	IV	Si	IV
4118.60					O	III	O	III		
4122.05							C	III	C	III
4131.63	N	III	N	III	N	III			N	III
4133.67	N	II	N	II	N	II	N	II		
4134.91							N	III	N	III
4146.78	N	III	N	III	N	III	N	III		
4150.17			Al	III						
4150.67			Ne	II						
4152.34	Fe	IV			Fe	IV				
4152.50							C	III	C	III
4156.50							C	III	C	III
4162.90							C	III	C	III
4164.79	Fe	III	Fe	III	Fe	III				
4166.86	Fe	III			Fe	III			Fe	III
4171.61			N	II						
4171.77	O	III								
4173.09							C	III		
4173.51			N	II						
4174.26	Fe	III			Fe	III				
4176.16	N	II	N	II						
4179.67	N	II	N	II						
4181.17	N	II	N	II	N	II				
4182.59			N	IV						
4184.23	Ca	III			Ca	III				
4185.44			O	II						
4186.90	C	III	C	III			C	III		

Table E.4: Table E.1 continued (3).

Wavelength [Å]	HD 127493		CD −31 4800		CD −24 9052		UVO 0832 −01		UVO 0904 −02	
4192.51					O	II				
4195.76	N	III	N	III	N	III	N	III		
4200.10	N	III	N	III	N	III	N	III		
4207.49	Ti	III	Ti	III						
4208.88							Fe	IV		
4212.40	Si	IV	Si	IV	Si	IV	Si	IV		
4215.77	N	III	N	III	N	III	N	III		
4217.17	Ne	II	Ne	II	Ne	II	Ne	II		
4218.52							Ti	III		
4219.75	Ne	II	Ne	II			Ne	II		
4220.28	Ti	III			Ti	III				
4220.89			Ne	II			Ne	II		
4222.20					P	III				
4224.13	Ti	III			Ti	III				
4226.14							Fe	III		
4227.74	N	II	N	II						
4231.64	Ne	II	Ne	II			Ne	II		
4233.74	Ca	III			Ca	III	Ca	III		
4233.85	Ne	II								
4235.56	Fe	III			Fe	III				
4237.00	N	II	N	II	N	II	N	II		
4239.95							Ne	II		
4240.74	Ca	III			Ca	III				
4241.78	N	II	N	II	N	II				
4243.89	Ti	III			Ti	III				
4246.72	P	III			P	III				
4247.31							C	III		
4248.54					Ti	III				
4249.66			P	IV	P	IV				
4250.65	Ne	II	Ne	II			Ne	II		
4253.59			S	III	S	III				
4255.38							C	III		
4256.45							C	III		
4257.18	Ne	II	Ne	II	Ne	II	Ne	II	Ne	II
4257.82			Ne	II			Ne	II	Ne	II
4260.76					Ti	III				
4261.90					Ti	III				
4267.02							C	II		
4267.27							C	II		
4267.38			Ne	II						
4275.99	O	II			O	II				
4279.72	Fe	III								
4282.96					O	II				
4284.39	Ca	III	Ca	III			Ca	III		
4284.99			S	III	S	III				
4286.16	Fe	III	Fe	III	Fe	III				
4288.66	Ti	III	Ti	III	Ti	III				
4288.82					O	II				
4289.25							Ti	III		
4290.37					Ne	II	Ne	II		

Table E.5: Table E.1 continued (4).

Wavelength [Å]	HD 127493		CD −31 4800		CD −24 9052		UVO 0832 −01		UVO 0904 −02	
4290.60							Ne	II		
4294.78	O	II	O	II	O	II	O	II		
4295.42					Ti	III				
4296.86					Fe	III				
4301.94			Si	III						
4302.81	Ca	III								
4302.86	O	II			O	II				
4303.07					O	II				
4303.83	O	II	O	II						
4304.08	O	II			O	II				
4309.00					O	II				
4310.36	Fe	III			Fe	III				
4312.80			C	II	C	II				
4314.10	Si	IV	Si	IV	Si	IV				
4315.39							O	II		
4317.42							C	II		
4317.98	Ti	III			Ti	III	Ti	III		
4318.78	N	III	N	III	N	III				
4319.56					Ti	III				
4319.63					O	II				
4321.39	N	III	N	III	N	III	N	III		
4323.68	Fe	III								
4325.43			N	III	N	III	N	III	N	III
4325.70							C	III		
4327.69					N	III				
4328.18	Si	IV	Si	IV	Si	IV	Si	IV		
4328.25					Ti	III				
4332.91			N	III	N	III	N	III		
4345.68	N	III								
4345.81			N	III			N	III		
4349.43			O	II						
4351.11	N	III	N	III						
4352.28	Ti	III			Ti	III				
4358.44									O	II
4358.89	Ti	III							Ti	III
4361.85							C	III	C	III
4366.90							O	II		
4367.68							Ti	III		
4367.97					C	II				
4368.14					C	II				
4368.56							Ti	III		
4369.77	Ne	II	Ne	II			Ne	II		
4372.49			C	II	C	II				
4372.81	Fe	III								
4374.28					C	II				
4377.98	Ne	II	Ne	II						
4379.20			N	III	N	III	N	III	N	III
4379.50									Ne	II
4380.73					Ti	III				
4382.90							C	III	C	III

Table E.6: Table E.1 continued (5).

Wavelength [Å]	HD 127493		CD −31 4800		CD −24 9052		UVO 0832 −01		UVO 0904 −02	
4384.70									O	II
4391.99	Ne	II	Ne	II			Ne	II		
4397.99	Ne	II	Ne	II			Ne	II	Ne	II
4399.59	Ca	III								
4403.45	Ti	IV			Ti	IV				
4403.73	Si	IV								
4406.29					Ca	III				
4409.30	Ne	II	Ne	II	Ne	II	Ne	II		
4411.52			C	II			C	II		
4412.59	Ne	II								
4413.21	Ne	II	Ne	II	Ne	II	Ne	II		
4421.38	Ne	II	Ne	II			Ne	II		
4422.62	N	V			N	V				
4427.21	N	II	N	II						
4428.54	Ne	II	Ne	II			Ne	II		
4429.60	Ne	II	Ne	II			Ne	II		
4430.90	Fe	III	Fe	III			Fe	III		
4432.26							Ne	II		
4432.74	N	II	N	II	N	II				
4433.48	N	II	N	II						
4440.29									C	IV
4440.80	Ne	II			Ne	II				
4441.50	C	IV					C	IV	C	IV
4441.99			N	II						
4443.52	O	II	O	II						
4445.58	Mg	III	Mg	III			Mg	III		
4446.44	Ne	II	Ne	II			Ne	II		
4447.03	N	II	N	II	N	II	N	II		
4448.19							O	II		
4453.97							O	II		
4457.05	Ne	II					Ne	II		
4463.40					Mg	III				
4466.23					O	II				
4467.21					O	II				
4479.03			Mg	III			Mg	III		
4479.91	N	IV	N	IV	N	IV	N	IV		
4481.2	Mg	II	Mg	II	Mg	II	Mg	II	Mg	II
4482.87			Si	III	Si	III	Si	III		
4486.34	Si	III								
4488.44	Si	III	Si	III	Si	III				
4491.23	O	II								
4492.27	S	II								
4493.37					O	III				
4495.87			N	IV						
4499.12							Ne	II		
4506.00					C	II				
4507.56	N	II	N	II						
4510.92	N	III	N	III	N	III	N	III	N	III
4511.58			Ti	III			Ti	III		
4512.56			Al	III			Al	III		

Table E.7: Table E.1 continued (6).

Wavelength [Å]	HD 127493		CD −31 4800		CD −24 9052		UVO 0832 −01		UVO 0904 −02	
4514.86	N	III	N	III	N	III	N	III		
4515.80	C	III			C	III	C	III	C	III
4516.80	C	III	C	III			C	III	C	III
4518.14	N	III	N	III	N	III	N	III	N	III
4522.66			Ne	II			Ne	II		
4523.56	N	III	N	III	N	III	N	III		
4527.29					O	III				
4527.86	N	III	N	III	N	III	N	III		
4528.54	N	III	N	III	N	III				
4529.19	Al	III	Al	III			Al	III		
4530.40	N	II	N	II						
4530.86	N	III	N	III	N	III				
4532.78							O	III		
4534.58	N	III	N	III	N	III	N	III		
4535.05	N	III	N	III	N	III				
4535.57	Ne	II								
4539.70	N	III	N	III						
4544.80	N	III	N	III	N	III				
4545.30	Mg	II								
4546.33	N	III	N	III	N	III	N	III		
4547.30	N	III	N	III			N	III		
4552.65	Si	III	Si	III	Si	III				
4554.00	Si	III			Si	III				
4555.39					O	III				
4555.46					Ti	III				
4557.91			O	III						
4558.94			O	II						
4563.18					O	II				
4565.00					N	V				
4567.87	Si	III	Si	III						
4569.01			Ne	II			Ne	II		
4569.26					O	III				
4570.80	Ti	III	Ti	III	Ti	III				
4572.20	Ti	III			Ti	III				
4572.85			Ti	III			Ti	III		
4574.49							Ne	II		
4574.78	Si	III	Si	III			Si	III		
4575.31					Ne	II				
4579.82					N	III				
4580.35							Ne	II		
4581.58	Mg	II	Mg	II	Mg	II				
4582.18	P	II								
4588.13							Ne	II		
4589.18					N	III				
4591.98			N	III	N	III				
4592.00	N	III								
4595.50					Ti	III				
4596.18					O	II				
4598.01			S	IV	S	IV				
4601.48	N	II	N	II	N	II				

Table E.8: Table E.1 continued (7).

Wavelength [Å]	HD 127493		CD −31 4800		CD −24 9052		UVO 0832 −01		UVO 0904 −02	
4602.13	O	II			O	II				
4602.93					S	IV				
4605.16	N	III								
4606.25							N	IV		
4607.15	N	II	N	II						
4609.70					Al	III				
4610.55	N	III	N	III	N	III	N	III		
4611.27			Si	IV	Si	IV				
4613.14							O	II		
4613.87	N	II	N	II	N	II				
4615.41	N	III	N	III	N	III	N	III		
4618.11	Ti	IV			Ti	IV				
4618.85									C	II
4619.66							Si	III	Si	III
4619.98	N	V	N	V	N	V				
4621.04	N	III								
4621.25					O	II				
4621.39	N	II	N	II						
4623.05	N	III	N	III						
4624.42							Fe	III	Fe	III
4625.71									C	II
4627.85							Ne	II		
4630.54	N	II	N	II	N	II				
4631.24	Si	IV	Si	IV	Si	IV	Si	IV	Si	IV
4634.14	N	III	N	III	N	III	N	III	N	III
4638.28	Si	III	Si	III	Si	III	Si	III		
4640.64	N	III	N	III	N	III	N	III	N	III
4641.90	N	III	N	III	N	III	N	III	N	III
4643.09	N	II	N	II						
4647.00									C	IV
4647.40	C	III	C	III			C	III	C	III
4650.25	C	III	C	III			C	III	C	III
4651.50	C	III	C	III			C	III	C	III
4652.86	Ti	III					Ti	III		
4654.32	Si	IV	Si	IV	Si	IV	Si	IV	Si	IV
4658.30					C	IV	C	IV	C	IV
4659.06							C	III		
4659.17			S	IV	S	IV				
4663.53					C	III	C	III	C	III
4665.87			Si	III						
4665.90							C	III	C	III
4667.14	Si	IV								
4667.28	N	II	N	II	N	II				
4670.60							N	IV	N	IV
4673.40			Ti	III	Ti	III				
4673.95			C	III			C	III	C	III
4674.98			N	II						
4677.06	O	II			O	II				
4699.22							O	II		
4702.50	N	II			N	II	N	II		

Table E.9: Table E.1 continued (8).

Wavelength [Å]	HD 127493		CD −31 4800		CD −24 9052		UVO 0832 −01		UVO 0904 −02	
4707.48	O	II			O	II				
4714.94					Ne	II				
4716.65	Si	III								
4719.37					Ne	II				
4721.58					N	II				
4737.00					C	IV				
4739.66							C	III	C	III
4752.49					N	IV				
4760.11					Ti	III				
4767.36					Ti	III				
4781.95					Ne	II				
4786.00					C	IV	C	IV	C	IV
4788.13	N	II	N	II	N	II				
4793.50			Ti	III						
4803.29	N	II	N	II	N	II				
4810.29			N	II	N	II				
4812.08			N	II	N	II	N	II		
4813.29			Si	III	Si	III				
4821.52	Mg	III								
4821.71					Si	III				
4828.97	Si	III	Si	III						
4832.24									C	II
4861.27			N	III						
4867.15	N	III	N	III	N	III	N	III		
4873.60	N	III	N	III	N	III				
4884.14	N	III	N	III	N	III	N	III		
4896.58	N	III								
4897.14	N	III	N	III						
4899.10	N	III	N	III	N	III	N	III		
4904.78	N	III	N	III	N	III	N	III		
4918.37									C	II
4936.37					Ne	II				
4950.11	Si	IV	Si	IV						
4952.00			N	V						
4973.49					N	IV				
4987.38			N	II						
4991.22			N	II						
4991.97	S	II								
4994.36	N	II	N	II	N	II				
5001.13	N	II	N	II						
5001.47	N	II	N	II	N	II	N	II		
5002.69	N	II	N	II	N	II				
5005.15	N	II	N	II	N	II	N	II		
5007.32	N	II	N	II	N	II				
5008.80					Ti	III				
5010.62	N	II	N	II	N	II				
5011.31	N	II	N	II						
5012.04	N	II	N	II						
5018.40							C	IV	C	IV
5018.92					Ti	III				

Table E.10: Table E.1 continued (9).

Wavelength [Å]	HD 127493		CD −31 4800		CD −24 9052		UVO 0832 −01		UVO 0904 −02	
5020.43					Ti	III				
5023.05	N	II	N	II						
5025.66			N	II						
5037.00	C	II			C	II	C	II		
5045.10	N	II	N	II	N	II				
5063.66					O	III				
5066.75					N	III				
5083.80							Ti	III		
5084.92	N	III								
5109.81					Ti	III				
5126.96									C	II
5127.32									Fe	III
5127.35									Ti	III
5139.21									C	II
5160.03					C	III				
5172.32					N	II				
5173.38	N	II								
5175.89	N	II	N	II	N	II				
5179.44	N	II	N	II	N	II				
5180.34			N	II						
5183.21			N	II	N	II				
5184.97			N	II						
5186.17					N	II				
5200.41	N	IV								
5204.28	N	IV	N	IV	N	IV	N	IV		
5219.32	S	III	S	III						
5243.30					Fe	III				
5244.66							C	III		
5247.49					Ti	III				
5249.11							C	III	C	III
5253.55							C	III	C	III
5270.57	N	III	N	III	N	III				
5272.56							C	III	C	III
5272.68	N	III	N	III	N	III				
5282.43	N	III								
5297.75	N	III	N	III						
5298.95	N	III	N	III						
5314.35	N	III	N	III	N	III				
5320.82	N	III	N	III	N	III	N	III		
5320.96	N	II								
5327.18	N	III	N	III			N	III		
5340.20			N	II						
5345.88							C	III		
5352.39	Ti	III								
5352.46			N	III						
5359.93							C	III		
5398.93					Ti	IV				
5462.58	N	II			N	II				
5480.10			N	II						
5481.31							Ti	III		

Table E.11: Table E.1 continued (10).

Wavelength [Å]	HD 127493		CD −31 4800		CD −24 9052		UVO 0832 −01		UVO 0904 −02	
5488.25			S	IV	S	IV	S	IV		
5492.43					Ti	IV				
5495.67	N	II	N	II						
5497.75			S	IV	S	IV	S	IV		
5530.24	N	II	N	II						
5535.36	N	II	N	II	N	II	N	II		
5536.00							C	II		
5541.19					P	II				
5543.47	N	II								
5592.25			O	III			O	III		
5599.25			Si	III						
5666.63	N	II	N	II	N	II				
5676.02	N	II	N	II	N	II				
5679.56	N	II	N	II	N	II				
5686.21	N	II	N	II						
5695.90			C	III			C	III	C	III
5696.60			Al	III						
5696.60	Al	III								
5710.77	N	II	N	II	N	II				
5722.73	Al	III								
5736.93			N	IV						
5739.73	Si	III	Si	III						
5747.29			N	II						
5767.43			N	II						
5801.33			C	IV			C	IV	C	IV
5811.98			C	IV			C	IV	C	IV
5820.57	N	III	N	III	N	III				
5826.43							N	IV	N	IV
5847.94	N	III			N	III				
5857.90							C	III		
5871.60							C	III		
5880.56							C	III		
5889.97							C	II		
5894.10							C	III		
5901.00							Fe	III		
5927.81							N	II		
5931.78							N	II		

Appendix F

Acknowledgements

First I would like to thank my parents for their patience over all the years. Without their generous support I would not have managed to finish my studies.

I am grateful to Uli Heber for the opportunity to work on an interesting field. His comments, suggestions and advises were most helpful. Together with Jörn Wilms the institute has two great directors.

Markus Firnstein's support and friendship throughout my whole university life cannot be emphasised enough. He was a valuable and reliable partner for our lab courses and homework assignments.

Stephan Geier always is valuable partner for discussions, within the field of astronomy as well as general topics. He is an abundant source of ideas. Norbert Przybilla with his unfailing knowledge in every field of astronomy, but especially in stellar atmospheres was a great help. Fernanda and Alfred were always available to answer questions. I thank Thomas Rauch for providing me with carbon and nitrogen model atoms, Simon Hügelmeyer and Stefan Dreizler for help with TMAP. In analysing the remaining stars from DR7, Sebastian Müller was a valuable help. Greetings to Simon O'Toole, who guided my first steps into astronomy.

Heinz Edelmann was a very valuable colleague and extremely helpful. His remarkable dedication to astronomy is astonishing. And, in spite of our disagreements over various movies and TV series, I always appreciated his opinion!

Stefan Neßlinger had to endure quite a lot of questions about the downhill simplex method and bootstrapping. His patience is really appreciated. Live long and prosper!

Thanks to Mrs Bues, for all her suggestions and helping advice. Greetings also to Rainer, Manfred and Ingo for maintaining our computers, and for their tireless commitment to the institute.

Finally, I would like to say thanks to the whole institute for the support and the amicable environment provided. It was a pleasure working with you!

I wish to say "Hello" and "Thanks" to the following people (in no particular order) for various reasons: Birte and Jörn, Konni, Moritz, Christian, Steffen, Jasmin, Christine Förtsch, Maria, Peter Banzer, Philipp, Jörg and Martin.

For this thesis I extensively used the NASA's Astrophysics Data System Abstract Service. Large parts of my data come from SDSS, the Sloan Digital Sky Survey. Funding for the SDSS and SDSS-II was provided by the Alfred P. Sloan Foundation, the Participating Institutions, the National Science Foundation, the U.S. Department of Energy, the National

Bibliography

Abazajian K., Adelman-McCarthy J. K., Agüeros M. A., et al., 2003, AJ, **126**, 2081–2086

Abazajian K., Adelman-McCarthy J. K., Agüeros M. A., et al., 2004, AJ, **128**, 502–512

Abazajian K., Adelman-McCarthy J. K., Agüeros M. A., et al., 2004, AJ, **129**, 1755–1759

Abazajian K., et al., for the Sloan Digital Sky Survey, 2008, arXiv:0812.0649

Adelman-McCarthy J. K., Agüeros M. A., Allam S. S., et al., 2006, ApJS **162**, 38–48

Adelman-McCarthy J. K., Agüeros M. A., Allam S. S., et al., 2007, ApJS **172**, 634–644

Adelman-McCarthy J. K., Agüeros M. A., Allam S. S., et al., 2007, ApJS **175**, 297–313

Altmann M., Edelmann H. and K. S. de Boer, 2004, A&A **414**, 181–201

Asplund M., Grevesse N and Sauval A. J., 2005, in ASP Conf. Ser. **336**: *Cosmic Abundances as Records of Stellar Evolution and Nucleosynthesis in honor of David L. Lambert*, eds. T. G. Barnes & F. N. Bash, (San Francisco), 25

Auer L. H. & Mihalas D., 1969, ApJ **158**, 641–655

Bauer F. and Husfeld D., 1995, A&A **300**, 481–492

Brassard P., Fontaine G., Billères M., Charpinet S., Liebert J. and Saffer R. A., 2001, ApJ **563**, 1013–1030

Buzzoni A. and Gonzáles-Lópezlira R. A., 2008, ApJ, **686**, 1007–1018

Brown T. M., Sweigart A. V., Lanz T. Landsman W. B. and Hubeny I., 2001, ApJ, **562**, 368–393

Brown D., Salaris M., Cassisi S. and Pietrinferi A., 2008, Mem. S. A. It., **79**, 579–583

Buser R., Rong J. & Karaali S., 1999, A&A, **348**, 98–112

Cassisi S., Schlattl H., Salaris M. and Weiss A., 2003, ApJ, **582**, 43–46

Castellani M. and Castellani V., 1993, ApJ, **407**, 649–656

Castellani M., Castellani V. and Prada Moroni, 2006, A&A, **457**, 569–573

Catelan M., 2007, in AIP Conference Proceedings **930**: *GRADUATE SCHOOL IN AS-TRONOMY: XI Special Courses at the National Observatory of Rio de Janeiro (XI CCE)*, 39-90

Catelan M., 2007, arXiv:0708.2445 [astro-ph]

Charpinet S., Fontaine G., Brassar P. and Dorman B., 1996, Astrophysics and Space Science, **471**, 103–106

Clayton, D. D., 1983, *Principles of Stellar Evolution and Nucleosynthesis*, University of Chicago Press

D'Cruz N. L., Dorman B., Rood R. T. and O'Connell R. W., 1996, ApJ, **466**, 359–371

Decker H., D'Odorico S., Kaufer A., Delabre B. and Kotzlowski H., 2000, in Proc SPIE, **4008**, *Optical and IR Telescope Instrumentation and Detectors*, eds. Iye M. & Moorwood A. F., 543

Dorman B., Rood R. T., and O'Connell R. W., 1993, ApJ, **419**, 596–614

Dreizler S., 1993, A&A **273**, 212–220

Dreizler S., 2003, in ASP Conf. Ser. **288**: Stellar Atmosphere Modeling, eds. I Hubeny, D. Mihalas & K. Werner, (San Francisco: ASP), 69–82

Driebe T., Schönberner D., Blöcker T., and Herwig F., 1998, A&A, **339**, 123–133

Driebe T., Blöcker T., Schönberner D., and Herwig F., 1999, A&A, **350**, 89–100

Drilling J. S., and Heber U., 1987, in *2nd Conference on Faint Blue Stars*, (Schenectady: L. Davis Press), 603–606

Drilling J. S., Moehler S., Jeffery C. S., Heber U. and Napiwotzki R., 2003, in *The Garrison Festschrift: held in Tucson, Arizona, at the Arizona Inn June 10–11, 2002*, eds. R. O. Gray, C. J. Corbally & A. G. D. Philip, (Schenectady: L. Davis Press), 27–38

Edelmann H., Heber U., Hagen H.-J., Lemke M., Dreizler S. Napiwotzki R. and Engels D., 2003, A&A, **400**, 939–950

Edelmann H., Heber U., Altmann M., Karl C. and Lisker T., 2005, A&A, **442**, 1023–1030

Edelmann H., Heber U. and Napiwotzki R., 2006, Baltic Astronomy, **15**, 103–106

Espey B. R. and Crowley C., 2008, arXiv:0803.1170 [astro-ph]

Fan X., Strauss M. A., Schneider D. P., et al., 2003, AJ, **125**, 1649–1659

Fonatine G., Brassard P., Green E. M., Chayer P., Charpinet S., Andersen M and Portouw J., 2008, A&A, **486**, 39–42

Green R. F., Schmidth M. and Liebert J., 1986, AJS, **61**, 305–352

Greenstein J. L. and Sargent A. I., 1974, ApJS, **28**, 157–209

Geier S., Nesslinger S., Heber U., Przybilla N., Napiwitzki R. and Kudritzki R.-P., 2007, A&A, **464**, 299–307

Geier S., Karl C. A., Edelmann H., Heber U. and Napiwotzki R., 2007, in ASP Conf. Ser. **372**: *15th European Workshop on White Dwarfs*, eds. R. Napiwotzki and M. R. Burleigh, (San Francisco), 401–406

Geier S., Karl C., Edelmann H., Heber U. and Napiwotzki R., 2008, in ASP Conf. Ser. **392**: *Hot Subdwarf Stars and Related Objects*, eds. U. Heber, C. S. Jeffery & R. Napiwotzki, (San Francisco), 207–

Geier S., 2009, *PhD thesis*, Friedrich-Alexander-Universität Erlangen-Nürnberg

Giddings J., 1980, *PhD thesis*, University of London

Gourgouliatos K. N. and Jeffery C. S., 2006, MNRAS, **371**, 1381–1389

Groth H. G., Kudritzki R. P. and Heber U., 1985, A&A, **152**, 107–116

Gruschinske J. and Kudritzki R. P., 1979, A&A, **77**, 341–346

Hagen H.-J., Groote D., Engels D. and Reimers D., 1995, A&AS, **111**, 195–203

Hamann W.-R., Gruschinske J., Kudritzki R. P. and Simon K. P., 1981, A&A, **104**, 249–255

Han Z., Podsiadlowski P., Maxted P. F. L., Marsh T. R. and Ivanova N., 2002, MNRAS, **336**, 449–466

Han Z., Podsiadlowski P., Maxted P. F. L. and Marsh T. R., 2003, MNRAS, **341**, 669–691

Han Z., Podsiadlowski P. and Lynas-Gray A., 2007, MNRAS, **380**, 1098–1118

Han Z., 2008, A&A, **484**, 31–34

Heber U., Hunger K., Jonas G. and Kudritzki R. P., 1984, A&A, **130**, 119–130

Heber U., 1986, A&A, **155**, 33–45

Heber U., Edelmann H., Lisker T. and Napiwotzki R., 2003, A&A, **411**, 477–480

Heber U., Maxted P. F. L., Marsh T. R., Knigge C. and Drew J. E., 2003, in ASP Conf. Ser. **288**: *Stellar Atmosphere Modelling*, eds. I. Hubeny, D. Mihalas & K. Werner, (San Francisco: ASP), 251–254

Heber U. and Edelmann H., 2004, Astrophyics and Space Science, **291**, 341–349

Hügelmeyer S. D., 2006, *Diploma thesis*, Georg-August Universität Göttingen

Humason M. L. and Zwicky F., 1947, ApJ, **105**, 85–91

Iben I. Jr and Tutukov A. V., 1986, ApJ, **311**, 753–761

Iben I. Jr, 1990, ApJ, **353**, 215–235

Iben I. Jr and Livio M., 1993, PASP, **105**, 1373–1406

Ivezić Ž., Tabachnik S., Rafikov R., et al., 2001, AJ **122**, 2749–2784

Jeffery C. S., Drilling J. S., Harrison P. M., Heber U. and Moehler S., 1997, A&AS, **125**, 501–510

Jeffery C. S., 2002, ASP Conf. Ser. **279**: *Exotic Stars as Challenges to Evolution*, eds. C. A. Tout & W. Van Hamme, (San Francisco: ASP), 53–58

Jeffery C. S. and Saio H., 2002, in ASP Conf. Ser. **263**: *Stellar Collisions, Mergers and their Consequences*, eds. M. M. Shara, (San Francisco: ASP), 239–251

Jeffery C. S. and Saio H., 2007, MNRAS, **263**, 379–383

Jester S., Schneider D. P., Richards G. T., et al., 2005, AJ, **130**, 873–895

Kalirai J. S., Bergeron P., Hansen B. M. S., Kelson D. D., Reitzel D. B., Rich R. M., and Richer H. B., 2009, arXiv:0705.0977v3 [astro-ph]

Karl C. A., 2004, *PhD thesis*, Friedrich-Alexander-Universität Erlangen-Nürnberg

Kaufer A., Stahl O., Tubbesing S., Nørregaard P., Avila G., Francois P., Pasquini L., and Pizella A., 1999, The Messenger, **95**, 8–12

Kilkenny D., Koen C., O'Donoghue D. and Stobie R. S., 1997, MNRAS **285**, 640–644

Kilkenny D., van Wyk F., Roberts G., Marang F. and Cooper D., 1997, MNRAS **294**, 93–104

Kudritzki R. P., 1976, A&A **52**, 11–21

Külebi B., Jordan S., Euchner F., Gänsicke B., and Hirsch H., 2009, arXiv:0907.2372v1 [astro-ph.SR]

Lanz T., Brown T. M., Sweigart A. V., Hubeny I. and Landsman W. B., 2004, A&A, **602**, 342–355

Lisker T., Heber U., Napiwotzki R., Christlieb N., Han Z., Homeier D. and Reimers D., 2005, A&A, **430**, 223–243

Livio M., 2000, in *Type Ia Supernovae Theory and Cosmolgy*, eds. J. C. Niemeyer & J. W. Truran, (Cambridge University Press), 33–48

Lynas-gray A. E., 2004, Astrophyics and Space Science, **291**, 197–203

Maxted P. F. L., Marsh T. R. and North R. C., 2000, MNRAS, **317**, 41–44

Maxted P. F. L., Heber U., Marsh T. R. and North R. C., 2001, MNRAS, **326**, 1391–1402

Mengel J. G., Norris J. and Gross P. G., 1976, ApJ, **204**, 488–492

Michaud G., Bergeron P., Heber U. and Wesemael F., 1989, AJ, **338**, 417–423

Miller Bertolami M. M., Althaus L. G., Unglaub K. and Weiss A., 2008, A&A, **491**, 253–265

Moehler S., Sweigart A. V., Landsman W. B., Hammer N. J. and Dreizler S., 2004, A&A, **415**, 313–323

Moehler S., Dreizler S., Lanz T., Bono G., Sweigart A. V., Calamida A., Monelli M. and Nonino M., 2007, A&A, **475**, L5–L8

Moni Bidin et al.(2006)Moni Bidin C., Moehler S., Piotto S., Recio-Blanco A., Momany Y. and Méndez, 2006, A&A, **451**, 499-513

Morales-Rueda L., Maxted P. F. L., Marsh T. R., North R. C. and Heber U., 2003, MNRAS, **338**, 752–764

Napiwotzki R., 1997, A&A, **322**, 256–265

Napiwotzki R., 1999, A&A, **350**, 101–119

Napiwotzki R., Christlieb N., Drechsel H., et al., 2003, The Messenger, **112**, 25–30

Napiwotzki R., Karl C. A., Lisker T., Heber U., Christlieb N., Reimers D., Nelemans G. and Homeier D., 2004, Astrophysics and Space Science, **291**, 321–328

Napiwotzki R., Yungelson L., Nelemans G., et al., 2004, in ASP Conf. Ser. **318**: *Spectroscopically and Spatially Resolving the Components of the Close Binary Stars*, eds. R. W. Hilditch, H. Hensberge & K. Pavlovski, (San Francisco: ASP), 402–410

Napiwotzki R., Karl C. A., Nelemans G., et al., 2005, in ASP Conf. Ser. **334**: *14th European Workshop on White Dwarfs*, eds. D. Koester & S. Moehler, (San Francisco: ASP), 375–380

Napiwotzki R., Karl C. A., Nelemans G., et al., 2007, in ASP Conf. Ser. **372**: *15th European Workshop on White Dwarfs*, eds. R. Napiwotzki & M. R. Burleigh, (San Francisco: ASP), 387–392

Napiwotzki R., 2008, in ASP Conf. Ser. **392**: *Hot Subdwarf Stars and Related Objects*, eds. U. Heber, S. Jeffery & R. Napiwotzki, (San Francisco: ASP), 139–150

Nelder J. A. and Mead R., 1965, Computer Journal **7**, 308–313

Newberg H. J., Yanny B. and Willett B. A., 2009, arXiv:0906.3291v1 [astro-ph.GA]

Newell E. B., 1973, ApJS, **26**, 37–82

O'Connell R. W., 1999, ARA&A, **37**, 603–648

O'Toole S. J., Jordan S., Friedrich S. and Heber U., 2005, A&A, **437**, 227–234

O'Toole S. J., Napiwotzki R., Heber U., Drechsel H., Frandsen S., Grundahl F. and Bruntt H., 2006, Baltic Astronomy, **15**, 61–64

Paczyński B., 1971, AcA, **21**, 1–14

Paczyński B., 1976, in *Structure and Evolution of Close Binary Systems*, eds. P. P. Eggleton, S. Mitton & J. Whelan, (Dordrecht: Kluwer) 75

Podsiadlowski P., 2008, in ASP Conf. Ser. **391**: *Hydrogen deficient stars*, eds. K. Werner & T. Rauch, (San Francisco: ASP), 323–333

Press W. H., Teukolsky S. A., Vetterling W. T. and Flannery B. P., 1986, *Numerical Recipes in FORTRAN: the art of scientific computing*, 2nd ed., Cambridge University Press, 402–406

Rauch T., 1993, A&A, **276**, 171–183

Raskin C., Timmes F. X., Scannapieco E., Diehl S., and Fryer C., 2009, arXiv:0907.3915v2 [astro-ph.SR]

Reimers D., 1975, Mém. Soc. Roy. Sci. Liége, vol. 8, p. 369–382

Renzini A., 1990, in ASP Conf. Ser. **11**: *Confrontation Between Stellar Pulsation and Evolution*, eds. C. Cacciari & G. Clementini, (San Francics: ASP), 549–556

Richter R., 2006, *Diploma thesis*, Friedrich-Alexander-Universität Erlangen-Nürnberg

Rodríguez-López C., Moya A., Garrido R., MacDonald J., Ulla A., Dreizler S., Hügelmeyer S. D. and Manteiga M., 2006, Baltic Astronomy, **15**, 313–316

Rodríguez-López C., Ulla A. and Garrido R., 2007, MNRAS, **379**, 1123–1132

Rosswog S., Kasen D., Guillochon J., and Ramirez-Ruiz E., 2009, arXiv:0907.3196v1 [astro-ph.HE]

Rybicki G. B. and Hummer D. G., 1991, A&A, **245**, 171–181

Saffer R. A., Bergeron P., Koester D. and Liebert J., 1994, ApJ, **432**, 351–366

Saio H. and Jeffery C. S., 2000, MNRAS, **313**, 671–677

Schlegel D.J., Finkbeiner D.P. and Davis M., 1998, ApJ, **500**, 525–553

Schönberner D., 1979, A&A, **79**, 108–114

Schönberner D., 1983, ApJ, **272**, 708–714

Simon K. P. 1982, A&A, **107**, 313–319

Skrutskie M. F., Cutri R. M., Stiening R., et al., 2006, AJ, **131**, 1163

Stoughton C., Lupton R. H., Bernandi M. et al., 2002, AJ, **123**, 485–548

Ströer A., Heber U., Lisker T., Napiwotzki R., Dreizler S., Chrislieb N. and Reimers D., 2007, A&A, **462**, 269–280

Sweigart A., 1997, in *3rd Conference on Faint Blue Stars*, eds. A. G. D. Philip, J. Liebert, R. Saffer & D. S. Hayes, (Schenectady: L. Davis Press), 3–25

Tegmark M., Blanton M. R., Strauss M. A., et al., 2004, ApJ, **606**, 702–740

Unglaub K., 2008, A&A, **486**, 923–940

Valyavin G., Bagnula S., Fabrika S., Reisenegger A., Wade G. A., Han I. and Monin D. 2006, ApJ, **648**, 559–564

Webbink R. F., 1984, ApJ, **277**, 355–360

Werner K. and Husfeld D., 1985, A&A, **148**, 417–422

Werner K. and Dreizler S., 1996, J. Comput. Appl. Math., **109**, 65–93

Werner K., Deetjen J. L., Dreizler S., Nagel T., Rauch T., and Schuh S. L., 2003, ASP Conf. Ser., **288**, *Stellar Atmosphere Modeling*, eds. I. Hubeny, D. Mihalas & K. Werner, 31–50

Wisotzki L., Wamsteker W. and Reimers D., 1991, A&A, **247**, 17–20

Woudt P. A., Kilkenny D., Zietsman E., et al., 2006, MNRAS, **371**, 1497–1502

York D. G., Adelman J., Anderson J. E., et al., 2000, AJ, **120**, 1579–1587

Lebenslauf

Name	Heiko Andreas Hirsch	
Geburtsdatum	05.03.1980	
Staatsangehörigkeit	deutsch	

Schulbildung	08/1980 - 07/1984	Grundschule Kleinschwarzenlohe
	08/1984 - 06/1999	Adam-Kraft-Gymnasium Schwabach
Grundwehrdienst	07/1999 - 03/2000	Donauwörth
Studium	10/2000 - 02/2006	Studium der Physik an der Friedrich-Alexander-Universität Erlangen-Nürnberg
	31.01.2006	Abschluß: Dipl.-Phys. Univ.
	ab 01.02.2006	Promotionsstudent an der Dr.-Remeis-Sternwarte Bamberg Betreuer: Prof. Dr. U. Heber
Berufliche Laufbahn	02/2005 - 01/2006	Studentische Hilfskraft an der Dr.-Remeis-Sternwarte Bamberg
	02/2006 - 05/2009	Wissenschaftl. Mitarbeiter an der Dr.-Remeis-Sternwarte Bamberg
	07/2009 - 08/2009	Studentische Hilfskraft an der Dr.-Remeis-Sternwarte Bamberg

Curriculum Vitae

Name	Heiko Andreas Hirsch	
Date of birth	Mar 5th 1980	
Citizenship	German	

University	since Feb 2006	PhD student at the Dr.-Remeis Observatory Bamberg, Germany Supervisor: Prof. Dr. U. Heber
	Jan 31st 2006	Degree: Dipl.-Phys. Univ.
	Oct 2000 - Feb 2006	Undergraduate studies of physics at the Friedrich-Alexander-University of Erlangen-Nuremberg, Germany

Secondary School	Aug 1984 - Jun 1999	Adam-Kraft-Gymnasium Schwabach
Primary School	Aug 1980 - Jul 1984	Grundschule Kleinschwarzenlohe

Military Service	Jul 1999 - Mar 2000	Donauwörth

Employment History	Jul 2009 - Aug 2009	Student assistant at the Dr.-Remeis Observatory Bamberg
	Feb 2006 - May 2009	Scientific assistant at the Dr.-Remeis Observatory Bamberg
	Feb 2005 - Jan 2006	Student assistant at the Dr.-Remeis Observatory Bamberg